Physics Reports 467 (2008) 1–116

Contents lists available at ScienceDirect

Physics Reports

journal homepage: www.elsevier.com/locate/physrep

# Discrete breathers — Advances in theory and applications

Sergej Flach [a,*], Andrey V. Gorbach [b]

[a] Max-Planck-Institut für Physik komplexer Systeme, Nöthnitzer Str. 38, D-01187 Dresden, Germany

[b] Centre for Photonics and Photonic Materials, Department of Physics, University of Bath, Bath BA2 7AY, UK

ARTICLE INFO

*Article history:*
Accepted 7 May 2008
Available online 20 May 2008
editor: I. Procaccia

*PACS:*
02.00.00
05.00.00
05.10.-a
45.00.00
45.10.-b
03.75.Lm
67.85.Hj
42.65.-k
63.00.00
63.20.Ry

*Keywords:*
Anharmonic lattice dynamics
Discrete breathers
Localization

ABSTRACT

Nonlinear classical Hamiltonian lattices exhibit generic solutions — discrete breathers. They are time-periodic and (typically exponentially) localized in space. The lattices have discrete translational symmetry. Discrete breathers are not confined to certain lattice dimensions. We will introduce the concept of these localized excitations and review their basic properties including dynamical and structural stability. We then focus on advances in the theory of discrete breathers in three directions — scattering of waves by these excitations, persistence of discrete breathers in long transient processes and thermal equilibrium, and their quantization. The second part of this review is devoted to a detailed discussion of recent experimental observations and studies of discrete breathers, including theoretical modelling of these experimental situations on the basis of the general theory of discrete breathers. In particular we will focus on their detection in Josephson junction networks, arrays of coupled nonlinear optical waveguides, Bose–Einstein condensates loaded on optical lattices, antiferromagnetic layered structures, PtCl based single crystals and driven micromechanical cantilever arrays.



**Contents**



*Abbreviations:* BEC, Bose–Einstein condensate; BEM, band edge mode; DB, discrete breather; DNLS, discrete nonlinear Schrödinger equation; DS, discrete soliton; FPU, Fermi, Pasta and Ulam; ILM, intrinsic localized mode; NLS, nonlinear Schrödinger equation; PDE, partial differential equation; PO, periodic orbit; QB, quantum breather; RWA, rotating wave approximation.

* Corresponding author. Tel.: +49 3518712103; fax: +49 3518712199.
*E-mail address:* flach@pks.mpg.de (S. Flach).

0370-1573/$ – see front matter © 2008 Elsevier B.V. All rights reserved.
doi:10.1016/j.physrep.2008.05.002

## 1. Introduction

This review is about localized excitations in spatially extended discrete systems, i.e. lattices. These systems are translationally invariant, implying the absence of disorder or defects. The common expectation (throw a stone into the water of a lake, and follow the evolution of the localized surface wave perturbation) is that an initially localized excitation should distribute its energy over the entire system in the course of time. What could stop such a delocalization process? It needs just two ingredients — the above-mentioned discreteness of a system, and evolution equations which are nonlinear. As a result a new paradigm of nonlinear science recently emerged — the concept of *discrete breathers* (DB), equally coined *intrinsic localized modes* (ILM) in solid state physics and *discrete solitons* (DS) in nonlinear optics. These exact solutions of a huge variety of underlying nonlinear lattice models are typically characterized by being *time-periodic* and *spatially localized*, independent of the actual (assumed to be large) size of the lattice, independent of the spatial dimension of the lattice, mostly independent of the actual choice of nonlinear forces acting on the lattice, etc. Mastering their mathematical properties in *Hamiltonian* lattices allows one with relative ease to include also effects of dissipation, driving, quantization, to name a few important ones.

Nonlinearity is inherent to many systems in nature [75]. Discreteness is common as well — e.g. solids (crystals) and molecules which provide a natural underlying lattice, and artificial systems, based e.g. on Bose–Einstein condensates, Josephson junctions, optical devices, or micromechanical devices, which involve lattice structures. It thus makes perfect

sense to understand the mechanisms of localization in nonlinear lattices and to apply the knowledge to various fields of physics, chemistry, biology and mechanics.

The first report by Ovchinnikov on localized excitations in one-dimensional chains of coupled anharmonic oscillators dates back to 1969 [298]. Kosevich and Kovalev reported on similar results in 1974 [226]. After a long temporal gap Sievers and Takeno took up the issue again considering the famous Fermi–Pasta–Ulam (FPU) chain and obtaining localized excitations there, starting in 1988 [369,380,378]. Page, and Sandusky et al., added the first studies of the stability of various mode patterns [301,345]. At that time Campbell and Peyrard observed (and coined the term for) these excitations – discrete breathers – in various lattice models, as a positive result of the unsuccessful search for breathers in nonlinear field equations [55]. From the beginning of the 1990s a large number of research groups began to study these localized excitations with great mathematical rigour and detail. The review [133], though published in 1998, was essentially written in 1996 — in the midst of this process. Since then a considerable amount of further mathematical beauty was (and still is being) added to the theory of localized excitations. Most importantly, since 1998 experimental studies were initiated, on a large variety of very different systems, demonstrating the fruitfulness of the concept of localization by discreteness and nonlinearity [43,54,57,387]. In the following we will review these new developments, briefly touching basic aspects known before. The interested reader can also consult the collection of lectures of a summer school in Les Houches in 2003 [74], as well as further reports in the field [18,20,121,368].

### 1.1. Nonlinearity and symmetry — the dimer

Nonlinearity has a crucial impact on the symmetry properties of dynamical systems. Consider the evolution of a linear system (say coupled ordinary differential equations, or a partial differential equation). Linearity implies that the solutions of the equations can be found by considering an eigenvalue problem. The symmetries of the original equations will also be represented in the eigenvalue problem. Excluding potential degeneracies, these symmetries will be transported to the solutions — the eigenvectors. By introducing nonlinearity we cannot reduce the dynamical equations to an eigenvalue problem, and consequently the solutions of the dynamical system do not have to obey the symmetries which the underlying dynamical system has.

Let us give a simple example using the Nonlinear Schrödinger dimer, which serves as a toy model for the energy exchange between two bonds in a small molecule, Bose–Einstein condensates trapped in two wells, a large spin with easy-axis anisotropy in a transverse magnetic field, among others. The Hamiltonian is given by

$$H = \Psi_1^*\Psi_1 + \Psi_2^*\Psi_2 + v_4\frac{1}{2}\left((\Psi_1^*\Psi_1)^2 + (\Psi_2^*\Psi_2)^2\right) + C\left(\Psi_1^*\Psi_2 + \Psi_2^*\Psi_1\right). \tag{1.1}$$

The equations of motion are $\dot{\Psi}_{1,2} = \mathrm{i}\partial H/\partial\Psi_{1,2}^*$:

$$-\mathrm{i}\dot{\Psi}_{1,2} = \Psi_{1,2} + v_4|\Psi_{1,2}|^2\Psi_{1,2} + C\Psi_{2,1}. \tag{1.2}$$

The Hamiltonian and the equations of motion are invariant under permutation of the two indices $1 \leftrightarrow 2$. What about the solutions? Can we find solutions where either $|\Psi_1|$ or $|\Psi_2|$ is strongly excited, while the other one is not?

For $v_4 = 0$ the equations become linear, and the solutions, after a trivial shift in time, become

$$\Psi_{1,2} = a_s\mathrm{e}^{\mathrm{i}\omega_s t} \pm a_a\mathrm{e}^{\mathrm{i}(\omega_a t+\phi)} \tag{1.3}$$

where $\omega_{s,a} = 1 \pm C$ and $a_{s,a}, \phi$ are real. It follows that

$$|\Psi_{1,2}|^2 = a_s^2 + a_a^2 \pm 2a_s a_a\cos(2Ct - \phi). \tag{1.4}$$

Whatever the choice of the initial conditions $a_s$, $a_a$, $\phi$ is — a shift of time $t \to t + \pi/(2C)$ will be equivalent to a permutation $|\Psi_1| \leftrightarrow |\Psi_2|$. The permutation symmetry of the equation is reflected in the permutation symmetry of the solutions.

For $v_4 \neq 0$ and $B = |\Psi_1|^2 + |\Psi_2|^2 > 2C/v_4$ Eq. (1.2) permits other solutions of the form

$$\Psi_{1,2} = A_{1,2}\mathrm{e}^{\mathrm{i}(1+v_4B)t}, \tag{1.5}$$

where the amplitudes satisfy $A_1 = A_+, A_2 = A_-$ or vice versa $A_1 = A_-, A_2 = A_+$ with

$$A_\pm^2 = \frac{1}{2}B\left(1 \pm \sqrt{1 - \frac{4C^2}{v_4^2B^2}}\right). \tag{1.6}$$

These solutions are not invariant under permutation $1 \leftrightarrow 2$. They are characterized by a strong excitation of either of the two sites, while the other one is weakly excited — for all times.

Having introduced nonlinearity, why do we then need discreteness, if we want to obtain localization of excitations? Or in other words, why don't we use spatially continuous partial differential equations (PDE) which describe the evolution of some physical fields? A detailed discussion on that issue can be found in [133]. Rather than repeating that discussion again, let us give here an essence of these thoughts. While a few cases of PDEs (in one spatial dimension) are known, which admit

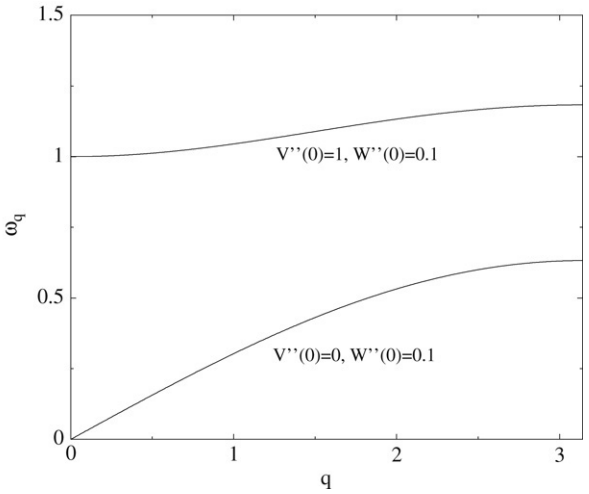


**Fig. 1.** The dispersion relation of small amplitude plane waves of the model (1.7). Only the positive frequency axis is shown.

localized (nontopological) excitations, decade-long efforts to generalize these results to other PDEs have failed, including also extension to larger space dimensions. Many studies indicated that the reason is simply resonances of the dynamics of a local excitation with the spectrum of plane waves of the nonexcited part of the system. These resonances lead to a radiation of energy out of the core of a local excitation and to its ultimate decay. The reader will see in the next section, why and how a spatial lattice solves this problem, thus removing all obstacles and making localized excitations exact solutions.

### *1.2. Spatial discreteness and nonlinearity*

Let us study the combined effect of nonlinearity and discreteness on the spatial localization of a discrete breather on a basic level. For that we look into the dynamics of a one-dimensional chain of interacting (scalar) oscillators or atoms with the Hamiltonian

$$H = \sum_n \left[ \frac{1}{2} p_n^2 + V(x_n) + W(x_n - x_{n-1}) \right]. \tag{1.7}$$

The integer $n$ marks the lattice site number of a possibly infinite chain, and $x_n$ and $p_n$ are the canonically conjugated coordinate and momentum of a degree of freedom associated with site number $n$. The on-site potential $V$ and the interaction potential $W$ satisfy $V'(0) = W'(0) = 0, V''(0), W''(0) \geq 0$. This choice ensures that the classical ground state $x_n = p_n = 0$ is a minimum of the energy $H$. The equations of motion read

$$\dot{x}_n = p_n, \quad \dot{p}_n = -V'(x_n) - W'(x_n - x_{n-1}) + W'(x_{n+1} - x_n). \tag{1.8}$$

Let us linearize the equations of motion around the classical ground state. We obtain a set of linear coupled differential equations with solutions being small amplitude plane waves:

$$x_n(t) \sim \mathrm{e}^{\mathrm{i}(\omega_q t - qn)}, \quad \omega_q^2 = V''(0) + 4W''(0) \sin^2\left(\frac{q}{2}\right). \tag{1.9}$$

These waves are characterized by a wave number $q$ and a corresponding frequency $\omega_q$. All allowed plane wave frequencies fill a part of the real axis which is called the linear spectrum. Due to the underlying lattice the frequency $\omega_q$ depends periodically on $q$ and its absolute value has always a *finite upper bound*. The maximum (Debye) frequency of small amplitude waves $\omega_\pi = \sqrt{V''(0) + 4W''(0)}$. The dispersion relation $\omega_q$ is shown in Fig. 1. Depending on the choice of the potential $V(x)$, it can be either acoustic- or optic-like, $V(0) = 0$ and $V(0) \neq 0$, respectively. In the first case the linear spectrum covers the interval $-\omega_\pi \leq \omega_q \leq \omega_\pi$ which includes $\omega_{q=0} = 0$. In the latter case an additional (finite) gap opens for $|\omega_q|$ below the value $\omega_0 = \sqrt{V''(0)}$. Two further characteristics of the linear spectrum are the group velocity $v_g$ and the phase velocity $v_{ph}$. The group velocity $v_g(q) = \mathrm{d}\omega_q/\mathrm{d}q$ is a periodic function of $q$ and describes the propagation speed of a wavepacket centered at $q$. At the edge of the linear spectrum $v_g = 0$. Otherwise its absolute value has a finite upper bound. The phase velocity $v_{ph} = \omega_q/q$ is a nonperiodic oscillating function of $q$. It covers the whole real axis for an optic-like linear spectrum since $\omega_{q=0} \neq 0$. Its absolute value has a finite upper bound $|v_{ph}| \leq v_g(q = 0)$ for acoustic-like linear spectra.

For large amplitude excitations the linearization of the equations of motion is no longer correct. Similar to the case of a single anharmonic oscillator, the frequency of possible time-periodic excitations will depend on the amplitude of the excitation, and thus may be located outside the linear spectrum. Let us assume that a time-periodic and spatially localized

state, i.e. a *discrete breather*, $\hat{x}_n(t+T_b) = \hat{x}_n(t)$ exists as an exact solution of Eqs. (1.8) with the period $T_b = 2\pi/\Omega_b$. Due to its time periodicity, we can expand $\hat{x}_n(t)$ into a Fourier series

$$\hat{x}_n(t) = \sum_k A_{kn} \mathrm{e}^{\mathrm{i}k\Omega_b t}. \tag{1.10}$$

The Fourier coefficients are by assumption also localized in space

$$A_{k,|n|\to\infty} \to 0. \tag{1.11}$$

Inserting this ansatz into the equations of motion (1.8) and linearizing the resulting algebraic equations for Fourier coefficients in the spatial breather tails (where the amplitudes are by assumption small) we arrive at the following linear algebraic equations:

$$k^2\Omega_b^2 A_{kn} = V''(0)A_{kn} + W''(0)(2A_{kn} - A_{k,n-1} - A_{k,n+1}). \tag{1.12}$$

If $k\Omega_b = \omega_q$, the solution to (1.12) is $A_{k,n} = c_1\mathrm{e}^{\mathrm{i}qn} + c_2\mathrm{e}^{-\mathrm{i}qn}$. Any nonzero (whatever small) amplitude $A_{k,n}$ will thus oscillate without further spatial decay, contradicting the initial assumption. If however

$$k\Omega_b \neq \omega_q \tag{1.13}$$

for any integer $k$ and any $q$, then the general solution to (1.12) is given by $A_{k,n} = c_1\kappa^n + c_2\kappa^{-n}$ where $\kappa$ is a real number depending on $\omega_q$, $\Omega_b$ and $k$. It always admits an (actually exponential) spatial decay by choosing either $c_1$ or $c_2$ to be nonzero. In order to fulfill (1.13) for at least one real value of $\Omega_b$ and any integer $k$, we have to request $|\omega_q|$ to be bounded from above. That is precisely the reason why the spatial lattice is needed. In contrast most spatially continuous field equations will have linear spectra which are unbounded. That makes resonances of higher order harmonics of a localized excitation with the linear spectrum unavoidable. The nonresonance condition (1.13) is thus an (almost) necessary condition for obtaining a time-periodic localized state on a Hamiltonian lattice [249,110].

The performed analysis can be extended to more general classes of discrete lattices, including e.g. long-range interactions between sites, more degrees of freedom per each site, higher-dimensional lattices etc. But the resulting non-resonance condition (1.13) keeps its generality, illustrating the key role of discreteness and nonlinearity for the existence of discrete breathers.

As with any rule, the nonresonance condition may also have exceptions. But as with any exception, there is a price to pay. When staying within the class of spatially continuous Hamiltonian systems, for the examples we will discuss below (Nonlinear Schrödinger equation, sin-Gordon equation) the price is imposing additional symmetries. While that may be of particular interest for a given application, in general additional symmetries restrict the richness of possible solutions. And losing the symmetries leads to a loss of localized excitations — at variance to the nonlinear lattice case, where no further symmetries are requested.

While the nonlinear lattice appears as a natural mathematical path to avoid resonances with plane waves as they happen in spatially continuous nonlinear Hamiltonian field equations, there are other ways the mind could take. If resonances with plane waves are an obstacle, then either remove the resonances or simply remove the plane waves! The first possibility can be realized by using a lattice, or restricting oneself to equations which either do not contain linear terms or where at least the linear interaction terms vanish making the linear spectrum degenerate — no matter whether for a lattice or a continuum. The second possibility – removing the plane waves – can be achieved by considering dissipative systems. Indeed dissipation will prevent the persistence of plane waves travelling over infinite distances. Thus delocalization by itself is not a problem then. The loss of energy inside a breather core due to dissipation has to be taken care of, by properly pumping the energy into the breather again. We will discuss examples, and note that a recently rapidly developing branch of *dissipative solitons* appears to follow exactly that latter path.

### 1.3. Why only time-periodic orbits?

In the previous section we demonstrated how the interplay between nonlinearity and discreteness supports time-periodic and spatially localized solutions — discrete breathers. What can we say about the existence of more general types of localized solutions with other than time-periodic dynamical behavior? An analogous approach yields, that for a quasi-periodic DB with $N$ incommensurate frequencies $\{\Omega_1, \Omega_2, \ldots, \Omega_N\}$ the non-resonance condition (1.13) transforms into [110]

$$\{k_1\Omega_1 + k_2\Omega_2 + \cdots + k_N\Omega_N\}^2 \neq \omega_q^2 \tag{1.14}$$

with $k_i$ being arbitrary integer numbers. In other words, neither any of the principal frequencies $\{\Omega_1, \Omega_2, \ldots \Omega_N\}$ nor any linear combination of their multiples should resonate with the linear spectrum. However any incommensurate pair of frequencies $\Omega_1$ and $\Omega_2$ with irrational ratio $\Omega_1/\Omega_2$ will generate an infinite number of pairs $k_1, k_2$ which violate the non-resonance condition (1.14) [110]. Therefore, in general quasiperiodic DBs are not expected to exist as exact spatially localized solutions.

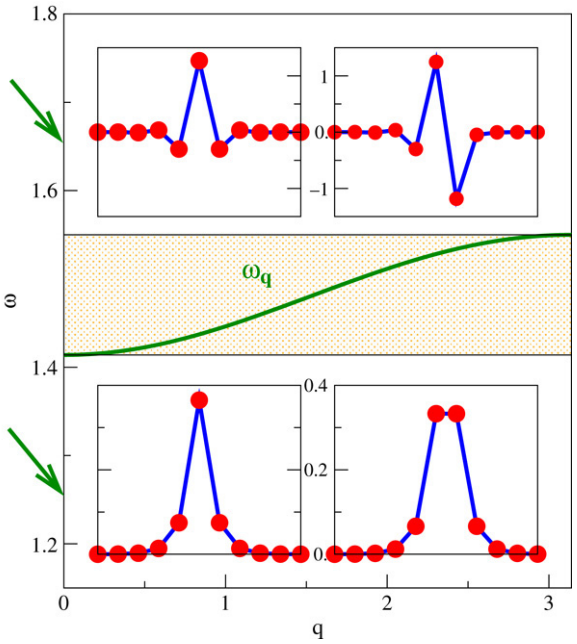


**Fig. 2.** The frequency versus wavenumber dependence of the linear spectrum for a one-dimensional chain of anharmonic oscillators with potentials (1.17). Chosen DB frequencies are marked with green arrows and lie outside the linear spectrum $\omega_q$. Red circles indicate the oscillator displacements for a given DB solution, with all velocities equal to zero. Lines connecting circles are guides for the eye. From [57].

Another question concerns the possibility of existence of moving DBs. A rather general definition of a moving DB assumes a localized object which translates $n$ sites in a certain direction after $m$ periods of internal oscillations with the ratio $n/m$ being in general irrational. In a one-dimensional chain such a moving DB corresponds to a solution of Eq. (1.8) in the form

$$x_n(t) = \phi(\xi, t), \quad \xi = n - Vt \tag{1.15}$$

$$\phi(\xi, t + T_b) = \phi(\xi, t), \quad \phi(\xi \to \pm\infty, t) \to 0. \tag{1.16}$$

A detailed analysis of possible resonances is discussed in chapter 4.5. It follows that one has to avoid resonances of the velocity $V$ with *phase velocities* $v_{ph}$ of small amplitude plane waves (of sometimes modified linear spectra as compared to the original underlying one). The essence is that these resonances cannot be avoided, so that moving DBs are not expected to be exact solutions for a general nonlinear lattice.

So moving DBs face the obstacle of resonances with phase velocities of plane waves. By removing the plane waves (c.f. previous section) we can again try to escape the above described resonances and construct quasiperiodic DBs and even moving DBs.

### *1.4. Examples of discrete breather solutions*

Let us show discrete breather solutions for various lattices. We start with a chain (1.7) with the functions

$$V(x) = x^2 + x^3 + \frac{1}{4}x^4, \qquad W(x) = 0.1x^2. \tag{1.17}$$

The spectrum $\omega_q$ is optic-like and shown in Fig. 2. Discrete breather solutions can have frequencies $\Omega_b$ which are located both below and above the linear spectrum. The time-reversal symmetry of (1.8) allows one to search for DB displacements $x_n(t = 0)$ when all velocities $\dot{x}_n(t = 0) = 0$. These initial displacements are computed with high accuracy (see following sections) and plotted in the insets in Fig. 2 [57]. We show solutions to two DB frequencies located above and below $\omega_q$ — their actual values are marked with the green arrows. To each DB frequency we show two different spatial DB patterns — among an infinite number of other possibilities, as we will see below. The high-frequency DBs ($\Omega_b \approx 1.66$) occur for large-amplitude, high-energy motion with adjacent particles moving out of phase. Low-frequency DBs ($\Omega_b \approx 1.26$) occur for small-amplitude motion with adjacent particles moving in phase.

In Fig. 3 we show two DB solutions for a Fermi–Pasta–Ulam chain of particles coupled via anharmonic springs $V(x) = 0$, $W(x) = \frac{1}{2}x^2 + \frac{1}{4}x^4$ (c.f. (1.7)) which has an acoustic-type spectrum [121]. The DB frequency is in both cases $\Omega_b = 4.5$. Again the displacements $x_n$ are shown for an initial time when all velocities vanish. In the inset we plot the strain $u_n = x_n - x_{n-1}$ on a log-normal scale. The DB solutions are exponentially localized in space.

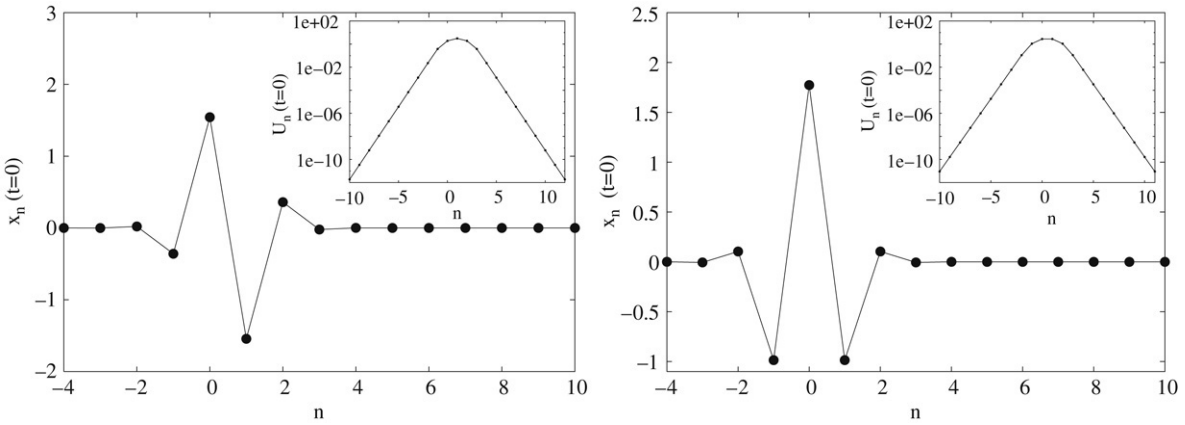


**Fig. 3.** Discrete breather solutions for a Fermi–Pasta–Ulam chain (see text). These states are frequently referred to as the Page mode (left) and the Sievers-Takeno mode (right). Figure from [121].

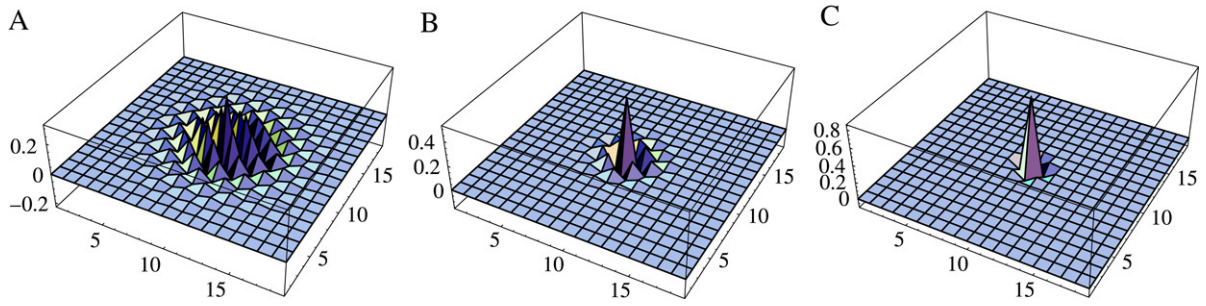


**Fig. 4.** Displacements of DBs on a two-dimensional lattice (1.18) with $k = 0.05$, all velocities equal to zero. (A) $\Omega_b = 1.188$; (B) $\Omega_b = 1.207$; (C) $\Omega_b = 1.319$. From [93].

Finally we show DB solutions for a *two-dimensional* square lattice of anharmonic oscillators with nearest neighbour coupling. The equations of motion read

$$\ddot{x}_{i,j} = k(x_{i+1,j} + x_{i-1,j} - 2x_{i,j}) + k(x_{i,j+1} + x_{i,j-1} - 2x_{i,j}) - x_{i,j} - x_{i,j}^3 \tag{1.18}$$

with oscillator potentials $V(x) = \frac{1}{2}x^2 + \frac{1}{4}x^4$. In Fig. 4 we plot the oscillator displacements with all velocities equal to zero for three different DB frequencies and $k = 0.05$ [93]. For all cases adjacent oscillators move out of phase.

We conclude this section by emphasizing that DB solutions can be typically localized on a few lattice sites, regardless of the lattice dimension. Thus little overall coherence is needed to excite a state nearby — just a few sites have to oscillate coherently, the rest of the lattice does not participate strongly in the excitation.

### *1.5. The discrete nonlinear Schrödinger equation*

One of the simplest discrete lattice models, which deserves special attention, is represented by the Discrete Nonlinear Schrödinger (DNLS) equation [89], which is a lattice generalization of the dimer example (1.1):

$$\mathrm{i}\frac{\mathrm{d}\psi_n}{\mathrm{d}t} + \epsilon\psi_n + C\,(\psi_{n+1} + \psi_{n-1}) + \gamma|\psi_n|^2\psi_n = 0. \tag{1.19}$$

Similar to the dimer case, this model allows time-periodic solutions where only one harmonic in the time evolution is excited. For that reason treatment of periodic orbits in DNLS models is relatively simple, making the model a playground to analyze basic nonlinear phenomena. On the other hand DNLS models can be derived as the approximate small-amplitude dynamics of more general nonlinear lattice models with on-site nonlinear potential (Klein–Gordon lattices) [133,285,73,212, 215], inter-site nonlinear interaction (Fermi–Pasta–Ulam lattices) [51,67,213,149] and for mixed type nonlinearities [181]. One essentially uses the Rotating Wave Approximation (RWA), which neglects the effect of higher harmonics generation. In the past decade a substantial growth of interest in DNLS models appeared due to their direct applicability to experimental setups of coupled nonlinear waveguide arrays [92] and Bose–Einstein condensates (BEC) trapped in periodical optical lattices [11]. We will discuss these experiments in more detail in Sections 10.2 and 10.3, respectively.

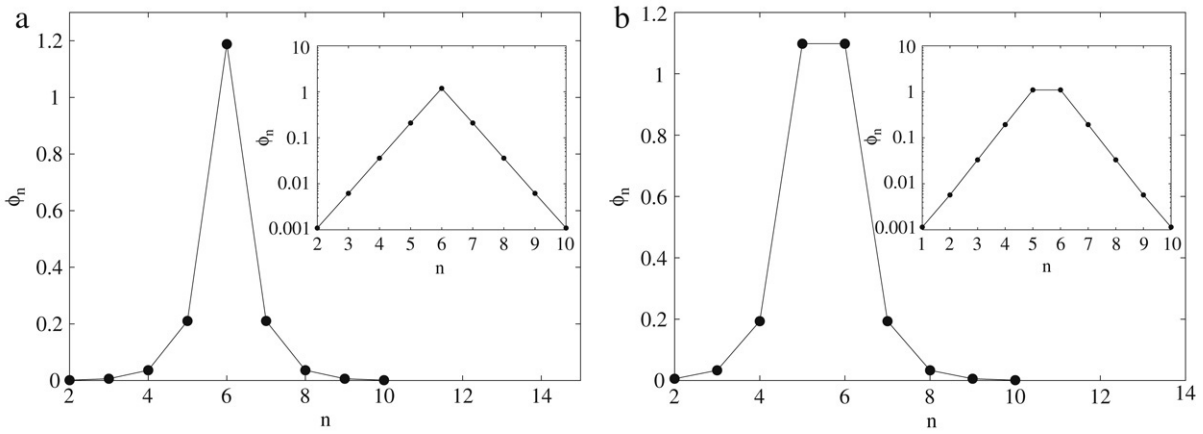


**Fig. 5.** Profiles of the single site (a) and two site (b) stationary DB solutions of Eq. (1.19) in a normal and log-normal (insets) plot. Parameter values are: $\Omega_b = 1.0,\ C = 0.25,\ \gamma = 1$. Lines are guiding the eye.

The DNLS possesses a gauge symmetry, i.e. if $\psi_n(t)$ is a solution to (1.19) then $\Psi_n(t) = \psi_n(t)\mathrm{e}^{-\mathrm{i}\epsilon t}$ is a solution to (1.19) with $\epsilon = 0$. So we can always gauge transform $\epsilon$ to zero. The staggering transformation $\psi_n \to (-1)^n\psi_n$ together with change of sign of time $t$ is equivalent to the change of sign of the nonlinear constant $\gamma$, therefore the latter can be always fixed to be positive. Furthermore, by rescaling the amplitudes $\psi_n \to \psi_n/\sqrt{\gamma}$ the coefficient $\gamma$ can be removed completely from Eq. (1.19). By additional scaling of time $t$ and amplitudes $\psi_n$ the coupling coefficient $C$ can be also fixed to be unity $C = 1$, however for the sake of considering the uncoupled limit $C \to 0$ it is sometimes useful to keep the coupling constant in Eq. (1.19).

The DNLS equation (1.19) (with $\epsilon = 0$) conserves the Hamiltonian

$$H = \sum_{n=1}^{N}\left[C(\psi_n^*\psi_{n+1} + \psi_n\psi_{n+1}^*) + \frac{\gamma}{2}|\psi_n|^4\right] \tag{1.20}$$

with canonically conjugated coordinates $\psi_n$ and momenta $i\psi_n^*$. In addition it also conserves the norm

$$N = \sum_n |\psi_n|^2. \tag{1.21}$$

The norm has a clear physical meaning being proportional to the total light power in the case of coupled optical waveguides or to the number of particles in a BEC. By scaling the amplitudes $\psi_n$ and the nonlinear coefficient $\gamma$ it is always possible to fix the norm to be unity $N = 1$. Alternatively, as mentioned above, by rescaling the amplitudes (and thus the norm) one can fix $\gamma = 1$.

The two conserved quantities, the Hamiltonian (1.20) and the norm (1.21), ensure integrability of Eq. (1.19) in the case of two coupled sites (dimer) (1.1) [178], while for more sites it is not integrable. It needs other structures of DNLS-type lattice models, like the Ablowitz–Ladik model [1] or the Izergin–Korepin model [170] to sustain integrability for arbitrary size.

Stationary solutions of the DNLS equation (1.19) have the form $\psi_n(t) = \phi_n \exp(\mathrm{i}\Omega_b t)$ with amplitudes $\phi_n$ satisfying algebraic equations

$$-\Omega_b\phi_n + C\,(\phi_{n+1} + \phi_{n-1}) + \gamma|\phi_n|^2\phi_n = 0. \tag{1.22}$$

Profiles of some basic stationary DB solutions are shown in Fig. 5. They were predicted and obtained by Christodoulides and Joseph [63]. In the uncoupled limit $C = 0$ (also known as anti-continuous limit [249,18]) these solutions asymptotically approach compact single-site or two-site excitations with one or two sites excited to the amplitude $\phi^{(0)} = \sqrt{\Omega_b/\gamma}$ and all the rest of the lattice amplitudes being exactly zero (see also [203,190]). Often these solutions are also coined site-centered and bond-centered DBs, respectively, referring to their spatial structures.

## 2. Existence proofs

This section is devoted to a brief discussion of existence proofs for discrete breathers. Certainly the fine mathematical aspects of rather different methods are outside the scope of the present work (but see for instance Ref. [20]). The situation is further complicated by the different possibilities of grouping various results. From a physics perspective, we prefer to group them according to the different model classes the proofs apply to. From a mathematics perspective, one would tend to group publications according to the techniques used — e.g. implicit function theorem, center manifold reductions, variational approaches, separation of variables, etc. This being a report for a physics community, we prefer the first way. The interested reader should consult Ref. [20], where the second way is explored. Additional results are summarized by Pankov [302].

### 2.1. Networks of weakly interacting anharmonic oscillators

From the present perspective the most important result in this field is due to MacKay and Aubry [249]. Though the case has been already discussed in [133,18], we nevertheless want to summarize these results. MacKay and Aubry consider d-dimensional lattice models of coupled anharmonic oscillators (cf. e.g. Eq. (1.18) for $d = 2$) in the limit of very weak interaction (anticontinuous limit). For zero interaction the oscillators decouple, and it is trivial to construct arbitrary spatially localized excitations. MacKay and Aubry choose those trajectories which are periodic in time, and time-reversible. These trajectories can be encoded by a sequence of time-periodic and time-reversible functions, where each of them is representing the time-dependence of the coordinate of an oscillator. Note that the period is one and the same for all functions. The sequence can be formally represented as a $N$-dimensional vector function, where $N$ is the number of oscillators, and each component is a time-periodic and time-reversible function. The vector can be embedded in a corresponding Banach space.

The original equations of motion are used to define a map of a vector from that Banach space onto another vector. Solutions of the equations of motion are those vectors which are mapped into the zero (origin) of the space. For zero interaction the simplest example is when one oscillator is excited and all others are at rest.

One of the most elegant parts of the existence proof of MacKay and Aubry is the use of the Implicit Function Theorem in order to show that when the interaction is small but nonzero, there is a new vector in the neighbourhood of the old one, which is still mapped into the origin, and thus there is a solution of the equations of motion. And moreover they use the norm properties of vectors from Banach space to show that the still existing but deformed vector solution corresponds to an exponentially localized excitation on the original lattice. Remarkably the necessary condition for the proof to work is the nonresonance condition (1.13). Note that in contrast to the localization argument in Section 1.2 the nonresonance is needed in the MacKay/Aubry paper not for the exponential localization, but for the very existence of the periodic orbit itself! However in particular cases even that restriction can be removed, as shown recently for purely harmonic oscillators with weak but purely anharmonic interaction potentials, where a strictly localized but noncompact excitation on the decoupled harmonic oscillator lattice is continued into the interaction case preserving its strong localization [116].

The power of that existence proof is that it is essentially insensitive to the lattice dimension, the type of interaction on the lattice, and the number of originally excited sites. Moreover the method turned out to be very flexible and can be adapted to many other situations as well. The above-mentioned restriction to time-reversible orbits helps to remove degeneracies, i.e. to exclude non-zero dimensional manifolds of vectors in the Banach space which contain the correct one, and which also map to the origin. In fact it is not time-reversibility itself, but the easy fixing of an overall phase for all periodic functions which is used. Later, the method has been modified to prove persistence of non-time-reversible periodic orbits as well [365].

### 2.2. Anharmonic interactions

Switching off the oscillator potentials, and leaving all the nonlinearity in the interactions makes things more complicated. The Fermi–Pasta–Ulam lattice is a prominent example. Here the above discussed proof does not apply, since for zero interactions we are left with free particles, which will not oscillate but propagate at constant velocities if excited. Therefore one needs other limiting cases that allow for a solution of the equations of motion. This requirement lead to an impressive series of mathematical studies which used different methods and techniques in order to tackle the problem.

The first proof of existence of DBs in such one-dimensional systems used the special case of homogeneous interaction potentials, which allows for a separation of time and space variables [111] (for a more detailed discussion see also Ref. [133]). This homoclinic orbit approach was recently also applied to nonlinear Schrödinger chains [325].

Livi, Spicci and MacKay considered more general potentials, but used the limit of strongly alternating particle masses instead [246]. In the limit of infinite (or zero) mass ratio the lattice dynamics is reduced to a special anticontinuous case of light masses oscillating between immobile heavy masses. With the help of the Implicit Function Theorem localized vibrations were continued into the regime of finite mass ratio. A similar approach was taken by Aubry, who dimerized a d-dimensional lattice, and considered the case of weak interactions between the dimers [19].

### 2.3. Breathers with frequencies close to the linear spectrum

So far we have discussed existence proofs which were limited to weak interactions, by literally cutting the interactions out, by choosing strongly alternating mass ratios, or by dimerizing the lattice. Another possibility is to consider the general case of finite interactions, but to take the limit of breathers having frequencies close to the linear spectrum. Aubry et al. performed a variational approach to rigorously prove the existence of DBs for essentially any lattices with pure convex interaction potentials [23]. James performed a center manifold reduction and proved the existence of weakly localized DBs in one-dimensional FPU chains [174], and extended together with Noble to arbitrary mass ratios of alternating masses [177] (see also Ref. [175] for an extensive review of that technique).

### 2.4. Applicability

A very important aspect of the existence proofs is the rigorous mathematical statement of existence by itself. Most of the above proofs are implicit, i.e. the existence of DBs is proven without explicit construction of the solutions. In exceptional

cases explicit solutions can be constructed [300,290] or even be obtained as part of a complete integration of the coupled lattice equations [1].

However, the case of weak interactions, and the limit of frequencies close to the linear spectrum, defines the precise form of the solutions in that very limit (e.g. [343,176]). Therefore, numerical continuation tools (see chapter 3) harvest on that information — they use the exact solution in the limit, the knowledge that it can be continued away from the considered limit, and therefore successfully generate solutions further and further away.

## 3. Computational methods for obtaining and analyzing discrete breathers

In this section we will briefly review the mostly widely used methods to observe DBs in numerical runs, to obtain them as exact solutions with high accuracy (basically, up or close to machine precision) and to analyze them. The interested reader can find more detailed information in [115].

### 3.1. Targeted initial conditions

One of the easiest ways to observe DBs in numerical runs is to use targeted initial conditions: put an initially localized excitation (strong enough so that the nonlinear terms become non-negligible in the corresponding equations of motion) in the otherwise non-excited lattice. Since the non-resonance condition (1.13) can be satisfied in a rather general class of discrete nonlinear lattices, the chances are very high, that localization will persist in the dynamics.

To illustrate this, let us take a 1D lattice with the Hamiltonian (1.7) and choose the potentials [133,131,134]

$$V(x) = \frac{x^2}{2} - \frac{x^3}{3} + \frac{x^4}{4}, \qquad W(x) = 0.1\frac{x^2}{2}. \tag{3.1}$$

At time $t = 0$ we displace site $l = 0$ by a certain amount $x_0(0)$, while all other sites are at rest $p_l(0) = 0, x_{l\neq 0}(0) = 0$. Then we integrate the equations of motion e.g. using the Verlet method [160]. We expect at least a part of the initially localized energy excitation to spread among the other sites. This may induce finite size effects due to recurrence of emitted waves which travel around the whole system and return to the original excitation point. The simplest way to avoid these effects is to choose the system size large enough, so that during the time of integration the radiation simply does not reach the boundaries. In our case the maximum group velocity of plane waves [derived from the dispersion relation (1.9)] is of the order 0.1. This implies, that, by taking the system size $N = 3000$, our simulation will emulate the behavior of an infinite chain with the above initial conditions up to $t_{\max} \sim 30\,000$.

To monitor the evolution of the system we define the discrete energy density

$$e_l = \frac{1}{2}p_l^2 + V(x_l) + \frac{1}{2}(W(x_l - x_{l-1}) + W(x_{l+1} - x_l)). \tag{3.2}$$

The sum over all local energy densities gives the total conserved energy. If DBs are excited, the initial local energy excitation should mainly remain at its initial excitation position. Thus, we will monitor the amount of energy stored in $(2m + 1)$ sites surrounding the central one

$$e_{(2m+1)} = \sum_{-m}^{m} e_l. \tag{3.3}$$

If this function does not decay to zero or does so on a sufficiently slow time scale, the existence of a breather-like object can be confirmed. The term 'slowly enough' has to be specified with respect to the group velocities of small amplitude plane waves, i.e. with respect to the characteristic time for linear phonons to escape a volume of size $m$. The estimate for $m = 2$ gives the corresponding time scale $t_{\min} \sim 10$ [131,134]. In Fig. 6 the time dependence of $e_{(5)}$ for an initial condition $x_0(t = 0) = 2.3456$ is shown [131,134]. Clearly a localized excitation is observed. After a short time period, of the order of 100 time units, nearly constant values of $e_{(5)}$ are achieved. The breather-like object is stable over a long period of time with some weak indication of energy radiation. The energy distribution within the object is shown in the inset of Fig. 6. Essentially three lattice sites are involved in the motion.

Analogous procedures can be performed with higher-dimensional lattices, leading to qualitatively the same result. In Fig. 7 the residual energy distribution in a DB-like excitation is shown, and the inset displays the time dependence of a local energy similar to $e_{(5)}(t)$, for the 2D generalization of the above model [125].

The method of targeted initial conditions is very effective for demonstration of the general concept of dynamical localization in nonlinear lattices. However, it is certainly not suitable for obtaining DB solutions with a reasonable precision. It suffers from transient times needed for the system to relax and for radiation to escape the localization region. Despite the relatively fast escape of the main radiative part indicated in Fig. 6, the relaxed localized structure in many cases is a DB with several localized modes excited on top of it. Performing quasiperiodic dynamics, such an object induces resonances with small-amplitude extended states resulting in further relaxation processes, which may be extremely slow [134]. Also one has to deal with the problem of finite size effects causing reflection of the radiated waves on the boundaries. The use of

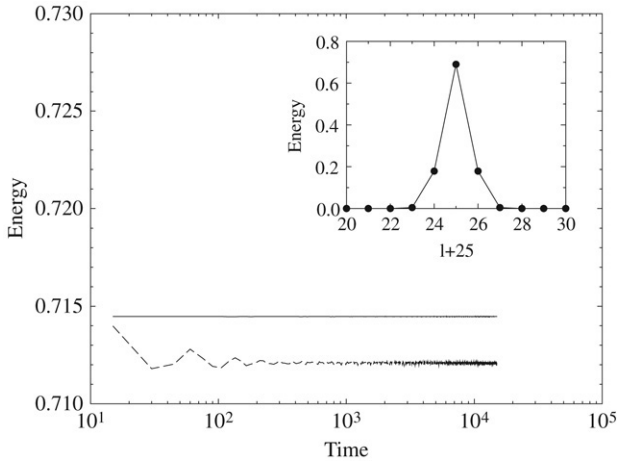


**Fig. 6.** $e_{(5)}$ versus time (dashed line). Total energy of the chain, solid line. Inset: energy distribution $e_l$ versus particle number for the same solution measured for $1000 < t < 1150$. Figure from [131].

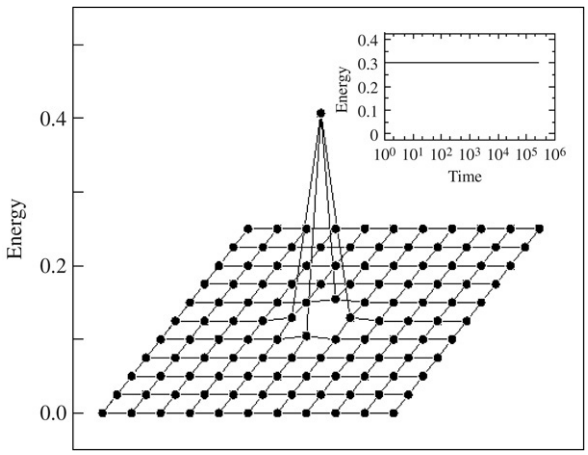


**Fig. 7.** Energy distribution with initial energy $E = 0.3$ after waiting time $t = 3000$. The filled circles represent the energy values for each particle; the solid lines are guides to the eye. Inset: Time dependence of the energy $e_{(5)}$. Figure from [127].

absorbing boundary conditions may essentially reduce this effect [127], but not remove it completely. The only way to avoid the boundary problem is to take a large enough system size, which is quite expensive from a computational point of view, especially when dealing with more than one spatial dimensions. Another obvious disadvantage of the described method is that it does not provide one with control of the parameters of a resulting DB. In particular, with such a technique one can not obtain dynamically unstable (but still existing as exact solutions!) DBs. Therefore, in order to perform a detailed analysis of possible DB solutions and their properties, including their stability, more careful methods are needed for computing DBs with a desired precision.

### *3.2. Obtaining DB solutions with high precision*

The general idea underlying most methods for computing DB solutions is to find the zero of a certain map. The set of relevant variables and the algorithm for searching for the zero might be quite different though, resulting in the number of approaches established nowadays [133,115]. Each of these methods has its own advantages and disadvantages, and the final choice very much depends on the concrete model and particular properties of the desired DB solution.

#### *3.2.1. Periodic orbits in phase space*

The mostly used, and very general, method for computing DB solutions is based on finding the corresponding periodic orbits (PO) in phase space. Generic POs of nonintegrable Hamiltonian systems are isolated, i.e. in a small neighborhood in phase space one cannot find other slightly deformed POs with identical values of conserved quantities like energy, action etc. At the same time, the fact that DBs usually belong to one-parameter families of solutions implies that for slightly different

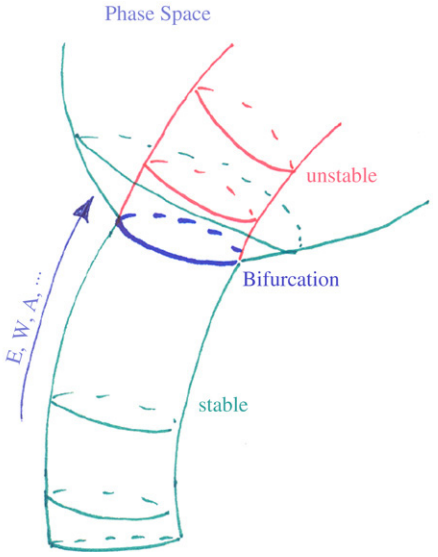


**Fig. 8.** Schematic representation of a family of isolated POs. Green sector — stable POs, red sector — unstable POs, blue line — bifurcation location of additional PO family detaching.

values of the conserved quantities one will generally find new slightly deformed POs. Thus, we can think of isolated POs residing on cylinders in phase space, where each point on a cylinder belongs to a closed loop which is a PO. Sliding along the cylinder, i.e. sliding along the family of the corresponding solutions, we change all the parameters of the PO. In particular, a PO can turn from stable to unstable, due to a bifurcation, possibly resulting in new families of POs, as indicated in Fig. 8.

Taking into account the described degeneracy, one has to fix some parameter of the desired PO (equivalently, the parameter of the corresponding family of DB solutions). The most natural way is to fix the corresponding period $T_b$, however some other parameters can be used as well, e.g. DB energy, amplitude of the central site etc. The next step is to construct the map. Consider a 1D lattice of size $N$ (it is straightforward to extend the procedure to any higher dimensional problem). Take an initial condition $\vec{R} = \{X_l, P_l\}$ in the $2N$-dimensional phase space with components

$$x_l(t = 0) \equiv X_l, \qquad p_l(t = 0) \equiv P_l \tag{3.4}$$

and integrate it over a certain time $T_b$:

$$x_l(T_b) \equiv I_l^x(\{X_{l'}, P_{l'}\}, T_b), \qquad p_l(T_b) \equiv I_l^p(\{X_{l'}, P_{l'}\}, T_b). \tag{3.5}$$

If $\vec{R}$ belongs to a PO with period $T_b$, then it should coincide with the point in phase space given by (3.5). In other words, the vector function $\vec{F}(\vec{R}) = \{F_l^x(\vec{R}), F_l^p(\vec{R})\}$ with components given by

$$F_l^x = I_l^x - X_l, \qquad F_l^p = I_l^p - P_l, \tag{3.6}$$

should be zero for any point $\vec{R}$ from a PO. This condition constitutes our map:

$$\vec{F}(\vec{R}) = 0. \tag{3.7}$$

Thus, the problem of finding a periodic orbit is equivalent to the problem of finding zeros of the function $\vec{F}(\vec{R})$ (3.6). Different methods can be used for this. The most common one is the generalized Newton–Raphson method in phase space [261], which gives an iterative scheme with the correction $\vec{\Delta}^{(i)}$ on the $i$-th step of iteration to the trial vector $\vec{R}^{(i-1)}$ given by

$$\vec{F}\left(\vec{R}^{(i-1)}\right) + \mathcal{M}\vec{\Delta}^{(i)} = 0, \tag{3.8}$$

where the elements of the tangent matrix $\mathcal{M}$ are:

$$\mathcal{M}_{nm} = \left.\frac{\partial F_n}{\partial R_m}\right|_{\vec{R}^{(i-1)}}. \tag{3.9}$$

We denote the components of the corresponding $L$-dimensional vectors by $R_n$ and $F_n$. $L < 2N$ is the dimensionality of the suitably defined subspace $S^L$ of the original $2N$-dimensional phase space (the issue of a relevant choice of the subspace $S^L$ will be addressed below). Since the function $\vec{F}(\vec{R})$ is defined through the integration of the model dynamical equations over

the period $T_b$, one has to integrate the system $L$ times with $L$ small orthogonal perturbations of the vector $\vec{R}^{(i-1)}$ to compute $\mathcal{M}_{nm}$ on each iteration step:

$$\mathcal{M}_{nm} = \frac{F_n\left(\vec{R}^{(i-1)} + \vec{l}_m\right) - F_n\left(\vec{R}^{(i-1)}\right)}{|\vec{l}_m|}, \tag{3.10}$$

where the vectors $\vec{l}_m$, $1 \le m \le L$ define a complete basis which spans the $L$-dimensional subspace $S^L$.

The main task is to compute the matrix elements $\mathcal{M}_{nm}$. Integrating a single perturbed trajectory yields a complete row (or line) of the matrix. The integration can be either done using the full nonlinear equations —then one has to make sure that the perturbation is small enough for the linearization of the phase space flow around the trajectory to hold. A much better way is to linearize the equations around a given trajectory explicitly (see 3.3) and to integrate the linearized equations.

In order to calculate the correction $\vec{\Delta}^{(i)}$ from Eq. (3.8), one needs to invert the matrix $\mathcal{M}$. Therefore, all possible degeneracies which lead to zero eigenvalues of the matrix should be removed. In other words, the function $\vec{F}(\vec{R})$ should have a unique zero (if any) in a vicinity of the initial point $\vec{R}^{(0)}$. The degeneracy associated with sliding along the family of POs is lifted by fixing the period $T_b$ in the map. However, there is at least one more degeneracy connected to the sliding along the given PO: if $\vec{R}$ belongs to the PO, then a 1D manifold of points belong to this PO. This degeneracy can be removed by fixing the initial phase, e.g. by adding one additional condition $P_m = 0$ in (3.4) (sliding along the PO one can always find a point, at which the momentum of the $m$th site is zero). The corresponding component of the function $\vec{F}(\vec{R})$ should also be removed, so that the problem is reduced to the $L = 2N - 1$ dimensional phase subspace. One has to take care, however, that a zero of this reduced $(2N - 1)$ dimensional problem together with the condition $P_m = 0$ uniquely fixes the zero of the initial $2N$ dimensional problem, e.g. through energy conservation. An essential further reduction of the problem can be obtained, when searching for time-reversible POs. In that case the momenta of all the sites can be fixed to zero, and we are left with an $N$ dimensional subspace [261,133,221].[1]

For a successful implementation of the Newton scheme a good initial guess is needed. The general idea is to choose the system parameters such that a known solution can be used, and afterwards change the parameters up to the desired values by small steps, tracing the solution. A good starting point is the *anti-continuous limit* [249,18] of uncoupled sites. In this limit an exact solution can be easily constructed by exciting individual sites with the given frequency (corresponding to the period $T_b$ of the desired PO). The basic prototype of a DB solution would be a single excited site with all the other sites having strictly zero amplitudes. However, more complicated localized patterns can be chosen as well. Each of these patterns corresponds to a *coding sequence*, indicating the state of each site. The simplest variant of the coding sequence consists of two code types: "0" corresponds to a site being at rest and "1" corresponds to an excited site. Thus, a single-site excitation will have the coding sequence (. . . 0001000 . . .). In this sense, the introduced coding sequence is a unique identifier of a given DB solution. Constructing DB solutions starting from the anti-continuous limit certainly does not work in the case of FPU-type lattices with nonlinear interaction between sites, but zero on-site potentials. Then more sophisticated methods are needed [246,19,23].

The advantage of the Newton scheme is, that it is relatively easy to write a code once we already have a good integrator. The map converges exponentially fast. Furthermore we may use one Newton matrix for several iterations, which may be useful when matrices get large. Disadvantages of the Newton scheme may be due to relatively large computational time $\sim N^2$ because of matrix inversion. Matrix inversions are sensitive to bifurcations, because at bifurcations additional degeneracies take place, which may lead to zero eigenvalues of $\mathcal{M}$. Sometimes we may need more subtle inversion routines, using e.g. singular value decomposition.

Similar to the Newton map one may also use a steepest descent method in phase space [125] to seek for zeros of the scalar nonnegative function $g(\vec{R}) \equiv |\vec{F}(\vec{R})|^2$. Starting from some point in phase space one follows the direction opposite to the gradient of this function and eventually falls down to the global minimum $g_{\min}(\vec{R}) = 0$. As in the above Newton scheme a good initial guess is needed, so that we are separated from any possible local minima of the function $g(\vec{R})$. The advantage of steepest descent is that the computational time grows proportional to $N$. Furthermore the method is insensitive to bifurcations, since no matrix inversion is needed. Disadvantages of the steepest descent are that the convergence is slower than that of Newton maps and that it may be hard to distinguish zero height minima from almost zero height minima.

Yet another twist is taken if the steepest descent method is considered as a map. The idea is to search for a minimum of $g(\vec{R})$ by approximating the function around the minimum with a quadratic form. Formally that seems to repeat the above discussed Newton method. Yet there is more to say. Indeed, as mentioned before, a Newton method which operates just on the amplitudes of oscillators when searching for a time-reversible orbit, will in general produce large errors on the velocities. The norm minimization can solve this problem. It does so by taking the mapping into the full phase space, but inverting only sub-blocks of the obtained matrix. And it can be used essentially for any case of a reduced number of variables as compared to the full phase space dimension. A nice example is to compute a time-reversible DB by choosing initially all velocities to be zero, and by fixing the amplitude of a (central) oscillator to a given amplitude. Then all trajectories are integrated up to

[1] Note however, that the true error $\epsilon$ will be larger than the one of the reduced dimensional problem ($\epsilon_r$). If the kinetic energy is a quadratic form of the momenta, $\epsilon \sim \sqrt{\epsilon_r}$. One can overcome this problem by using modified Newton schemes [58,68,219].

the time when the velocity of the central oscillator vanishes again, and its amplitude has the same sign as at the beginning. The above Newton map can be done solely on the $N-1$ remaining coordinates. To improve the precision on the velocities as well, the norm minimization can be used again. We first define a scalar nonnegative function $g(\vec{R})$, and then define the relevant variables which should minimize that function.

*3.2.2. Periodic orbits from Fourier space*

Instead of working in phase space, one can also reformulate the problem of finding a DB solution in terms of the Fourier coefficients [110,112]. Despite the fact, that the number of variables will drastically increase in this case (typically up to 20–30 per lattice site), the main advantage is that one has to deal with algebraic equations for the Fourier coefficients. In particular, the method becomes extremely efficient once the equations for the Fourier coefficients can be written down explicitly. Then one can again use the Newton algorithm to solve these equations, but this time the coefficients of the Newton matrix are known explicitly, and there is no need to integrate the system over a desired DB period in order to obtain them. Further optimizations can be done e.g. by using specific maps to solve the algebraic equations for the Fourier coefficients [112], however such methods have unpredictable convergence criteria. Yet if they converge to something meaningful, it happens very quickly.

*3.2.3. Use of symmetries*

In some specific cases one can use symmetries of the system to develop special methods or to simplify the above listed. As we already mentioned, while searching for time-reversible solutions one can reduce the effective dimensionality of the phase space by a factor of 2 (keep in mind, however, the discussed issue of the accuracy of solutions, obtained by such reduced schemes). This means, that the rank of the Newton matrix $\mathcal{M}$ in (3.8) will be reduced by a factor of 2, and the procedures for calculating its coefficients and for inverting $\mathcal{M}$ will run faster. Another simplification can be made in the case of symmetric on-site and inter-site potentials, which support an additional symmetry of DB solutions with period $T_b$: $x_n(t+T_b/2) = -x_n(t)$, $p_n(t+T_b/2) = -p_n(t)$. In this case the map in the phase space (3.6) can be redefined for the half-period $T_b/2$, again saving computational time [115]. A very specific example is given by homogeneous potentials which support time–space separation $x_n(t) = \phi_n G(t)$ [214,110,155]. In this case one deals with a single equation for the time-periodic function $G(t)$ and a set of algebraic coupled equations for a DB profile $\phi_n$. These equations can be then solved separately e.g. by using the Newton method. Similarly, as mentioned in Section 1.5, stationary DB solutions in DNLS models satisfy algebraic equation (1.21).

*3.2.4. Dissipative DBs*

Computing DB solutions in dissipative systems deserves special attention. In such systems DBs no longer form continuous families of solutions, but they may survive as attractors, provided some sources of incoming energy are present e.g. by applying an external bias, see Section 4.6. In terms of POs in the phase space, only some slices of the cylinder in Fig. 8 may survive in non-Hamiltonian systems. In most of the cases the parameters of these POs are unknown *a priori*, therefore one has to modify the map (3.6) and (3.7), incorporating the period $T_b$ in the set of variables $\vec{R}$ to be defined. Note, that the degeneracy associated with sliding along the PO persists. As earlier, it can be removed by fixing $P_m = 0$. Thus, $\vec{R}$ is defined as

$$\vec{R} = \{X_1, X_2, X_3, \ldots, X_N, P_1, P_2, P_3, \ldots, P_{m-1}, P_{m+1}, \ldots, P_N, T_b\}\,, \tag{3.11}$$

and the function $\vec{F}(\vec{R})$ (3.6) includes now the error on the variable $P_m$, so that both $\vec{F}$ and $\vec{R}$ are $2N$ dimensional vectors. Zeros of $\vec{F}(\vec{R})$ can be found then by Newton or steepest descent methods. As usual, a good initial guess is needed.

*3.3. Perturbing discrete breathers*

Once a DB solution is found, one has to characterize its stability and the related question of interaction of the DB with other types of excitations. For that one has to study the evolution of a perturbation $\epsilon_n(t)$ added to the DB solution $\hat{x}_n(t)$. If the perturbation amplitude is large enough, one may expect generic dynamical features of a nonintegrable system, which are usually rather complicated and hard to address analytically. However, assuming that the size of perturbation is suitably small, one may linearize the resulting equations for $\epsilon_n(t)$ [18,262]:

$$\ddot{\epsilon}_n = -\sum_m \left.\frac{\partial^2 H}{\partial x_m \partial x_n}\right|_{\{\hat{x}_l(t)\}} \epsilon_m, \tag{3.12}$$

where $H$ is the Hamiltonian of the system. Within that linear approximation in the perturbation amplitude $\epsilon_n(t)$, the DB acts as a parametric time-periodic driver, and the Eq. (3.12) corresponds to a time-dependent Hamiltonian $\widetilde{H}(t)$:

$$\widetilde{H}(t) = \sum_n \left[\frac{\pi_n^2}{2} + \frac{1}{2}\sum_m \left.\frac{\partial^2 H}{\partial x_n \partial x_m}\right|_{\{\hat{x}_l(t)\}} \epsilon_n \epsilon_m\right], \tag{3.13}$$

$$\dot{\epsilon}_n = \frac{\partial \widetilde{H}}{\partial \pi_n}, \qquad \dot{\pi}_n = -\frac{\partial \widetilde{H}}{\partial \epsilon_n}. \tag{3.14}$$

The specific structure of the Hamiltonian $\widetilde{H}$ ensures that the conservation law $\dot{I} = 0$ [18,16] for the symplectic product

$$I = \sum_n \left[\epsilon_n(t)\pi'_n(t) - \epsilon'_n(t)\pi_n(t)\right] \tag{3.15}$$

holds for any pair of trajectories $y = \{\epsilon_n, \pi_n\}$ and $y' = \left\{\epsilon'_n, \pi'_n\right\}$. It can be written as the scalar product

$$I = (Jy, y'), \tag{3.16}$$

where $J$ is the $2N \times 2N$ matrix

$$J = \begin{pmatrix} 0 & I \\ -I & 0 \end{pmatrix}, \tag{3.17}$$

and $I$ is the $N \times N$ unit matrix. The conservation of the symplectic product $I$ implies that the evolution matrix $U(t)$, which maps the linearized phase space flow around the given PO onto itself,

$$\begin{Bmatrix} \epsilon(t) \\ \pi(t) \end{Bmatrix} = U(t) \begin{Bmatrix} \epsilon(0) \\ \pi(0) \end{Bmatrix}, \tag{3.18}$$

is symplectic:

$$U^{\mathrm{T}} J U = J. \tag{3.19}$$

Consequently it follows that if $y$ is a *right* eigenvector of the matrix $U$ with the corresponding eigenvalue $\lambda$

$$Uy = \lambda y, \tag{3.20}$$

then $Jy$ is the *right* eigenvector of the transposed matrix $U^{\mathrm{T}}$ (or equivalently the *left* eigenvector of the same matrix $U$) with the corresponding eigenvalue $1/\lambda$ [115]

$$U^{\mathrm{T}}(Jy) = \frac{1}{\lambda}(Jy). \tag{3.21}$$

Since the spectra of transposed matrices coincide, both $\lambda$ and $1/\lambda$ are eigenvalues of the matrix $U$. But in general, there is no straightforward relation between the corresponding eigenvectors (in other words, there is no connection between the *left* eigenvector $Jy$ and the *right* eigenvector $y'$ which corresponds to one and the same eigenvalue $1/\lambda$).[2] If $U$ is real, its complex eigenvalues form complex conjugated pairs. Thus, if $\lambda$ is an eigenvalue of $U$, then so are $\lambda^*$, $1/\lambda$ and $1/\lambda^*$.

Due to the time-periodicity of all the coefficients in the r.h.s. of Eq. (3.12), the dynamics of a small-amplitude perturbation $\epsilon_n(t)$ is fully determined by the Floquet matrix $\mathcal{F} \equiv U(T_b)$, i.e. by the evolution matrix over one DB period $T_b$. Thus, the problem is reduced to determining the eigenvalues and eigenvectors of the symplectic Floquet matrix $\mathcal{F}$. The coefficients of this matrix are determined in a similar way to the coefficients of the Newton matrix $\mathcal{M}$ (3.10), discussed above, but with use of the vector function $\vec{I}(\vec{R})$ (3.5) instead of $\vec{F}(\vec{R})$ used in (3.10):

$$\mathcal{F}_{nm} = \frac{I_n\left(\vec{R} + \vec{\delta}^{(m)}\right) - I_n\left(\vec{R}\right)}{|\vec{\delta}^{(m)}|}, \tag{3.22}$$

where the vectors $\vec{\delta}_n^{(m)}$, $m = 1, 2, \ldots, 2N$ form a basis of orthogonal perturbations in the $2N$ dimensional phase space and $\vec{R}$ defines a point on the PO orbit corresponding to the DB solution. In other words, there is a simple relation between the Floquet and the Newton matrices: $\mathcal{F} = \mathcal{M} + I$. Therefore, to reduce computational time one can use the Newton matrix $\mathcal{M}$ obtained on the last step of the Newton iteration scheme (i.e. reasonably close to the exact DB solution) in order to determine most of the coefficients of the Floquet matrix $\mathcal{F}$. The still missing elements of the Floquet matrix $\mathcal{F}$ have to be calculated separately.[3]

In many cases one works with real valued variables $x_n(t)$ and $\epsilon_n(t)$. Then the Floquet matrix will be also real, but its eigenvalues and eigenvectors are complex. Take a complex valued eigenvector $y = y_r + \mathrm{i}y_i$ corresponding to the eigenvalue

[2] Dealing with time-reversible DB solutions, one may nevertheless conjecture this connection: if $y = \{\epsilon_\lambda, \pi_\lambda\}$ is the eigenvector corresponding to an eigenvalue $\lambda$, then $y' = \{\epsilon_\lambda, -\pi_\lambda\}$ should be the eigenvector corresponding to the eigenvalue $1/\lambda$. However, we are not aware of any strict proof of this conjecture, although the numerical studies show that it is fulfilled.

[3] It is worth mentioning, that being symplectic, the Floquet matrix $\mathcal{F}$ can be easily inverted: $F^{-1} = -JF^{\mathrm{T}}J$. However the Newton matrix $\mathcal{M} = \mathcal{F} - I$ introduced in (3.8) is no longer symplectic. It is a challenging task to construct a modified map in phase space, which would involve a symplectic Newton matrix.

$\lambda = \lambda_r + \mathrm{i}\lambda_i$. How is it related to the original real phase space variables $\epsilon_n, \pi_n$? Using $\mathcal{F}y = \lambda y$ it is straightforward to obtain

$$\mathcal{F}y_r = \lambda_r y_r - \lambda_i y_i, \tag{3.23}$$

$$\mathcal{F}y_i = \lambda_i y_r + \lambda_r y_i. \tag{3.24}$$

Thus, taking any linear combination of $y_r$ and $y_i$ as an initial condition for $\epsilon_n, \pi_n$, the Floquet map will perform a rotation and expansion (contraction) in the subspace spanned by the real and imaginary parts of the complex conjugate pair of eigenvectors $y$ and $y^*$. In other words, this subspace is invariant under application of the Floquet mapping. If $|\lambda| = 1$, this mapping simply performs a rotation, otherwise it adds a contraction $|\lambda| < 1$ or an expansion $|\lambda| > 1$, related to DB instabilities. This issue will be addressed in detail in Section 4.2.

## 4. Basic properties of discrete breathers

This section is devoted to a discussion of the main mathematical properties of discrete breathers. It will include a brief discussion of aspects which have been already published, and include a more focussed analysis on subfields which emerged in the past years. Among the latter ones are such topics as long range interaction, quasicompact discrete breathers, and also recent developments in the area of modulational instability and the influence of dissipation.

### *4.1. Spatial localization*

Discrete breathers are generic solutions on nonlinear, typically nonintegrable, lattices. The price to pay is that we usually do not have a closed analytical expression for these states. Thus we need approximation tools to analyze their properties, by assuming that, for a given system, DBs with certain properties exist. As concerning their localization properties in space, we can consider both the profile inside the core of the DB, as well as the decay properties in its spatial tails. The former aspect is the hardest one, since it needs the mastering of the full nonlinear equations. The latter one is more accessible, since breather amplitudes in their tails become small. A linearization of the equations of motion in the tails is then usually expected to correctly describe the tail asymptotics. However, one can even systematically go beyond such a linearization and treat nonlinear corrections as well. Tail analysis is the focus of this chapter.

To make things precise, we will consider a model with one degree of freedom per unit cell. Generalizations to more complicated cases should be straightforward. The Hamiltonian reads

$$H = \sum_l \left[ \frac{1}{2} P_l^2 + V(X_l) + \sum_{l'} W_{l,l'}(X_l - X_{l'}) \right]. \tag{4.1}$$

The hypercubic lattice has dimension $d$, and the lattice index $l$ is a d-dimensional vector with integer components. The interaction potential $W_{l,l'} = W_{l+m,l'+m}$, and thus the model, are translationally invariant. All zero and first derivatives of the potential functions vanish for zero arguments. By the virtue of the discreteness the frequency spectrum $\omega_q$ of small amplitude plane waves is bounded in absolute value.

A discrete breather solution is given by

$$X_l(t) = \sum_k A_{kl} \mathrm{e}^{\mathrm{i}k\Omega_b t}. \tag{4.2}$$

Here the Fourier number $k$ is a scalar integer independent of the lattice dimension $d$. The breather is localized in space which implies

$$A_{k,|l|\to\infty} \to 0. \tag{4.3}$$

Assuming that the potential functions have nonzero second derivatives at their origin, i.e. $V''(0) = v_2 \neq 0$ and $W''_{0,l} = w_{0,l} \neq 0$ for some $l$, we may linearize the algebraic equations for the Fourier coefficients $A_{kl}$ in the spatial tails $|l| \to \infty$:

$$k^2\Omega_b^2 A_{kl} = v_2 A_{kl} + \sum_{l'} w_{l,l'}(A_{kl} - A_{kl'}). \tag{4.4}$$

Since the Fourier amplitude equations decouple after linearization, we can solve each of these equations separately. Recalling that the necessary condition for the localization of each Fourier amplitude is the nonresonance condition $k\Omega_b \neq \omega_q$, the spatial decay of the $k$-th amplitude is then given by the lattice Green's function [84]

$$G_\lambda(l) = \int_{1.BZ} \frac{\cos(ql)}{\omega_q^2 - \lambda} \mathrm{d}^d q, \quad \lambda = k^2\Omega_b^2. \tag{4.5}$$

Here the integration extends over the first Brillouin zone of the reciprocal wavevector space $q$. We note that the spectrum $\omega_q$ is periodic in $q$, with its irreducible multidimensional period residing exactly in the first Brillouin zone. Fixing the direction

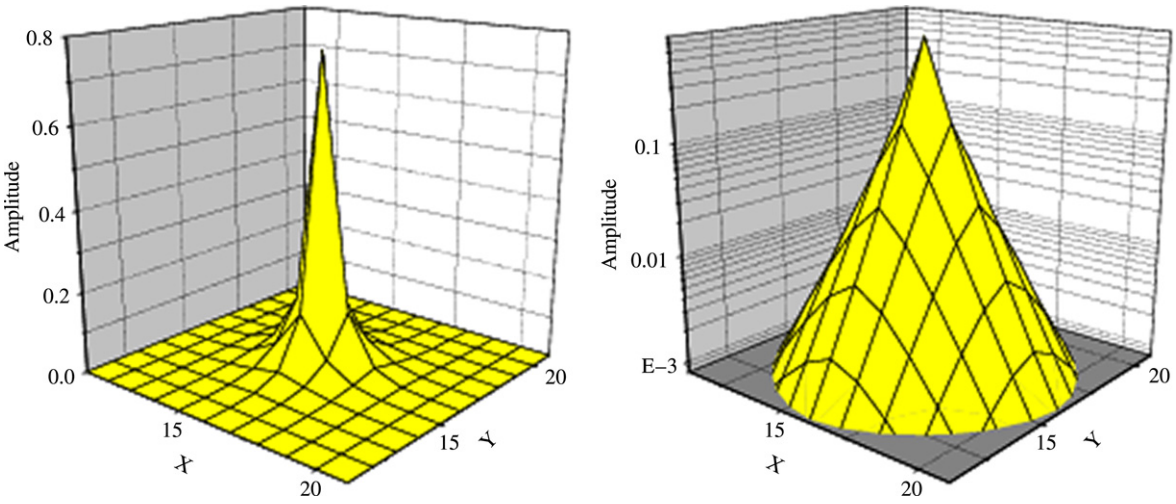


**Fig. 9.** Amplitude distribution of a breather solution of the three-dimensional DNLS system (4.6) with linear size $N = 31$. Only a distribution in a cutting $(x; y)$ plane is shown (the plane cuts the center of the breather). The intersections of the grid lines correspond to the actual amplitudes, the rest of the grid lines are guides to the eye. Left panel — amplitudes are shown on a linear scale. Right panel — the same solution with amplitudes plotted on a logarithmic scale. Data are from Fig. 2 in [125].

of $l$ and changing its absolute value, Eq. (4.5) will then generate the Fourier coefficients of the periodic function $(\omega_q^2 - \lambda)^{-1}$. The spatial decay of the breather is thus characterized by the convergence properties of the corresponding Fourier series. Also the convergence properties of Fourier series are defined through the analytical properties of the generating periodic function.

*4.1.1. Short-range interactions*

We define a lattice having short-range interactions, if the corresponding squared spectrum $\omega_q^2$ is an analytical function on the extended wavevector space $q$, i.e. when all its derivatives at any point $q$ exist and are finite. Examples are lattices with nearest neighbour interaction, or more general lattices with finite-size interactions where $w_{0,l} = 0$ for $|l| > r$ with $r$ being a positive real number. However, we can even generalize by considering lattices where the harmonic interaction potential extends over the whole lattice, with exponentially decaying amplitudes [25] $w_{0,l} \sim \mathrm{e}^{-|l|/r}$ for $|l| \gg r$. For all these cases the denominator $(\omega_q^2 - \lambda)^{-1}$ which enters (4.5) is an analytical periodic function of $q$, and thus the convergence of its Fourier series and the spatial localization of a DB is bounded by exponential tails [412]. The exponent will depend on $\lambda = k^2\Omega_b^2$. The localization length will grow whenever any of the multiples $k\Omega_b$ comes close to an edge of the spectrum $\omega_q$.

In the insets in Fig. 3 the exponential localization of two DBs is shown for a one-dimensional FPU chain with nearest neighbour interaction. In the insets of Fig. 5 a similar exponential localization is plotted for DBs of the one-dimensional DNLS chain with nearest neighbour interaction. The comparison between the numerically obtained localization length and the prediction from Eq. (4.5) has been extensively analyzed for various one-dimensional lattices [110,112] and is discussed extensively in Ref. [133].

Here we also show the amplitude distribution of a DB solution for a three-dimensional cubic DNLS lattice with nearest neighbour interaction

$$\dot{\Psi}_l = \mathrm{i}\left(\Psi_l + |\Psi_l|^2\Psi_l + 0.1\sum_{m\in N_l}\Psi_m\right), \tag{4.6}$$

where $N_l$ denotes the set of nearest neighbours of $l$. Making the substitution $\Psi_l = A_l\mathrm{e}^{\mathrm{i}\Omega_b t}$ the algebraic equations are solved for the real amplitudes $A_l$ [125] for a lattice with linear size 31. To visualize the solution, we place the DB center at the lattice site $l = (16, 16, 16)$ and plot its amplitude distribution as a function of the $x$, $y$ coordinates in a plane with fixed coordinate $z = 16$ which contains the lattice site with the maximum breather amplitude. Note that the DB is strongly localized on a few lattice sites (left plot in Fig. 9). The same solution, when displayed on a logarithmic amplitude scale, shows a conical structure (right plot in Fig. 9) as expected from the predicted exponential decay in space.

*4.1.2. Long-range interactions*

We define a lattice having long-range interactions, if the corresponding squared spectrum $\omega_q^2$ is a nonanalytical function on the extended wavevector space $q$, i.e. some of its derivatives at some points $q$ do not exist or diverge. That happens e.g. when the harmonic interaction potential extends over the whole lattice, and decays algebraically with increasing distance $w_{0,l} \sim |l|^{-s}$ with some positive exponent $s$. Despite the slow decay of interactions, discrete breathers still exist,

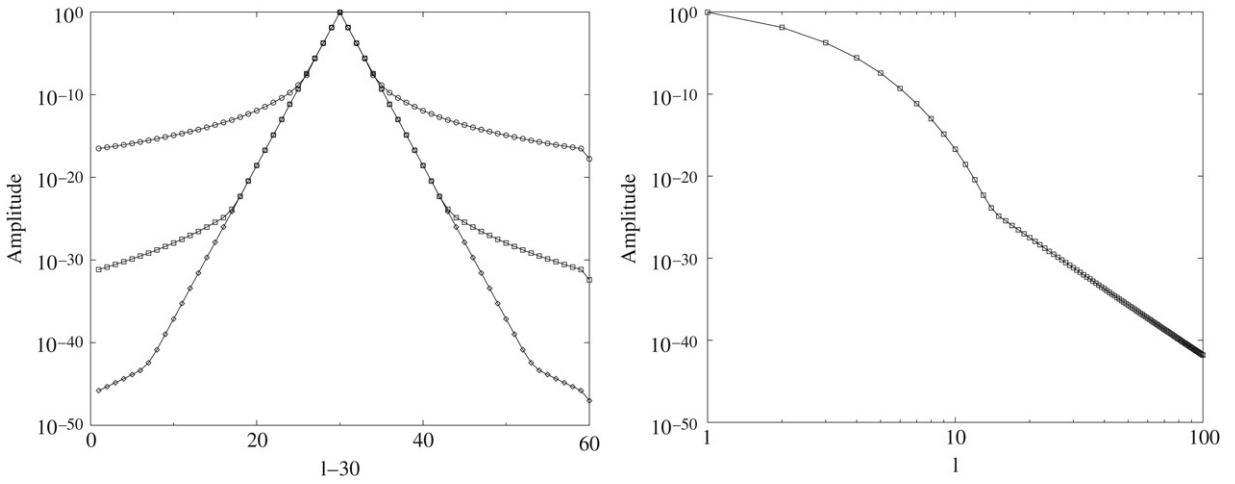


**Fig. 10.** Left panel: breather solution at time $t = 0$ with $P_l(t = 0) = 0$. The corresponding displacements (amplitudes) $X_l(t = 0)$ are plotted versus lattice site. The nonzero model parameters are $v_2 = v_4 = 1$, $C = 0.01$. The period of the solutions $T = 4.7682$. Circles: $s = 10$, squares: $s = 20$, diamonds: $s = 30$. Lines are guides to the eye. Right panel: same as in left panel but only for $s = 20$ in a log–log plot. Data from [114].

but will now localize slower than exponentially. In fact what matters is the analysis of the degree of nonanalyticity of $\omega_q^2$, which straightforwardly gives a power law convergence of the Fourier series (4.5) (see [412]) and thus an algebraic spatial localization of DBs.

We will present the results obtained in Ref. [114] to illustrate that the true DB localization can be more complicated even for simple one-dimensional lattices. We consider the Hamiltonian

$$H = \sum_l \left[ \frac{1}{2} P_l^2 + V(X_l) + \sum_{l'} W_{|l-l'|}(X_l - X_{l'}) \right]. \tag{4.7}$$

The on-site potential $V(z) = \sum_{\mu=2}^{\infty} \frac{v_\mu}{\mu} z^\mu$ generates an optical phonon spectrum, and the interaction $W_l(z) = \sum_{\mu=2}^{\infty} \frac{\phi_\mu(l)}{\mu} z^\mu$ incorporates long range interactions with $\phi_2(l) = \frac{C}{2} \frac{1}{l^s}$. For small values of $P_l$ and $X_l$ the classical Hamiltonian equations of motion $\dot{X}_l = \frac{\partial H}{\partial P_l}, \dot{P}_l = -\frac{\partial H}{\partial X_l}$ can be linearized in $X_l$. Solving the corresponding eigenvalue problem with plane waves $X_l(t) \sim \exp^{i(ql - \omega_q t)}$, one obtains

$$\omega_q^2 = v_2 + 2C \sum_{m=1}^{\infty} \frac{1}{m^s} (1 - \cos(qm)). \tag{4.8}$$

Let us discuss the properties of $E_s(q) = \omega_q^2 \geq 0$. $E_s(q)$ is bounded from above for all $s > 1$ and periodic in $q$ with period $2\pi$. Most important is that $E_s(q)$ is a nonanalytic function in $q$, i.e. its $\kappa = (s-1)$-st derivative with respect to $q$ is discontinuous at $q = 0$ (when $s$ is noninteger, $(s-1) < \kappa < s$). This follows already from the fact that the convergence radius of (4.8) is zero for nonzero imaginary components in $q$. Indeed for even integers $s$ one finds [412] $(E_s(q) - v_2) \sim B_s(q/(2\pi))$ for $0 \leq q \leq 2\pi$. Here $B_s(z)$ is the Bernoulli polynomial of $s$-th order. Consequently at small $q$ the expansion of $E_s(q)$ contains a term $q^{s-1}$ which, together with the periodicity of $E_s(q)$, leads to the mentioned nonanalyticity. For odd integers $s$ the expansion of $E_s(q)$ contains a term $q^{s-1} \ln(q)$, and for noninteger $s$ a term $q^{s-1}$ (follows from $\mathrm{d}^2 E_s(q)/\mathrm{d}q^2 = -E_{s-2}(q) + 2C\zeta(s-2)$ with $\zeta(z)$ being the Riemann Zeta function). Finally for small $q$ the leading term in the expansion of $E_s(q)$ is $v_2 + C\zeta(s-2)q^2$ for $s > 3$ and $v_2 + 2Ca(s)q^{s-1}$ for $1 < s < 3$ with $a(s) = \int_0^\infty (1 - \cos x)/x^s \mathrm{d}x$. Note that the dispersion at the upper band edge $(q = \pi)$ is in leading order always proportional to $(q - \pi)^2$. Some of these results have been discussed at length in [260] (see also original references therein).

Now we can turn to the first problem of the spatial decay of a breather. In order to generate a breather solution we chose $v_4 \neq 0$ and all other anharmonic terms in $V(z)$ and $W(z)$ being zero. Since we can only simulate finite system sizes $N$, we use periodic boundary conditions. In that case we have to define a cutoff length in the interaction which we chose to be $N/2$. Calculated breather solutions for $s = 10, 20, 30$ are shown in Fig. 10. We observe that the spatial decay of the breather is *exponential* for small distances from the center, while it becomes *algebraic* (in fact exactly $1/l^s$) after a crossover at some distance $l_c$ (see right panel in Fig. 10). Note that $l_c$ is $s$-dependent. Moreover, $l_c$ is also dependent on the parameter which selects a given breather solution from its one-parameter family (this parameter could be the breather frequency, its energy, action or something else).

The asymptotic spatial decay of the breather is given by the convergence properties of the Fourier series (4.5). Nonanalytic functions with discontinuities in the $(s-1)$st derivative produce Fourier series which converge algebraically $1/l^s$ [412]. From

that it follows that at large distances the spatial decay of the breather will be algebraic, which is what we found in Fig. 10. To obtain the exponential decay at small distances, let us first slide along the breather family such that the breather frequency (or one of its multiples) approaches the edge of the phonon band $\omega_q$. Then the integrand in (4.5) will become very large for wave numbers close to the band edge approached. Applying a stationary phase approximation to (4.5), i.e. expanding the integrand around the band edge we obtain

$$G_\lambda(l) \sim \int_{-\infty}^{\infty} \frac{\cos(ql)}{v_2 - \lambda + C\zeta(s-2)q^2} \mathrm{d}q \tag{4.9}$$

for $s > 3$ and

$$G_\lambda(l) \sim \int_{0}^{\infty} \frac{\cos(ql)}{v_2 - \lambda + 2Ca(s)q^{s-1}} \mathrm{d}q \tag{4.10}$$

for $1 < s < 3$. Standard evaluation of (4.9) (closing the integration contour in the complex plane by adding a half circle with infinite radius and evaluating the residua) yields $G_\lambda(l) \sim \mathrm{e}^{-\sqrt{v_2-\lambda}l}$ for $s > 3$, i.e. exponential decay [147]! On the other side, (4.10) yields (closing the integration contour in the complex plane by adding a quarter circle and returning to zero along the positive imaginary axis, and noticing that there are no poles of the integrand in the enclosed first quadrant including the imaginary axis) $G_\lambda(l) \sim 1/l^s$ for $1 < s < 3$ [147].

Now we can explain the observed crossover from exponential to algebraic decay in Fig. 10. Indeed, the stationary phase approximation for these cases leads to (4.9) in the limit $(v_2 - \lambda) \to 0$. This approximation neglects higher order terms in the expansion of $E_s(q)$ around $q = 0$ which necessarily contain nonanalytic terms. Consequently (4.9) probes (4.5) over not too large distances (this is counterintuitive to the assumption that the stationary phase approximation is correct for large $l$ [147], which it is not). Thus we can explain the observed crossover. We can also estimate the crossover distance $l_c$ using a simple argument. A tagged site with index $l < l_c$ and $l > 0$ (the center of the breather is located at $l_b = 0$) will experience forces from all other sites with index $l'$ according to (4.7). The amplitude of these forces will monotonously decay to zero for increasing $l'$ with $l' > l$. However the amplitude of the forces for decreasing $l'$ will be given by $(l - l')^{-s}\mathrm{e}^{\nu(l-l')}$ for $0 < l' < l$ (here $\nu$ is the given exponent of the spatial decay for $|l| < l_c$). Since for negative $l'$ the amplitude of these forces will again monotonously decay to zero, the worst case is reached when $l' = 0$. If this force acting from the center of the breather on site $l$ is comparable to the forces acting on $l$ from its nearest neighbours, the exponential decay will be violated. This condition yields $l_c^{-s}\mathrm{e}^{\nu l_c} = 1$ or

$$\frac{\ln l_c}{l_c} = \frac{\nu}{s}. \tag{4.11}$$

Especially we find that $l_c \to \infty$ if $\nu/s \to 0$. Thus for $s > 3$ exponential decay is reobtained either for large $s$ or for breathers with frequencies close to the phonon band edge. Since we are considering a lattice, the exponential decay part will disappear if $l_c \approx 1$ or smaller. For $s = 20$ and $\nu = 4.2724$ we obtain $l_c = 11.39$, and for $s = 30$ and the same value of $\nu$ the result is $l_c = 21.56$. We miss the observed crossovers in (4.2) by just two sites.

For $1 < s < 3$ no exponential decay is observed provided the breather frequency is located in the gap below the phonon band. For breather frequencies above the phonon band the dispersion at the upper band edge always yields quadratic dependence in $q$ (see above) and thus there will always be a crossover from exponential to algebraic decay (provided $l_c > 1$). All these results were verified by calculating corresponding breather solutions (see also [47,50]).

To conclude this part we want to stress that a modified interaction $\phi_2(l) \sim (-1)^l/l^s$ will simply exchange the notation of upper and lower phonon band edges, and the case of acoustic interactions is obtained by letting $v_2 \to 0$.

#### 4.1.3. Almost compact discrete breathers

A subclass of systems (4.1) is characterized by space–time separation (see [214,106,110,111,261,300,77,155]). Consider

$$H = \sum_l \left[\frac{1}{2}p_l^2 + \frac{v_2}{2}x_l^2\right] + POT, \tag{4.12}$$

with

$$POT = \sum_l \left[\frac{v_{2m}}{2m}x_l^{2m} + \frac{w_{2m}}{2m}(x_l - x_{l-1})^{2m}\right], \quad m = 2, 3, 4, \ldots \tag{4.13}$$

being a homogeneous function of the coordinates. The equations of motion take the form

$$\ddot{x}_l + v_2 x_l = -v_{2m}x_l^{2m-1} - w_{2m}(x_l - x_{l-1})^{2m-1} + w_{2m}(x_{l+1} - x_l)^{2m-1}. \tag{4.14}$$

These systems allow for time space separation for a sub-manifold of all possible trajectories:

$$x_l(t) = A_l G(t). \tag{4.15}$$

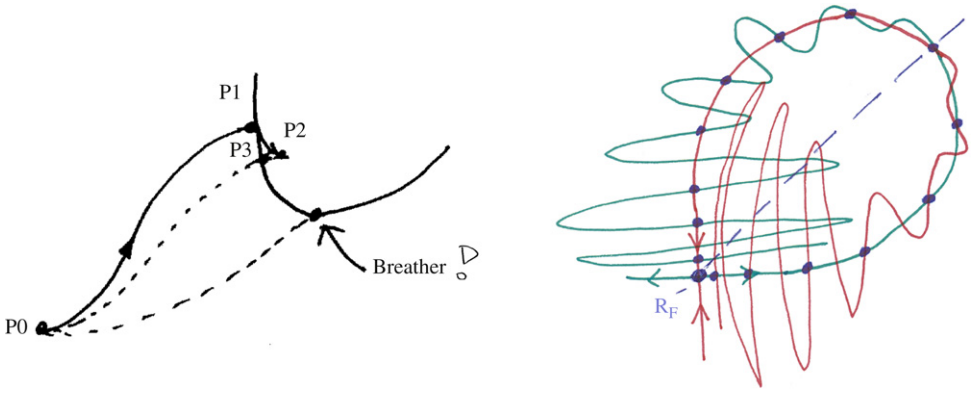


**Fig. 11.** Left panel: Schematic representation of function $S$ (4.20) and the pathway to a breather being a saddle. Right panel: Schematic representation of the map (4.23) and (4.24). Red line — stable invariant manifold, green line — unstable invariant manifold, black spots — intersection points of both manifolds for a given breather solution. Dashed blue line — diagonal $x = y$.

Inserting (4.15) into (4.14) we obtain

$$\frac{\ddot{G} + v_2 G}{G^{2m-1}} = -\kappa, \tag{4.16}$$

$$-\kappa = \frac{1}{A_l}\left[-v_{2m}A_l^{2m--1} - w_{2m}(A_l - A_{l-1})^{2m-1} + w_{2m}(A_{l+1} - A_l)^{2m-1}\right]. \tag{4.17}$$

Here $\kappa > 0$ is a separation parameter, which can be chosen freely. The master function $G$ obeys a trivial differential equation for an anharmonic oscillator

$$\ddot{G} = -v_2 G - \kappa G^{2m-1}. \tag{4.18}$$

Its solution sets the temporary evolution of the breather.

The spatial profile is given by

$$\kappa A_l = \left.\frac{\partial POT}{\partial x_l}\right|_{\{x_{l'} \equiv A_{l'}\}}, \tag{4.19}$$

or better by the extrema of a function $S$:

$$\frac{\partial S}{\partial A_l} = 0, \qquad S = \frac{1}{2}\kappa \sum_l A_l^2 - POT(\{x_l' \equiv A_l'\}). \tag{4.20}$$

Let us discuss some properties of $S$. This function has a minimum at $A_l = 0$ for all $l$ with height $S = 0$ (point $P0$ in left panel of Fig. 11). When choosing a certain direction in the $A_l$ space starting from $P0$, $S$ will first increase, then pass through a maximum and further decrease to $-\infty$. So there is a rim surrounding the minimum $A_l = 0$. Since breathers are spatially localized solutions, variation of the amplitudes $A_l$ in the tails of a breather around zero will increase $S$. At the same time the breather corresponds to an extremum of $S$, but there is only one trivial minimum of $S$ located at $P0$. Thus breathers are saddles of $S$.

It is remarkably easy to compute such a saddle. First choose a direction in the $N$-dimensional space of all $A_l$, e.g. $(\ldots 0001000\ldots)$, $(\ldots 0001001000\ldots)$ etc. Then start from the space origin $P0$, $A_l = 0$, move with small steps in the chosen direction, compute $S$. It will first increase and then pass through a maximum $P1$. Now we are on the rim. Compute the gradient of $S$ here and make a small step in opposite direction, to arrive at $P2$. Maximize $S$ on the line $P0 - P2$ to be on the rim again. Repeat until you reach a saddle with required accuracy.

This method has been used to compute various types of breathers and multi-breathers. Note that it is very simple to extend the computation to two- or three-dimensional lattices [106].

Another approach valid strictly for one-dimensional lattices is to obtain breathers as homoclinic orbits of a two-dimensional map [111,164,163,218,32,48,33,31]. Indeed, we may rewrite (4.17) in the following way:

$$A_{l+1} = A_l + \left[v_{2m}A_l^{2m-1} + w_{2m}(A_l - A_{l-1})^{2m-1} - \kappa A_l\right]^{\frac{1}{2m-1}} \tag{4.21}$$

where we can compute a given amplitude profile starting with a given pair of nearest neighbor amplitudes (both to the right and to the left of course). Using a two-dimensional vector

$$\vec{R}_l = (x_l, y_l) = (A_{l-1}, A_l) \tag{4.22}$$

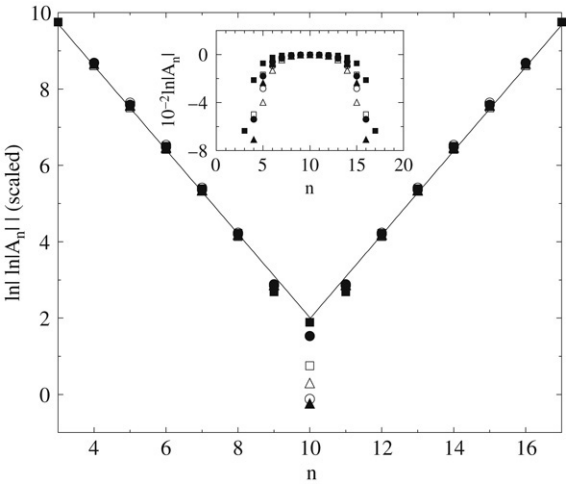


**Fig. 12.** Dependence of the double logarithm of the breather amplitude for different cases versus $n$ from [77]. Note that curves are vertically shifted to observe a master curve in the tails. The straight lines have slopes $\pm \ln 3$. Inset: Dependence of the logarithm of the breather amplitude versus $n$ for same cases. Note the scale of the $y$ axis.

the procedure can be cast into the form of a two-dimensional map with

$$x_{l+1} = y_l \tag{4.23}$$

$$y_{l+1} = y_l + \left[v_{2m} y_l^{2m-1} + w_{2m}(y_l - x_l)^{2m-1} - \kappa y_l\right]^{\frac{1}{2m-1}} . \tag{4.24}$$

This map (right panel in Fig. 11) has a fixed point $\vec{R}_F = (0, 0)$. The absence of differentiability at the fixed point can be taken care of by adding small linear interactions, and to consider the limit of their vanishing [111]. The fixed point belongs both to a stable (red) and unstable (green) one-dimensional invariant manifold. Taking a point on the stable manifold and iterating forward, we will approach the fixed point. The same happens with a point on the unstable manifold when iterated backwards. These manifolds intersect at many points. By definition any of these intersection points, when iterated either forward or backward, will converge to $\vec{R}_F$ and thus corresponds to a breather solution. Such map trajectories are also called homoclinic orbits. Note that many intersection points belong to the same homoclinic orbit or to the same breather, as indicated by the ones marked with black spots in the right panel of Fig. 11. However since the above map is locally (around $\vec{R}_F$) volume preserving, the structure of the invariant manifold lines will generically show up with horseshoe patterns (wiggles in the right panel of Fig. 11). These patterns generate additional intersection points. Consequently there will be an infinite number of different homoclinic orbits and thus breathers. They will differ by the amplitude distribution inside the breather core, which can become arbitrary complicated, and an exponential tail outside. Thus in addition to single site breathers discussed so far, also so-called multi-breather solutions can exist, i.e. localized excitations with a complex pattern of energy distribution inside the breather core (see also [249]).

Due to the space-reflection symmetry of the map there will be always one intersection point on the line $x = y$. The position of this point will depend only parametrically on $\kappa$. Thus it is possible to design simple search routines by e.g. fixing $x_0 = y_0$ and varying $\kappa$ (see [111]). The numerical scheme has been even used for a formal existence proof of breathers as homoclinic orbits [111].

In order to understand the tail behaviour of quasicompact DBs in one-dimensional lattices, we first note that due to the lack of harmonic interaction terms in (4.13) the spectrum of small amplitude oscillations is degenerate $\omega_q^2 = v_2$. Using (4.5) and performing the limit to such a degenerate case, we would arrive at a spatial decay which is faster than any exponential one. We note that the separation parameter $\kappa$ in (4.17) can be always chosen to be of absolute value one. Then in leading order we find the asymptotic law (to the right of the breather center):

$$A_n \approx A_{n-1}^{2m-1}. \tag{4.25}$$

This spatial decay is a superexponential one, since

$$\ln|\ln|A_n\|| \approx n \ln(2m-1). \tag{4.26}$$

For $m = 1$ various numerically obtained quasicompact DB solutions have been obtained e.g. in Refs. [110,261,77], and the superexponential decay (4.26) has been confirmed (see Fig. 12). These quasicompact DB states are characterized by a very fast decay of the amplitude in the tails, which is imprinted just by the type of interaction, independent of the DB amplitude, frequency etc, see e.g. [261].

These quasicompact DB states can be suitably continued by deforming the underlying equations to the well-known compacton solutions of nonlinear PDE equations as demonstrated by Rosenau and Hyman [332,331], though these limits

have to be taken with corresponding care [333,334,155]. Moreover making the purely nonlinear interactions decay algebraically along the lattice [155], introduces competition between extremely different length scales, and results in many interesting anomalies in the DB tail. Yet another aspect of purely nonlinear interactions is the absence of a linear spectrum $\omega_q$, and thus the possibility of constructing DB states which evolve quasiperiodically (and possibly even chaotically?) in time [155].

*4.1.4. Resonances with Goldstone modes*

It is a widespread expectation that breathers play an important role in the dynamics of anharmonic crystals [368]. Since any crystal has acoustic phonon branches, and the interparticle interaction potentials are in general not symmetric around their minimum, one has to face the fact that a breather will be accompanied by a strain field (gradient of the dc component of the breather) and that the resonance of the dc component with the acoustic phonon branches has to be considered.

As already mentioned, the breather frequency $\Omega_b$ should fulfill a nonresonance condition $n\Omega_b \neq \omega_q$ for all integer $n = 0, \pm 1, \pm 2, \ldots$. This is necessary in general in order to have spatial localization of the corresponding Fourier mode. In the case of weakly coupled oscillators a proper choice of the breather frequency always ensures nonresonance. In the case of homogeneous interaction potentials the symmetry of the potential $\Phi(z) = \Phi(-z)$ is found also in the breather solution, which implies that only odd Fourier components are present in the breather solution. Thus the dc component $(0 \times \Omega_b = 0)$ which is in resonance with the mentioned degenerated phonon band is strictly zero, and the resonance is harmless.

If any nonzero multiple of $\Omega_b$ resonates even with an edge of a phonon band, this leads either to the vanishing of the whole breather, or to a delocalization of the breather and to a divergence of its energy. The resonance of the dc component to be considered here is special — it resonates with a Goldstone mode, and one can expect the resonance to be not as destructive to the breather as any resonance at nonzero frequency. From the theory of elastic defects we know the characteristic feature of the strain decay to be algebraic in the distance (from the defect center). The exponent is only dependent on the dimension of the system and on the symmetry of the defect (monopole, dipole etc.), but independent of the defect strength.

We will treat the simplest case of hypercubic lattices with one degree of freedom per lattice site and nearest neighbour interaction, which can be considered as generalized Fermi–Pasta–Ulam (FPU) systems:

$$H = \sum_l \left[ \frac{1}{2} P_l^2 + \sum_{l' \in \mathrm{DNN}} \Phi(X_l - X_{l'}) \right]. \tag{4.27}$$

Here $P_l$ and $X_l$ are canonically conjugated scalar momenta and displacements of a particle at lattice site $l$. Note that depending on the lattice dimension $d$ the lattice site label $l$ is a $d$-component vector with integer components. The inner sum in (4.27) goes over all *directed nearest neighbours*, e.g. for $d = 1$ and $l = n$ we sum over $l' = n + 1$, for $d = 2$ and $l = (n, m)$ we sum over $l' = \{(n + 1, m); (n, m + 1)\}$ etc. The interaction potential $\Phi(z)$ is given by

$$\Phi(z) = \frac{1}{2}\phi_2 z^2 + \frac{1}{3}\phi_3 z^3 + \frac{1}{4} z^4, \tag{4.28}$$

which turns out to be generic enough for the purposes discussed below.

Breathers for such a system can be represented in the form (4.2). We will restrict ourselves to solutions invariant under time reversal, so that all $A_{kl} = A_{-k,l}$ are real. The spatial localization property of (4.2) implies $A_{k,|l|\to\infty} \to 0$ for $k \neq 0$ and $A_{0,|l|\to\infty} \to$ const. The dc component of the breather is given by $A_{0l}$.

Numerical and approximate analytical studies for one-dimensional lattices show that the acoustic breather exists as a solution to finite energy [37,166,210]. Its peculiarity is that the dc component of the breather versus lattice site number has a kink shape $A_{0,l\to\pm\infty} \to \pm$const. for free boundaries (Fig. 13). For periodic boundary conditions one would find a linear decay of $A_{0l}$ far from the breather, but the gradient of the dc components (the strain) is inverse proportional to the size of the chain, so that in the limit of an infinite chain the result is again a constant for the dc component (zero strain). An analytical proof of existence has been given by Spicci, Livi and MacKay [246]. The proof considers a diatomic chain with asymmetric interaction potential (note that the corresponding Hamiltonian differs from (4.27) in that one has to introduce an additional parameter $1/M \neq 1$ in front of each kinetic energy term for say all even lattice site indices). The breather is continued from the limit of zero mass ratio (heavy masses are infinitely heavy). The problem of resonance with the Goldstone mode is solved by coordinate transformation and by imposing a strain field of compact support. This means that the dc displacements at this limit are given by a step-like kink. The breather is then continued into a sector of the Hamiltonian with nonzero mass ratio (see also [177]).

Let us now turn to the general $d$-dimensional case. Suppose that a breather exists, which creates some strain field. The dc displacements $A_{0l}$ will have some dependence on the lattice site vector $l$. The strain $E_l$ is given by the lattice gradient of $A_{0l}$. The far field energy is given by the integral over the squared strain. Assuming that the strain does decay algebraically, we can use continuum theory far from the breather. The corresponding equation is equivalent to the electrostatic equations in $d$ dimensions. Consider $d = 1$. A monopole far field $E = c \neq 0$ and the corresponding energy diverges. Also in this case the (electrostatic) potential $A_{0l} = \mathrm{sgn}(l)a + cl$. This is clearly not what was observed for acoustic breathers in 1d. A dipole far field instead will yield $E = 0$, $A_{0l} = \mathrm{sgn}(l)a$, and the energy is finite. This is the situation observed. So the known

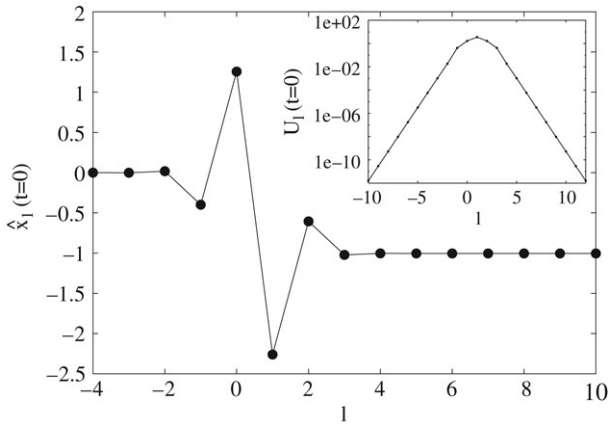


**Fig. 13.** An acoustic DB solution for the $d = 1$ case. Displacements $X_l(t = 0)$ for $\phi_2 = \phi_3 = \phi_4 = 1$ and $\Omega_b = 4.5$ are plotted versus lattice site number $l$. At this initial time all velocities $P_l(t = 0) = 0$. Inset: Staggered deformation $u_l = (-1)^l(x_l - x_{l-1})$ for the same solution on a logarithmic scale versus lattice site number $l$. This DB is linearly unstable. Data from [121].

acoustic breather solutions are accompanied by a dipole strain field. The request that the acoustic breather is a solution to finite energy limits the strain fields to dipole or higher order multipole symmetries. In this special case the potential $A_{0l}$ is constant far away from the breather, so the corresponding exponent of the algebraic decay is simply zero. That is the reason why the analytical proof of existence [246] can go through, because a kink-like field for $A_{0l}$ can have the limiting form of a compact step function, which is precisely the case for the limit of zero mass ratio (see above).

For $d = 2$ (square lattice) the situation is the following. A monopole will generate a strain $E \sim 1/l$ and a potential $A_{0l} \sim \ln(l)$. The energy of such a field diverges. If we search for acoustic breathers with finite energy, we would have to exclude a monopole field. A dipole generates a strain $E \sim 1/l^2$ (we skip angular dependencies here) and a potential $A_{0l} \sim 1/l$. The energy for this field is finite. The predicted exponents of the algebraic decay are nonzero, and no simple limit exists, which makes the strain to be of compact support. So already at this stage it is clear, that existence proofs of acoustic breathers in two-dimensional systems are much more complicated than for $d = 1$. Notice that for $d = 3$ (cubic lattice) a monopole generates $E \sim 1/l^2$ and the energy of this field is finite. Aubry has obtained existence proofs, together with the correct algebraic decay properties of the lattice deformation [19].

Next we will present numerical calculations of acoustic breathers of (4.27) for $d = 2$ and $\phi_2 = \phi_3 = 0.01$ [126]. The results show, up to numerical accuracy, that acoustic breathers exist on finite lattices with free boundaries. The symmetry and spatial decay properties are in accord with the expectations given above. The maximum lattice size is $70 \times 70$, but no profound size effects were observed on the existence and symmetry of the acoustic breather when considering smaller systems. The only size effect (to be expected) is observed even for the largest systems with respect to the algebraic decay properties. The ac components of the found solution decay exponentially in space and essentially vanish at a distance of 5–7 lattice constants from the center of the breather. In Fig. 14 we show the dc displacements of a DB solution. We do observe dipole symmetry of the dc field.

To analyse the spatial behaviour of the strain, we plot in Fig. 15 the variation of the absolute values of the strain along the two diagonals, as in those directions we have the largest distance and can hope that finite size effects are suppressed in some bulk region. The results depend on the choice of the diagonal. The diagonal which is directed along the dipole moment gives poor results — the finite size effects are too strong to observe any power law in the double logarithmic plot. The second diagonal perpendicular to the dipole moment however, though still with strong influence from the boundaries, allows the fitting of some part of the bulk data with a power law (solid line in Fig. 15). The resulting exponent is 1.85, and considering the small system size, quite close to the expected value 2.

These results support the expectations that breathers can exist in real crystals. Moreover at any finite temperature excited breathers will decay after some time. Since they are accompanied by a strain field, those strain fields will be dispersed in the form of low-lying acoustic modes after the decay of a breather. Thus breathers can act as an efficient energy transfer from high-frequency excitations into low-frequency acoustic phonons.

### *4.1.5. Nonlinear corrections*

The linearization of the equations of motion in the spatial tail of a DB seems to be fine by virtue of the localized character of the solution. Yet there may be nonlinear corrections in the tails, which will happen typically whenever any of the multiples of the DB frequency comes close to the spectrum $\omega_q$. While the Fourier amplitude $A_{kl}$ with the weakest spatial decay, as predicted from linearization, will always decay accordingly, it will do so very slowly by the above assumption. Consequently nonlinear terms which contain this amplitude and enter the equations for other Fourier amplitudes, e.g. the one with $k' = 3k$, will induce a nonlinear but much slower spatial decay than the linearized one. Details can be found in Ref. [112], and a discussion is also given in [133]. Here we want to add that these nonlinear corrections also allow one

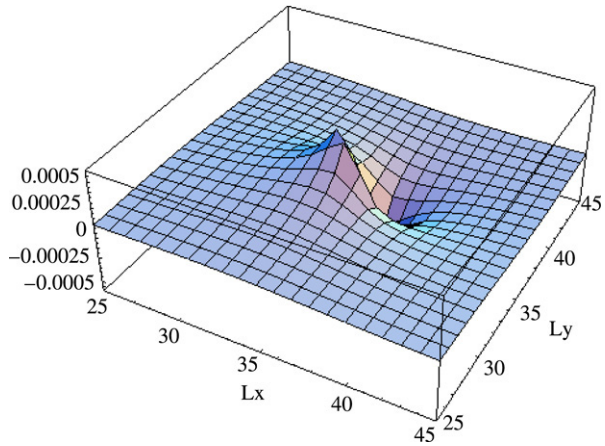


**Fig. 14.** dc displacements of a breather as a function of the lattice vector *l*. Figure from [126].

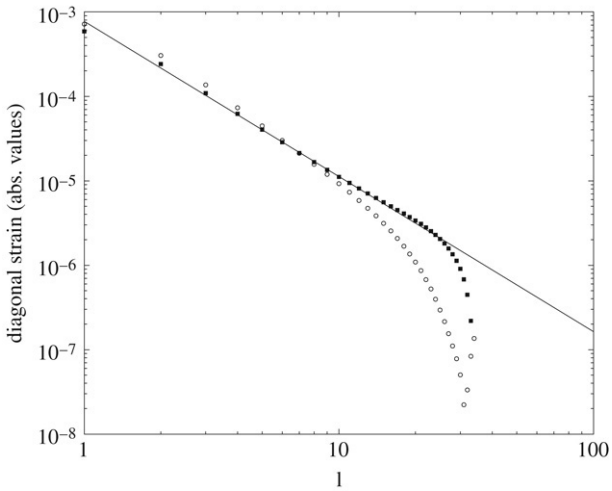


**Fig. 15.** Variation of the absolute value of the strain along the diagonals of the lattice on a double logarithmic plot. Open circles — (1, 1) direction; filled squares — (−1, 1) direction. Figure from [126].

to systematically account for the surprising localization of all higher harmonics of a breather solution in the continuous sine-Gordon equation, despite the fact that $\omega_q$ is unbounded there. It comes together with the property of the sine-Gordon equation being integrable. This implication of a (perhaps uncountable) infinite number of conservation laws is equivalent to a corresponding number of symmetries confining the dynamics to high dimensional tori no matter where one starts in phase space. It has been since conjectured that it is these symmetries which for some reason also guarantee that the breather exists, since one has to satisfy an infinite number of additional constraints – one for each resonant higher harmonics – in order to suppress the nondecaying linear solution for it, leaving one with the nonlinear correction only.

### *4.2. Dynamical stability of perturbed discrete breathers*

One of the important problems, associated with discrete breathers, is their dynamical stability, i.e. stability of these solutions with respect to small perturbations in initial conditions. The issue of dynamical stability of DBs has been also discussed at length in Refs. [133,18]. Here we will briefly summarize the most important aspects of this problem, and give some examples.

#### *4.2.1. Linear stability*

The most common approach to the problem of dynamical stability of discrete breathers is to consider the linearized phase space flow around the periodic orbit, corresponding to a given DB solution [263]. We have already discussed the computational aspects of such an approach in chapter 3.3. Imposing certain restrictions on the perturbation amplitude, the dynamics of small perturbations $\epsilon_n(t)$ to the DB solution $\hat{x}_n(t)$ is described by the linear equation (3.12). Within this approximation, the DB acts as a parametric time-periodic driver, and all the necessary information about the dynamics of

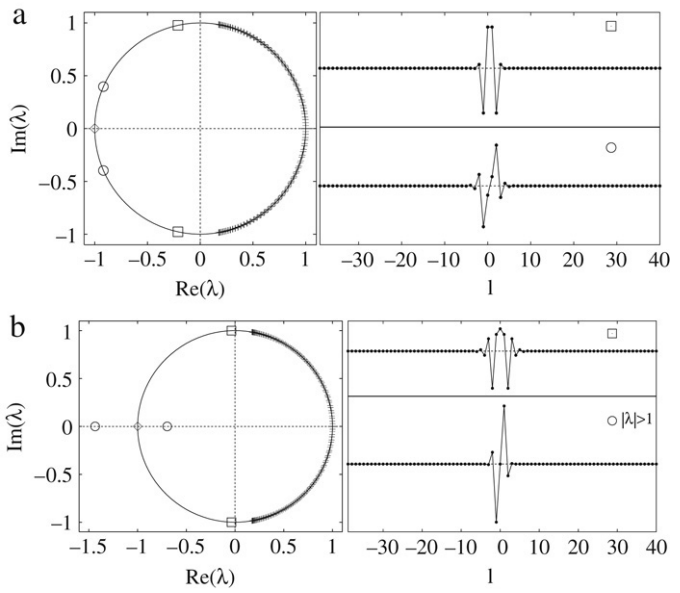


**Fig. 16.** Floquet spectra and profiles of localized eigenvectors for a bond-centered (a) and site-centered (b) DB in the 1D Fermi–Pasta–Ulam chain with even interaction potential (the irreducible Floquet period is $T = T_b/2$). The corresponding DB profiles are shown in Fig. 3. Left panels: location of Floquet eigenvalues $\lambda$ in the complex plane (crosses, diamonds, squares, circles). The unit circle is shown to guide the eye. Right panels: real part of the displacement components of the Floquet eigenvectors marked with the corresponding symbols (squares and circles). Data from [121].

perturbations is contained in the associated symplectic Floquet matrix (3.22). The period of the Floquet problem generally coincides with the DB period, $T = T_b$. However, for symmetric potentials (cf. chapter 3.2.3) the DB solution contains only odd Fourier harmonics with respect to time, and the Floquet driver is periodic with one half of the DB period, $T = T_b/2$. The condition of linear (marginal) stability of the DB solution is that all perturbations stay bounded in time. This implies that all the Floquet eigenvalues $\lambda_\nu$ are located on the unit circle in the complex plane: $|\lambda_\nu| = 1$.

It may become quite difficult to assure numerically that a particular eigenvalue is of modulus one. Aubry suggested [18] an extended eigenvalue problem by adding the term $E \cdot \epsilon_n$ to the r.h.s. of Eq. (3.12) and searching only for states with modulus one. Then, the reformulated eigenvalue problem becomes analogous to the one arising in solid state theory when calculating dispersion curves of electrons, phonons, magnons, etc. The spectrum will form a set of $2\pi$-periodic symmetric bands $E_\nu(\theta)$, $E_\nu(-\theta) = E_\nu(\theta)$. The argument $\theta$ (wave vector) can be chosen, for convenience, in the interval $[-\pi, \pi]$ (Brillouin zone). Any eigenvalue $\lambda_\nu = \exp(\mathrm{i}\theta_\nu)$ lying on the unit circle of the original Floquet problem corresponds to a zero of a dispersion curve $E(\theta_\nu) = 0$. At the expense of more computations, this procedure may allow for a safer elimination of errors in determining the Floquet eigenvalues located on the unit circle. The trick is that one searches for a curve which intersects a horizontal line. Such intersection points can be determined with finite numerical accuracy.

All Floquet eigenvalues for a typical DB solution can be divided into two groups: those having spatially localized and spatially extended eigenvectors. Since the DB is exponentially localized in a finite region of the lattice, the extended eigenvectors are locally deformed linear modes (standing waves) of the system. The corresponding eigenvalues form one or several pairs of arcs on the unit circle (depending on the number of bands in the linear spectrum), and their eigenvalues are indicated by crosses in Fig. 16. If the linear spectrum of the system has an acoustic-like band, i.e. it includes frequency zero, the corresponding pair of arcs on the unit circle will merge at $+1$. Fixing the DB parameters, the number of eigenvalues, corresponding to extended perturbations, increases while increasing the size of the system. In contrast, the number of eigenvalues, corresponding to spatially localized perturbations (internal modes of the DB), depend solely on the DB parameters and does not depend on the size of the system.

For Hamiltonian systems there are always two isolated eigenvalues corresponding to fundamental (so called marginal) localized Floquet modes [18,21]: the phase mode describing a rotation of the overall phase of the breather (i.e. a sliding along the periodic orbit in phase space), and the growth mode describing a change of DB frequency/energy (i.e. a sliding along the DB family). The oscillation period of the perturbation along the phase mode equals $T_b$. The perturbation along the growth mode, in addition to a periodic oscillation like the phase mode, growths linearly in time (due to the change of the DB frequency along the family of solutions). The pair of these two modes corresponds to an irreducible Jordan form of the Floquet matrix, so that the corresponding eigenvalues are located at $+1$ ($-1$), when the Floquet driving period is $T = T_b$ ($T = T_b/2$), see eigenvalues indicated by diamonds in Fig. 16. The number of fundamental DB modes can increase pairwise, if additional conservation laws (integrals of motion) exist. Furthermore, pair(s) of eigenvalues can appear at $+1$ for specific control parameter values corresponding to a bifurcation point of the DB. Note, that eigenvalues $\lambda = +1$ of the

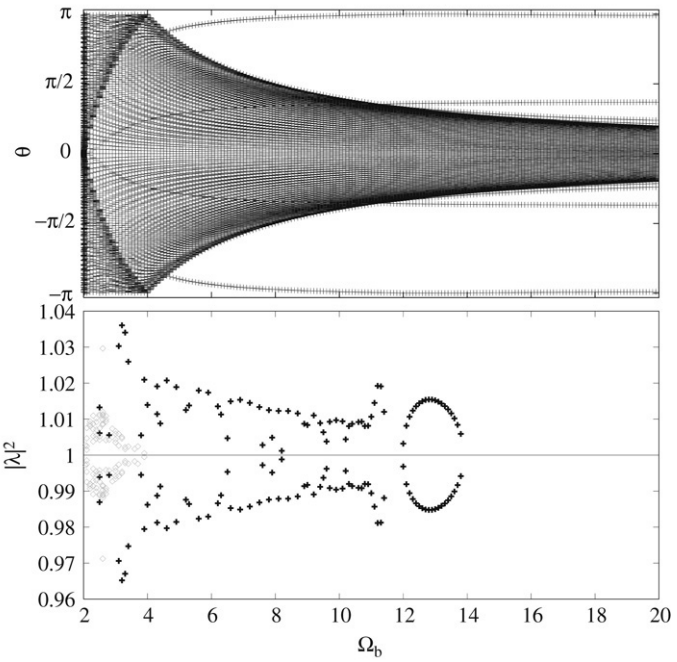


**Fig. 17.** All Floquet phases $\theta$ and the squared eigenvalue length $|\lambda|^2$ corresponding to unstable perturbations for a bond-centered DB in the 1D Fermi–Pasta–Ulam chain with an asymmetric interaction potential, as a function of the DB frequency $\Omega_b$. The corresponding DB profile for $\Omega_b = 4.5$ is shown in Fig. 13. Eigenvalues which correspond to finite size instabilities are shown using gray symbols. Data from [121].

Floquet problem correspond to zero eigenvalues of the Newton matrix (3.9), used to compute the DB solution. Therefore, the Newton method, described in Section 3.2.1, usually has a bad convergence in a vicinity of such bifurcation points.

Another important localized Floquet mode, indicated by circles in Fig. 16, is coined the "pinning" or "translational" mode [21]. This perturbation tends to shift the DB along the lattice and has a spatial symmetry which differs from that of the DB itself. For stable DBs the corresponding eigenvalues are shifted away from $+1$, staying on the unit circle. For unstable DBs they may be located off the unit circle on the real axis, cf. Fig. 16(a) and (b). Perturbing a linearly stable DB along its pinning mode will cause oscillations of the DB around its stable position. Perturbation along an unstable pinning mode can result in the DB motion along the lattice [21,58]. However, during this motion the DB loses energy through radiation of phonons, and eventually it becomes trapped again by the effective lattice potential.

Changing the control parameters of the model, as well as the DB solution parameter (its frequency or energy), Floquet eigenvalues will move in the complex plane. But the only way a particular eigenvalue can leave the unit circle is through a collision with another eigenvalue having an opposite Krein signature [18,17], defined for each pair of complex conjugate eigenvalues $\{\lambda_\nu, \lambda_\nu^*\}$ as

$$\kappa(\lambda_\nu) = \mathrm{sign}\left\{iI(\epsilon_n^{(\lambda)}, \epsilon_n^{(\lambda)*})\right\}. \tag{4.29}$$

Here $I(.,.)$ is the symplectic product defined in Eq. (3.15) and $\epsilon_n^\lambda$ is the eigenvector corresponding to the eigenvalue $\lambda_\nu$. The Krein signature is the sign of the Hamiltonian energy carried by the corresponding eigenvector [49,371]. The above criterion of a DB instability implies a resonance between two perturbations, one of which takes energy from the DB and passes it to the other perturbation. Another interpretation of the Krein criterion was given by Aubry [18]. In terms of the dispersion bands $E_\nu(\theta)$, the Krein signature (4.29) is the sign of the slope of the dispersion curve at its intersection point $\theta = \theta_\nu$ with the zero axis $E = 0$:

$$\kappa\left[\lambda_\nu \equiv \exp(i\theta_\nu)\right] = \mathrm{sign}\left\{\frac{dE_\nu(\theta)}{d\theta}\right\}\Bigg|_{\theta=\theta_\nu}. \tag{4.30}$$

Any deviation of a pair (quadruplet) of eigenvalues from the unit circle happens when a band $E_\nu(\theta)$ looses two (four) zeros. The opposite signs of slopes (4.30) at the points, corresponding to the colliding eigenvalues, is a necessary (but not sufficient!) condition for such a scenario to occur.

Often, the above collisions occur when a pair of isolated eigenvalues, associated with a localized perturbation, enters the band of eigenvalues associated with extended perturbations, see Fig. 17 in the region $4.6 \lesssim \Omega_b \lesssim 12$. Colliding quadruplets of eigenvalues leave the unit circle, resulting in oscillatory (Krein) instabilities of the DB [180]. Here the term *"oscillatory"* is used to underline the fact, that the period of the unstable perturbation is incommensurate with the DB period. The corresponding unstable perturbations have maximum amplitudes in the DB core together with nonvanishing tails, see

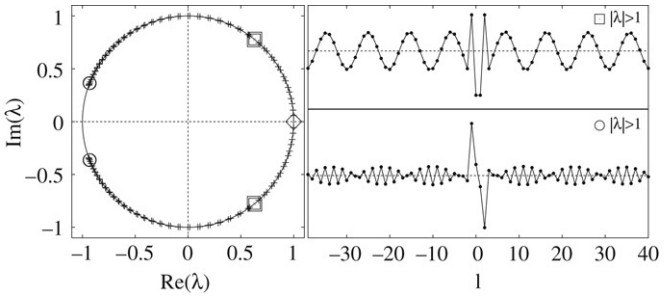


**Fig. 18.** Floquet spectrum and profiles of unstable eigenvectors corresponding to $\Omega_b = 4.5$ in Fig. 13. Left panel: location of Floquet eigenvalues $\lambda$ in the complex plane (crosses, diamonds, squares, circles). The unit circle is shown to guide the eye. Right panels: real part of the displacement components of the Floquet eigenvectors marked with the corresponding symbols (square and circle). Data from [121].

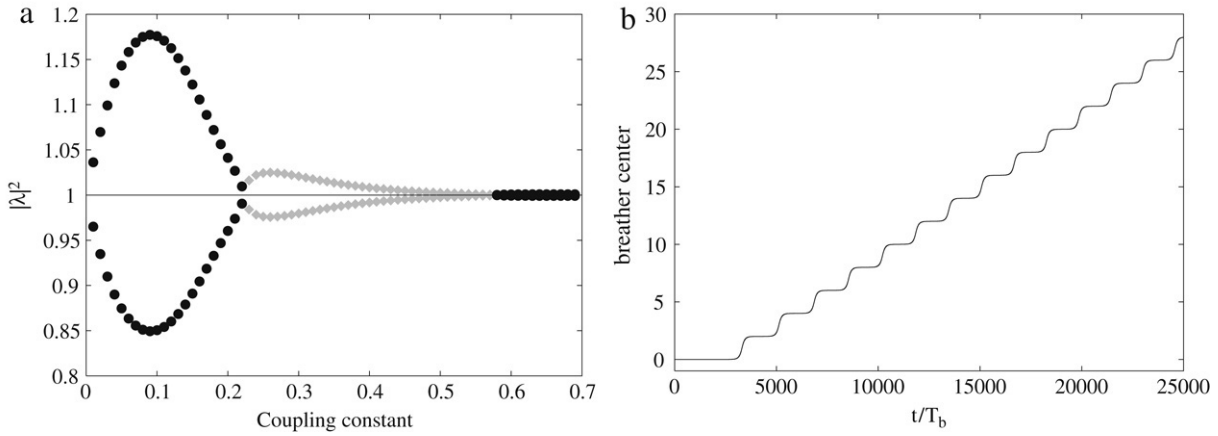


**Fig. 19.** (a) Eigenvalues, corresponding to the unstable pinning mode for bond-centered (black circles) and site-centered (gray diamonds) DBs, as functions of the intersite coupling strength. (b) Position of the DB center in dynamics with small perturbation along the unstable pinning mode. Model parameters are chosen close to the exchange of stability region. Data from [152].

Fig. 18. Similar oscillatory instabilities, but with localized unstable perturbations, can occur when two pairs of complex conjugate eigenvalues, corresponding to two different DB internal modes, collide on the unit circle [153].

The above oscillatory instabilities result from a resonant coupling between two different perturbations. The breather provides the coupling between perturbations. A quite different scenario is observed whenever a pair of complex conjugate eigenvalues collide at $\pm 1$. Note, that, by definition, two complex conjugate eigenvalues have opposite Krein signatures, so that such collisions will often cause the eigenvalues to deviate from the unit circle along the real axis. The associated instabilities (sometimes coined *real* instabilities) result from a resonant coupling between the corresponding perturbations and the DB itself. The impact of real instabilities on the DB dynamics is quite different for extended and localized perturbations.

Complex conjugate eigenvalues, corresponding to extended perturbations, can collide on the unit circle whenever the corresponding arcs of eigenvalues overlap at $-1$, see Fig. 17 in the region $\Omega_b \leq 4$. The resulting instabilities cause the DB to resonantly pump energy into the unstable mode. Obviously, the strength of real instabilities with extended modes should depend on the system size. Indeed, such instabilities are known to be finite size effects [262,19,23]. Deviations of the corresponding eigenvalues from the unit circle are inversely proportional to the linear system size: $|\lambda| - 1 \sim 1/N$.

In contrast, any collision of two complex conjugate eigenvalues, corresponding to localized perturbations, at $+1$ or $-1$ will cause instabilities independently of the size of the system (see the corresponding ellipse structure in Fig. 17 in the region $12 \lesssim \Omega_b \lesssim 14$). The corresponding unstable perturbations have a localized structure, cf. the above pinning instability in Fig. 16(b). The appearance of such instabilities is usually connected to bifurcations of the DB solution.

In some models a related mechanism of the exchange of stability [296,152,394] between bond-centered and site-centered DBs can be observed: while changing the model parameters the two principal types of DB solutions exchange their stability with respect to the pinning perturbation, see Fig. 19(a). In a vicinity of model parameters, where the exchange of stability occurs, DBs are reported to possess an enhanced mobility, see Fig. 19(b). Furthermore, it was shown [296,394], that the process of exchange of stability is accompanied by bifurcations of bond-centered and site-centered DB solutions, and the appearance of an intermediate type DB solution, having no spatial symmetry. Remarkably, in the one-dimensional DNLS model with saturable nonlinearity these intermediate DB solutions are reported to belong to the one-parameter family of exact solutions having an *analytical* sech-shaped form [205,394], despite the fact that the model is non-integrable.

The details of the various cases of switching between linearly stable and unstable DB states can be quite complicated. While that may seem as a strange complication of the rather straightforward picture of emergence of DB solutions, it is a consequence that we deal with periodic orbits in a high-dimensional phase space of nonintegrable systems. The good thing here is, that this richness may be used for various spectroscopical tools in various settings.

#### *4.2.2. Going beyond linearization*

The above linear stability analysis is a powerful tool to predict different types of instabilities of a given DB solution. Still, there are many questions remaining when one considers the long-time dynamics of perturbed DBs. Do there exist other possible mechanisms of DB instabilities, apart from exponentially growing perturbations? Does a perturbed linearly stable DB remain as a localized object for infinitely large times, or does it eventually decay into radiative modes of the system? If an unstable DB is perturbed along the growing perturbation, the symplectic analysis of the linearized phase space flow tells that the perturbation grows, with a given fixed Floquet (DB) driving. But the original problem is Hamiltonian, and the growth of the perturbation has to go on the expense of the DB energy. Even more surprising is the situation when we perturb along the exponentially decaying perturbation. Then after some transient in time the energy will disappear. In the original Hamiltonian setting that should imply that this energy is transferred to the breather.

In order to answer these questions one has to return to the original nonlinear equations. Unfortunately, not much can be done analytically in this case (but see [250]). Several numerical experiments [134,127,133] demonstrate, that a perturbed linearly stable DB can evolve close to the exact time-periodic orbit for large times. Being no longer an exact time-periodic excitation, such objects will radiate their energy by exciting small amplitude phonons. Yet, the rate of energy losses can be tremendously small. Furthermore, for some perturbations, while losing energy, the localized object may asymptotically approach a periodic orbit corresponding to an exact DB solution at lower but still finite energy. In some other cases internal resonances can trigger chaotic local dynamics and increase the radiation losses by orders of magnitude. Still, even in those cases the radiation may eventually be strongly suppressed [134,133], and the residual object again starts to slowly relax toward another, low-energy, DB orbit.

These findings are supported by several analytical estimates. Bambusi showed [26,27], that periodic orbits corresponding to DB solutions are exponentially stable in the anticontinuous limit. Namely, in the limit of small interaction between sites, any deviation from the periodic orbit, which is orders of magnitude smaller than the square root of interaction strength, will stay close to the periodic orbit for times proportional to the exponential of some inverse power of the interaction strength. MacKay and Sepulchre derived general conditions at the anticontinuous limit such that discrete breathers are $l_2$-linearly stable for weak enough coupling.

Certain estimates can be made by considering higher order (nonlinear) corrections to the above linear perturbation theory. Following this path, on the basis of a simple DNLS model, Johansson and Aubry have shown [183] that nonlinear interactions between a DB and single-mode small-amplitude perturbations can lead to breather *growth*, but not to breather decay. Further investigations have revealed [179], that the description of breather *decay* requires simultaneous excitation of at least two independent linear modes of the system, while in certain particular cases the DB decay can be realized only through third- and higher-order radiation processes.

### *4.3. Modulational instability of extended states and discrete breathers*

Consider a family of DB solutions. Let us slide along that family in either of the two directions, exploring also additional branches which may cross our way at bifurcations. Where do these branches end? Certainly there are many terminating situations possible. One of them could be where the amplitude of the DB vanishes. This is indeed quite typical, though there may be families (examples will follow) which do not possess such limiting solutions. So let us assume that we found a DB family with an end point of zero amplitude. By definition all solutions on the family are localized in space. Thus all multiples $k\Omega_b$ of the DB solutions are located outside the plane wave spectrum $\omega_q$. Since the DB solutions with small amplitudes are very close to plane waves, the only possibility we are left with is to conclude that in the limit of zero amplitude the main harmonic of the DB solution $\Omega_b$ tends to an edge of the spectrum $\omega_q$. Thus we may expect that in that limit DB solutions occur through bifurcations of band edge plane waves or simply band edge modes (BEM). Moreover, since the frequency (and thus period) of both the BEM and the limiting DB solution coincide in the discussed limit, we are interested in tangent bifurcations of the band edge plane wave. The study of the bifurcation properties of BEMs thus serves as a valuable source of information about DB properties in the limit of small amplitudes — and as it will be shown below, not only in that limit.

#### *4.3.1. Tangent bifurcations of band edge plane waves*

There exists a well-known approach to analyze plane wave instabilities which is called modulational instability. Originally this approach was designed for the study of waves in continuous media — some older papers also use the term Benjamin-Feir instability instead [402]. Within this approach a plane wave solution of the linearized equations of motion is continued into the weakly nonlinear regime. Small plane wave perturbations (of different wave length) are then added and the stability of the perturbed wave is analyzed. This approach has been very helpful in connecting the instability of certain modulated plane waves with spatially localized solutions, which exist because the nonlinearity of the system effectively

prevents a dispersion of the object. Thus the stability study of plane waves can become crucial when predicting the existence of localized solutions without actually calculating the latter.

Modulational instability has been analyzed for lattices with respect to discrete breathers in a number of publications by Kivshar and Peyrard [212], Flytzanis, Pnevmatikos and Remoissenet [143], Tsurui [389] and Sanduski and Page [344]. Extensions to the stability of standing waves with frequencies inside the linear spectrum have been also performed [185]. Dreyer et al. have used it in order to study the transition from micro- to macrostates [83].

Here we follow the approach from [113], where the stability analysis was performed for finite systems. Strictly speaking we have to analyze the stability properties of a periodic orbit (plane wave). For that we have to linearize the phase space flow around the periodic orbit — just as we did for the discrete breather. Then we have to find the eigenmodes and eigenfrequencies. Thus it is reasonable to perform a stability analysis of plane waves for a large but finite system. This will then lead to results which depend on the size of the system. The stability dependence on the size of the system is crucial when understanding properties of discrete breathers in different lattice dimensions (cf. Section 4.4). Moreover in this case we can connect the instability of a plane wave with a bifurcation of new periodic orbits — a connection hard to make for infinite systems. Further we can prove that the new bifurcating periodic orbits can not be invariant under discrete translations along the lattice — as expected for discrete breather solutions [113,133].

The most complete analysis of these bifurcations has been recently reported by Dorignac et al. [80], where particular emphasis was placed on partial and full isochronicity properties of periodic orbits. In what follows we will mainly discuss these results, referring to previous publications as well [113,133].

Let us now define the concept of partially isochronous BEMs more precisely. Let us first remark that in one-dimensional convex potentials, the motion is always periodic. To any given energy we find a unique orbit whose frequency is determined by the features of the potential (basically, its shape). We will say an orbit is *isochronous* if its frequency does not depend on its energy. Given the one-to-one correspondence between the potential and its orbits, if the motion is isochronous the potential can be said to be isochronous as well.

The most famous example of a 1D isochronous potential is the harmonic well $V(x) = \omega^2 x^2/2$ whose frequency $\omega$ is well known to be energy-independent. Nevertheless, isochronism is not the privilege of the latter and it can be shown that appropriate shears of the parabolic curve produce other *non symmetric* isochronous potentials $V(x) \neq V(-x)$ [45].

Now, for generic convex potentials, the frequency of a given periodic orbit can be expanded at low energies $E$ (bottom of the potential) as a power series in $E$. Its behaviour is generally linear with $E$ around the equilibrium position. We will call *partially isochronous* or, more precisely *isochronous up to order n*, orbits whose frequency behaves instead as a nonlinear function of the energy when expanded around $E = 0$. Typically, $\omega^2(E) = \omega_0^2 + \gamma_n E^n + \circ(E)^n$, $n \geq 2$, $\omega_0 > 0$ and $\gamma_n \neq 0$. For $n = 1$, we recover the case of non isochronous motions or, equivalently in our terminology, of orbits isochronous up to order 1. Completely isochronous orbits verify $\omega^2(E) = \omega_0^2$.

We will investigate the dynamical properties of a lattice described by the Hamiltonian

$$H = \sum_{n=1}^{N} \left[ \frac{1}{2} p_n^2 + V(x_n) + W(x_{n+1} - x_n) \right] \tag{4.31}$$

with periodic boundary conditions $x_{n+N} = x_n$. For the sake of simplicity, we consider an even number of sites $N$. The on-site ($V(x)$) and the interaction ($W(x)$) potentials are both assumed to possess a minimum at $x = 0$ around which they can be expanded as

$$V(x) = \sum_{\mu=2}^{\infty} \frac{1}{\mu} v_\mu x^\mu; \qquad W(x) = \sum_{\mu=2}^{\infty} \frac{1}{\mu} \phi_\mu x^\mu. \tag{4.32}$$

The Hamiltonian equations of motion for (4.31) are given by

$$\begin{aligned} \dot{x}_n &= p_n, \\ \dot{p}_n &= -V'(x_n) - W'(x_n - x_{n-1}) + W'(x_{n+1} - x_n). \end{aligned} \tag{4.33}$$

Let us introduce the normal coordinates

$$Q_q = \frac{1}{N} \sum_{n=1}^{N} \mathrm{e}^{\mathrm{i}qn} x_n, \quad q = \frac{2\pi l}{N}, l \in \left\{ -\frac{N}{2} + 1, \ldots, \frac{N}{2} \right\}. \tag{4.34}$$

Their properties are

$$Q_{q+2\pi} = Q_q \quad \text{and} \quad Q_{-q} = Q_q^* \quad (x_n \in \mathbb{R}), \tag{4.35}$$

and inverting the transform (4.34) yields

$$x_n = \sum_q \mathrm{e}^{-\mathrm{i}qn} Q_q. \tag{4.36}$$

Rewritten in terms of normal coordinates, Eqs. (4.33) now read

$$\ddot{Q}_q + F_q(Q) = 0, \tag{4.37}$$

where

$$F_q(Q) = \frac{1}{N}\sum_{n=1}^{N} e^{iqn}\left[V'\left(\sum_{q'} e^{-iq'n}Q_{q'}\right) + W'\left(\sum_{q'}(1-e^{iq'})e^{-iq'n}Q_{q'}\right) - W'\left(\sum_{q'}(e^{-iq'}-1)e^{-iq'n}Q_{q'}\right)\right]. \tag{4.38}$$

A linearization of $F_q(Q)$ around $Q_q = 0$ leads to the equations of motion of a harmonic lattice, namely

$$\ddot{Q}_q + \omega_q^2 Q_q = 0, \tag{4.39}$$

where

$$\omega_q^2 = v_2 + 4\phi_2 \sin^2\left(\frac{q}{2}\right) \tag{4.40}$$

represents the squared frequency of each *linear* mode $q$.

In what follows, we will be interested in the stability of two particular nonlinear modes corresponding to the natural continuation of the linear $q = 0$ and $q = \pi$ modes defined by (4.39). These nonlinear modes are time-reversible periodic solutions of (4.37) which converge to their respective standing wave linear modes as their energy tends to zero. Notice that the linear frequency $\omega_0$ of the in-phase mode is always nondegenerate and because the number of sites $N$ is even, the linear frequency $\omega_\pi$ of the out-of-phase mode is nondegenerate as well. All other modes $q \neq 0, \pi$ are twofold degenerate ($\omega_q = \omega_{-q}$).

The system of equations (4.37) is of the form $\ddot{Q} + F(Q) = 0$, where $Q$ and $F(Q)$ denote two vectors of components $Q_q$ and $F_q(Q)$ respectively, $q \in \{0, 2\pi/N, \ldots, 2(N-1)\pi/N\}$. A perturbation $\eta$ of the system around the solution $Q$ gives rise to the following variational system

$$\ddot{\eta} + DF(Q)\eta = 0 \tag{4.41}$$

where $DF(Q)$ is the Jacobian matrix of $F$ evaluated in $Q$ whose components are $DF_{qk}(Q) = \frac{\partial F_q}{\partial Q_k}(Q)$.

To evaluate the Jacobian matrix, we use (4.38) and find

$$\frac{\partial F_q}{\partial Q_k}(Q) = \frac{1}{N}\sum_{n=1}^{N} e^{i(q-k)n}\left[V''\left(\sum_{q'} e^{-iq'n}Q_{q'}\right) + (1-e^{ik})W''\left(\sum_{q'}(1-e^{iq'})e^{-iq'n}Q_{q'}\right) - (e^{-ik}-1)W''\left(\sum_{q'}(e^{-iq'}-1)e^{-iq'n}Q_{q'}\right)\right]. \tag{4.42}$$

We will follow the method described in [113] in order to obtain the critical amplitudes and energies, if any, at which orbits I and II become unstable and bifurcate tangentially to give rise to other types of periodic orbits which break the translational invariance of the lattice.

Once the periodic solution for $Q$ has been introduced in the Jacobian matrix $DF(Q)$, the variational system (4.41) presents itself as a vectorial Hill's equation for the perturbation $\eta$. This type of systems is known as *parametrically excited* as the Jacobian matrix generally depends on several parameters. In our case, such parameters are the energy (or the amplitude) of the solution $Q$ as well as the frequencies of the modes we are interested in. Once expanded as a Fourier series, the Jacobian matrix may be decomposed into a static (dc-) part (its zero mode) and a driving (ac-) part.

A paradigmatic example of Hill's equation is the Mathieu equation $\ddot{x}(t) + (\delta + 2\epsilon\cos(2t))x(t) = 0$. For a comprehensive treatment of this equation the reader is invited to consult, for example, Ref. [288]. In one dimension (the Jacobian matrix is reduced to a single element in this case), the parameter $\delta$ plays the role of the static part and $2\epsilon\cos(2t)$ the role of the driving. It is known from the stability analysis of this equation that the behaviour of its solution varies according to the values of the parameters $\delta$ and $\epsilon$. The solution can be stable, unstable or periodic. In the $\epsilon\delta$-plane ($\delta$ as $x$-axis and $\epsilon$ as $y$-axis), the regions of instability present themselves as tongues (the so-called Arnold's tongues) starting from the $\delta$-axis at the values $\delta_n = n^2$, $n \in \mathbb{N}$ and widening as $\epsilon$ increases. In these regions the motion is unbounded, whereas outside it is stable (bounded).

Of particular interest are the boundaries of such regions called *transition curves* that separate stable from unstable motions. Along these curves, the solution is periodic of period $\pi$ ($n$ even) or $2\pi$ ($n$ odd). For small $\epsilon$ values, a perturbative treatment of the Mathieu equation which consists in expanding both $x(t)$ and the parameter $\delta$ as series in $\epsilon$ allows for the determination of the transition curves of the form $\delta_n = n^2 + \sum_l A_{nl}^{s/a}\epsilon^l$. The coefficients $A_{nl}^{s/a}$ depend on the tongue ($n$) as well as on the *branch* (that is, the boundary) we are interested in. It can be shown that one of these branches is related to time reversal symmetric solutions $\eta$ (denoted by the subscript $s$) whereas the second one is associated with time reversal antisymmetric solutions ($a$).

Let us suppose now that we fix the value of $\delta$ close to a transition point $\delta_n = n^2$. At $\epsilon = 0$, the point corresponding to the state of the system in the parameter space is located in a region of stability. Let us increase the value of $\epsilon$ at fixed $\delta$. If the corresponding vertical line crosses the transition curve nearby, the solution $x(t)$ becomes unstable above the crossing point. And right at the intersecting point, the solution is periodic.

*4.3.2. Tangent bifurcations of the in-phase mode*

Oscillators are said to be in phase when they perform identical periodic motions. This corresponds to

$$Q_q = Q_0 \delta_{q,0} \tag{4.43}$$

where $\delta_{q,q'} = 1$ if $q = q'$ $[2\pi]$ and 0 else. The previous expression is a solution of the equations of motion (4.37) provided

$$\ddot{Q}_0 + V'(Q_0) = 0. \tag{4.44}$$

The solution $Q_q = Q_0 \delta_{q,0}$ represents the in-phase periodic orbit. We call it orbit I. The total energy of the lattice evolving according to orbit I is

$$E_I = H(\{x_n = Q_0\}) = N\left(\frac{1}{2}\dot{Q}_0^2 + V(Q_0)\right). \tag{4.45}$$

We will use an energy density (or energy per site) rather than the total energy $E_I$ to describe this orbit. It is given by $\varepsilon_I = E_I/N$ and represents the energy of the oscillator $Q_0$ evolving according to (4.44).

Evaluated along orbit I, the Jacobian matrix (4.42) is diagonal

$$DF_{qk}(Q_I) = \left[V''(Q_0) + 4\phi_2 \sin^2\left(\frac{k}{2}\right)\right]\delta_{q,k}. \tag{4.46}$$

All perturbations decouple from each other and their equations of motion are

$$\ddot{\eta}_q + \left[V''(Q_0) + 4\phi_2 \sin^2\left(\frac{q}{2}\right)\right]\eta_q = 0. \tag{4.47}$$

As stated in [113], the perturbation $\eta_0$ describes the continuation of orbit I along itself. It cannot be responsible for a bifurcation of $Q_0$ as it simply operates a shift in time or modifies the energy (or the frequency) along the one-parameter family. We then look for the perturbation able to give rise to the required tangent bifurcation. The first to occur will be for the closest (linear) frequency to the linear in-phase frequency, that is for $q_c = 2\pi/N$.

Details of the evaluation of these equations are found in [80]. The final outcome is that the critical energy density of the out-of-phase BEM at the tangent bifurcation for $n = 1$ (non isochronous potential) is given by [113,80]

$$\varepsilon_0^{(1)} = \frac{12\phi_2 v_2^2 \sin^2(\frac{\pi}{N})}{10v_3^2 - 9v_2 v_4} + o\left(N^{-2}\right), \quad N \to \infty. \tag{4.48}$$

For partial isochronicity of order $n = 2$

$$\varepsilon_0^{(2)} = \left(\frac{54 v_2^3 \phi_2}{378 v_3 v_5 v_2^2 - 280 v_3^4 - 135 v_6 v_2^3}\right)^{1/2} v_2 \sin\left(\frac{\pi}{N}\right) + o\left(N^{-1}\right), \quad N \to \infty \tag{4.49}$$

which replaces (4.48) when the denominator in the fraction on the right hand side exactly vanishes. The general case for partial isochronicity of order $n$ has been treated in Ref. [80]. Note that it always requires positive energy densities and thus positive denominators in the corresponding expressions like (4.48) and (4.49). This is equivalent to requesting that the BEM frequency is tuned away from the spectrum $\omega_q$ when increasing the amplitude.

*4.3.3. Tangent bifurcations of the out-of-phase mode*

If the potential $V(x)$ is not symmetric ($V(-x) \neq V(x)$), its Taylor expansion around 0 contains at least one nonzero odd coefficient. This has no influence on the previous result concerning the in-phase motion because any oscillator of the chain performs the same motion in the same time. That reduces the set of $N$ Eqs. (4.37) to a single one (4.44), representing the equation of motion of a single oscillator in the on-site potential $V$. But as soon as we are interested in an out-of-phase like motion, we have to consider a dimerization of the chain, each dimer being made of two neighbouring units oscillating in opposite phase. The lack of symmetry of $V$ induces two different motions to the right and to the left. This prevents us from finding a pure out-of-phase solution to (4.37) which would imply $Q_q = Q_\pi \delta_{q,\pi}$ or in real space $x_{2n} = -x_{2n+1}$. Instead, we can look for a solution of the type

$$Q_q = Q_0 \delta_{q,0} + Q_\pi \delta_{q,\pi} \tag{4.50}$$

involving both in- and out-of-phase variables, the others being zero. Using (4.36), we obtain $x_n = Q_0 + (-1)^n Q_\pi$ or $x_{2n} = Q_0 + Q_\pi$ and $x_{2n+1} = Q_0 - Q_\pi$. Adding and subtracting the equations of motion for $x_{2n}$ and $x_{2n+1}$, we finally get

$$\begin{aligned} &\ddot{Q}_0 + \frac{1}{2}\left[V'(Q_0 + Q_\pi) + V'(Q_0 - Q_\pi)\right] = 0, \\ &\ddot{Q}_\pi + \frac{1}{2}\left[V'(Q_0 + Q_\pi) - V'(Q_0 - Q_\pi)\right] + W'(2Q_\pi) - W'(-2Q_\pi) = 0. \end{aligned} \tag{4.51}$$

The total energy of the system, which evolves according to orbit II is

$$E_{II} = H(\{x_{2n} = Q_0 + Q_\pi, x_{2n+1} = Q_0 - Q_\pi\}) = \frac{N}{2}\left(\dot{Q}_0^2 + \dot{Q}_\pi^2 + V(Q_0+Q_\pi) + V(Q_0-Q_\pi) + W(2Q_\pi) + W(-2Q_\pi)\right). \tag{4.52}$$

Evaluated along orbit II, the Jacobian matrix (4.42) now reads

$$DF_{qk}(Q_{II}) = \frac{1}{2}\left[V''(Q_0+Q_\pi) + V''(Q_0-Q_\pi) + 4\sin^2\frac{k}{2}\{W''(2Q_\pi) + W''(-2Q_\pi)\}\right]\delta_{k,q} + \frac{1}{2}\left[V''(Q_0+Q_\pi) - V''(Q_0-Q_\pi) - 2i\sin k\{W''(2Q_\pi) - W''(-2Q_\pi)\}\right]\delta_{k,q+\pi} \tag{4.53}$$

and the corresponding dynamics,

$$\ddot{\eta}_q + \frac{1}{2}\left[V''(Q_0+Q_\pi) + V''(Q_0-Q_\pi) + 4\sin^2\frac{q}{2}\{W''(2Q_\pi) + W''(-2Q_\pi)\}\right]\eta_q + \frac{1}{2}\left[V''(Q_0+Q_\pi) - V''(Q_0-Q_\pi) + 2i\sin q\{W''(2Q_\pi) - W''(-2Q_\pi)\}\right]\eta_{q+\pi} = 0. \tag{4.54}$$

Similar to the in-phase mode, the out-of-phase mode will eventually undergo a first tangent bifurcation via the perturbation $\eta_{q_c}$ whose frequency is the closest to $\omega_\pi$, that is, for $q_c = \pi - 2\pi/N$. As $N$ tends to infinity, $q = 2\pi/N$ plays the role of the small parameter in the variational equations. But at variance with the in-phase variational equation where $\Delta \propto \sin^2(\pi/N)$ was the unique small parameter, Eq. (4.54) possesses two small parameters through $\sin^2((q_c+\pi)/2) \sim (\pi/N)^2$ and $\sin(q_c) \sim \pi/N$. Notice that these two parameters are not of the same order.

Details of the evaluation of these equations are found in [80]. The final outcome is that the critical energy density of the in-phase BEM at the tangent bifurcation for $n = 1$ (non isochronous potential) is given by [113]

$$\varepsilon_\pi^{(1)} = \frac{4(v_2+4\phi_2)\phi_2}{3(v_4+16\phi_4) + \frac{2v_3^2}{3v_2+16\phi_2} - \frac{4v_3^2}{v_2}}\sin^2\left(\frac{\pi}{N}\right) + o\left(N^{-2}\right), \quad N\to\infty. \tag{4.55}$$

Let us notice first that, when $v_3 = 0$ this expression reduces to formula (3.20) of [80] obtained in the special case of a symmetric on-site potential $V(x)$. The correction introduced by the asymmetry of $V(x)$ (i.e. the term proportional to $v_3^2$ in the denominator of (4.55)) has the interesting feature always being negative. Therefore, the following inequality

$$v_3^2 < \frac{3v_2(v_4+16\phi_4)(3v_2+16\phi_2)}{2(5v_2+32\phi_2)} \tag{4.56}$$

has to be satisfied for the out-of-phase mode to undergo a tangent bifurcation. This corresponds, as we have seen in the section above, to requiring that the frequency increases with the energy.

Another interesting result easily drawn from (4.55) concerns the case of partially isochronous *on-site* potentials. It is found in this case that a certain amount of nonlinearity ($\phi_4$) in the interaction potential is needed in order to ensure a bifurcation of the *out-of-phase mode*. Indeed, the relation between the first coefficients of the Taylor expansion of $V(x)$ is $10v_3^2 = 9v_2v_4$ in this case. The denominator of (4.55) is then positive provided

$$\phi_4 > \frac{1}{5}\frac{v_4\phi_2}{3v_2+16\phi_2}. \tag{4.57}$$

So that, in a chain of harmonically coupled partially isochronous oscillators, no discrete breather (if any) stems from the tangent bifurcation of the out-of-phase mode. At the same time we can conclude, that breathers appear for fully isochronous harmonic oscillators ($v_4 = 0$) when coupled anharmonically ($\phi_4 > 0$). This statement is to some extent confirmed by a recent proof that breathers exist and can be continued from zero anharmonic coupling for harmonic oscillators coupled by a purely quartic interaction [116].

For a first degree of isochronism ($n = 2$), we obtain [80]

$$\varepsilon_\pi^{(2)} = \frac{v_2+4\phi_2}{2}\left(\frac{-\phi_2}{2(v_2+4\phi_2)\tilde{T}_4}\right)^{1/2}\sin\left(\frac{\pi}{N}\right) + o\left(N^{-1}\right), \quad N\to\infty, \tag{4.58}$$

where $\tilde{T}_4$ is a function of the expansion parameters of the potentials [80].

A special case is $v_2 = 0$ and $\phi_3 \neq 0$. In such a case the spectrum $\omega_q$ is acoustic, but the interaction potential $W$ is asymmetric. In the lowest order $n = 1$ of isochronicity we obtain [113]

$$\varepsilon_\pi^{(1)} = \frac{16\pi^2}{N^2}\frac{\phi_2^3}{3\phi_2(v_4+16\phi_4) - 64\phi_3^2}. \tag{4.59}$$

A tangent bifurcation takes place if

$$3\phi_2(v_4 + 16\phi_4) \geq 64\phi_3^2. \tag{4.60}$$

Consequently for an acoustic spectrum case the condition – that the band edge plane wave frequency is repelled from the linear spectrum with increasing amplitude – is only necessary but not sufficient for a tangent bifurcation to occur.

Let us give an example where no small amplitude discrete breathers are expected. The one-dimensional Toda chain is characterized by [385] $v_\mu = 0$, $\phi_2 = 1$, $\phi_3 = -1/2$, $\phi_4 = 1/6$. Clearly (4.60) is not satisfied (note that in that case the frequency of the upper zone boundary plane wave *is* repelled from the linear spectrum with increase of energy, so the repelling condition is a necessary condition, but not a sufficient one). Thus in the limit of large system size no tangent bifurcation occurs at small energies, and no discrete breathers should occur.

#### 4.3.4. Symmetry breaking

At the bifurcation point of the plane wave new periodic orbits occur. Because the bifurcation is tangent, the new orbits have the same period as the plane wave orbit (at the bifurcation point). Any periodic orbit is a closed loop in the phase space of the system. Consequently the new bifurcating orbits can be obtained by deformations of the loop corresponding to the plane wave orbit at the bifurcation. It was proven [113] that there is no possibility to simultaneously deform the plane wave loop and to keep its invariance with respect to the permutations, i.e. to discrete translations of the lattice. Consequently there are at least $N$ families of periodic orbits bifurcating from the plane wave orbits at a tangent bifurcation. The spatial structure of these orbits corresponds to the spatial structure of a discrete breather [113].

#### 4.3.5. Energy thresholds for tangent bifurcations of BEMs

We then turn to the determination of the (total) bifurcation energy $E_q^{(n)}$ of a BEM partially isochronous up to order $n$, in the thermodynamic limit. We find that [80]

$$E_q^{(n)} = N\varepsilon_q^{(n)} \sim N^{1-\frac{2}{n}} \quad (N \to \infty). \tag{4.61}$$

Now, if the BEM is not isochronous, ($n = 1$), its total bifurcation energy vanishes as the lattice becomes infinite and so does the breather energy in this limit. No energy threshold exists in this case as already mentioned in [113]. However, as soon as the band edge mode bears some degree of isochronism, ($n > 1$), its total bifurcation energy either converges to a finite value ($n = 2$) or simply diverges ($n > 2$) and energy thresholds are thus expected.

We note incidentally that expression (4.61), although valid for a one-dimensional chain, bears some striking resemblance with its multi-dimensional counterpart in the *non isochronous* case which reads $E_q^{(d)} \sim N^{1-\frac{2}{d}}$ where $d$ is the dimension of the lattice [80]. Combination of both isochronism ($n$) and dimensionality ($d$) leads immediately to the conclusion that the total bifurcation energy of a BEM scales like

$$E^{(n,d)} \sim N^{1-\frac{2}{nd}} \quad (N \to \infty). \tag{4.62}$$

Energy thresholds for discrete breather families bifurcating tangentially from BEMs are thus expected as soon as one of the positive integers $n$ or $d$ is strictly greater than one. In general we can identify a critical lattice dimension $d_c$ which separates zero from nonzero energy thresholds for tangent bifurcations of BEMs:

$$d_c = \frac{2}{n}. \tag{4.63}$$

For the general nonisochronous case $n = 1$ we have $d_c = 2$, for $n = 2$ it follows $d_c = 1$, and for larger values of $n \geq 3$ the result is $d_c < 1$.

### 4.4. Energy thresholds of discrete breathers

DB solutions come in one-parameter families. The parameter can be the amplitude (measured at the site with maximum amplitude), the energy $E$ or the breather frequency $\Omega_b$. Its amplitude can be lowered to arbitrarily small values, at least for some of the families for an infinite lattice. In this zero amplitude limit, the DB frequency $\Omega_b$ approaches an edge of the phonon spectrum $\omega_q$. This happens because the nonresonance condition $\omega_q/\Omega_b \neq 0, 1, 2, 3, \ldots$ has to hold for all solutions of a generic DB family. In the limit of zero amplitude, the solutions have to approach solutions of the linearized equations of motion, thus the frequency $\Omega_b$ has to approach some $\omega_q$, but at the same time not to coincide with any phonon frequency. This is possible only if the breather's frequency tends to an edge $\omega_E$ of the phonon spectrum in the limit of zero breather amplitude. If we consider the family of nonlinear plane waves which yields the corresponding band edge plane wave in the limit of zero amplitude $A$, then its frequency $\omega$ will depend on $A$ as

$$|\omega - \omega_E| \sim A^z \tag{4.64}$$

for small $A$, where the detuning exponent $z$ depends on the type of nonlinearity of the Hamiltonian (4.1), and can be calculated using standard perturbation theory [288]. Note that at low amplitudes the energy of such a state $E \sim A^2$ and thus

$$z = 2n, \tag{4.65}$$

so the detuning exponent $z$ is two times the order of isochronicity $n$ from chapter 4.3.1.

From the analysis in chapter 4.3 we expect that in that limit the energy of a DB solution may tend to infinity with decreasing amplitude, since in the tangent bifurcation point it meets the unstable BEM whose energy may diverge there, depending on the dimension and the isochronicity order $n$. In the limit of small amplitudes the energy density in the DB solution decreases, but the DB itself localizes less and less, spreading over larger and larger parts of the lattice. The divergence of the total DB energy can thus only originate from a divergence of its energy in the DB spatial tails.

*4.4.1. Short range interaction case*

Here we follow the lines of argument in Ref. [125]. Let us assume that we have a system with short range interactions (see chapter 4.1.1) and estimate the discrete breather energy in the limit of small amplitudes. Define the amplitude of a DB to be the largest of the amplitudes of the oscillations over the lattice. Denote it by $A_0$ where we define the site $l = 0$ to be the one with the largest amplitude. The amplitudes decay in space away from the breather center, and by linearizing about the equilibrium state and making a continuum approximation, the decay is found to be given by $A_l \sim CF_d(|l|\delta)$ for $|l|$ large, where $F_d$ is a dimension-dependent function

$$F_1(x) = \mathrm{e}^{-x}, \qquad F_3(x) = \frac{1}{x}\mathrm{e}^{-x} \tag{4.66}$$

$$F_2(x) = \int \frac{\mathrm{e}^{-x\sqrt{1+\zeta^2}}}{\sqrt{1+\zeta^2}}\mathrm{d}\zeta, \tag{4.67}$$

$\delta$ is a spatial decay exponent to be discussed shortly, and $C$ is a constant which we shall assume can be taken of order $A_0$. To estimate the dependence of the spatial decay exponent $\delta$ on the frequency of the time-periodic motion $\Omega_b$ (which is close to the edge of the linear spectrum) it is enough to consider the dependence of the frequency of the phonon spectrum $\omega_q$ on the wave vector $q$ when close to the edge. Generically this dependence is quadratic $(\omega_E - \omega_q) \sim |q - q_E|^2$ where $\omega_E \neq 0$ marks the frequency of the edge of the linear spectrum and $q_E$ is the corresponding edge wave vector. Then analytical continuation of $(q - q_E)$ to $\mathrm{i}(q - q_E)$ yields a quadratic dependence $|\Omega_b - \omega_E| \sim \delta^2$. Finally we must insert the way that the detuning of the breather frequency from the edge of the linear spectrum $|\Omega_b - \omega_E|$ depends on the small breather amplitude. Assuming that the weakly localized breather frequency detunes with amplitude as the weakly nonlinear band edge plane wave frequency this is $|\Omega_b - \omega_E| \sim A_0^z$. Then $\delta \sim A_0^{z/2}$.

Now we are able to calculate the scaling of the energy of the discrete breather as its amplitude goes to zero by replacing the sum over the lattice sites by an integral

$$E_b \sim \frac{1}{2}C^2 \int r^{d-1}F_d^2(\delta r)\mathrm{d}r \sim A_0^{(4-zd)/2}. \tag{4.68}$$

This is possible if the breather persists for small amplitudes and is slowly varying in space. We find that if $d > d_c = 4/z$ the breather energy diverges for small amplitudes, whereas for $d < d_c$ the DB energy tends to zero with the amplitude. Remarkably this result for the critical dimension coincides precisely with the result (4.63) using (4.65). Inserting $z = 2$ we obtain $d_c = 2$, which is in accord with the exact results on the plane wave stability [113] and thus strengthens the conjecture that discrete breathers emerge through tangent bifurcations from band edge plane waves. Note that for $d = d_c$ logarithmic corrections may apply to (4.68), which can lead to additional variations of the energy for small amplitudes.

An immediate consequence is that if $d \geq d_c$, the energy of a breather is bounded away from zero. This is because for any non-zero amplitude the breather energy can not be zero, and as the amplitude goes to zero the energy goes to a positive limit ($d = d_c$) or diverges ($d > d_c$). Thus we obtain an energy threshold for the creation of DBs for $d \geq d_c$. This new energy scale is set by combinations of the expansion coefficients in (4.1). If $z = 2$ with $|\Omega - \omega_E| \sim \beta A^2$ for the nonlinear plane waves, and the energy per oscillator $E \sim gA^2$ and the spatial decay exponent $\delta$ is related by $|\Omega_b - \omega_E| \sim \kappa\delta^2$, then the energy threshold $E_{\min}$ is of the order of $\kappa g/\beta$, and the minimum energy breather in 3D has spatial size of the order of the lattice spacing, independently of $\kappa$, $g$ and $\beta$. One should allow for a factor of $(2 + d)$ for underestimating the true height of the minimum and the contributions of nearest neighbours.

Many numerical results have since confirmed the above results. For the d-dimensional DNLS model (4.6) the left panel in Fig. 20 shows the variation of the DB energy with its central amplitude, and a clear notion of an energy threshold starting with $d = 2$ [125]. Note that in that case $n = 1$. The minimum energy DB profile for $d = 3$ is the one plotted in Fig. 9 and is indeed (still) strongly localized on the lattice. In order to observe the effect of partial isochronicity $n \geq 2$ on the appearance of energy thresholds, we present results for a modified DNLS system in one spatial dimension $d = 1$:

$$\dot{\Psi}_l = \mathrm{i}\left(\Psi_l + |\Psi_l|^{\mu-1}\Psi_l + C\sum_{m\in N_l}\Psi_m\right). \tag{4.69}$$

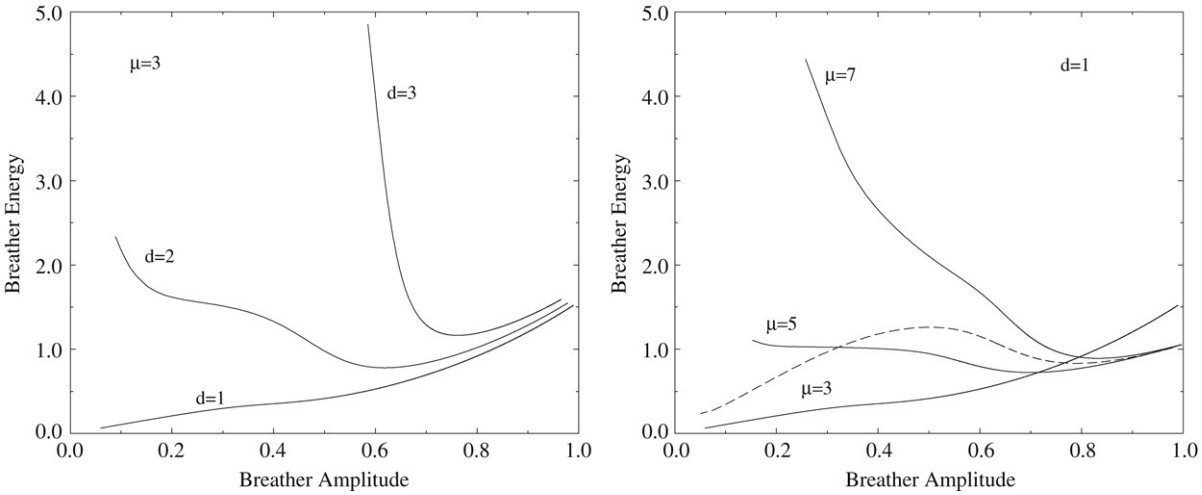


**Fig. 20.** Left panel: Breather energy versus amplitude for the DNLS system in one, two and three lattice dimensions. System sizes for $d = 1, 2, 3$: $N = 100$, $N = 25^2$, $N = 31^3$, respectively. Right panel: Breather energy versus maximum amplitude for the DNLS system in one lattice dimension and for three different exponents $\mu = 3, 5, 7$ (solid lines). The system size is $N = 100$ and the parameter $C = 0.1$. The dashed line is for the modified system (cf. text). Data are from Figs. 1, 3 in [125].

By tuning $\mu$ we can realize different orders of isochronicity:

$$n = \frac{\mu - 1}{2}. \tag{4.70}$$

In the right panel in Fig. 20 we show results for $d = 1$ and $\mu = 3, 5, 7$. Again we find full agreement with the predictions from above. Note that even one-dimensional lattices exhibit positive lower bounds on breather energies if $\mu \geq 5$. Weinstein has obtained rigorous proofs of these results for any value of $\mu$ [399].

We can predict that a modified DNLS system with an additional term $v_{\mu'}|\Psi_l|^{\mu'-1}\Psi_l$ can exhibit complex curves $E_b(A_0)$. For example, for $d = 1$, $\mu = 7$, $\mu' = 3$ and $v_{\mu'} = 0.1$, the $E_b(A_0)$-dependence will be nearly identical to the case $v_{\mu'} = 0$ already considered, if the amplitude $A_0$ is not too small. Then $E_b(A_0)$ will show a minimum at a non-zero value of $A_0$. For small $A_0$ however the energy of the breather will ultimately decay to zero, so the curve has a maximum for smaller amplitudes! The dashed line in the right panel in Fig. 20 shows the numerical calculation, which coincides with our prediction.

Another example is the two-dimensional lattice system (1.18) which is characterized by $n = 1$, and thus the critical dimension is $d = 2$. The energy thresholds have been computed and reported in [93]. The profiles of DB solutions in Fig. 4 correspond to (A) a low amplitude DB, (B) the minimum energy DB, and (C) a high amplitude DB.

### *4.4.2. Long range interactions*

Let us consider the case of a one-dimensional lattice already discussed in chapter 4.1.2. For $s \geq 3$ the critical distance from the DB core $l_c$ (which separates exponential from algebraic decay) tends to infinity in the limit of small DB amplitudes, i.e. when $\Omega_b$ approaches a BEM frequency. Consequently the breather energy will have the same qualitative behaviour as in the case of short range interaction (the results are similar to those obtained in [125], but the height and the position of the energy minima shift to larger values with decreasing values of $s$).

However for $\Omega_b < \omega_q$ and $1 < s < 3$ no exponential decay is observed and the far distance energy of the breather is given by $\sim A^2 \int \frac{1}{r^{2s}} \mathrm{d}^d r$ where $A$ is the amplitude of the breather center. This energy will always vanish in the limit of zero amplitude. We currently do not know how to estimate the tail energy correctly in such a case. Below we will outline an alternative approach to this problem [114].

We follow the second line of argument for the behaviour of the breather energy at small amplitudes. For that we consider a finite system of $N$ sites. As was shown in chapter 4.3, band edge modes undergo tangent bifurcations, which creates discrete breathers. The amplitude $A_c$ of the BEM at the bifurcation point (for nonvanishing cubic and/or quartic terms in the Hamiltonian) is given by [113]:

$$A_c \sim \sqrt{|\Omega^2_{BEPW} - \Omega^2_{q_1}|}, \tag{4.71}$$

where $q_1$ denotes the wavevector closest to the band edge wavevector. Here we consider periodic boundary conditions and a cutoff in the long range interaction at one half of the system size. This cutoff will induce finite size corrections to the

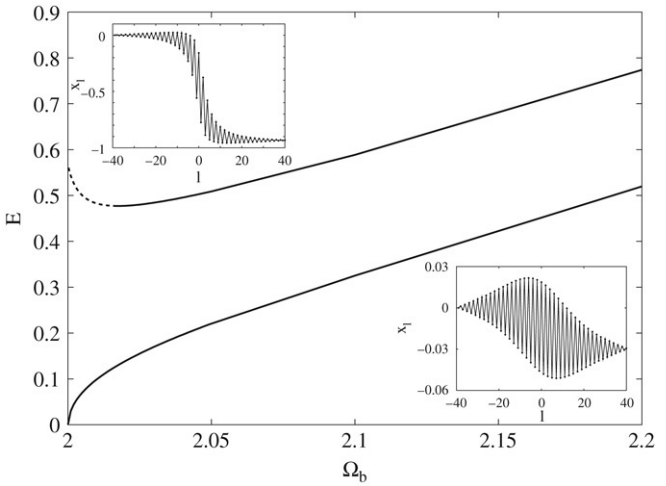


**Fig. 21.** DB energy $E$ versus DB frequency $\Omega_b$ for the FPU chain with $\phi_2 = \phi_4 = 1$ and $\phi_3 = 0.5$ (lower curve) and $\phi_3 = 1$ (upper curve). Insets: Displacements $\hat{x}_l(t = 0)$ for $\Omega_b = 2.001$ versus lattice site number $l$. Upper left inset for $\phi_3 = 1$, lower right inset for $\phi_3 = 0.5$. From [121].

dispersion $\omega_q^2$ for all $q$ except for the band edge points. With $q_1 = \frac{2\pi}{N}$ this correction amounts to

$$\Delta_{q_1} = \omega_{q_1}^2(\infty) - \omega_{q_1}^2(N) = 2C \sum_{m=N/2+1}^{\infty} \frac{1}{m^s} \left(1 - \cos\left(\frac{2\pi}{N} m\right)\right). \tag{4.72}$$

Evaluation of (4.72) for $s > 1$ gives

$$\frac{\Delta_{q_1}}{2C} \approx b(s) \left(\frac{2\pi}{N}\right)^{s-1} - 2\left(\frac{2}{N}\right)^s \tag{4.73}$$

with $b(s) = \int_{\pi}^{\infty} \frac{1}{x^s}(1 - \cos x)\mathrm{d}x$. Consequently the correct result for (4.71) and $1 < s < 3$ is $A_c^2 \sim c(s)/N^{s-1}$ with $c(s) = \int_0^{\pi} \frac{1}{x^s}(1 - \cos x)\mathrm{d}x$. The total energy $E_c \sim NA_c^2$ in the bifurcation point for $1 < s < 3$ is finally given by

$$E_c \sim N^{2-s}. \tag{4.74}$$

Note that the considered system has the lowest degree of isochronicity $n = 1$. This has to be contrasted to the results for short range interactions in one-dimensional systems which can be obtained from (4.74) by choosing $s = 3$ and is $E_c \sim 1/N$. We thus find, that anomalous dispersion at the band edge $\sim q^{s-1}$ for $1 < s < 3$ even further supports the divergence of the breather energy at small amplitudes, since for cubic and quartic anharmonicities in the Hamiltonian, for which no divergence in energy is found for short range interactions, energy divergence is obtained for long range interaction with $s < 2$. These results confirm studies of nonlinear Schrödinger chains with long range interactions, where $s < 2$ marks the appearance of two stable soliton solutions compared to one for $s > 2$ [147].

The existence of energy thresholds for breather solutions is supported by long range interactions, and can take place when short range interactions (e.g. in one-dimensional systems) are not capable of producing these thresholds.

### *4.4.3. No bifurcation but finite thresholds*

Let us discuss a result on the one-dimensional acoustic (Fermi–Pasta–Ulam) model (4.31) with vanishing onsite potential $V(x) = 0$. From the BEM stability analysis (4.60) we conclude that for $\phi_2 = \phi_4 = 1$ the critical value of $\phi_3 = 0.75$ separates existence of DB solutions at small amplitude ($\phi_3 < 0.75$) from the nonexistence of DB solutions at small amplitude ($\phi_3 \geq 0.75$). In Fig. 21 the case $\phi_3 = 0.5$ confirms the absence of an energy threshold, and the DB solution close to the tangent bifurcation indeed has small amplitudes. What will happen if we choose $\phi_3 = 1$? According to the tangent bifurcation analysis *small amplitude* breathers should not exist. However, assuming for the moment large amplitude excitations, we may conclude that the cubic potential terms ($\phi_3$) may be neglected together with the harmonic ones, as compared to the strongest quartic terms ($\phi_4$). But then we should expect DB solutions for large energies! Indeed, a computation of that situation yields DB solutions for large amplitudes and energies (Fig. 21). Since these branches cannot be continued to small amplitudes, they have to terminate with finite amplitudes, and thus with finite energies. So we conclude that for such a case DB solutions apparently exist, but since we ruled out the existence of any small amplitude DB solutions, the observed breathers show up with a nonzero energy threshold (see also [175] and references therein, and [200,199]).

#### 4.4.4. Some concluding remarks

Finally we want to briefly mention other relevant situations. First, for purely nonlinear interactions from chapter 4.1.3 DB solutions are given by a spatial profile which is independent of their actual amplitude, energy etc. Thus we can always choose arbitrarily small amplitudes, and obtain arbitrarily small energies for DBs, irrespectively of the lattice dimension and other effects.

Even in the case when a DB family allows for a limit of small amplitudes and has zero energies in that limit, it may coexist with other DB families which do not share this property. Thus the general situation is that there exist many DB families, and most of them will possess a family specific energy threshold. The results discussed in the present chapter allow one to rule out or to confirm the existence of at least one DB family which does have a zero energy threshold.

### 4.5. Moving discrete breathers?

Once the existence of discrete breathers is established, a natural question is whether these spatially localized excitations may also coherently move along certain lattice directions without any loss. Let us give a plain answer to this question. As a rule for Hamiltonian systems discrete breathers can not move indefinitely. Exceptions confirm the rule.

There are good reasons for this result. Below we will give a summary of the main arguments which lead to that conclusion below. Before proceeding, we want to encourage the reader to consult Chapter 9 from Ref. [133] (which mainly focusses on discussing the impossibility of introducing a so-called Peierls–Nabarro potential for the general case) and the very recent chapter 7.1 from Ref. [20] (which summarizes the many numerical efforts to obtain moving DBs), where this neverending problem of moving DBs has been extensively reviewed from different perspectives and different times. We also want to stress, that despite the above rigorous 'NO', moving DB states have been frequently observed in some lattice models at least on relatively large times, with losses being reasonably low. For some integrable models like the Ablowitz–Ladik chain (an integrable version of the DNLS) even exact travelling DBs are known to exist [1]. Also moving DB-like objects have been numerically observed for certain dissipative networks. The argument below will give some reasons why these observations coexist with the plain 'NO' from above.

To look for moving breather solutions we need to have some good definition of them. We could define the simplest type of a moving DB as a solution that repeats itself after the time $T_s$ shifted by one lattice site. Such a solution is a fixed point of the map $RG_{T_s}$ where $G_t$ is the evolution operator in the phase space of the system, and $R$ is the translation operator that shifts all indices by 1. More sophisticated solutions can be obtained by considering fixed points of the map $R^nG$, i.e. solutions that repeat themselves after the time $T_s$ shifted by $n$ sites. We assume the lattice spacing to be 1 so the velocity $V$ is then just $n/T_s$.

The method of analyzing the decay properties in the tail of a breather is very fruitful. From such an analysis one precisely derives the nonresonance conditions a stationary nonmoving breather must fulfill in general to exist. This concept has been extremely useful to explain why stationary breathers are generic in discrete systems, while they are nongeneric in field theories. A breather is localized in space. Then we can analyze the tails, where all amplitudes are small, and check whether the solution really CAN decay to zero at infinite distance. This leads to the well-established nonresonance condition for stationary breathers.

Since a stationary breather is characterized by an internal frequency $\Omega_b$, we have to incorporate this inverse time scale into the definition of a moving breather. Consider a one-dimensional lattice, describing the interaction of degrees of freedom associated to each lattice site. Each degree of freedom is given by a pair of canonically conjugated variables (e.g. displacement and momentum) labeled with the site index. Call one of those variables $u_n(t)$. We define a one-frequency discrete moving breather solution as[4]

$$u_n(t) = F(\Omega_b t, n - Vt). \tag{4.75}$$

Here $F(x, y)$ is a function $2\pi$ periodic with respect to $x$ and localized with respect to $y$:

$$F(x + 2\pi, y) = F(x, y), \quad F(x, y \to \pm\infty) \to 0. \tag{4.76}$$

If $1/V$ and $2\pi/\Omega_b$ are commensurate so $k/V = l2\pi/\Omega_b$, where $k$ and $l$ are integers, then such a breather repeats itself after time $T_s = k/V$ shifted by $k$ sites and belongs to the simplest moving breathers defined above. In the general incommensurate case the breather will never repeat itself although it will come arbitrarily close to it.

In the same manner breathers having more internal frequencies can be defined. This hierarchy incorporates everything that we intuitively perceive as an object moving through the lattice.

Thinking of moving breathers in terms of fixed points allows one to define other interesting objects on a discrete lattice. Consider a fixed point of some general map $G_{T_s}X$ where $X$ is an element of the lattice symmetry group. If $X$ is the identical transformation we get stationary breathers. The translation operator gives us moving ones. For a one-dimensional lattice the only symmetry group element left is the reflection, which gives us reflecting breathers, which mirror themselves after time $T_s$. Such hypothetical states would tunnel in space similar to a quantum particle, back and forth between possibly

[4] Of course one can choose more complicated forms, which will not be discussed here.

very distant lattice sites. Higher dimensional lattices provide us with more choices, e.g. by taking a rotation for $X$ we get rotation breathers, i.e. states which consecutively tunnel from one site to another on some possibly large loop in the lattice. This list could be continued, but it leads to nowhere, since we first should check whether the simplest case of a moving DB persists.

*4.5.1. The tail analysis for a Klein–Gordon chain*

Consider

$$\ddot{u}_n = -\alpha u_n - C(2u_n - u_{n-1} - u_{n+1}) + F_{nl}(u_n). \tag{4.77}$$

We search for a moving solution in the form (cf. Eq. (4.75))

$$u_n(t) = \sum_k A_k(n - Vt)\mathrm{e}^{\mathrm{i}k\Omega_b t}. \tag{4.78}$$

Linearizing the equation in the tails of the assumed existing solution we obtain

$$V^2\frac{\mathrm{d}^2A_k(z)}{\mathrm{d}z^2} - 2\mathrm{i}k\Omega_b V\frac{\mathrm{d}A_k(z)}{\mathrm{d}z} = (\Omega^2 - \alpha - 2C)A_k(z) + C(A_k(z+1) + A_k(z-1)). \tag{4.79}$$

We make the ansatz $A_k(z) \sim \mathrm{e}^{\lambda_k z}$. Decomposing $\lambda$ into real and imaginary parts $\lambda = R + \mathrm{i}I$ ($R$, $I$ real) we find (note that we skip the index $k$, so below $\omega = k\Omega_b - VI$):

$$\omega = -\frac{C}{VR}\sinh R \sin I, \tag{4.80}$$

$$\left[\frac{C}{VR}\right]^2 \sinh^2 R \sin^2 I = V^2R^2 + \alpha + 2C(1 - \cosh R \cos I). \tag{4.81}$$

A detailed analysis of these equations [124] yields that for any $V \neq 0$ we can generate a moving breather solution in the tails, for any value of $\Omega_b$! Surprisingly the problem of resonances, as in the case of a stationary breather, does not appear on that stage. The formal reason for this strange result is that as opposed to the case of a stationary DB, the Fourier amplitudes $A_k(z)$ are now functions which should satisfy differential equations. We simply increased the corresponding space of possible solutions, and end up with stating that anything is possible so far. Of course that implies only that we can construct a solution of the type (4.78) in the assumed tails independently for each $k$. Whether these solutions can then be continued into the nonlinear core of a DB state, is completely untouched here.

*4.5.2. A numerical method and analytical consequences*

Consider the full equations of motion given by $\ddot{u}_n = -\partial H/\partial u_n$. Then the ansatz (4.78) yields equations of the type

$$V^2\frac{\mathrm{d}^2A_k(z)}{\mathrm{d}z^2} - 2\mathrm{i}k\Omega_b V\frac{\mathrm{d}A_k(z)}{\mathrm{d}z} = \Omega^2 A_k(z) + \sum_n f_n(\{A_{k'}(z)\}, \{A_{k'}(z+n)\}, \{A_{k'}(z-n)\}). \tag{4.82}$$

The essential feature is that these coupled differential equations contain advanced and retarded terms. These terms arise due to the interaction on the lattice. Instead of directly trying to solve these equations, we consider a lattice governed by the equations

$$V^2\ddot{A}_{kn}(t) - 2\mathrm{i}k\Omega_b V\dot{A}_{kn}(t) = \Omega^2 A_{kn}(t) + \sum_{n'} f_{n'}(\{A_{k'n}(t)\}, \{A_{k',n+n'}(t)\}, \{A_{k',n-n'}(t)\}). \tag{4.83}$$

Here $n$ is again the lattice site label, and with each lattice site $n$ we have an associated infinite set of variables $\{A_{kn}\}$, $k = 0, \pm1, \pm2, \ldots$. Eq. (4.83) define a phase space flow in the phase space of all variables $A_{kn}$, $\dot{A}_{kn}$. In general trajectories generated by those dynamics are not related to solutions of (4.82). However all fixed points of the map $RG_{t=1}$ ($G_t$ is the evolution operator defined by (4.83) and $R$ the translation operator that shifts all lattice indices by 1) are solutions of (4.82). The main reason for that is that all delay and advance intervals are integers. Thus we defined a rigorous map on a phase space, and can search for fixed points of this map. Once a fixed point (solution) is found, it can be continued using generalized Newton methods or steepest descent methods.

Assume that a moving DB exists. It will be a fixed point of the above introduced map. Let us consider the spectrum of the corresponding linearized map around the fixed point. That spectrum should have unusual properties as compared to the Floquet spectrum of stationary breathers. It will fill the unit circle densely. Especially there exist eigenvalues with value $+1$ and those with values arbitrarily close to $+1$, which would in general make continuation impossible for stationary breathers. The existence of these eigenvalues can be simply explained. Linearizing the map around a moving breather fixed point, we obtain an infinite set of eigenvalues with spatially extended eigenvectors. At large distances from the breather center these eigenvectors will correspond to linear waves. Such a linear wave is given by

$$\mathrm{e}^{\mathrm{i}(\omega_q t - qn)}. \tag{4.84}$$

It is always possible to cast it into the form

$$e^{ik\Omega_b t} e^{-iq(n-Vt)} \tag{4.85}$$

with given numbers $\Omega_b$, $V$ by solving

$$\omega_q = k\Omega_b + Vq. \tag{4.86}$$

If we can always find $q$-values which will do the job, then the spectrum is dense around $+1$, and continuation (and thus existence at first hand) seems to be impossible. For the case of a stationary breather $V = 0$, and we essentially recover the nonresonance condition, which can be fulfilled by choosing $\Omega_b$ to be outside the phonon band. Eq. (4.86) was derived for the DNLS model ($k = 1$) in [124], and later obtained for FPU and KG models e.g. in Refs. [150,168].

Eq. (4.86) is the central result. In order to be able to generically have and continue a moving DB, we have to request the generalized nonresonance condition

$$\omega_q \neq k\Omega_b + Vq \tag{4.87}$$

for all $k$. But recall that $\omega_q$ is a periodic function in $q$. Consequently Eq. (4.87) can be never fulfilled for nonzero velocities $V \neq 0$.

On a more physical language, the unavoidable resonances (4.86) are generalized resonances between the velocity of a moving DB and the phase velocity $\omega_q/q$ of linear waves. So we expect a moving DB to radiate energy in the form of small amplitude plane waves with frequencies which match (4.86). In other words, exact travelling waves will typically encounter nondecaying tails, as beautifully analyzed e.g. in Ref. [150].

One can add many more words and discuss various issues of the strength of these resonances etc. But the strict bottom line is that exact moving DBs do not exist in general because (4.87) cannot be satisfied for a given nonzero $V$ and all integers $k$.

We finish this chapter by giving a good reason for the exception to the cases where exact or approximate moving DBs have been obtained or observed. If the resonances are weak enough, then moving DB-like objects can be observed over sufficiently long times. If the system is integrable like the Ablowitz–Ladik chain, then it possesses an infinite number of symmetries, and their existence could be the reason for effectively switching off the resonances, just like the stationary breather persists in the integrable sine-Gordon field equation despite the formal presence of resonances. Furthermore, for DNLS-type chains an inverse construction method [135] has been applied to construct potentials which support a given travelling pulse shape (note that simple moving breathers in DNLS type models can be gauge transformed into a moving pulse). In a next step the thus obtained lattice model was used to numerically continue the exact (!) moving pulses to other velocities. As expected, their tails immediately get dressed with nondecaying waves due to the above resonances. The conclusion is then, that moving pulses may exist for a given lattice problem, but only for a countable set of velocity values (and sometimes this set can be empty). So for DNLS-type models some exact moving pulses (breathers) with fixed velocity values may exist, see also recent results for DNLS with saturable nonlinearity in Ref. [274]. This also explains why we can safely assume that such a set must be empty for the case of a general nonlinear lattice which yields equations of the type (4.82). Just manually decouple the equations for different $k$. Then for each truncated equation we may find a discrete set of velocities which support travelling pulses. But these sets will in general be different for different $k$s, since the equations are different. Switching the interaction between the equations back on, it would be a miracle if all equations now support moving pulses with one and the same velocity. Many further numerical and analytical investigations have shown since, that whatever small, oscillatory tails are typically unavoidable when constructing moving breather states [264,6,251,34,151,248,168,370,53,408].

### 4.6. Dissipative discrete breathers

So far we have been discussing breathers in Hamiltonian lattices. Any experiment will however show up with some dissipation. When this dissipation is of a fluctuating nature, it could be simulated using a heat bath. However it is possible to consider also simple deterministic extensions of the above problems. In Josephson junction systems (see chapter 10.1) this is actually even implemented experimentally. Here we will only mention some of the basic new features one is faced with when studying dissipative breathers and their properties [261,142,265].

#### 4.6.1. Obtaining dissipative breathers

Consider the following set of equations of motion:

$$\ddot{x}_l = -\frac{\partial H}{\partial x_l} - \gamma \dot{x}_l - I \tag{4.88}$$

with

$$H = \sum_l \left[ \frac{\dot{x}^2}{2} + 1 - \cos x_l - C\,(1 - \cos(x_l - x_{l-1})) \right]. \tag{4.89}$$

For $\gamma = I = 0$ this system is Hamiltonian and corresponds to the Takeno–Peyrard model of coupled pendula [261, 379]. This model allows both for usual discrete breathers, but also for so-called roto-breathers. While for a usual breather $x_l(t + T_b) = x_l(t)$ for all $l$, for the simplest version of a roto-breather one pendulum is performing rotations

$$x_0(t + T_b) = x_0(t) + 2\pi m. \tag{4.90}$$

Here $m$ is a winding number characterizing the roto-breather (the simplest realization is $m = 1$). Note that roto-breathers are not invariant under time reversal.

For nonzero $\gamma$ and $I = 0$ the dissipation will lead to a decay of all breather and roto-breather solutions. But for nonzero time-independent $I$ roto-breathers may still exist. The reason is that the rotating pendulum will both gain energy due to the nonzero torque $I$ and dissipate energy due to the nonzero friction $\gamma$, so an energy balance is possible (whereas that is impossible for breathers with $m = 0$).

In contrast to families of breather periodic orbits in Hamiltonian systems, dissipative roto-breathers will be attractors in the phase space [250]. Attractors are characterized by a finite volume basin of attraction surrounding them. Any trajectory which starts inside this basin, will be ultimately attracted by the roto-breather. Thus dissipative breathers form a countable set of solutions.

To compute such a dissipative roto-breather, we can simply make a good guess in the initial conditions and then integrate the equations of motion until the roto-breather is reached. This method is very simple, but may suffer from long transient times, and also from complicated structures of the boundaries of the basin of attraction.

The Newton method can be applied here as well. Although we do not know the precise period of the roto-breather, we do not need it either. Instead of defining a map of the full phase space over a given time $T_b$, we may define a map of the phase space of all but the rotating pendulum coordinate. The mapping time $t_{\mathrm{map}}$ is trajectory-dependent and is determined by $x_0(t = 0) = 0$ and $x_0(t_{\mathrm{map}}) = 2\pi m$. The only two things we have to worry about are: to find a trajectory which leads to a rotation of $x_0$, and, as usual, to be sufficiently close to the desired solution in order for the Newton map to converge to the fixed point. Once the solution is found, $T_b = t_{\mathrm{map}}$.

### 4.6.2. Perturbing dissipative breathers

As long as a dissipative roto-breather is stable, the volume of its basin of attraction is finite, and small deviations will return the perturbed trajectory back to the breather. Upon the change of some control parameter the breather may still persist but become unstable. Consider the linearized phase space flow around the roto-breather of (4.88) and (4.89):

$$\ddot{\epsilon}_l = -\sum_m \left.\frac{\partial^2 H}{\partial x_l \partial x_m}\right|_{\{x_{l'}(t)\}} \epsilon_m - \gamma \dot{\epsilon}_l. \tag{4.91}$$

In analogy with chapter 4.2 we may introduce a (quasi-symplectic) matrix $\mathcal{R}$ which maps the phase space of the perturbations onto itself by integration of (4.91) over one breather period [265]. By using the transformation

$$\epsilon_l(t) = \mathrm{e}^{-\frac{1}{2}\gamma t}\kappa_l(t) \tag{4.92}$$

we obtain

$$\ddot{\kappa}_l = -\sum_m \left.\frac{\partial^2 H}{\partial x_l \partial x_m}\right|_{\{x_{l'}(t)\}} \kappa_m - \frac{1}{4}\gamma^2 \kappa_l. \tag{4.93}$$

Eq. (4.93) defines a Floquet problem with a symplectic matrix $\mathcal{F}$ which properties are discussed above. By backtransforming to $\mathcal{R}$ we find that those eigenvalues which are located on the unit circle for $\mathcal{F}$ now reside on a circle with a smaller radius

$$R(\gamma) = \mathrm{e}^{-\gamma T_b/2}. \tag{4.94}$$

If $\mu$ is an eigenvalue of $\mathcal{R}$, so are

$$\mu^*, \mathrm{e}^{-\gamma T_b}\frac{1}{\mu}, \quad \mathrm{e}^{-\gamma T_b}\frac{1}{\mu^*}. \tag{4.95}$$

There is still one eigenvalue $\mu = 1$ which corresponds to perturbations tangent to the breather orbit. The related second eigenvalue is located at $\mathrm{e}^{-\gamma T_b}$, contrary to the Hamiltonian case. The schematic outcome of a Floquet analysis of a dissipative breather is shown in Fig. 22. We close by noting that the above properties of the quasi-symplectic matrix $\mathcal{R}$ follow directly from (4.91) and apply to many other situations when studying the stability of periodic orbits in dissipative systems.

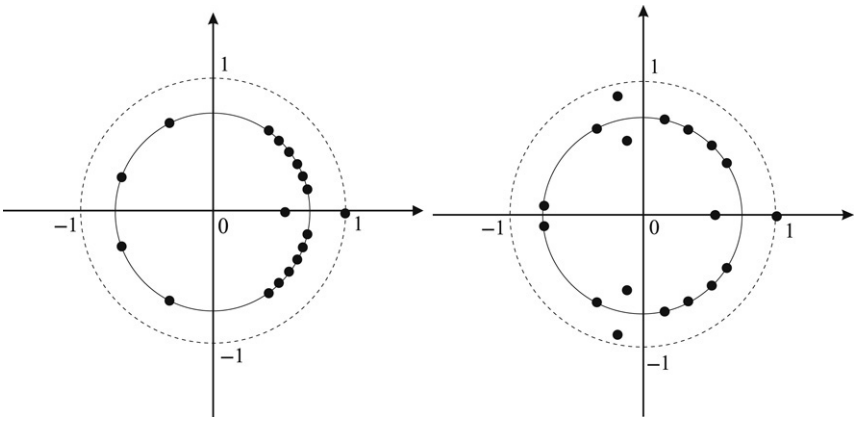


**Fig. 22.** Schematic view of an outcome of the Floquet analysis of a dissipative breather. Floquet eigenvalues (filled circles), the unit circle (large radius) and the inner circle of radius $R$ (4.94) are plotted in the complex plane. Left picture: stable breather (all eigenvalues are located on the circle with radius $R$). Right picture: stable breather close to instability (two eigenvalues have collided on the inner circle, and one is departing outside towards the unit circle). Note that the group of closely nearby lying eigenvalues on the unit circle correspond to the plane wave continuum (extended Floquet eigenstates), while the separated eigenvalues on the inner circle correspond to localized Floquet eigenstates.

### *4.7. Resonances again, and how to remove them*

Discrete breathers in a Hamiltonian setting are periodic orbits. An outcome of the study of basic properties of DBs is that one has to pay attention to various resonances (in order to avoid them). Let us remind the reader, that breathers are nongeneric for nonlinear field equations, because the small amplitude wave spectrum $\omega_q$ there is typically unbounded. So the simple trick of making DBs generic objects on lattices is to use the fact that on a lattice $\omega_q$ is bounded and thus the nonresonance condition

$$k\Omega_b \neq \omega_q \tag{4.96}$$

can be in principle satisfied for all integer $k$ and proper choices of $\Omega_b$, which are regulated by the nonlinearity of the system. But there is no free lunch. We have to pay for that by giving up the idea pf generically observing DBs which evolve quasiperiodically in time, or DBs which can move without losses across the lattice. The quasiperiodic DB does not exist in general due to an extension of the very nonresonance condition (4.96) which even for the simplest case of two incommensurate frequencies $\Omega_{b1}$, $\Omega_{b2}$ would read

$$k_1\Omega_{b1} + k_2\Omega_{b2} \neq \omega_q. \tag{4.97}$$

As discussed in chapter 1.3, that condition can not be fulfilled in general, since any quasiperiodic spectrum is dense in the frequency domain. Finally, mobility at some velocity $V$ would be possible in general only if

$$k\Omega_b + Vq \neq \omega_q \tag{4.98}$$

holds. Again that is not the case, as shown in chapter 4.5. All these issues are about resonances of DB frequencies with plane wave frequencies or about matching of DB velocities and phase velocities of plane waves.

There is of course a simple way to remove these resonances and to expect both quasiperiodic and mobile breathers to appear. For that one only has to remove the objects with which the DB would otherwise resonate. So it is about removing the plane waves. We can think of two ways doing so.

We can consider the (strictly speaking nongeneric) case of vanishing harmonic interactions (see chapter 4.1.3). Then $\omega_q$ becomes a constant (possibly zero) independent of $q$, and the corresponding group velocities vanish. While that does not clearly satisfy any of the two conditions (4.97) and (4.98), numerical results in [155,255] show that quasiperiodic DB states persist for extremely long times, several orders of magnitude longer than the main DB period. Most importantly, Yuan published an existence proof of quasiperiodic breathers via a KAM technique construction [409]. Even chaotic DB-like states seemingly do not show any significant portion of radiation [255]. To the best of our knowledge, mobile DBs were not reported for such a case. Note also, that reports on quasiperiodic DBs in DNLS models [182,184] do not contradict the above conclusions, since these special states have a discrete and *equidistant* temporal Fourier spectrum. After a phase gauge these states in fact become strictly time-periodic DBs again.

Another way to remove plane waves is to add dissipation. Then plane wave type excitations may simply decay in time. If a DB is launched in the system, of course it has to be sustained by some proper energy supply. Suppose now that such a DB is modified so that (4.96) is violated (here $\omega_q$ is the plane wave spectrum in the absence of dissipation). Then the DB will start to radiate plane waves. But these waves will decay at some distance from the DB. Thus, if the energy influx into the DB core is strong enough, such a DB could survive. Indeed such situations have been predicted already in Ref. [130] and observed both for some toy models in [265] and in the theoretical and experimental investigation of breathers in Josephson junction

networks (see chapter 10.1). Using the same line of argument, we may now imagine quasiperiodic DBs which violate (4.97). A rigorous existence proof was recently supplied by Chung and Yuan [66]. Such states have been observed both for some toy models in [46,161,265,267] and in the theoretical and experimental investigation of breathers in Josephson junction networks (see chapter 10.1). And finally we can predict the existence of mobile DBs, violating (4.98). Such states have been observed in [265,267]. So the bottom line is, that even weak dissipation allows us to construct DBs which resonate with the spectrum $\omega_q$, quasiperiodic DBs, and mobile DBs. That allows to use weakly dissipative DBs as spectroscopic tools to measure the frequency spectrum of the nonexcited lattice (chapter 10.1). It also may allow coherent motion of weakly dissipative DBs along a lattice.

## 5. Wave scattering by discrete breathers

The stability analysis of various DB solutions, discussed in Section 4.2, in many cases demonstrates surprisingly high robustness of these objects with respect to perturbations. Practically, the presence of small amplitude extended states ('phonons') in the system hardly affects the dynamics of DBs. The opposite, however, is generally not true: a DB acts as a time-periodic scattering potential for phonons. Early results of numerical simulations performed on a one-dimensional lattice [132,133] showed strong reflection of plane waves by DBs with reflectivity properties being dependent on the incoming plane wave frequency. More recent analytical and numerical investigations [69,207,208,128,129] revealed resonances and anti-resonances in frequency resolved transmission characteristics. In this chapter we will discuss the problem of wave scattering by DBs in detail.

### 5.1. Setting up the problem

Small amplitude (linear) wave scattering by a DB can be treated within the framework of the discussed linear stability analysis in Sections 3.3 and 4.2, using the Floquet analysis of the linearized phase space flow around the DB periodic orbit, Eq. (3.12). Of crucial importance now are not the Floquet eigenvalues, but the profiles of the corresponding *eigenvectors*.

Since the DB is localized in a finite region of the lattice, it essentially does not affect propagation of small amplitude waves far away from the DB core. We may thus treat the problem by means of standard scattering theory, and consider incoming and outgoing excitations as plane waves. At variance to a standard time-independent potential scattering, the DB-induced scattering potential is time-periodic. Denoting by $\omega_q$ and $\Omega_b$ the frequencies of the incoming plane wave and DB, respectively, the scattering states of (3.12) can be represented in the form

$$\epsilon_n(t) = \sum_k e_{nk} \mathrm{e}^{\mathrm{i}(\omega_q + k\Omega_b)t}. \tag{5.1}$$

As the result of interaction between the incoming plane wave and the DB, new frequency channels are created. Each of these frequencies corresponds to a separate propagation *channel*, and the DB generates a spatially localized coupling between different channels [69,128,129]. If a frequency $\omega_{q'} = \omega_q + k\Omega_b$ is located inside the linear wave spectrum, the corresponding excitation is extended over the lattice and forms an *open channel*. Otherwise, the linear mode has to be exponentially localized around the scattering region and forms a *closed channel*.

Assume one degree of freedom per lattice site. The generic nonresonance condition, that the harmonics $k\Omega_b$ of the breather are not resonating with the linear spectrum $\pm\omega_q$, implies that the width $\Delta$ of the positive (or negative) part of the linear spectrum $\omega_q$ is narrow enough: $0 < \Delta < \Omega_b$. Thus, either all channels with $k \neq 0$ are closed (single channel scattering), or there exists exactly one additional open channel with a value of $k$ uniquely defined by $\Delta$ and $q$ (two-channel scattering). In the latter situation, the breather may be linearly unstable for finite size systems but recovers its linear stability for infinite system size (see chapter 4.2.1). As a result, two situations are possible:

- a one-channel scattering when for any $k \neq 0$, $\omega_q + k\Omega_b$ is not in the phonon band. Only channel $k = 0$ is open and propagates waves at infinity. An incoming wave with frequency $\omega_q$ and wave vector $q$, will generate propagating outgoing waves at the same frequency $\omega_q$ and wave vector $\pm q$ (see Fig. 23).
- a two-channel scattering, when a unique value of $k \neq 0$ exists such that $\omega_{q'} = \omega_q + k\Omega_b$. An incoming wave with frequency $\omega_q$ and wave vector $q$ will generate outgoing waves not only at frequency $\omega_q$ and wave vector $\pm q$ but also at frequency $\omega_{q'}$ and wave vector $\pm q'$.

A generalization to $m$ degrees of freedom per lattice site leads to a maximum of $2m$ open channels.

A *single-channel* scattering process is *elastic* [69], so that the total energy flux of the scattered waves coincides with that of the incoming wave. In contrast, the general case of *two-channel* scattering corresponds to an *inelastic* process, in which the DB, even though being linearly stable, loses energy [69].

Most of the studies of wave scattering by DBs were focused on one-dimensional lattices [133,132,69,207,208,128,129]. This is caused, on one hand, by the fact, that scattering in higher dimensional lattices is much harder to be treated numerically. On the other hand, DBs, being analogues of point scatterers, scatter more weakly, the higher the dimension. For a one-dimensional lattice, a single-channel scattering process can by analyzed via computation of the transmission coefficient as a function of the incoming plane wave frequency/wavenumber. In the following Section 5.2 a general method

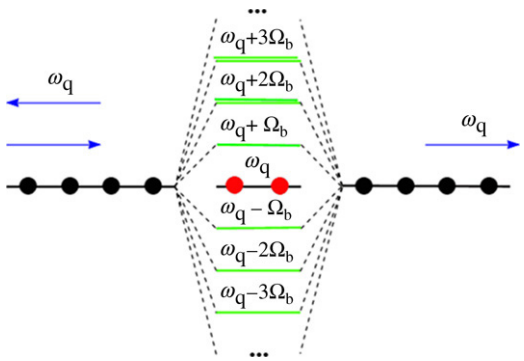


**Fig. 23.** Schematic representation of the single-channel wave scattering process by a DB.

to compute transmission will be introduced. We will discuss the main results, obtained for different 1D models, in Sections 5.3–5.5. Some remarks regarding generalization of the problem towards higher dimensional lattices will be made in Section 5.6. We conclude with a short discussion of inelastic scattering in chapter 5.7.

### *5.2. A general method to compute transmission*

In order to compute the transmission coefficient for plane waves, one has to fix a large enough system size, so that extended Floquet states of the corresponding problem are approximated (with exponential accuracy) by plane waves at large distances from the DB. In other words, the system size should be essentially larger than the localization length of any Fourier component of the DB solution, see Section 4.1, as well as the localization length of any closed channel [69,115]. Once the appropriate system size is chosen, the transmission coefficient can be measured numerically by launching a small amplitude monochromatic wave packet towards the DB [132]. The advantage of this method is that it describes the real interaction of the small-amplitude excitation with the DB without truncating any nonlinear terms. However, this method requires long calculations in order to produce accurate results. Moreover, it fails to analyze scattering of plane waves with too small a group velocity [132].

A highly accurate and effective method to compute the transmission coefficient has been proposed by Cretegny et al. [69], which is based on the assumption, that the DB is spatially symmetric. That allows one to separate the Floquet eigenstates into symmetric and antisymmetric ones. Computing a pair of symmetric and antisymmetric eigenvectors at a given frequency $\omega_q$, a linear combination of the two can be constructed, which yields a scattering situation (say that to the right of the DB only outgoing waves exist) [69].

A further generalization of this method, which does not require any spatial symmetry of the DB, was developed in [128]. One emulates an infinite system with proper designed boundary conditions:

$$\epsilon_{N+1}(t) = \mathrm{e}^{-\mathrm{i}\omega_q t}, \qquad \epsilon_{-N-1} = (A + \mathrm{i}B)\mathrm{e}^{-\mathrm{i}\omega_q t}. \tag{5.2}$$

Here the amplitude of the transmitted wave is assumed to be unity, while the amplitudes and relative phases of the incoming and reflected waves are implicitly determined via the coefficients $A$ and $B$. At the first stage coefficients $A$ and $B$ are chosen arbitrarily. With the specified boundary conditions (5.2), one has to find the zeros of the following map:

$$G\left(\vec{\epsilon}(0), \dot{\vec{\epsilon}}(0)\right) \equiv \begin{pmatrix} \vec{\epsilon}(0) \\ \dot{\vec{\epsilon}}(0) \end{pmatrix} - \mathrm{e}^{\mathrm{i}\omega_q T_b} \begin{pmatrix} \vec{\epsilon}(T_b) \\ \dot{\vec{\epsilon}}(T_b) \end{pmatrix}. \tag{5.3}$$

The obtained eigenstate, however, generally does not correspond to the scattering setup, since there is no guarantee that in the right tail it approaches a plane wave traveling to the right only. One has to find the values of $A$ and $B$, such that

$$\epsilon_N = \mathrm{e}^{-\mathrm{i}q - \mathrm{i}\omega_b t}. \tag{5.4}$$

This can be done in a subsequent Newton map, involving coefficients $A$ and $B$ [115]. Both Newton maps can be combined into a single one.

After the proper values of coefficients $A$ and $B$ are found, the transmission coefficient $T(q)$ is obtained through the relation [128,115]:

$$T(q) = \frac{4\sin^2 q}{|(A + \mathrm{i}B)\mathrm{e}^{-\mathrm{i}q} + \epsilon_{-N}(0)|^2}. \tag{5.5}$$

The described method is remarkably easy to handle, essentially it takes a single step for the Newton map to converge (since the map is *linear*). At the same time it determines the transmission coefficient up to machine precision and does not care about any symmetries and structures of the DB solution.

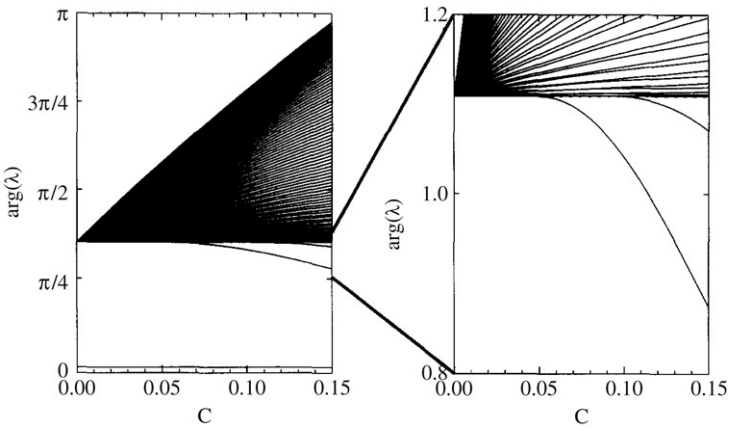


**Fig. 24.** Dependence of the Floquet spectrum on the coupling constant $C$ for a symmetric DB in a 1D Klein–Gordon chain (see text for details). Right panel zooms the region where two localized modes detach from the band of extended states. Figure from [69].

### 5.3. Resonant transmission

Wave scattering by a DB and the linear stability properties of a DB are closely related. Therefore one can establish certain links between particularities in the transmission and some features in the Floquet spectrum of the DB. Indeed, certain (but not all!) resonances in the transmission can be connected to the appearance of isolated eigenvalues in the Floquet spectrum, which correspond to localized modes [206,69]. The underlying mechanism can be illustrated for a particular case of wave scattering by a spatially symmetric DB [69].

Far away from the DB core the solution of Eq. (3.12) is the sum of two plane waves propagating in opposite directions:

$$\epsilon_n = a_+ \mathrm{e}^{\mathrm{i}qn - \mathrm{i}\omega_q t} + b_- \mathrm{e}^{-\mathrm{i}qn - \mathrm{i}\omega_q t}, \quad n \to -\infty, \tag{5.6}$$

$$\epsilon_n = b_+ \mathrm{e}^{\mathrm{i}qn - \mathrm{i}\omega_q t} + a_- \mathrm{e}^{-\mathrm{i}qn - \mathrm{i}\omega_q t}, \quad n \to +\infty. \tag{5.7}$$

The amplitudes of the incoming and outgoing waves are related through the unitary *scattering matrix* $M(q)$ [69]:

$$\begin{pmatrix} b_+ \\ b_- \end{pmatrix} = M(q) \begin{pmatrix} a_+ \\ a_- \end{pmatrix}, \qquad M(q) = \begin{pmatrix} M_{++} & M_{+-} \\ M_{-+} & M_{--} \end{pmatrix}. \tag{5.8}$$

For spatially symmetric DBs, $\epsilon_{-n}(t)$ is also a solution of Eq. (3.12). This implies the symmetry of the scattering matrix [69]: $M_{++} = M_{--}, M_{+-} = M_{-+}$. With this condition the unitary matrix $M(q)$ can be written in the form

$$M(q) = \mathrm{e}^{\mathrm{i}\gamma(q)} \begin{pmatrix} \mathrm{i}\sin\alpha(q) & \cos\alpha(q) \\ \cos\alpha(q) & \mathrm{i}\sin\alpha(q) \end{pmatrix}. \tag{5.9}$$

The symmetric and antisymmetric scattering schemes are expressed through the eigenmodes of the matrix $M(q)$:

$$\epsilon_n^{(\pm)} = \pm\cos(qn - \delta_\pm/2)\mathrm{e}^{-\mathrm{i}\omega(q)t}, \quad n \to -\infty, \tag{5.10}$$

$$\epsilon_n^{(\pm)} = \cos(qn + \delta_\pm/2)\mathrm{e}^{-\mathrm{i}\omega(q)t}, \quad n \to +\infty, \tag{5.11}$$

where $\delta_\pm(q) = \gamma \pm \alpha$ are the phase shifts of spatially symmetric and antisymmetric states. Then it is straightforward to express the transmission coefficient $T(q)$ through the phase shifts [69]:

$$T(q) = \sin^2 \frac{\delta_+(q) - \delta_-(q)}{2}. \tag{5.12}$$

According to the extended *Levinson theorem* [69], the behavior of the phase shifts $\delta_\pm$ at the boundaries of the Brillouin zone $q = 0, \pi$ determines the number of spatially symmetric $N_{b+}$ and antisymmetric $N_{b-}$ localized states of the Floquet operator:

$$N_{b+} = -\mathrm{Int}\left(\frac{-\delta_+(0)}{2\pi}\right) - \mathrm{Int}\left(\frac{\delta_+(\pi)}{2\pi}\right), \tag{5.13}$$

$$N_{b-} = \mathrm{Int}\left(\frac{\delta_-(0) + \pi}{2\pi}\right) + \mathrm{Int}\left(-\frac{\delta_-(\pi) + \pi}{2\pi}\right). \tag{5.14}$$

Here the function $\mathrm{Int}(x)$ is defined as the largest integer smaller than or equal to $x$.

The appearance or disappearance of localized states in the Floquet spectrum of the DB can lead to sharp changes in the phase shifts $\delta_\pm$ at $q = 0$ or $q = \pi$. As a result, sharp changes in the transmission $T(q)$ (5.12) are observed at the corresponding band edge. In Figs. 24 and 25 this scenario is illustrated for a symmetric DB in a one-dimensional Klein–Gordon lattice (1.7)

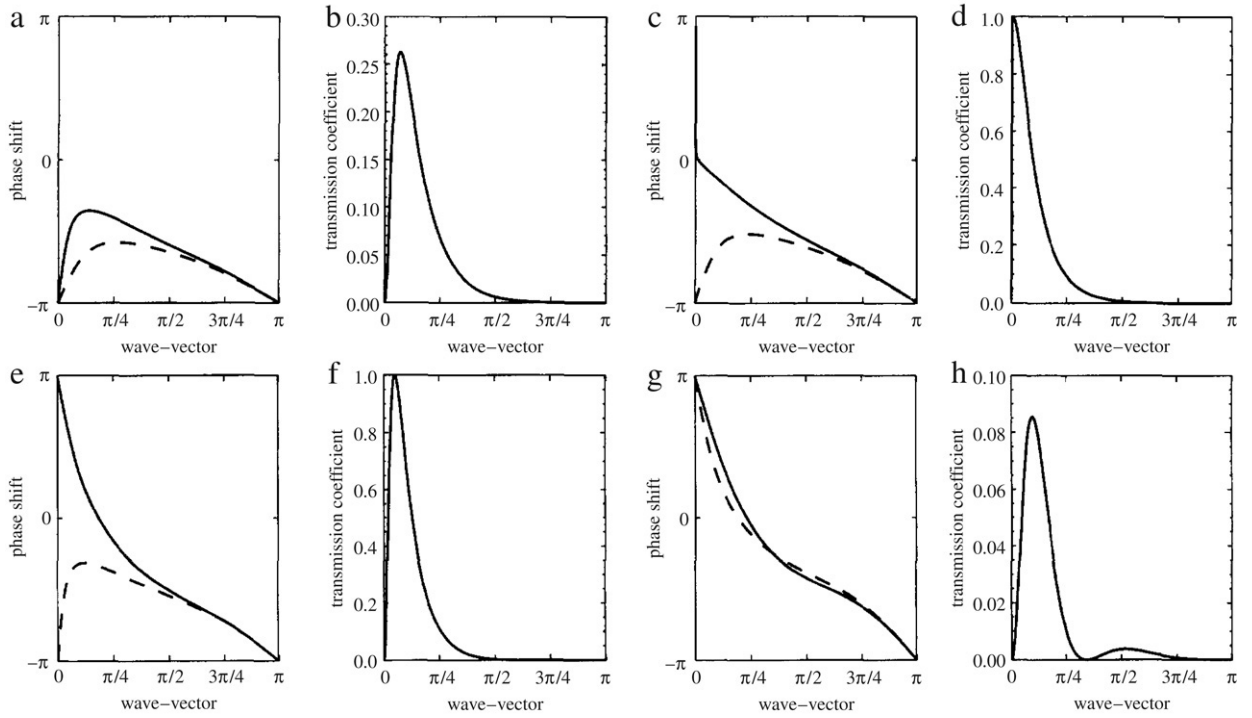


**Fig. 25.** Phase shifts $\delta_+$ (solid lines) and $\delta_-$ (dashed lines) and transmission coefficient of plane waves by a symmetric DB in a 1D Klein–Gordon lattice for different values of the coupling constant: (a), (b) $C = 0.04$; (c), (d) $C \approx 0.05$; (e), (f) $C = 0.08$; (g), (h) $C = 0.15$. Figure from [69].

with cubic on-site potential $V(x) = x^2/2 - x^3/3$ and harmonic interaction potential $W(x) = Cx^2/2$. Increasing the coupling strength $C$ at a given DB frequency, $\Omega_b = 0.85$, symmetric and antisymmetric localized modes bifurcate from the edge of the extended states band for $C \approx 0.05$ and $C \approx 0.11$, respectively, see Fig. 24. At the localization threshold of the first mode, $C \approx 0.05$, the symmetric phase shift abruptly changes from $\delta_+(0) = -\pi$ to $\delta_+(0) = 0$, cf. Fig. 25(a) and (c). Simultaneously, a resonant transmission peak $T = 1$ appears at the band edge $q = 0$, see Fig. 25(d). In the interval $0.05 \lesssim C \lesssim 0.11$ the resonant transmission peak gradually drifts towards the opposite band edge $q = \pi$, see Fig. 25(f). It disappears at the localization threshold of the second mode, when a similar abrupt change of the antisymmetric shift $\delta_-(0)$ occurs, cf. Fig. 25(e) and (g).

Note, that the location of localized states in the Floquet spectrum does not predict the position (and even existence!) of resonant transmission. But the fact, that a particular localized state appears or disappears, while changing the model parameters, can serve as an indication of the appearance of the resonant transmission in a vicinity of the corresponding parameter.

As follows from the expression (5.12), the transmission coefficient can strictly vanish if $\delta_+(q) - \delta_-(q) = 0 \,(\mathrm{mod}\, \pi)$ for some value of $q$. Apparently, this condition is satisfied at the boundaries $q = 0, \pi$, where the corresponding total reflection of plane waves can be regarded as the result of vanishing group velocities $\mathrm{d}\omega_q/\mathrm{d}q$. However, the phases $\delta_+(q)$ and $\delta_-(q)$ can satisfy the condition for zero transmission at intermediate values of $q$, where group velocities do not vanish, see Fig. 25(g) and (h). In contrast to the discussed resonant transmission, one can not generally establish any connection between the total reflection of plane waves and some features of the Floquet spectrum. This issue will be discussed in the next section.

### 5.4. Resonant reflection and relation to Fano resonances

An interesting effect, observed in many numerical studies of wave scattering by discrete breathers, is the total reflection of plane waves $T = 0$ for wave numbers with nonzero group velocities [132,206,69,207,128,121,119,282]. The observed effect is due to the time-periodicity of the DB which induces an effective time-periodic scattering potential for plane waves. It can be interpreted as a destructive interference between different co-existing propagation channels, see Fig. 23. The observed total reflection was shown to be closely related to the well-known Fano resonance [129].

#### 5.4.1. Scattering by a DNLS breather

To explore the origin of this resonance we consider the simple example of plane wave scattering by a single site DB in the DNLS model (1.19) with $\epsilon = 0$ and $\gamma = 1$, cf. Fig. 5(a). The linear wave spectrum in this model is given by

$$\omega_q = 2C\cos(q), \tag{5.15}$$

and constitutes the *open channel* of the scattering problem.

Consider a highly localized DB with $\Omega_b \gg C$. The corresponding DB solution $\psi_n = A_n \exp(\mathrm{i}\Omega_b t)$ can be approximated by a single site excitation: $A_0^2 = \Omega_b, A_{n\neq 0} = 0$. Due to the gauge invariance of the DNLS model (1.19), there are only two propagation channels, which correspond to the terms with $k = 0$ and $k = -2$ in (5.1). With $X_n \equiv e_{n,0}$ and $Y_n \equiv e_{n,-2}$, the coupled equations for the two channels are [129]:

$$\omega_q X_n = C(X_{n+1} + X_{n-1}) + \Omega_b \delta_{n,0}\,(2X_0 + Y_0)\,, \tag{5.16}$$

$$(2\Omega_b - \omega_q) Y_n = C(Y_{n+1} + Y_{n-1}) + \Omega_b \delta_{n,0}\,(2Y_0 + X_0)\,. \tag{5.17}$$

It is straightforward to show, that $2\Omega_b - \omega_q \neq \omega_{q'} \forall q, q'$, so that the channel $Y_n$ is always *closed*.

It is instructive to consider a generalised problem given by [129]

$$\omega_q X_n = C(X_{n+1} + X_{n-1}) - \delta_{n,0}\,(V_x X_0 + V_a Y_0)\,, \tag{5.18}$$

$$(\Omega - \omega_q) Y_n = C(Y_{n+1} + Y_{n-1}) - \delta_{n,0}\left(V_y Y_0 + V_a X_0\right), \tag{5.19}$$

which is reduced to the system (5.16) and (5.17) when $\Omega = 2\Omega_b$, $V_x = V_y = 2V_a = -2\Omega_b$. Note, that for a particular case $V_a = 0$, i.e. when the closed channel $Y$ is completely uncoupled from the open channel $X$, the former possesses exactly one localized eigenstate for nonzero $V_y$ [129]:

$$\omega_L^{(y)} = \Omega - \sqrt{V_y^2 + 4C^2}. \tag{5.20}$$

Using the transfer matrix technique, the transmission coefficient $T$ for the generalized problem (5.18) and (5.19) is given by [129]:

$$T = \frac{4\sin^2 q}{\left(2\cos q - a - \frac{d^2\kappa}{2-b\kappa}\right) + 4\sin^2 q} \tag{5.21}$$

$$a = \frac{V_x + \omega_q}{C}, \qquad b = \frac{V_y + \Omega - \omega_q}{C}, \qquad d = \frac{V_a}{C}, \tag{5.22}$$

where $\kappa$ is the inverse localization length of the closed channel:

$$\kappa = \frac{\Omega - \omega_q + \sqrt{\left(\Omega - \omega_q\right)^2 - 4C^2}}{2C}. \tag{5.23}$$

The transmission coefficient $T$ vanishes, when the condition

$$2 - b\kappa = 0 \tag{5.24}$$

is satisfied. It is equivalent to the resonance condition $\omega_q = \omega_L^{(y)}$, which has a clear physical meaning: total reflection occurs when the frequency of the incoming wave $\omega_q$ in the open channel $X$ resonates with that of the local mode $\omega_L^{(y)}$ of the closed channel $Y$. Thus the resonance is equivalent to the Fano resonance [98], resulting from a local state interacting and resonating with the continuum of extended states. An intriguing peculiarity of the case under consideration is that the local state itself (belonging to the closed channel) is created *dynamically*, through an *interaction* between the incoming plane wave and the scattering DB.

Coming back to the original problem (5.16) and (5.17), the transmission coefficient is given by

$$T = \frac{4\sin^2 q}{\left(\frac{2\Omega_b}{C} - \frac{\Omega_b^2}{2C^2}\frac{\kappa}{1+\kappa\cos q}\right)^2 + 4\sin^2 q}. \tag{5.25}$$

For highly localized DBs with $\Omega_b/C \gg 1$ the total reflection occurs in a close vicinity of $q = \pi/2$, see Fig. 26. The above result is obtained within the approximation, in which the DB is strictly localized on a single site. The actual *finite extension* of the DB causes small discrepancies between the analytical result (5.25) and the results of direct numerical computations of the transmission coefficient. In particular, the position of resonant reflection is slightly shifted, see inset in Fig. 26.

### 5.4.2. A more general example: Klein–Gordon lattice

The specific type of nonlinearity in the above DNLS model results in a single closed channel being excited in the scattering process. However, in the more general case of weakly interacting nonlinear oscillators, one should expect several closed channels to be excited, as shown in Fig. 23. As an example, we take a Klein–Gordon lattice (1.7) with potentials

$$V(x) = \frac{x^2}{2} + \frac{x^3}{3} + \frac{x^4}{4}, \qquad W(x) = C\frac{x^2}{2}. \tag{5.26}$$

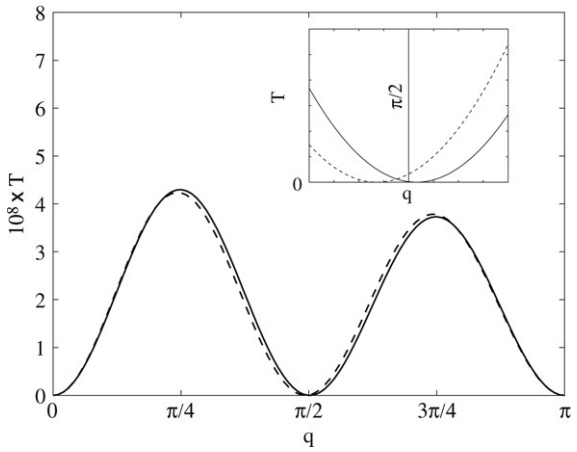


**Fig. 26.** Transmission coefficient $T(q)$ for a single site breather in DNLS with $\Omega_b = 1$ and $C = 0.01$. Solid line: analytical result given by expression (5.25), dashed line: numerical result. Figure from [129].

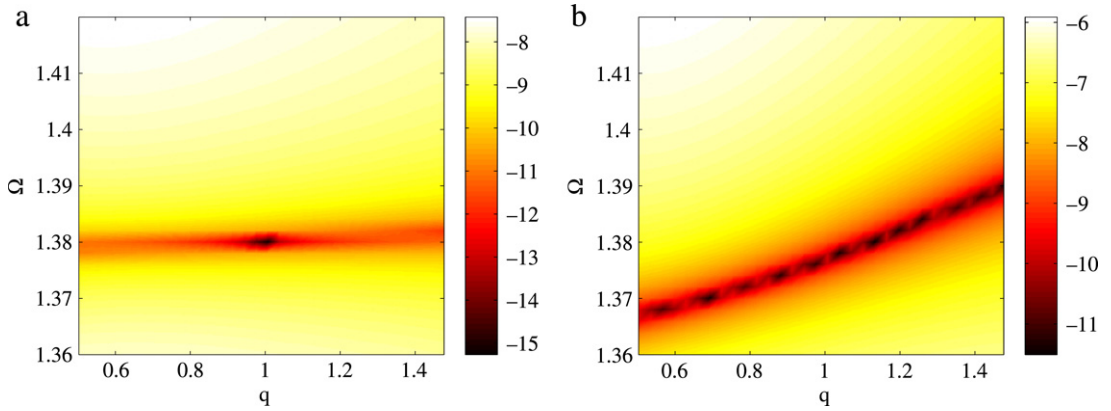


**Fig. 27.** Density plot of the logarithm of plane waves transmission coefficient by the single-site DB in a Klein–Gordon model with $C = 0.001$ (a) and $C = 0.01$ (b).

The linear wave spectrum of this model

$$\omega_q^2 = 1 + 4C\sin^2(q/2), \tag{5.27}$$

and profiles of the basic types of DBs are shown in Fig. 2 for a particular choice of the coupling constant $C = 0.1$.

As in the previous example of the DNLS model, a highly localized DB solution $\hat{X}_n(t)$ can be approximated by a single site excitation, $\hat{X}_{n\neq 0}(t) \equiv 0$, so that the linearized equation (3.12) takes the following form:

$$\ddot{\epsilon}_n = -\epsilon_n + C(\epsilon_{n+1} + \epsilon_{n-1} - 2\epsilon_n) - \delta_{n,0}\left\{V''\left[\hat{X}_0(t)\right]\right\}\epsilon_0. \tag{5.28}$$

Using the Fourier expansion (5.1) and expanding $V''\left[\hat{X}_0(t)\right] = \sum_k v_k e^{ik\Omega_b t}$, one arrives at the set of equations [129]:

$$(\omega_q + k\Omega_b)^2\epsilon_{0k} = \sum_{k'} v_{k-k'}\epsilon_{0k'}, \tag{5.29}$$

which describe the coupling between the open channel $\epsilon_{n0}$ and different closed channels $\epsilon_{nk}$ at site $n = 0$, where the single site DB is excited.

Following the same arguments as in the previous example, we "turn off" the interaction between the open channel and all the closed channels and look for those localized states of closed channels, which resonate with the open channel. In contrast to the DNLS case, such a case is not necessarily realized for an arbitrary value of $\Omega_b$. Generally, in the anticontinuous limit $C = 0$ (where the DB is located on a single site), there will be a discrete set of DB frequencies, at which the total reflection can be observed [129]. An increase of the coupling constant $C$ transforms each of these frequency values into finite-width stripes on the real axis, which will continue to expand for higher values of $C$, see Fig. 27.

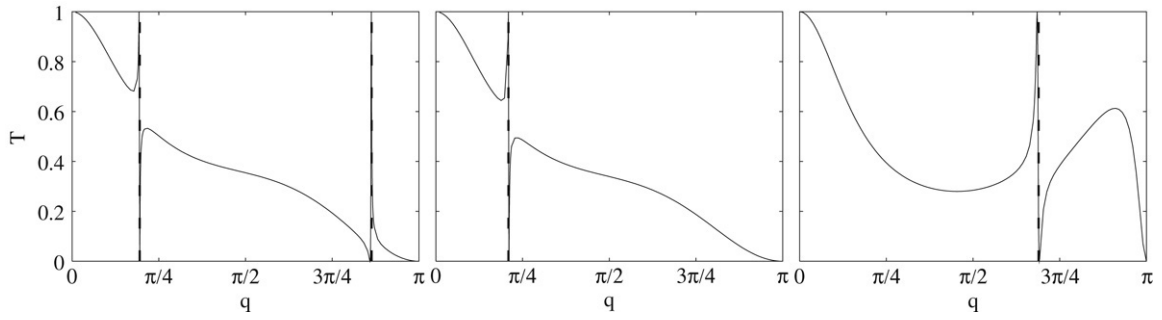


**Fig. 28.** Transmission coefficient $T$ for a bond-centered breather in an FPU chain. Model parameters are: $\phi_2 = \phi_4 = 1$, $\phi_3 = 0.5$. DB frequency from left to right: $\Omega_b = 4.5, 4.7, 10$. The vertical dashed lines indicate the positions of the oscillatory instabilities, cf. Fig. 17. Figure from [121].

*5.4.3. The strength of inter-channel coupling*

An important feature of the Fano resonance, often referred to in literature, is the characteristic *asymmetry* of the line shape in the proximity of the resonance [98]. Usually such an asymmetry is caused by the simultaneous co-existence of a slightly detuned pair of resonant transmission and reflection. At this point it is instructive to revisit the generalized problem of wave scattering by a DNLS breather, introduced in Eqs. (5.18) and (5.19). Apart from the above resonant reflection of waves, the transmission coefficient $T$, Eqs. (5.21)–(5.23), can become unity when

$$(2 - b\kappa)(2\cos q - a) - d^2\kappa = 0. \tag{5.30}$$

Using definitions in Eqs. (5.22) and (5.23), the condition for resonant transmission reads

$$\omega_q = \Omega - \sqrt{4C^2 + \left(V_y + \frac{V_a^2}{2V_x}\right)^2}. \tag{5.31}$$

In the limit $\mu \equiv V_a^2/V_x \to 0$ it coincides with the condition $\omega_q = \omega_L^{(y)}$ for resonant reflection of plane waves (anti-resonance), cf. Eqs. (5.20) and (5.24). In the case of a *weak inter-channel coupling*, $\mu \ll 1$, there exists a pair of a nearby resonance ($T = 1$) and anti-resonance ($T = 0$) in transmission, causing a strong asymmetry of the transmission curve. Increasing the coupling strength $\mu$, the detuning between the resonance and anti-resonance becomes more pronounced, and the resonant transmission peak shifts toward the band edge. Finally, when the inter-channel coupling is strong, $\mu \sim 1$, the resonance $T = 1$ is situated outside the transmission band, and the transmission curve becomes nearly symmetric around the anti-resonance $T = 0$, cf. Fig. 26.

*5.4.4. The FPU chain*

The discussed examples of wave scattering by a DB in DNLS and Klein–Gordon lattices represent cases of strong inter-channel couplings. The opposite regime is obtained for DBs in a Fermi–Pasta–Ulam (FPU) lattice, i.e. in the Hamiltonian system (1.7) with potentials

$$V(x) = 0, \qquad W(x) = \phi_2\frac{x^2}{2} + \phi_3\frac{x^3}{3} + \phi_4\frac{x^4}{4}. \tag{5.32}$$

The resonant reflection of plane waves by a bond-centered DB can be observed for asymmetric potentials $W(x)$ with $\phi_3 \neq 0$ [128,121], and it is accompanied by a nearby situated resonant transmission peak, see Fig. 28. The resonant transmission can be linked to a localized Floquet state entering the band of extended states [121], as discussed in Section 5.3. Vertical dashed lines in Fig. 28 indicate positions of the unstable Floquet states, which appear as the result of resonance between a (former) localized state and an extended state, cf. Fig. 17.

*5.5. Plane wave scattering versus wave packet scattering*

So far all resonances in the process of wave scattering by DBs have been discussed in terms of the transmission coefficient for plane waves. How appropriate are these results for the description of a more realistic situation of wavepacket scattering by a DB? This issue is of particular importance from the point of view of potential experimental studies of the resonances.

Strictly speaking, the plane wave approach is relevant only within the linear approximation, i.e. when the amplitude of the incoming wave is small enough. Provided this condition is fulfilled, each component of the incoming wavepacket will be scattered in accordance to the above results for plane waves. Then, the proper averaging (over frequencies/wavenumbers) of the transmission coefficient for plane waves leads to the effective transmission coefficient for the wavepacket. In order to resolve a resonance in transmission, one has to operate with wavepackets, whose spectral width is significantly smaller, than the effective resonance width. Recently, a promising setup has been proposed, based on coupled Josephson junctions [282]. As anticipated in Ref. [282], boundary conditions, practically identical to that corresponding to plane wave scattering scheme, can be relatively easily created for this setup.

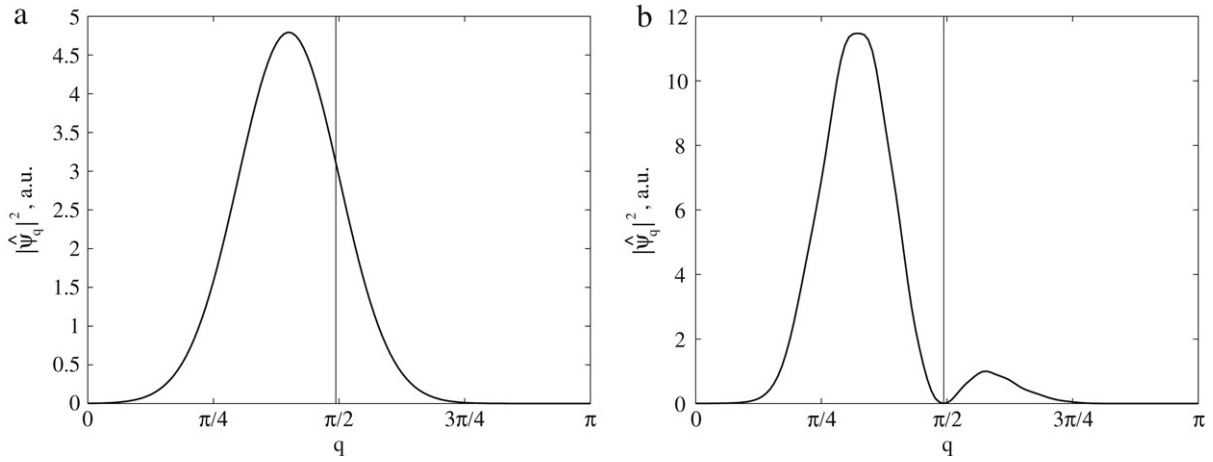


**Fig. 29.** Spatial Fourier transform of the incoming (a) and transmitted (b) wavepackets. DB parameters are the same as in Fig. 26. The vertical line in both figures indicates the position of the resonant reflection for plane waves.

Yet, an alternative way to observe resonances in transmission is to deal with spectrally broad wavepackets. Instead of computing the averaged transmission coefficient for the wavepacket, one may analyze the spectral characteristics of the transmitted and reflected waves. The resonant components will be filtered out from the transmitted (resonant reflection) and reflected (resonant transmission) wavepackets [156]. This mechanism is illustrated for the case of wavepacket scattering by the DNLS breather in Fig. 29. Such a spectral hole burning effect opens a promising way for an experimental detection of the resonant reflection and transmission, e.g. by using nonlinear optical waveguides [156].

For high amplitude (nonlinear) wavepacket scattering the above plane wave approach obviously fails. Some attempts have been made to estimate nonlinear corrections to the plane waves transmission coefficient and to the position of resonant reflection within a modified Fano-Anderson model [281]. The most intriguing one is the appearance of bistable transmission for the case of a continuous wave input, as opposed to the case of wavepacket scattering.

### 5.6. Extension to higher dimensional lattices

One-dimensional lattices represent a unique sub-class of models, in which DBs strongly interact with spatially extended excitations. In higher-dimensional systems the interaction is weaker, as the DB-induced scattering potential is spatially localized and interacts only with a finite region of the wave front. As a consequence, total resonant transmission and reflection of plane waves will be replaced by a more subtle resonant angle-dependent scattering.

Following essentially the same way, as discussed in Sections 5.3 and 5.4, one can predict the appearance of some resonant features in the scattering for multi-dimensional systems. Then, it is the matter of a careful numerics to explore the corresponding resonances. This strategy has been successfully applied to a two-dimensional extension of the Fano-Anderson model [395]. In the one-dimensional case the model is known to possess a total resonant reflection of plane waves [98,12]. The resonance is demonstrated to persist in the two-dimensional case for the process of wavepacket scattering [395], see Fig. 30. Remarkably, the total intensity of scattered waves at resonance, as well as the width of resonance, can be estimated by means of a simple effective one-dimensional model [395], see Fig. 31. Indeed, taking into account the spatial localization of the scattering potential, one can assume that only a quasi-1D part of the original wavepacket strongly interacts with the scatterer, while the rest passes through without any essential changes. The more localized in space the incoming wavepacket is, the larger the portion of it is, which strongly interacts with the defect and is scattered. On the other hand, high localization of the wavepacket in real space implies delocalization in the reciprocal space. This, in turn, causes the total scattered intensity at resonance to vanish, as discussed in Section 5.5. Therefore, the peak intensity of scattered waves at resonance is balanced by the broadening of the original wavepacket in real and reciprocal spaces [395].

### 5.7. Inelastic scattering

So far we discussed elastic scattering only, where only one channel is open, and all others are closed. Here we briefly discuss the effects of inelastic scattering in the case of a one-dimensional Klein–Gordon system (5.26) [69].

As discussed in chapter 5.1, inelastic scattering of waves by a DB is possible, if two open channels coexist, i.e. $\omega_{q_2} = \omega_{q_1} + k\Omega_b$ for $k \neq 0$ integer. In that case, a single incoming wave at frequency $\omega_{q_1}$ generates outgoing waves not only at frequency $\omega_{q_1}$ but also at $\omega_{q_2}$.

The real (or the imaginary) part $\phi_n(t) = \mathrm{Re}\epsilon_n(t)$ is a solution which carries an energy flux (per unit of time) $\frac{1}{2}C\langle\phi_n(t)\dot{\phi}_{n+1}(t)\rangle$ from site $n$ to $n+1$ (it is the average power of the force of the oscillator $n$ acting on the oscillator $n+1$) [69].

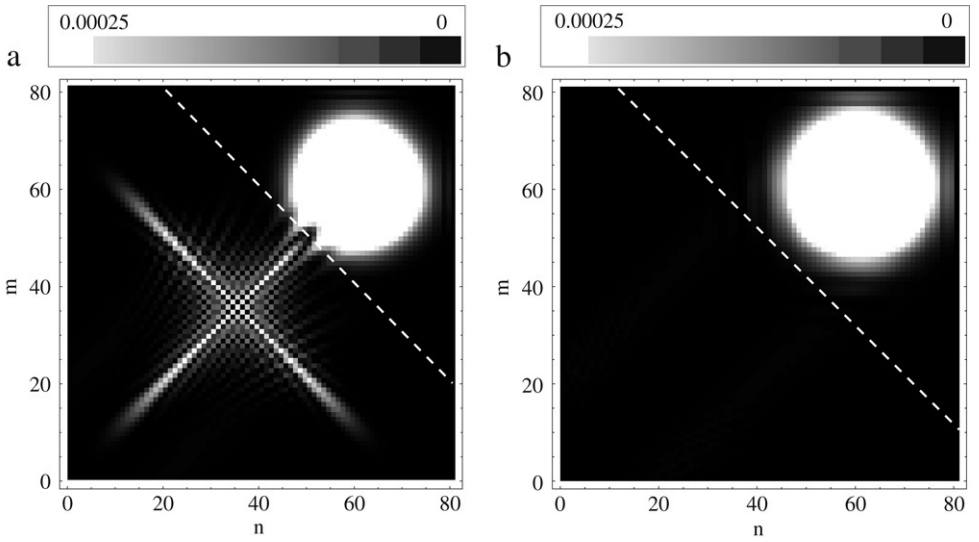


**Fig. 30.** Intensity distribution of transmitted and scattered waves after the scattering process in the two-dimensional Fano-Anderson model. The Fano-Anderson defect is located at site {40, 40}, in the middle of the square lattice. The central frequency of the incoming wavepacket is chosen to be: (a) close to the predicted resonance for plane waves; (b) away from the resonance. The boundary between "transmitted" (T) and "reflected" (R) regions, used for numerical computations of the transmitted and scattered waves intensities, is indicated by the dashed line. Figures from [395].

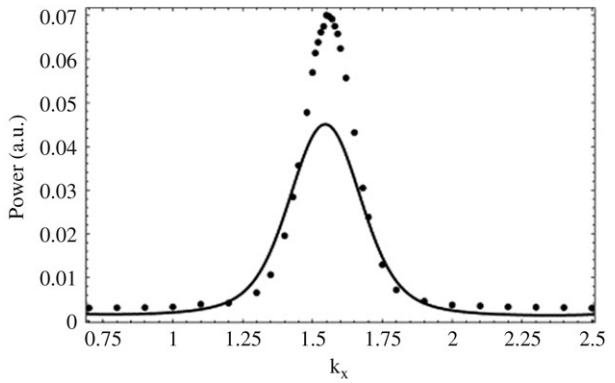


**Fig. 31.** The total scattered power for the propagating wavepacket calculated from numerical simulations (points) and by means of a one-dimensional approximation (lines). Data from [395].

The energy flux, carried by a single plane wave $a\cos(qn-\omega t)$ is $\frac{1}{2}C|a|^2\omega\sin q=\frac{1}{2}C\omega J$ and is proportional to its momentum multiplied by the frequency $\omega$. Thus for single channel scattering, where the incoming and outgoing waves have the same frequency, momentum conservation is equivalent to energy flux conservation. In that case, the scattering process is *elastic* which means that the incoming flux of energy is identical to the outgoing flux. This is no longer true for multichannel scattering.

Consider an incoming wave (assuming that $\omega_1$ and $q_1$ are positive) carrying energy towards the breather and outgoing waves carrying energy away from the breather. The asymptotic form of this state is (note that $\omega_2$ and $q_2$ are negative)

$$\begin{aligned}\epsilon_n &= \mathrm{e}^{\mathrm{i}q_1 n-\mathrm{i}\omega_1 t}+r_1\mathrm{e}^{-\mathrm{i}q_1 n-\mathrm{i}\omega_1 t}+r_2\mathrm{e}^{-\mathrm{i}q_2 n-\mathrm{i}\omega_2 t} \quad n\to-\infty\\ \epsilon_n &= t_1\mathrm{e}^{\mathrm{i}q_1 n-\mathrm{i}\omega_1 t}+t_2\mathrm{e}^{\mathrm{i}q_2 n-\mathrm{i}\omega_2 t} \quad n\to+\infty.\end{aligned} \tag{5.33}$$

Let $\{\epsilon_n(t)\}$ be a solution of the linearized equation (3.12). Let us multiply both sides of these equations by $\epsilon_n^*$ and compute the imaginary part. We obtain

$$C\,\mathrm{Im}\,(\epsilon_n^*\epsilon_{n-1}-\epsilon_n\epsilon_{n+1}^*)=\mathrm{Im}\,\epsilon_n^*\ddot{\epsilon}_n=\mathrm{Im}\,\frac{\mathrm{d}}{\mathrm{d}t}\epsilon_n^*\dot{\epsilon}_n. \tag{5.34}$$

Averaging over time, one finds

$$\langle\mathrm{Im}\,\epsilon_n^*\epsilon_{n-1}\rangle=\langle\mathrm{Im}\,\epsilon_{n+1}^*\epsilon_n\rangle=-J. \tag{5.35}$$

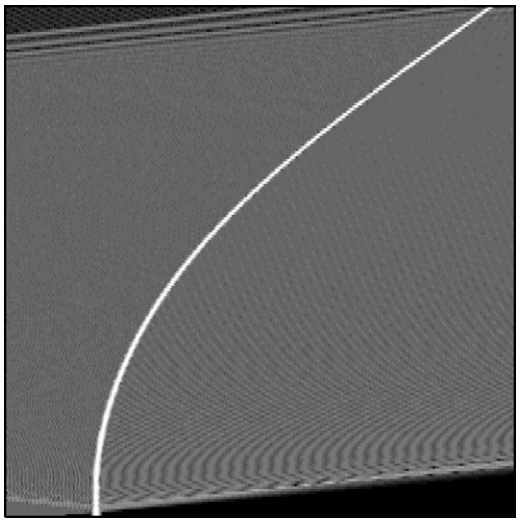

**Fig. 32.** Energy density in space–time representation for a two-channel inelastic scattering process of a wave by a breather (space along horizontal, time along vertical axis). Parameters are $C = 0.2$ and $\Omega_b = 0.7$ for the KG chain with Morse potential $V(x) = \frac{1}{2}(1 - e^{-x})^2$, the wave vector of the incoming wave is $q = 0.8$ and its amplitude is $2 \times 10^{-2}$. The breather location (high energy density) versus time appears as the white line. The breather starts to move at the instability threshold when $\Omega_b = 0.73$. Figure from [69].

The momentum $J$ of the solution $\epsilon_n(t)$ is independent of $n$. The momentum of a single plane wave $ae^{i(qn-\omega t)}$ is $J = |a|^2 \sin q$. For large $|n|$, $\epsilon_n(t)$ is just a sum of plane waves in the open channels. One finds readily that $J$ is the sum of the contributions of each wave and has to be the same far away from the breather at the right side and the left side.

The momentum conservation (5.35) yields

$$\sin q_1(1 - |r_1|^2) - \sin q_2|r_2|^2 = \sin q_1|t_1|^2 + \sin q_2|t_2|^2. \tag{5.36}$$

The energy flux carried by the real (or the imaginary) part of (5.33), is the sum of the plane waves contributions.[5] It can be decomposed into the sum of an incoming, a reflected and a transmitted flux of energy $I$, $R$, $T$:

$$I = \frac{C}{2}\omega_1 \sin q_1 \tag{5.37}$$

$$R = \frac{C}{2}(\omega_1 \sin q_1|r_1|^2 + \omega_2 \sin q_2|r_2|^2) \tag{5.38}$$

$$T = \frac{C}{2}(\omega_1 \sin q_1|t_1|^2 + \omega_2 \sin q_2|t_2|^2). \tag{5.39}$$

Using Eq. (5.36), the difference between the outgoing flux and the incoming flux of energy

$$R + T - I = \frac{C}{2}(\omega_1 - \omega_2)\sin(-q_2)(|r_2|^2 + |t_2|^2) > 0 \tag{5.40}$$

is necessarily positive. Consequently, the scattering process is *inelastic*.

This result has been illustrated by a calculation of the transmission coefficient through a single breather with band overlap (Fig. 6 in [69]).

All above results consider the incoming wave as being scattered by a *given* time periodic scattering potential, generated by the breather. Then, the energy flux which is radiated per unit of time (5.40) is generated by the time dependence of potential. In reality, the incoming wave is scattered by the breather and the change in the outgoing energy flux is taken at the expense of the internal breather energy. Then, the breather energy should decay slowly in time with a linear rate given by (5.40). When the amplitude of the incoming wave is small, the energy loss of the breather found in a direct simulation, is negligible during the numerical experiment and the expected results for the transmitted and reflected energy flux are recovered. It has been shown (Fig. 6 in [69]) that in addition to the wave vector $q_1$, wave vector $q_2$ is also present in the transmitted wave.

When the amplitude of the incoming wave is not too small, the rate of radiation of the breather becomes large enough to be observable. Then, the breather frequency changes in order to accommodate its loss of energy. For example for a soft potential (e.g. the Morse potential), its frequency $\Omega_b$ will increase slowly. This situation will last until either the two-channel scattering ends or the breather becomes linearly unstable. Then another scenario will continue the breather evolution.

The example shown in Fig. 32 concerns a single breather of the KG chain with a Morse potential for which a two channel scattering is expected. It is exposed to an appropriate monochromatic wave with wave vector $q_1$ at the left side. Then,

[5] This is not true for the special case $\omega_2 = -\omega_1$ (and $q_1 = -q_2$) which has to be treated separately.

its frequency increases (while the breather remains located at the same site), until it reaches an instability threshold. In that example, the unstable mode is a pinning mode (see chapter 4.2.1). Then, continuing the experiment, the marginal component [21] of this pinning mode gets excited by the incoming wave and the breather starts to move, "surfing" on the incoming wave. It accelerates until it reaches a limit velocity.

## 6. Statistical properties of discrete breathers

This chapter is devoted to a discussion of the role of discrete breathers in statistical properties of nonlinear lattices. We will begin with analytical results for DNLS lattices, and discuss the possibility to extend and interpret these findings for other nonlinear lattices. We will then review recent progress in computational tools to measure distribution functions which characterize DBs. Finally we will slightly touch the extensive body of numerical studies regarding both thermal equilibrium and transient processes.

### 6.1. Discrete breathers in thermal equilibrium

So far we have discussed the generic occurrence of discrete breathers in many different nonlinear lattices. The question then arises whether DBs can play a role in the statistical properties of nonlinear lattices in thermal equilibrium. Before answering that question, we remind the reader that various approaches exist to emulate a thermal equilibrium. One way would be to take a very large system and study the microcanonical evolution of it. Another one would be to add friction and stochastic forces. The latter path leads on one side to faster equilibration, but at the expense that on long enough time scales the equilibration processes are completely determined by the heat bath which is coupled to the original system. If we want to first understand the equilibrium properties of the lattice itself, it is better to consider the microcanonical evolution.

An exact DB will of course almost never be realized in a nonlinear lattice at finite temperatures and thus at finite energy densities. But the evolution of the system could allow for time intervals during which a DB-like state is formed somewhere on the lattice. Such nonlinear localized excitations (NLE) will be characterized by their spatial localization and their lifetime. Thus observation of DBs in thermal equilibrium amounts to the observation and characterization of NLEs. We expect that the properties of these NLEs will be closely related to the properties of exactly corresponding DB solutions.

Thermal equilibrium is characterized by distribution functions, averages and correlation functions. Suppose NLEs are frequently generated, and their lifetimes are sufficiently large (compared to the DB periods). Which distribution functions and correlation functions are they affecting? A reasonable expectation is that DBs and NLEs are most strongly influencing time-dependent correlation functions. Indeed, think of a system of coupled weakly anharmonic oscillators. Compute some correlation function which is the average of a function of only the displacements, measured at the same time. Assuming a Gibbs distribution, we can immediately integrate the momentum part out, and are left with integrals over the displacements only. Whether the dynamical evolution generates NLEs frequently or not, seems not to have strong impact on the outcome. But time-dependent correlation functions will be sensitive, since they not only probe the chance to have say a large energy fluctuation in a small part of the lattice, but they will also store the information whether this fluctuation was able to stay there (once created) for sufficiently long times or not. In the most general setting, distribution functions which measure correlations both in time and space are of interest, since they are directly probing coherent excitations which are local in space and time.

#### 6.1.1. Analytical results for DNLS and spin systems

A number of analytical treatments of DNLS and spin lattices have been recently published. These systems have the property that besides the total energy another quantity is conserved — the total norm, or spin, or particle number. Note that these quantities are very different from e.g. total momentum which may be conserved for acoustic lattices. The point is that systems with different total momentum are easily related by a Galilean transformation. That is not true for the particle numbers or total spins.

Let us begin by closely following the work of Rasmussen et al. [329]. They consider the one-dimensional DNLS equation in the form

$$\mathrm{i}\dot{\psi}_m + \psi_{m+1} + \psi_{m-1} + |\psi_m|^2\psi_m = 0. \tag{6.1}$$

The corresponding conserved energy $\mathcal{H}$ is given by

$$\mathcal{H} = \sum_m \left(\psi_m^*\psi_{m+1} + \psi_m\psi_{m+1}^*\right) + \sum_m \frac{1}{2}|\psi_m|^4.$$

In addition the norm (or particle number) $\mathcal{A} = \sum_m |\psi_m|^2$ is also conserved by the dynamics of Eq. (6.1).

In order to study the statistical mechanics of the system, one calculates the classical grand-canonical partition function $\mathcal{Z}$. Applying the canonical transformation $\psi_m = \sqrt{A_m}\exp(\mathrm{i}\phi_m)$ the energy

$$\mathcal{H} = \sum_m 2\sqrt{A_m A_{m+1}}\cos(\phi_m - \phi_{m+1}) + \frac{1}{2}\sum_m A_m^2$$

and the partition function

$$\mathcal{Z} = \int_0^\infty \int_0^{2\pi} \prod_m \mathrm{d}\phi_m \mathrm{d}A_m \exp[-\beta(\mathcal{H} + \mu\mathcal{A})], \tag{6.2}$$

where the multiplier $\mu$ is introduced in analogy with a chemical potential to ensure conservation of $\mathcal{A}$. Integration over the phase variables $\phi_m$ reduces the symmetrized partition function to

$$\mathcal{Z} = (2\pi)^N \int_0^\infty \prod_m \mathrm{d}A_m I_0(2\beta\sqrt{A_m A_{m+1}}) \mathrm{e}^{-\beta\sum_m \left(\frac{1}{4}(A_m^2 + A_{m+1}^2) + \frac{\mu}{2}(A_m + A_{m+1})\right)}.$$

This integral can be evaluated exactly in the thermodynamic limit ($N \to \infty$) using the eigenfunctions and eigenvalues of the transfer integral operator [329],

$$\int_0^\infty \mathrm{d}A_m \kappa(A_m, A_{m+1}) y(A_m) = \lambda y(A_{m+1}),$$

where the kernel $\kappa$ is

$$\kappa(x, z) = I_0\left(2\beta\sqrt{xz}\right) \mathrm{e}^{-\beta\left(\frac{1}{4}(x^2+z^2) + \frac{\mu}{2}(x+z)\right)}. \tag{6.3}$$

One obtains $\mathcal{Z} \simeq (2\pi\lambda_0)^N$, as $N \to \infty$ where $\lambda_0$ is the largest eigenvalue of the operator. The averaged energy density, $h = \langle\mathcal{H}\rangle/N$, and the average norm density, $a = \langle\mathcal{A}\rangle/N$ are given by

$$a = -\frac{1}{\beta\lambda_0}\frac{\partial\lambda_0}{\partial\mu}, \qquad h = -\frac{1}{\lambda_0}\frac{\partial\lambda_0}{\partial\beta} - \mu a.$$

The average norm density $a$ can also be calculated as

$$a = \frac{1}{\mathcal{Z}} \int_0^\infty \prod_m \mathrm{d}A_m A_m \exp\left[-\beta\left(\mathcal{H} + \mu\mathcal{A}\right)\right],$$

where the integral is obtained with the help of the transfer technique [329]. It yields $a = \int_0^\infty y_0^2(A) A \mathrm{d}A$, where $y_0$ is the normalized eigenfunction corresponding to the largest eigenvalue $\lambda_0$ of the kernel $\kappa$ (6.3). Thus $p(A) = y_0^2(A)$ is the probability distribution function (PDF) for the amplitudes $A$.

The problem is now reduced to finding the largest eigenvalue $\lambda_0$ and the corresponding eigenfunction $y_0$ of the transfer operator (6.3). Two limits ($\beta \to \infty$ and $\beta \to 0$) are amenable to analytical treatment.

The Hamiltonian is bounded from below, and this minimum is realized by a plane wave, $\psi_m = \sqrt{a}\exp \mathrm{i}m\pi$, whose energy density is $h = -2a + \frac{1}{2}a^2$. This relation defines zero temperature, or the $\beta = \infty$ line.

In the high temperature limit $\beta \ll 1$. The modified Bessel function in the transfer operator can be approximated, to leading order, by unity (this amounts to neglecting the coupling term in the Hamiltonian). This reduces the remaining eigenvalue problem to the approximate solution valid for thermalized independent units,

$$y_0(A) = \frac{1}{\sqrt{\lambda_0}} \exp\left[-\frac{\beta}{4}\left(A^2 + 2\mu A\right)\right].$$

Using this approximation and enforcing the constraint $\beta\mu = \gamma$ (where $\gamma$ remains finite as one takes the limits $\beta \to 0$ and $\mu \to \infty$), one obtains $h = 1/\gamma^2$ and $a = 1/\gamma$. Thus, $h = a^2$ at $\beta = 0$.

The left panel in Fig. 33 depicts the two parabolas in the $(a, h)$-space corresponding to the $T = 0$ and $T = \infty$ limits (thick lines). Within this region all considerations of statistical mechanics in the grand-canonical ensemble are normally applicable and there is a one-to-one correspondence between $(a, h)$ and $(\beta, \mu)$. Within this range of parameter space one expects the system to thermalize in accordance with the Gibbs formalism. However, the region of the parameter space that is experimentally (numerically) accessible is actually wider since it is possible to initialize the lattice at any energy density $h$ and norm density $a$ above the $T = 0$ line in an infinite system. A statistical treatment of the remaining domain of parameter space can be accomplished introducing formally negative temperatures. But the partition function (6.2) is not suited for that purpose since the constraint expressed in the grand-canonical form fails to bound the Hamiltonian from above. A discontinuity has to be assigned to the chemical potential. This discontinuity will destroy the analyticity of the partition function as the transition line is crossed, and will indicate a phase transformation according to standard statistical mechanics. From the microcanonical point of view it is also natural to consider negative temperatures because it is possible to maximize the energy under the constraint of a fixed norm in a finite system. It can be seen that the configuration which realizes this maximum is an exact breather solution, whose total energy and frequency scale as $\mathcal{A}^2$ and $N$, respectively. Thus, the number of microstates sharing the same energy $E$ will decrease with increasing $E$ if the norm $\mathcal{A}$ is kept fixed. Due to the definition of temperature ($1/T = \partial S/\partial E|_{\mathcal{A}}$), $T$ becomes negative at high energy density and the $\beta = 0$ line is the line of maximum entropy. Actually the constraint of fixed norm $\mathcal{A}$ is a topological one, as we will see later.

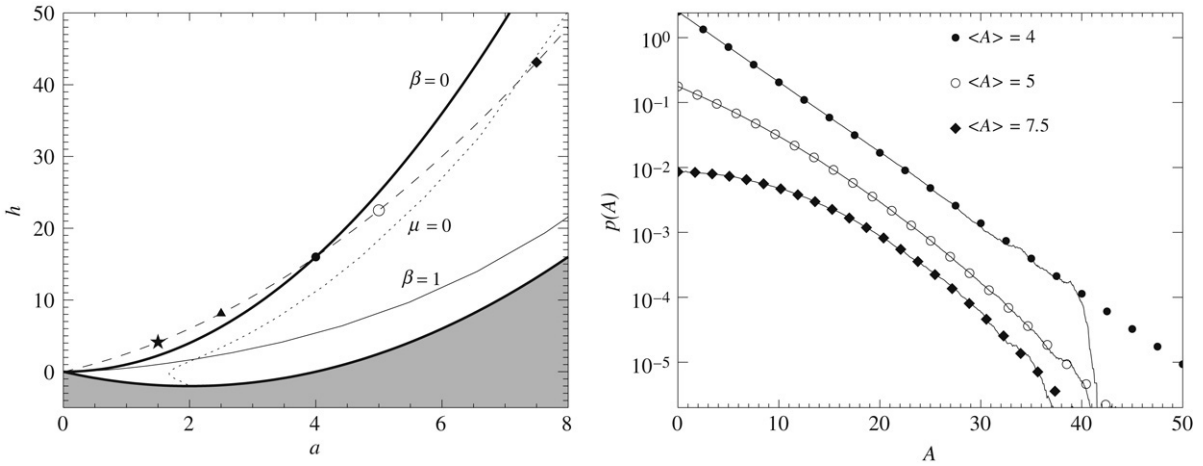


**Fig. 33.** Left panel: Parameter space $(a, h)$, where the shaded area is inaccessible. The thick lines represent the $\beta = \infty$ and $\beta = 0$ lines and bound the Gibbs regime. The dashed line represents the $h = 2a + \frac{1}{2}a^2$ line along which the reported numerical simulations were performed (pointed by the symbols). Figure from [329]. Right panel: Distribution of $A = |\psi|^2$ for three cases below (and on) the transition line. The solid lines show the results of simulations and the symbols are given by the transfer operator. Curves are vertically shifted to facilitate visualization. Figure from [329].

In order to characterize the dynamics of both phases (above and under the $\beta = 0$ line) and to verify that the system does relax to a thermalized state, numerical experiments were performed. The parameters $(a, h)$ are restricted to the dashed line in the left panel of Fig. 33, choosing a perturbed wave with wavevector $q = 0$ ($\psi_m = \sqrt{a}$) as an initial condition, for which the energy norm relationship is $h = 2a + \frac{1}{2}a^2$. This state is modulationally unstable, and can be expected to relax into some equilibrium. For these initial conditions, the important question is whether one can observe different qualitative behavior on the two sides of the $\beta = 0$ line.

The right panel in Fig. 33 shows three typical examples of what can be observed when the energy-norm density point lies below the $\beta = 0$ line. The $q = 0$ wave is unstable and the energy density forms small localized excitations but their lifetime is not very long and a stationary distribution of the amplitudes $A_m$ is reached. The system reaches an equilibrium state which is recovered by means of the transfer operator method. The curvature of $\log p(A)$ (i.e., $-\beta$) tends to zero when $h = a^2$ (the cut-off at high amplitudes is due to finite size effects). In this domain of parameter space, high amplitude excitations are highly improbable and can be considered as rare fluctuations.

The scenario is very different when the energy and norm densities are above the $\beta = 0$ line. A rapid creation of breather excitations due to modulational instability is observed. It is accompanied by a thermalization of the rest of the lattice. Once created, these localized excitations remain mostly pinned. This introduces new time scales in the thermalization process.

Typical distribution functions of the amplitudes are shown in the left panel in Fig. 34. The system size does influence the amplitude of the breathers with largest amplitude. The positive curvature of the PDF at small amplitudes indicates that the system evolves in a regime of negative temperature. A number of numerical simulations give further support to that surprising behaviour [62,328,327,186].

A very similar analysis of the anisotropic Heisenberg spin chain in classical formulation was performed by Rumpf and Newell [340]. There the $z$-component of the total spin for the Heisenberg chain is the analogous quantity to the conserved norm of the DNLS model. The authors also provided an argument using entropies of different states. They assume that the system tends to decompose the excitations into few large amplitude localized excitations and a delocalized background. The conclusion is that the formation of strongly localized excitations does not contradict entropic reasoning, since one has to compute the total entropy balance. The assumption of a binary mixture of localized and delocalized excitations allows one to conclude that decrease of the entropy due to the formation of localized excitations can be counterbalanced well by the increase in the entropy of the delocalized background. In the right panel of Fig. 34 the results of another study of Rumpf [338] are shown, where the negative or positive temperature situations are achieved by initial conditions of extended waves with different wave numbers. The formation of the binary mixture is clearly observed for the former one (see also [339]).

### *6.1.2. Getting the essential, and generalization to other systems*

Assuming a Gibbs distribution for the DNLS, we have to fix the values for the inverse temperature $\beta$ and the chemical potential $\mu$. For each pair of these values we can compute the average energy and norm densities $h$ and $a$. The Gibbs distribution generates a map of the control parameter space $\{\beta, \mu\}$ onto $\{h, a\}$. It follows, that a part of the accessible $\{h, a\}$ space is reachable only for formally negative inverse temperatures $\beta < 0$. That is a hallmark of a phase transition, and simulations of the DNLS with $\{h, a\}$ values from that region show the formation of extremely long-lived breathers on a cold background of delocalized waves.

In fact this had to be expected, for the following simple reasons. Let us take a large but finite DNLS system in the anomalous parameter region. Let us fix for convenience the norm density $a$, and continue to increase the energy density $h$.

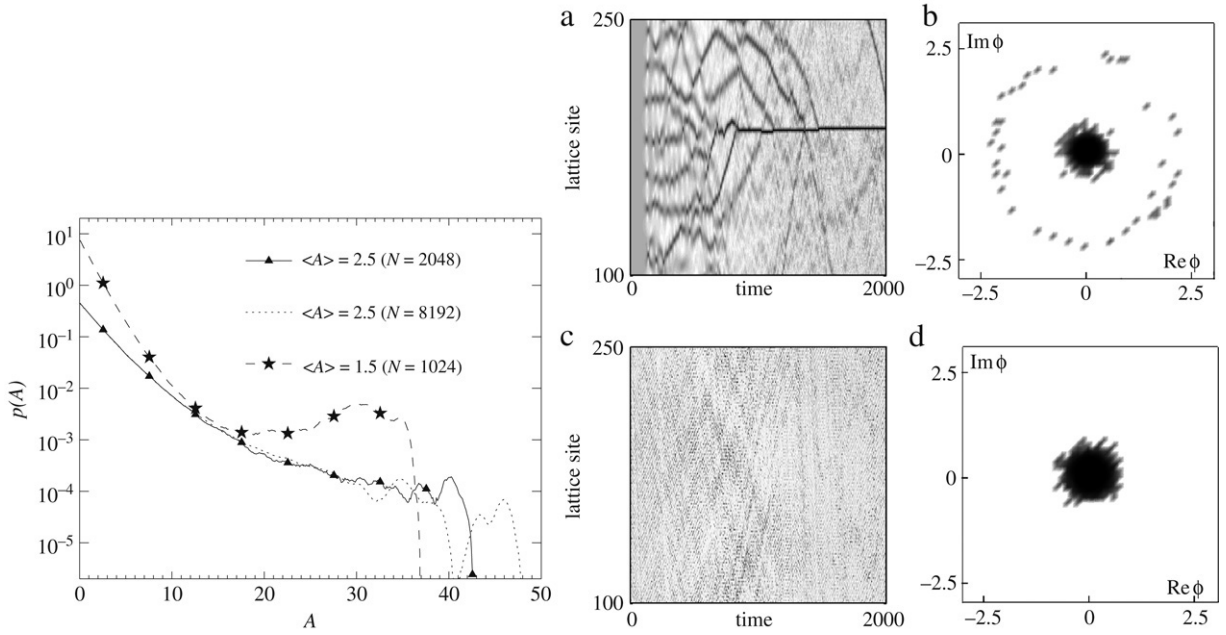


**Fig. 34.** Left panel: Distribution of $A = |\psi|^2$ for parameters $(h, a)$ above the transition line (triangles and stars in Fig. 33). Figure from [329]. Right panel: Numerical integration of the DNLS with 4096 oscillators. The initial conditions are waves with the wavenumber $k = 0$ (a), (b), and with $k = \pi/2$ (c), (d) for $|\phi| = 0.3$. (a), (c): Spatiotemporal pattern of high-amplitude states (dark gray) in a small sector of the chain for the first 2000 time steps. (b), (d): Distribution of $\psi_n$ (coined $\phi$ in the plot) after $2 \times 10^5$ time steps. Figure from [338].

That can be done up to a limiting value of $h$, when all the norm is initially concentrated on a single site. Of course we are free to choose the site at which that happens, so there is $N$-fold degeneracy of such states, where $N$ is the total number of sites. This happens because of the nonlinearity, which allows one to increase the energy by concentrating the available norm in a small volume of the system. Thus in that very limit there is no other way but to violate the translational invariance of the dynamical evolution of the system for all times. And that of course contradicts the results for a Gibbs distribution which treats all sites equally. That means that we have to introduce a new phase of condensed norm (or particles) which evolves in a mostly coherent and spatially localized manner, and may coexist with the old phase of spatial regions where all sites are equally sharing the energy and the norm. In other words, we are facing here the fact of the condensation of particles into lumps (or breathers) upon increase of the energy (or temperature).

We can give further evidence of why this condensation should happen. First, there is a simple energy balance argument. Assume again that all the norm is concentrated on a single site. Can this state decay into delocalized waves? The energy of the initial state is $\frac{\mathcal{A}^2}{2}$, but the energy of a delocalized state would be bounded from above by $2\mathcal{A} + \frac{\mathcal{A}^2}{2N}$. For large enough initial norm $\mathcal{A}$ the initial state has too large an energy and can not be distributed homogeneously over the lattice. The reason is very simple — the lattice itself imposes an upper limit on the energy of delocalized waves, and decay is thus prevented. This effect is well known in quantum physics, where two particles which repel each other strongly, form a bound state which can not decay because the kinetic energy of each particle is bounded by the lattice itself.[6] Second, the condensation effect is already observed for the simplest case of a DNLS dimer as discussed at the beginning of this review in chapter 1.1. Indeed let us fix the norm to be $B > 2C/v_4$ in that dimer. Then there will be an allowed parameter range for the energy, bounded from below and above. The second restriction follows from the fact that we can not realize an infinitely large energy state with a finite norm at hand. Now it is a simple task to understand, that for all energies larger than some value in that range, all states are not invariant under permutation of the two sites. Vice versa all states with energies less than that intermediate value are invariant under permutation. Consequently we are faced again with the fact that given a norm and a large enough energy, the dimer allows only for strongly asymmetric states, when more norm is concentrated on one site as compared to the other one. Moreover, we can fix the energy and vary the norm instead. Again we find, that the norm can vary in a certain interval bounded from above and below. All states with norm less than some intermediate value are not invariant under permutation, while those with norm larger than this intermediate value are invariant. So we can as well expect another unusual condensation scenario — fixing the energy density and decreasing the norm density should lead to a transition into a condensate in a large system. Note that large energies are replaced by low energies, if the sign of the nonlinear term in the equations of motion is inverted.

[6] A beautiful experimental verification of this result has been conducted with cold atoms in optical lattices [401], see chapter 10.3.

Let us return to the case of a large lattice. The additional conservation of the norm can be considered as a global constraint, which may lead to long range correlations. This argument has been used to justify the presence of a phase transition in a one-dimensional system with otherwise short range interactions. Note also that apart from the extreme case of largest energy (or smallest norm) the condensed DB fraction of the system may still fluctuate in time. But these time scales must be very large, since they evidently tend to infinity in the case of extremal energy or norm. Away from them, a given large amplitude DB can not completely dissolve in the bath of extended waves in order to form again at another site. It can only give away a small fraction of its own to another site, and wait until other DBs are contributing to that site some excitation fraction as well. So the process of DB diffusion along the lattice is hindered, and solely based on the collective diffusion of many DB excitations. That is why the observed DB configurations appear to be frozen on the time scales of the numerical experiments.

What happens if we consider a system which does not conserve that norm or a similar quantity? Strictly speaking nothing forbids individual DBs from relaxing into delocalized waves anymore. Yet it is tempting to search for almost conserved quantities, which change in time perhaps adiabatically slowly. Indeed Johansson and Rasmussen [186] have shown how to derive a DNLS type model by perturbative expansion of a lattice of interacting anharmonic oscillators, and Johansson extended that approach to other models as well [181]. These papers show how to derive a map from an original model to a DNLS one. The norm conservation comes in through an additional constraint on the ratio between the harmonic and anharmonic potential energy parts. In fact that ratio will be not fixed, but will fluctuate in the original model, leading to a fluctuation of the norm in the DNLS model. Thus we will smear out the transition line in Fig. 33, and visit different parts of that region with a certain probability. If the smeared-out region shows considerable overlap with the non-Gibbs part in Fig. 33, considerable and long-lasting generation of discrete breathers in thermal equilibrium could be expected.

Let us finish by adding another related pathway of understanding the generation of DBs in thermal equilibrium for many other models. If a DB is excited somewhere in the system due to fluctuations, that process and the persisting nature of the DB cannot be related to the dynamics of the lattice at too distant points. Roughly speaking we could expect that the effective size of the system which is relevant for a given DB is determined by its lifetime and the largest distance a plane wave can cover during that time. And even that will serve as an upper bound in distance. But the idea of additional conservation laws which make a DB a generic fluctuation in thermal equilibrium, is very tempting. A trace of that idea is found in the study of reduced problems, which are defined by allowing only a small fraction of sites to be excited, and by fixing all other sites to their classical groundstate. Then it was shown [133] that these few degree of freedom problems have a mixed phase space. A part of that phase space is filled by chaotic trajectories, which cannot penetrate certain islands with regular trajectories. Some of these islands correspond to DB excitations in the full system. Each island contains a central periodic orbit — the DB itself, which may be characterized by an action $J_1$. Quasiperiodic perturbations of this orbit constitute excitations which strictly speaking cannot live forever in the full system, but may persist for a long time due to weak resonances. These quasiperiodic perturbations correspond to additional actions $J_2, J_3, \ldots$. And these actions imply the existence of locally conserved quantities. They are simply constants of motion for the reduced problem, and change only adiabatically slowly in the full lattice. Their presence and number is directly related to the number of localized Floquet eigenstates of the DB itself. The size of the regular island measures the statistical weight or possibility of ending up in such a state. Thus it is tempting to say that in a general lattice the localized Floquet eigenstates of a DB and the maximum amplitude of their excitation while preserving a DB-like evolution are a measure for the statistical relevance of such a DB.

### *6.1.3. Computational measurement tools for distribution functions*

Computational studies of DBs in thermal equilibrium are essential in order to observe and compare the findings to analytical results. The code should be able to distinguish a DB from a delocalized state or simply from a accidental fluctuation which may happen in otherwise almost harmonic lattices. In order to do so we can follow different approaches. The first one needs the definition of an energy (amplitude, norm) scale and a time scale. We may define a DB as an object which exceeds the given energy scale, and persists for longer times than the given time scale. The time scale may be reasonably chosen as at least ten times the characteristic oscillation periods. The energy scale is much harder to chose, since the only other scale at hand is the average energy density. So the energy scale should be chosen to be suitably larger than the average energy density. But how much larger? And is the choice of the time scale reasonable? There is clearly a lot of ambiguity in answering these questions ([169] and references therein).

Other approaches try to separate localized from delocalized excitations dynamically. A second approach is suitable for lattice dimensions $d \geq 2$ and for DB excitations which are pinned to their lattice points. Then the simple trick is to thermalize the system (let it evolve for sufficiently long in time so that we can expect it to have good thermal equilibrium, and start measuring correlation functions in a reproducible way, independent of the initial conditions). Then we switch on radiative boundaries (for details see e.g. [388,169]). After some transient in time all delocalized excitations will eventually hit the boundary and be dissipated away. DBs will remain in the system. Then their distribution properties can be measured [93]. This approach cannot be used for one-dimensional systems, because DBs strongly scatter waves there, and efficiently trap delocalized excitations [169]. That is not the case for higher dimensions, where DBs still scatter waves, but as point defects.

A third approach attaches to each lattice site an auxiliary chainlet of particles. Each chainlet is a purely linear system, and has a frequency spectrum which resonates with the linear mode spectrum of our system under study. Then we add damping at the ends of these chainlets. As a result we will efficiently damp out excitations in the original system which resonate in frequency with the normal mode spectrum. DB excitations are off resonance, do not leak into the chainlets, and will not be dissipated away.

Finally a fourth method consists of taking the evolution of the original system in time, making a Fourier decomposition of its evolution at each site, and cutting out the frequency part of the linear spectrum. The rest is backtransformed into real time, giving the evolution of DB like objects [148].

All these methods have their advantages and disadvantages, which still have to be studied in more detail. But it is already clear, that a combination of all methods will give more confidence from the computational side, and should be further developed in order to study statistical properties of DBs.

### 6.2. Discrete breathers in transient processes

Discrete breathers can also form during transient processes, independent of whether the corresponding thermal equilibrium supports them or not. The most prominent example is the modulational instability of plane waves [308], discussed in Section 4.3. In some cases it leads to the formation of one large amplitude DB, on the background of cold delocalized waves (also coined 'chaotic' breather), see e.g. [70,228,279,227]. Cooling at the boundaries (see previous chapter), kicking the system with strong local kicks, and perhaps other nonstationary lattice evolutions can be used to generate discrete breathers along such transients. We will not focus on the growing amount of numerical data available in the literature [388,38,390,313,330,241,318]. The interested reader may check a collection of results on all these aspects in Ref. [169], and the reference list therein. We mention a very recent theoretical proposal by Hennig et al. [165,162], where a self-organized escape of harmonically coupled oscillators from a metastable state over a potential barrier is discussed. Modulational instability (see Section 4.3) is used to form spontaneously emerging localized modes, which grow into a critical nucleus. After passing the transition state, the nonlinear chain performs a collective escape event. The average escape times are much shorter than those assisted by a continuously impacting thermal noise.

We close the section on statistical properties of discrete breathers by first stating, that we intentionally did not try to review the quite large amount of literature on various numerical studies, since a coherent picture is still missing. We secondly think, that the issue of statistics and discrete breathers has still to be explored, and a few of the above ideas might help to guide future efforts, which hopefully will give us a more systematic picture of this intriguing subject [383].

## 7. Discrete vortices

So far we discussed discrete breather solutions which are invariant under time reversal. However, as explained in chapter 1.1, nonlinearity permits us to search also for solutions which are not invariant under symmetry operations, but leave the equations of motion (and the Hamiltonian) untouched. Violating time-reversal symmetry is equivalent to generating an energy current or flow. In one-dimensional chains it follows, that a localized DB solution must be time-reversal invariant, since the energy flow can be directed only along the chain, and due to energy conservation it thus must be one and the same in the core and the tails of the DB. In the tails of a DB the amplitudes tend to zero, so that the energy flow should do so as well. Therefore only zero energy flow is allowed, thus the DB is invariant under time reversal.

In higher dimensional lattices we may think of energy flowing in ring currents, so that spatial localization and energy conservation no longer forbid the existence of a local nonzero energy flow. A DB solution which carries such a nonzero ring flow of energy, is also coined *a discrete vortex*. Two- and higher-dimensional lattices can support discrete breather solutions carrying a nonzero angular momentum — discrete vortices. Due to the discreteness, the angular momentum is generally not a conserved quantity. It manifests itself as a screw dislocation of the phase on a closed contour encircling the discrete vortex excitation [71,72,230], see Fig. 35. Similar to vortices in various continuum models, discrete vortices can be characterized by the corresponding angular momentum number $S$ (topological charge, also known as vorticity), i.e. the number of complete $2\pi$ twists of the phase along the contour. In two-dimensional lattices we consider a contour at large distances from the core of the discrete vortex. In the 2D DNLS model, see e.g. Eqs. (1.19) and (4.6), the simplest example of a stationary $S = 1$ discrete vortex is given by four neighboring sites excited with different phases (in the anti-continuous limit):

$$\Psi_{n_0,m_0} = -\Psi_{n_0+1,m_0+1} = a, \qquad \Psi_{n_0,m_0+1} = -\Psi_{n_0+1,m_0} = \mathrm{i}a, \tag{7.1}$$

where $a$ is the amplitude. In the anti-continuous limit one can design more complicated structures with different contours and different topological charges and then continue these solutions to non-zero values of the coupling constant using e.g. numerical methods discussed in Section 3.2.

The existence of discrete breather solutions carrying a nonzero angular momentum has been suggested in Refs. [249, 18], and later some examples of discrete vortices have been numerically obtained for Klein–Gordon [71,72] and DNLS [187] lattices. As mentioned in Refs. [71,72,187], and later confirmed in Ref. [252], $S = 1$ discrete vortices can be linearly stable for small enough values of the coupling constant. The instability occurring at higher values of the coupling constant and leading to the vortex breakup into two single localized excitations has been explicitly illustrated in Ref. [252], see Fig. 36. Later the existence of stable $S = 3$ discrete vortices in the DNLS model has been confirmed [202]. Recently a more rigorous study of persistence and stability of various discrete vortices in the DNLS model has been performed [303]. As indicated in Ref. [303], super-symmetric vortices with topological charges $S \geq 2$ can be stabilized by modifications of the discrete contour. An important update has been reported by Öster and Johansson [297], who studied discrete vortices with various contours in the DNLS model and explicitly demonstrated an example of a stable $S = 2$ vortex.

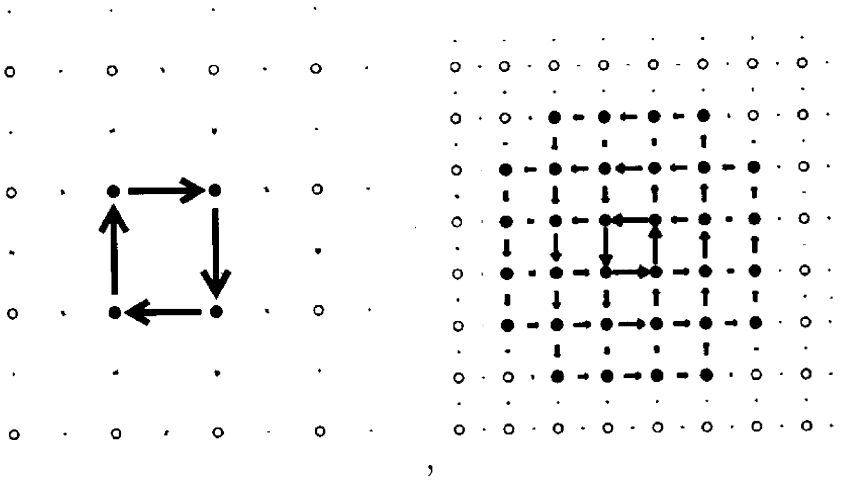

**Fig. 35.** A small and a large $S = 1$ vortex in the 2D Klein–Gordon lattice with quartic anharmonicity. Circles indicate lattice sites, the orientation of each arrow corresponds to the phase of the site. Figure from Ref. [71].

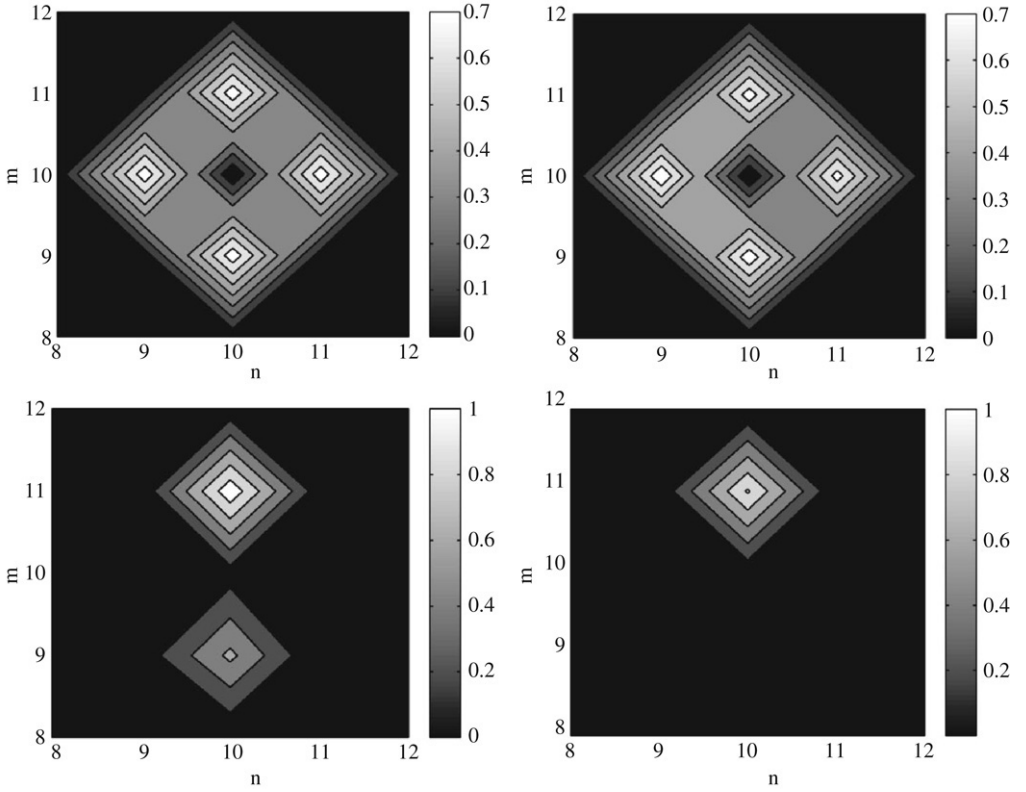


**Fig. 36.** Time evolution of the unstable $S = 1$ discrete vortex in the 2D DNLS model. Grayscale contour plots indicate snapshots of absolute values of amplitudes of lattice sites at four consecutive time instants. The initial vortex breaks up into two localized excitations with $S = 0$, bottom left panel, with subsequent symmetry breaking eventually evolving into a single localized excitation, bottom right panel. Figure from Ref. [252].

Recently Ferrando and co-workers discussed restrictions on the topological charge of discrete vortices imposed by the lattice symmetry [104,103,198]. It was argued, that lattices with a discrete point symmetry of order $n$ ($n = 4$ for square lattices), cannot support vortices of charge larger than $n/2$. However, as indicated in Ref. [297], this statement is related to the phase twist belonging solely to the plane-wave part of the Bloch mode associated with the vortex, and does not contradict earlier findings in Refs. [202,303], where overall phase twists have been considered.

Discrete vortices with the unity charge $S = 1$ have been successfully observed in experiments with photonic lattices [289, 137,29], see also Section 10.2. Observation of higher order discrete vortices still remains to be the open issue.

## 8. Discrete breathers in classical spin lattices

An interesting extension of the breather concept happens when considering a lattice of interacting spins. Spin waves in magnetically ordered media have been used to analyze nonlinear phenomena and soliton dynamics in condensed matter already for several decades [225]. Both interactions between spins, and spin anisotropy, are intrinsically nonlinear, allowing all possible types of nonlinearities in the corresponding macroscopic phenomenological models. Quasi one-dimensional magnetic crystals, such as layered ferro- and antiferromagnetics, have attracted attention recently. In this section we will briefly discuss some examples of magnetic discrete breathers, among which there are excitations existing solely due to the discreteness of the underlying model.

### 8.1. Heisenberg interaction Hamiltonian and equations of motion

A standard approach to describe spin excitations in ordered magnetic materials is to consider classical interacting spins with the Heisenberg XYZ interaction Hamiltonian

$$H = -\frac{1}{2}\sum_{\mathbf{n}\neq\mathbf{m}}\sum_{\alpha=(x,y,z)} J_\alpha^{(\mathbf{nm})} S_\mathbf{n}^\alpha S_\mathbf{m}^\alpha - D\sum_\mathbf{n}\left(S_\mathbf{n}^z\right)^2, \tag{8.1}$$

where $S_\mathbf{n}^\alpha$ are the components of the $\mathbf{n}$th spin vector for the classical spin

$$\left(S_\mathbf{n}^x\right)^2 + \left(S_\mathbf{n}^y\right)^2 + \left(S_\mathbf{n}^z\right)^2 = S^2. \tag{8.2}$$

The total spin is normalized to unity: $S = 1$, $\mathbf{n}$ labels the lattice site (in 1, 2 or 3 dimensions), $J_\alpha^{(\mathbf{nm})}$ are the exchange integrals, $J_\alpha^{(\mathbf{nm})} > 0$ ($J_\alpha^{(\mathbf{nm})} < 0$) corresponds to ferromagnetic (antiferromagnetic) interaction, $D$ is the single-ion anisotropy constant, and the dipolar interaction between spins is neglected for simplicity.

The equation of motion for the $\mathbf{n}$th spin is the well-known Landau-Lifshitz equation [242,225]:

$$\frac{\mathrm{d}\vec{S}_n}{\mathrm{d}t} = -\vec{S}_\mathbf{n}\times\vec{H}_\mathbf{n}^{\mathrm{eff}} - \epsilon\vec{S}_\mathbf{n}\times\left(\vec{S}_\mathbf{n}\times\vec{H}_\mathbf{n}^{\mathrm{eff}}\right), \tag{8.3}$$

where $\vec{H}_\mathbf{n}^{\mathrm{eff}} = -\delta H/\delta\vec{S}_\mathbf{n} + \vec{H}_\mathbf{n}$ is the effective magnetic field which describes the interaction with other spins and the external field $\vec{H}_\mathbf{n}$. The last term in the r.h.s. of Eq. (8.3) corresponds to the Landau-Gilbert damping which preserves the magnitude of individual spins, $\epsilon$ is a small parameter which controls the strength of dissipation, and the gyromagnetic ratio is scaled to unity. We will discuss only the case of a homogeneous external field applied along the single-ion anisotropy axis $z$: $\vec{H}_\mathbf{n} \equiv \vec{z}H_0$, where $\vec{z}$ is the unit vector along the $z$ axis.

Neglecting the dissipation and considering only nearest neighbours interactions and a one-dimensional lattice, Eqs. (8.3) reduce to

$$\dot{S}_n^x = \frac{1}{2}\left[J_y S_n^z\left(S_{n-1}^y + S_{n+1}^y\right) - J_z S_n^y\left(S_{n-1}^z + S_{n+1}^z\right)\right] - \left(2DS_n^z + H_0\right)S_n^y, \tag{8.4}$$

$$\dot{S}_n^y = \frac{1}{2}\left[J_z S_n^x\left(S_{n-1}^z + S_{n+1}^z\right) - J_x S_n^z\left(S_{n-1}^x + S_{n+1}^x\right)\right] + \left(2DS_n^z + H_0\right)S_n^x, \tag{8.5}$$

$$\dot{S}_n^z = \frac{1}{2}\left[J_x S_n^y\left(S_{n-1}^x + S_{n+1}^x\right) - J_y S_n^x\left(S_{n-1}^y + S_{n+1}^y\right)\right]. \tag{8.6}$$

The generalization to higher lattice dimensions is straightforward.

### 8.2. Easy-axis anisotropy

In the case of easy-axis anisotropy the ground state corresponds to all spins directed along a given axis, which is assumed to be the $z$ axis. This can be achieved by introducing either a strong exchange anisotropy ($J_z, J_y \ll J_z$), or by the on-site anisotropy term $2D + H_0 > 0$.

In the case of ferromagnetic interaction ($J_x, J_y, J_z > 0$) the two ground states are given by $S_n^z = \pm 1$, $S_n^x = S_n^y = 0$. Linearizing Eqs. (8.4)–(8.6) around one of these groundstates and taking $S_n^x = \delta_x \sin(qn - \omega t)$, $S_n^y = \delta_y \cos(qn - \omega t)$, the dispersion law for linear spin waves is obtained [410]:

$$\omega_L^2(q) = (J_z - J_x\cos q)(J_z - J_y\cos q) + 2(2D + H_0)\left(J_z - \frac{J_x + J_y}{2}\cos q\right) + (2D + H_0)^2. \tag{8.7}$$

Due to the anisotropy, it has a gap, i.e. frequencies are limited not only from above by $\omega_\pi \equiv \omega_L(\pi)$ but also from below by $\omega_0 \equiv \omega_L(0) > 0$, see Fig. 37.

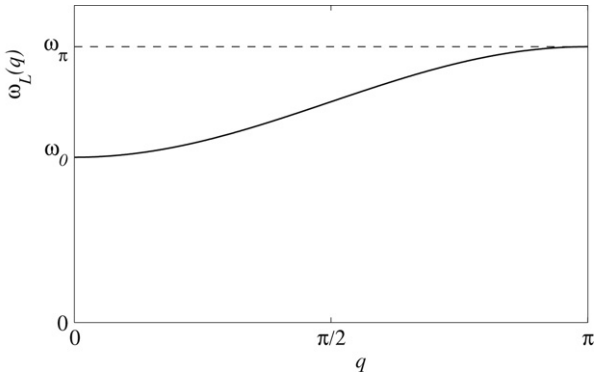


**Fig. 37.** Dispersion law for the ferromagnetic chain with strong exchange anisotropy. Figure from [410].

In the case of antiferromagnetic interaction ($J_x, J_y, J_z < 0$) the two ground states are $S_n^z = \pm(-1)^n$, $S_n^x = S_n^y = 0$. The dispersion law for linear spin waves can be obtained by changing $J_y \to -J_y$ in Eq. (8.7). It has qualitatively the same structure, as for the case of ferromagnetic lattice shown in Fig. 37.

Spin waves in an easy-axis crystal correspond to precessions of spins around one of the ground states, and discrete breathers can be viewed as localized excitations with the effective radius of precession decreasing to zero as $n \to \pm\infty$.

*8.2.1. The case of XY isotropic exchange interaction*

When the exchange interaction in the $xy$ plane is isotropic ($J_x = J_y = J$), one can search for solutions where the $z$-component of each spin is conserved. For such states, it is convenient to introduce new variables $S_n^+ = S_n^x + \mathrm{i}S_n^y$ which satisfy [396]

$$i\dot{S}_n^+ = \frac{J}{2}S_n^z\left(S_{n-1}^+ + S_{n+1}^+\right) - \frac{J_z}{2}S_n^+\left(S_{n-1}^z + S_{n+1}^z\right) - (2DS_n^z + H_0)S_n^+, \tag{8.8}$$

with $S_n^z = (-1)^k\sqrt{1-|S_n|^+}$, $k = 2n$ ($k = n$) for the case of ferromagnetic (antiferromagnetic) interactions. Eq. (8.8) allows separation of time and space variables: $S_n^+ = A_n \exp(\mathrm{i}\omega t)$ (note that the structure of the equations is similar to the ones of the DNLS model discussed in Section 1.5) [410].

The anharmonicity due to spin interactions is intrinsically soft [10,243], so that for $D = 0$ one needs to have a gap in the linear wave spectrum for localized excitations to exist: $\Omega_b < \omega_0$ for DBs. This gap is generated by the anisotropy $J_z \neq J_x, J_y$, see Eq. (8.7). When $D > 0$, the anharmonicity due to single-ion anisotropy is also soft, so the situation remains qualitatively similar. In this case the gap is present even for the completely isotropic interaction $J_z = J_x = J_y$, which is the most studied case in literature, partially due to its relative simplicity. For the case of an antiferromagnetic lattice, by using lattice Green's function techniques, Takeno and Kawasaki have shown that even and odd parity localized states exist in the gap, supported by soft anharmonicity of the system [381,377,382]. A more detailed study of these localized states based on path-integral formulation has been performed in Ref. [294]. Various localized excitations have been analyzed for the case of small amplitude spin deviations by using the continuum approximation [225,167,65]. Within the continuum approximation, the localized states correspond to envelope solitons — magnetic gap solitons. With the appearance of publications on discrete breathers, the one-dimensional Heisenberg antiferromagnetic chain was re-considered by Lai, Kiselev and Sievers [232,233], who numerically found site-centered and bond-centered discrete breathers and studied stability and mobility properties of these solutions. A rigorous proof of existence of such stationary discrete breathers has been performed by Zolotaryuk et al. [410], and Speight and Sutcliffe [372]. Several experiments aimed to detect discrete breathers in layered antiferromagnetic crystals have been performed. We discuss these results in more detail in Section 10.5.

One can see from Eq. (8.8), that the external field can be removed by transforming into a rotating frame of reference $S_n^+ \to S_n^+ \exp(-\mathrm{i}H_0 t)$. Thus, if Eq. (8.8) does not have localized solutions for $H_0 = 0$, nothing changes for the case of a nonzero $H_0$. However, a large enough magnetic field can change the ground state, and that will call for a new dispersion relation of small amplitude waves, may destroy the preservation of the $z$-component of each spin on certain solutions, etc. E.g. for negative single-ion isotropy, $D < 0$, the external field can be used to make the frequency space above the linear dispersion accessible for DBs. For $H_0 = 0$ and negative $D$ the $z$ axis will be the hard axis of the ferromagnetic crystal, so that the system becomes of the easy-plane type. However, by applying a strong magnetic field along the $z$ axis ($H_0 > 2|D|$), one can enforce the ground state to be aligned again along the $z$ axis (similar to easy-axis anisotropy). Negative $D$ implies hard anharmonicity which starts to dominate over the soft anharmonicity due to spin–spin interactions in the limit of a strongly localized excitation. Then, stationary discrete breathers can be found above the linear spectrum, $\Omega_b > \omega_\pi$ [396,326].

*8.2.2. The case of anisotropy in the XY plane*

Breaking the isotropy in the $xy$ plane, $J_x \neq J_y$, the $z$ component of each spin will be no longer conserved for periodic DB solutions, and the separation of time and space variables is not valid. It is still possible to find discrete breather solutions with

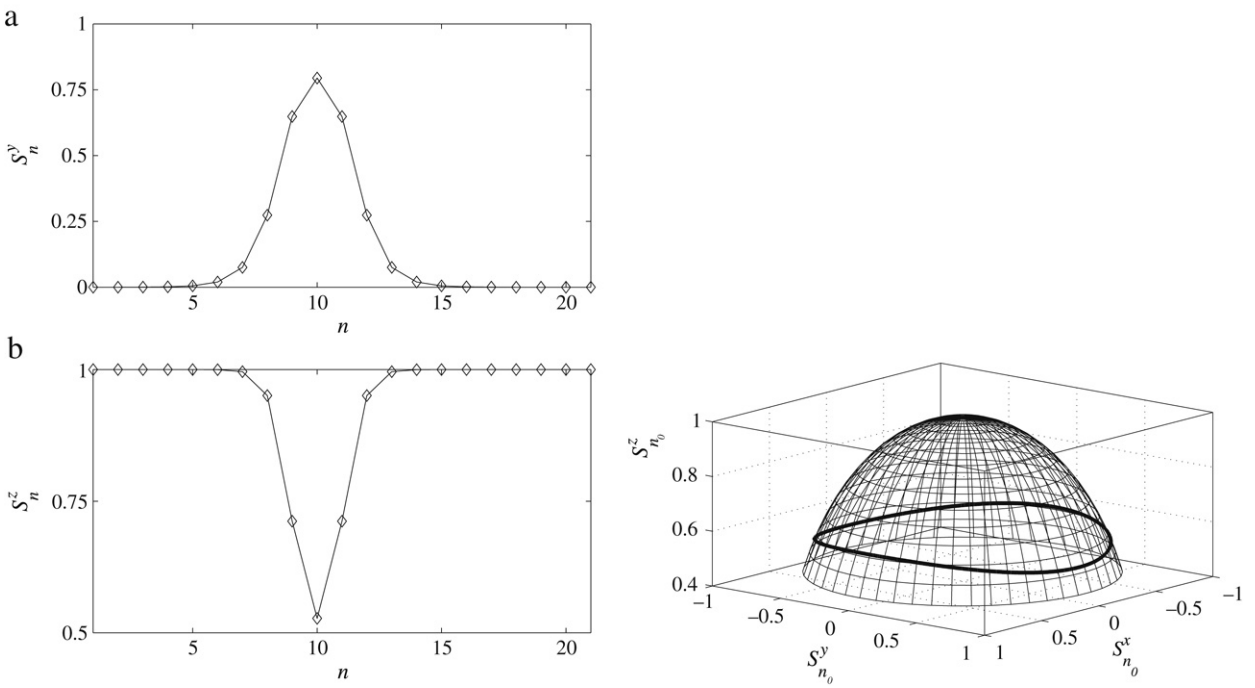


**Fig. 38.** *Left panel* — Discrete breather profile at a fixed instant of time, $J_x = 0.1, J_y = 0.23, J_z = 1, D = 0$. The $S^x_n$ component is not shown, but it a structure similar to the $S^y_n$ component. *Right panel* — Dynamics of the central spin for the DB shown in the left panel. Figures from [410].

the main frequency located inside the gap, however they involve an infinite number of higher harmonics. A rigorous proof of existence of such DB solutions has been performed by Zolotaryuk et al. [410] for the case of strong anisotropy, and later was extended to a larger range of parameters, including the case of easy-plane anisotropy discussed below, by Noble [293]. The precessions of spins around the $z$ axis are no longer symmetric, each spin draws an "elliptic" trajectory on the unit sphere, elongated towards the larger component of $J_x$ or $J_y$, see Fig. 38. The lattice is crucial for the existence of such solutions, so that one can avoid resonances of higher harmonics with the linear wave spectrum, see Section 1.3. Linear stability analysis yields that site-centered DBs are stable at least in the limit of small exchange constants (i.e. close to the anticontinuous limit), while their bond-centered counterparts are unstable [410]. This generalizes earlier results for stationary DBs [233].

### 8.3. Easy-plane anisotropy

Consider the simplest example of easy-plane anisotropy given by $J_x = J_y = J_z = J$ and $D < 0$. Without loss of generality, the ground state of the system can be assumed to be $S^x_n = 1, S^y_n = S^z_n = 0$. It is degenerated, so that the spins can be oriented arbitrarily in the $xy$ plane, but they must stay parallel to each other (ferromagnetic case). The linear dispersion law is now given by [410]

$$\omega^2(q) = J^2(1 - \cos q)^2 + 2J|D|(1 - \cos q). \tag{8.9}$$

It is acoustic-like (i.e. it has no gap), but negative $D$ implies hard anharmonicity, so that strongly localized discrete breathers (for which anharmonicity due to single-ion anisotropy dominates over that due to spin interactions) can be excited above the linear band, $\omega > \omega_\pi$ [410,293]. A discrete breather in this case corresponds to a few spins performing out-of-plane precessions around the hard $z$ axis, while the rest are precessing around the ground state (directed along the $x$ axis) with decreasing radius of precession as $n \to \pm\infty$, see Fig. 39. Two examples of highly localized (narrow) and weakly localized (wide) discrete breathers are illustrated in Fig. 40. Approaching the edge of the linear band, DBs become more delocalized, simultaneously the amplitude of precession of the central spin becomes larger. Hence, even when very close to the linear band, such DBs have a structure that has no analog in the continuum case and do not asymptotically approach the band-edge spin wave. This topological difference is the reason for the appearance of nonzero energy thresholds for these DBs [410].

Linear stability analysis yields that the site-centered DB is unstable close to the anticontinuous limit, while its bond-centered counterpart with two out-of-plane spins is stable [410]. This result is typical for FPU-type lattices with an acoustic spectrum, see Section 4.2.1. Modulational instability of extended spin waves was studied in [292].

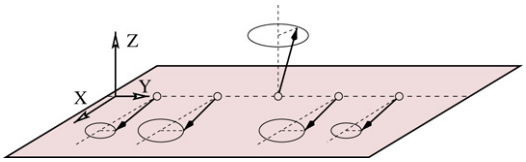


**Fig. 39.** Schematic representation of a discrete breather with one 'out-of-plane' spin in the easy-plane magnet. Figure from [410].

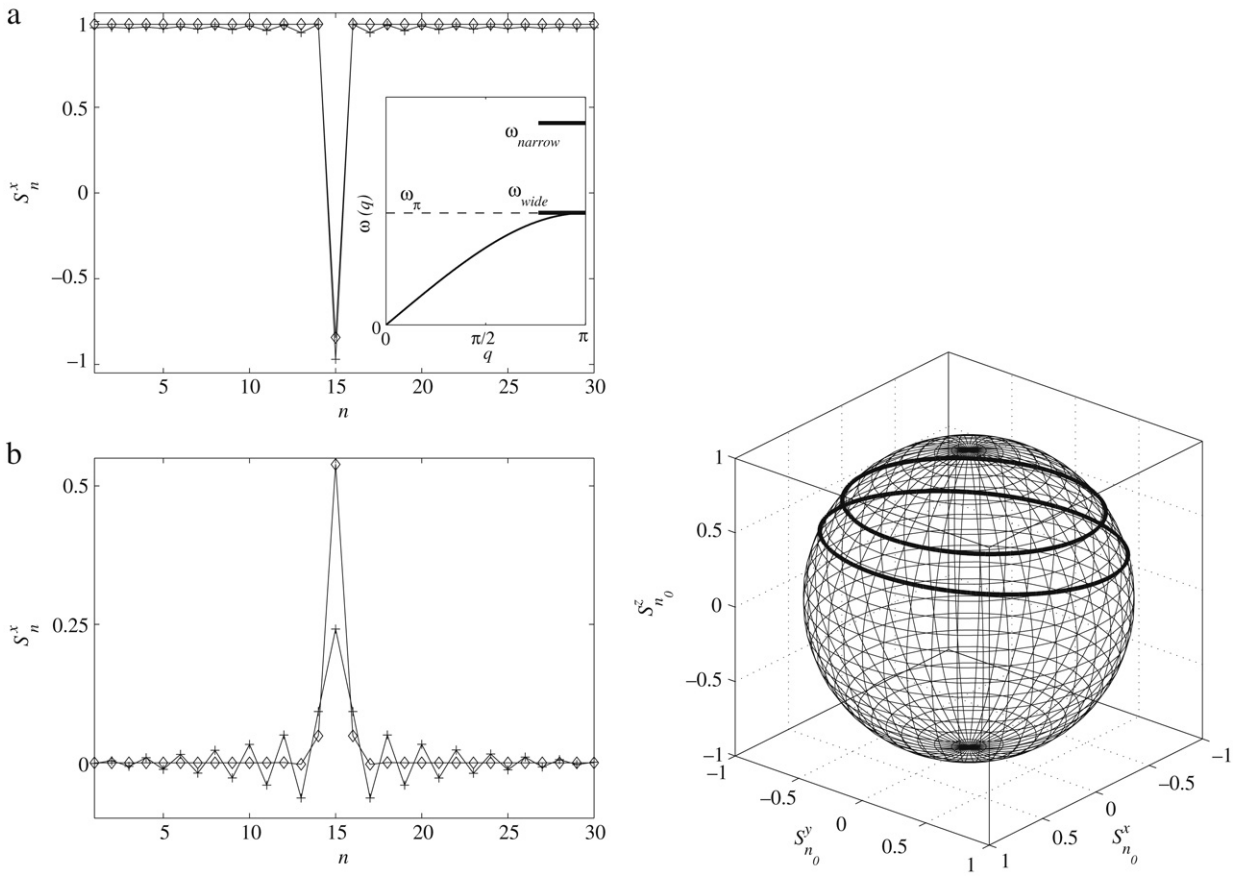


**Fig. 40.** *Left panel* — Discrete breather profile for $J = 0.1, D = -1, \omega_{\text{narrow}} = 1.1967$ (diamonds) and $\omega_{\text{wide}} = 0.6649$ (crosses). The inset shows the linear dispersion law and the location of breather frequencies. *Right panel* — Dynamics of the central spin for the two DBs shown in the left panel. The lower latitude orbit corresponds to the lower frequency DB. Figures from [410].

### *8.4. Discrete breathers in higher-dimensional spin lattices*

Finally, we mention the existence of discrete breathers in higher dimensional spin lattices, some examples of which have been discussed in Refs. [410,204] for the case of a two-dimensional ferromagnetic lattice with easy-plane anisotropy. Apparently, no stable DB with a single out-of-pane precessing spin can be found, similar to the one-dimensional case. Also different two and three out-of-plane precessing spins configurations are unstable at least close to the anticontinuous limit. Thus the simplest stable configurations found so far involve four spins [410].

## 9. Quantum breathers

A natural question is what remains of discrete breathers if the corresponding quantum problem is considered [247, 139]. The many-body Schrödinger equation is linear and translationally invariant, therefore all eigenstates must obey the Bloch theorem. Thus we cannot expect eigenstates of the Hamiltonian to be spatially localized (on the lattice). What is the correspondence between the quantum eigenvalue problem and the classical dynamical evolution?

The concept of tunneling is a possible answer to this puzzle. Naively speaking we quantize the family of periodic orbits associated with a discrete breather located somewhere on the lattice. Notice that there are as many such families as there are lattice sites. The quantization (e.g., Bohr–Sommerfeld) yields some eigenvalues. Since we can perform the same procedure with any family of discrete breather periodic orbits which differ only in their location on the lattice, we obtain $N$-fold degeneracy for every thus obtained eigenvalue, where $N$ stands for the number of lattice sites. Unless we consider the trivial case of uncoupled lattice sites, these degeneracies will be lifted. Consequently, we will instead obtain bands of states with finite band width. These bands will be called quantum breather bands. The inverse tunneling time of a semiclassical breather from one site to a neighboring one is a measure of the bandwidth.

We can then formulate the following expectation: if a classical nonlinear Hamiltonian lattice possesses discrete breathers, its quantum counterpart should show up with nearly degenerate bands of eigenstates, if the classical limit is considered. The number of states in such a band is $N$, and the eigenfunctions are given by Bloch-like superpositions of the semiclassical eigenfunctions obtained using the mentioned Bohr–Sommerfeld quantization of the classical periodic orbits. By nearly degenerate we mean that the bandwidth of a quantum breather band is much smaller than the spacing between different breather bands and the average level spacing in the given energy domain, and the classical limit implies large eigenvalues.

Another property of a quantum breather state is that such a state shows up with exponential localization in appropriate correlation functions [398]. This approach selects all many-particle bound states, no matter how deep one is in the quantum regime. In this sense quantum breather states belong to the class of many-particle bound states.

For large energies and $N$ the density of states becomes large too. What will happen to the expected quantum breather bands then? Will the hybridization with other non-breather states destroy the particle-like nature of the quantum breather, or not? What is the impact of the nonintegrability of most systems allowing for classical breather solutions? Since the quantum case corresponds to a quantization of the classical phase space, we could expect that chaotic trajectories lying nearby classical breather solutions might affect the corresponding quantum eigenstates.

From a computational point of view we are very much restricted in our abilities to study quantum breathers. Ideally we would like to study quantum properties of a lattice problem in the high energy domain (to make contact with classical states) and for large lattices. This is typically impossible, since solving the quantum problem amounts to diagonalizing the Hamiltonian matrix with rank $b^N$ where $b$ is the number of states per site, which should be large to make contact with classical dynamics. Thus typically quantum breather states have been so far obtained numerically for small one-dimensional systems [398,358,276].

### 9.1. The Bose–Hubbard chain and related models

One of the few exceptions is the quantum discrete nonlinear Schrödinger equation (also called Bose–Hubbard model) with the Hamiltonian [364]

$$H = -\sum_{l=1}^{N}\left[\frac{1}{2}a_l^\dagger a_l^\dagger a_l a_l + C(a_l^\dagger a_{l+1} + h.c.)\right] \tag{9.1}$$

and the commutation relations

$$a_l a_m^\dagger - a_m^\dagger a_l = \delta_{lm} \tag{9.2}$$

with $\delta_{lm}$ being the standard Kronecker symbol. This Hamiltonian conserves the total number of particles

$$B = \sum_l n_l, \qquad n_l = a_l^\dagger a_l. \tag{9.3}$$

For $b$ particles and $N$ sites the number of basis states is

$$\frac{(b+N-1)!}{b!(N-1)!}. \tag{9.4}$$

For $b = 0$ there is just one trivial state of an empty lattice. For $b = 1$ there are $N$ states which correspond to one-boson excitations. These states are similar to classical extended wave states. For $b = 2$ the problem is still exactly solvable, because it corresponds to a two-body problem on a lattice. A corresponding numerical solution is sketched in Fig. 41. Note the wide two-particle continuum, and a single band located below. This single band corresponds to quasiparticle states characterized by one single quantum number (related to the wavenumber $q$). These states are two-particle bound states. The dispersion of this band is given [364] by

$$E = -\sqrt{1 + 16C^2\cos^2\left(\frac{q}{2}\right)}. \tag{9.5}$$

Any eigenstate from this two-particle bound state band is characterized by exponential localization of correlations, i.e. when represented in some set of basis states, the amplitude or overlap with a basis state where the two particles are separated by some number of sites is exponentially decreasing with increasing separation distance. Note that a compact bound state

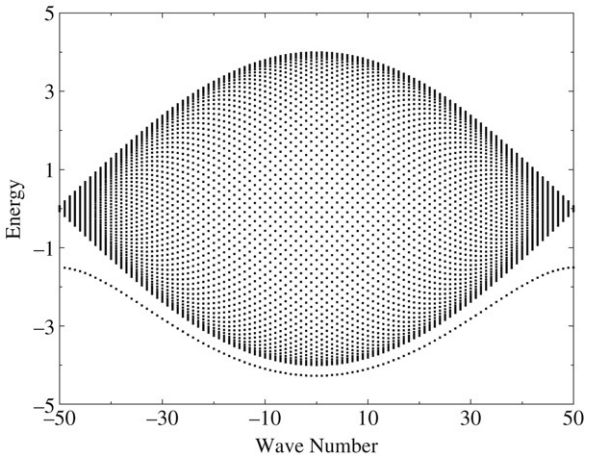


**Fig. 41.** Spectrum of the quantum DNLS with $b = 2$ and $N = 101$. The energy eigenvalues are plotted versus the wavenumber of the eigenstate. Figure from [364].

is obtained for $q = \pm\pi$, i.e. for these wave numbers basis states with nonzero separation distance do not contribute to the eigenstate at all [88].

Increasing the number of particles to $b = 3$ or larger calls for computational tools. Eilbeck [88] has recently provided updated codes in Maple in order to deal with systems with up to $b = 4$ and $N = 14$ [78], implying a Hilbert space dimension of 2380 (there are $\left(\frac{N+b-1}{b}\right)$ ways to distribute $b$ identical particles on $N$ sites). Extensions to higher-dimensional lattices are also possible [88].

Further progress was achieved by using efficient number state representations for systems without conservation of number of quanta [323,321,322,324], for systems where the effective phonon–phonon interaction comes through an electron–phonon interaction [397], for various models of molecular lattices [320,319,97], and for broken translational symmetry [90].

While these studies revealed a lot of new structures of the corresponding spectra, we still have to wait for more systematic studies. Since the classical limit is still not easily reachable for these large systems, we will mainly discuss in the next sections systematic studies of small systems, which allow one to boost the energies into the semiclassical domain.

### 9.2. The dimer

A series of papers was devoted to the properties of the quantum dimer [35,36,22,191]. This system describes the dynamics of bosons fluctuating between two sites. The number of bosons is conserved, and together with the conservation of energy the system appears to be integrable. Of course, one cannot consider spatial localization in such a model. However, a reduced form of the discrete translational symmetry — namely the permutational symmetry of the two sites — can be imposed. Together with the addition of nonlinear terms in the classical equations of motion the dimer allows for classical trajectories which are not invariant under permutation. The phase space can be completely analyzed, all isolated periodic orbits can be found. There appears exactly one bifurcation on one family of isolated periodic orbits, which leads to the appearance of a separatrix in phase space. The separatrix separates three regions — one invariant and two non-invariant under permutations. The subsequent analysis of the quantum dimer demonstrated the existence of pairs of eigenstates with nearly equal eigenenergies [35]. The separatrix and the bifurcation in the classical phase space can be traced in the spectrum of the quantum dimer [22].

The classical Hamiltonian may be written as

$$H = \Psi_1^*\Psi_1 + \Psi_2^*\Psi_2 + \frac{1}{2}\left((\Psi_1^*\Psi_1)^2 + (\Psi_2^*\Psi_2)^2\right) + C\left(\Psi_1^*\Psi_2 + \Psi_2^*\Psi_1\right) \tag{9.6}$$

with the equations of motion $\dot{\Psi}_{1,2} = \mathrm{i}\partial H/\partial\Psi_{1,2}^*$. The model conserves the norm (or number of particles) $B = |\Psi_1|^2 + |\Psi_2|^2$.

Let us parameterize the phase space of (9.6) with $\Psi_{1,2} = A_{1,2}\mathrm{e}^{\mathrm{i}\phi_{1,2}}$, $A_{1,2} \geq 0$. It follows that $A_{1,2}$ is time independent and $\phi_1 = \phi_2 + \Delta$ with $\Delta = 0, \pi$ and $\dot{\phi}_{1,2} = \omega$ being also time independent. Solving the algebraic equations for the amplitudes of the IPOs we obtain

$$\mathrm{I}: A_{1,2}^2 = \frac{1}{2}B, \qquad \Delta = 0, \qquad \omega = 1 + C + \frac{1}{2}B, \tag{9.7}$$

$$\mathrm{II}: A_{1,2}^2 = \frac{1}{2}B, \qquad \Delta = \pi, \qquad \omega = 1 - C + \frac{1}{2}B, \tag{9.8}$$

$$\mathrm{III}: A_1^2 = \frac{1}{2}B\left(1 \pm \sqrt{1 - 4C^2/B^2}\right), \qquad \Delta = 0, \qquad \omega = 1 + B. \tag{9.9}$$

IPO III corresponds to two elliptic solutions which break the permutational symmetry. IPO III exists for $B \geq B_b$ with $B_b = 2C$ and occurs through a bifurcation from IPO I. The corresponding separatrix manifold is uniquely defined by the energy of IPO I at a given value of $B \geq B_b$. This manifold separates three regions in phase space — two with symmetry broken solutions, each one containing one of the IPOs III, and one with symmetry conserving solutions containing the elliptic IPO II. The separatrix manifold itself contains the hyperbolic IPO I. For $B \leq B_b$ only two IPOs exist — IPO I and II, with both of them being of elliptic character. Remarkably there exist no other IPOs, and the mentioned bifurcation and separatrix manifolds are the only ones present in the classical phase space of (9.6).

To conclude the analysis of the classical part, we list the energy properties of the different phase space parts separated by the separatrix manifold. First it is straightforward to show that the IPOs (9.7)–(9.9) correspond to maxima, minima or saddle points of the energy in the allowed energy interval for a given value of $B$, with no other extrema or saddle points present. It follows

$$E_1 = H(\text{IPO I}) = B + \frac{1}{4}B^2 + CB, \tag{9.10}$$

$$E_2 = H(\text{IPO II}) = B + \frac{1}{4}B^2 - CB, \tag{9.11}$$

$$E_3 = H(\text{IPO III}) = B + \frac{1}{2}B^2 + C^2. \tag{9.12}$$

For $B < B_b$ we have $E_1 > E_2$ (IPO I — maximum, IPO II — minimum). For $B \geq B_b$ it follows $E_3 > E_1 > E_2$ (IPO III — maxima, IPO I — saddle, IPO II — minimum). If $B < B_b$, then all trajectories are symmetry conserving. If $B \geq B_b$, then trajectories with energies $E_1 < E \leq E_3$ are symmetry breaking, and trajectories with $E_2 \leq E \leq E_1$ are symmetry conserving.

The quantum eigenvalue problem amounts to replacing the complex functions $\Psi$, $\Psi^*$ in (9.6) by the boson annihilation and creation operators $a, a^\dagger$ with the standard commutation relations (to enforce the invariance under the exchange $\Psi \Leftrightarrow \Psi^*$ the substitution has to be done on rewriting $\Psi\Psi^* = 1/2(\Psi\Psi^* + \Psi^*\Psi)$):

$$H = \frac{5}{4} + \frac{3}{2}\left(a_1^\dagger a_1 + a_2^\dagger a_2\right) + \frac{1}{2}\left((a_1^\dagger a_1)^2 + (a_2^\dagger a_2)^2\right) + C\left(a_1^\dagger a_2 + a_2^\dagger a_1\right). \tag{9.13}$$

Note that $\hbar = 1$ here, and the eigenvalues $b$ of $B = a_1^\dagger a_1 + a_2^\dagger a_2$ are integers. Since $B$ commutes with $H$ we can diagonalize the Hamiltonian in the basis of eigenfunctions of $B$. Each value of $b$ corresponds to a subspace of the dimension $(b+1)$ in the space of eigenfunctions of $B$. These eigenfunctions are products of the number states $|n\rangle$ of each degree of freedom and can be characterized by a symbol $|n, m\rangle$ with $n$ bosons in the site 1 and $m$ bosons in the site 2. For a given value of $b$ it follows $m = b - n$. So we can actually label each state by just one number $n$: $|n, (b-n)\rangle \equiv |n\rangle$. Consequently the eigenvalue problem at fixed $b$ amounts to diagonalizing the matrix

$$H_{nm} = \begin{cases} \frac{5}{4} + \frac{3}{2}b + \frac{1}{2}\left(n^2 + (b-n)^2\right) & n = m \\ C\sqrt{n(b+1-n)} & n = m+1 \\ C\sqrt{(n+1)(b-n)} & n = m-1 \\ 0 & \text{else} \end{cases} \tag{9.14}$$

where $n, m = 0, 1, 2, \ldots, b$. Notice that the matrix $H_{nm}$ is a symmetric band matrix. The additional symmetry $H_{nm} = H_{(b-n),(b-m)}$ is a consequence of the permutational symmetry of $H$. For $C = 0$ the matrix $H_{nm}$ is diagonal, with the property that each eigenvalue is doubly degenerate (except for the state $|b/2$ for even values of $b$). The classical phase space contains only symmetry broken trajectories, with the exception of IPO II and the separatrix with IPO I (in fact in this limit the separatrix manifold is nothing but a resonant torus containing both IPOs I and II). With the exception of the separatrix manifold, all tori break permutational symmetry and come in two groups separated by the separatrix. Then quantizing each group will lead to pairs of degenerate eigenvalues — one from each group. There is a clear correspondence to the spectrum of the diagonal ($C = 0$) matrix $H_{nm}$. The eigenvalues $H_{00} = H_{bb}$ correspond to the quantized IPOs III. With increasing $n$ the eigenvalues $H_{nn} = H_{(b-n),(b-n)}$ correspond to quantized tori further away from the IPO III. Finally the states with $n = b/2$ for even $b$ or $n = (b-1)/2$ for odd $b$ are the tori most close to the separatrix. Switching the side diagonals on by increasing $C$ will lead to a splitting of all pairs of eigenvalues. In the case of small values of $b$ these splittings have no correspondence to classical system properties. However, in the limit of large $b$ we enter the semiclassical regime, and due to the integrability of the system, eigenfunctions should correspond to tori in the classical phase space which satisfy the Einstein–Brillouin–Keller quantization rules. Increasing $C$ from zero will lead to a splitting $\Delta E_n$ of the eigenvalue doublets of $C = 0$. In other words, we find pairs of eigenvalues, which are related to each other through the symmetry of their eigenvectors and (for small enough $C$) through the small value of the splitting. These splittings have been calculated numerically and using perturbation theory [35,22]. In the limit of large $b$ the splittings are exponentially small for energies above the classical separatrix energy

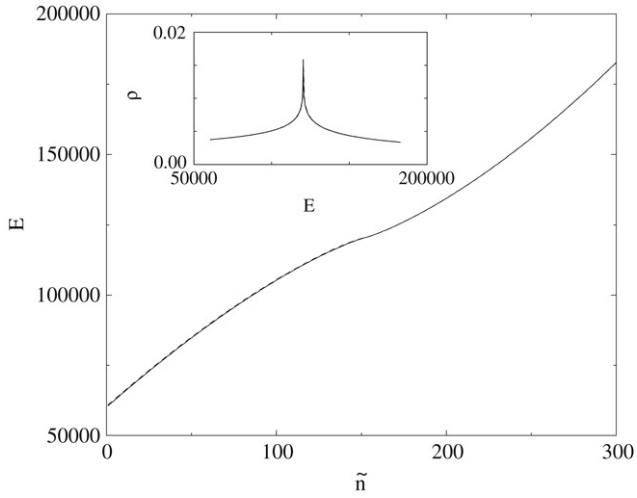


**Fig. 42.** Eigenvalues versus ordered state number $\tilde{n}$ for symmetric and antisymmetric states ($0 < \tilde{n} < b/2$ for both types of states). Parameters: $b = 600$ and $C = 50$. Inset: Density of states versus energy. Figure from [22].

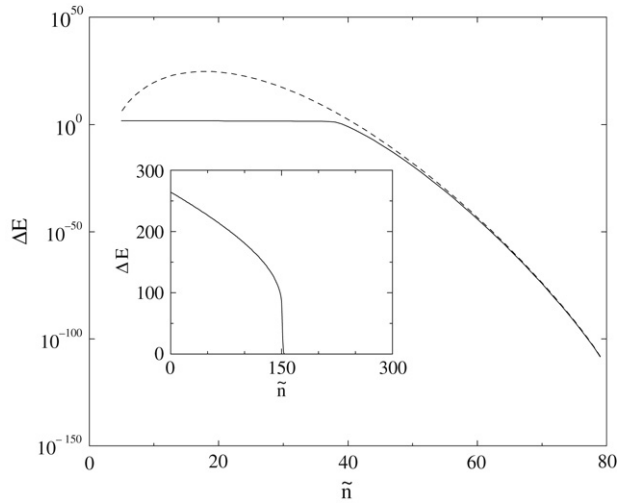


**Fig. 43.** Eigenvalue splittings versus $\tilde{n}$ for $b = 150$ and $C = 10$. Solid line — numerical result, dashed line — perturbation theory. Inset: Same for $b = 600$ and $C = 50$. Only numerical results are shown. Figure from [22].

(i.e. for classical trajectories which are not invariant under permutation). If the eigenenergies are lowered below the classical separatrix energy, the splittings grow rapidly up to the mean level spacing.

In Fig. 42 the results of a diagonalization of a system with 600 particles ($b = 600$) is shown [22]. The inset shows the density of states versus energy, which nicely confirms the predicted singularity at the energy of the separatrix of the classical counterpart. In order to compute the exponentially small splittings, we may use e.g. a Mathematica routine which allows one to choose arbitrary values for the precision of computations. Here we chose precision 512. In Fig. 43 the numerically computed splittings are compared to perturbation theory results. As expected, the splittings become extremely small above the separatrix. Consequently these states will follow for a long time the dynamics of a classical broken symmetry state.

### 9.3. The trimer

The integrability of the dimer does not allow a study of the influence of chaos (i.e. nonintegrability) on the tunneling properties of the mentioned pairs of eigenstates. A natural extension of the dimer to a trimer adds a third degree of freedom without adding a new integral of motion. Consequently the trimer is nonintegrable. A still comparatively simple numerical quantization of the trimer allows a study of the behavior of many tunneling states in the large-energy domain of the eigenvalue spectrum [117].

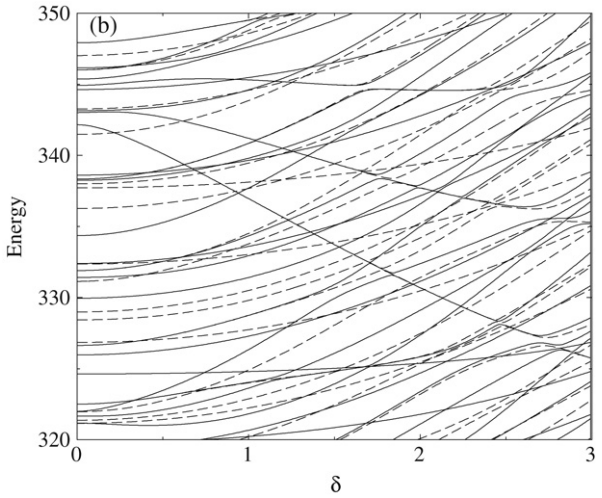


**Fig. 44.** A part of the eigenenergy spectrum of the quantum trimer as a function of $\delta$ with $b = 40$ and $C = 2$. Lines connect data points for a given state. Solid lines — symmetric eigenstates; thick dashed lines — antisymmetric eigenstates. Figure from [117].

Similarly to the dimer, the quantum trimer Hamiltonian is represented in the form

$$H = \frac{15}{8} + \frac{3}{2}(a_1^\dagger a_1 + a_2^\dagger a_2 + a_3^\dagger a_3) + \frac{1}{2}\left[(a_1^\dagger a_1)^2 + (a_2^\dagger a_2)^2\right] + C(a_1^\dagger a_2 + a_2^\dagger a_1) + \delta(a_1^\dagger a_3 + a_3^\dagger a_1 + a_2^\dagger a_3 + a_3^\dagger a_2). \tag{9.15}$$

Again $B = a_1^\dagger a_1 + a_2^\dagger a_2 + a_3^\dagger a_3$ commutes with the Hamiltonian, thus we can diagonalize (9.15) in the basis of eigenfunctions of $B$. For any finite eigenvalue $b$ of $B$ the number of states is finite, namely $(b+1)(b+2)/2$. Thus the infinite dimensional Hilbert space separates into an infinite set of finite dimensional subspaces, each subspace containing only vectors with a given eigenvalue $b$. These eigenfunctions are products of the number of states $|n\rangle$ of each degree of freedom and can be characterized by a symbol $|n, m, l\rangle$ where we have $n$ bosons on site 1, $m$ bosons on site 2, and $l$ bosons on site 3. For a given value $b$ it follows that $l = b - m - n$. So we can actually label each state by just two numbers $(n, m)$: $|n, m, (b - n - m)\rangle \equiv |n, m\rangle$. Note that the third site added to the dimer is different from the first two sites. There is no boson–boson interaction on this site. Thus site 3 serves simply as a boson reservoir for the dimer. Dimer bosons may now fluctuate from the dimer to the reservoir. The trimer has the same permutational symmetry as the dimer.

The matrix elements of (9.15) between states from different $b$ subspaces vanish. Thus for any given $b$ the task amounts to diagonalizing a finite dimensional matrix. The matrix has a tridiagonal block structure, with each diagonal block being a dimer matrix (9.14). The nonzero off-diagonal blocks contain interaction terms proportional to $\delta$. We consider symmetric $|\Psi\rangle_s$ and antisymmetric $|\Psi\rangle_a$ states. The structure of the corresponding symmetric and antisymmetric decompositions of $H$ is similar to $H$ itself. In the following we will present results for $b = 40$. We will also drop the first two terms of the RHS in (9.15), because these only lead to a shift of the energy spectrum. Since we evaluate the matrix elements explicitly, we need only a few seconds to obtain all eigenvalues and eigenvectors with the help of standard Fortran routines. In Fig. 44 we plot a part of the energy spectrum as a function of $\delta$ for $C = 2$ [117]. As discussed above, the Hamiltonian decomposes into noninteracting blocks for $\delta = 0$, each block corresponding to a dimer with a boson number between 0 and $b$. For $\delta \neq 0$ the block–block interaction leads to typical features in the spectrum, like, e.g., avoided crossings. The full quantum energy spectrum extends roughly over $10^3$, which implies an averaged spacing of order $10^0$. Also the upper third of the spectrum is diluted compared to the lower two thirds. The correspondence to the classical model is obtained with the use of the transformation $E_{cl} = E_{qm}/b^2 + 1$ and for parameters $C/b$ and $\delta/b$ (the classical value for $B$ is $B = 1$).

The main result of this computation so far is that tunneling pairs of eigenstates of the dimer persist in the nonintegrable regime $\delta \neq 0$. However at certain pair-dependent values of $\delta$ a pair breaks up. From the plot in Fig. 44 we cannot judge how the pair splittings behave. In Fig. 45 we plot the pair splitting of the pair which has energy $\approx 342$ at $\delta = 0$ [120]. Denote with $x, y, z$ the eigenvalues of the site number operators $n_1, n_2, n_3$. We may consider the quantum states of the trimer at $\delta = 0$ when $z$ is a good quantum number and then follow the evolution of these states with increasing $\delta$. The state for $\delta = 0$ can be traced back to $C = 0$ and be thus characterized in addition by $x$ and $y$. The chosen pair states are then characterized by $x = 26(0), y = 0(26)$ and $z = 14$ for $C = \delta = 0$. Note that this pair survives approximately 30 avoided crossings before it is finally destroyed at coupling strength $\delta \approx 2.67$ as seen in Fig. 44.

From Fig. 45 we find that the splitting rapidly increases gaining about eight orders of magnitude when $\delta$ changes from 0 to slightly above 0.5. Then this rapid but nevertheless smooth rise is interrupted by very sharp spikes when the splitting $\Delta E$ rises by several orders of magnitude with $\delta$ changing by mere percents and then abruptly changes in the opposite direction sometimes even overshooting its pre-spike value. Such spikes, some larger, some smaller, repeat with increasing $\delta$ until

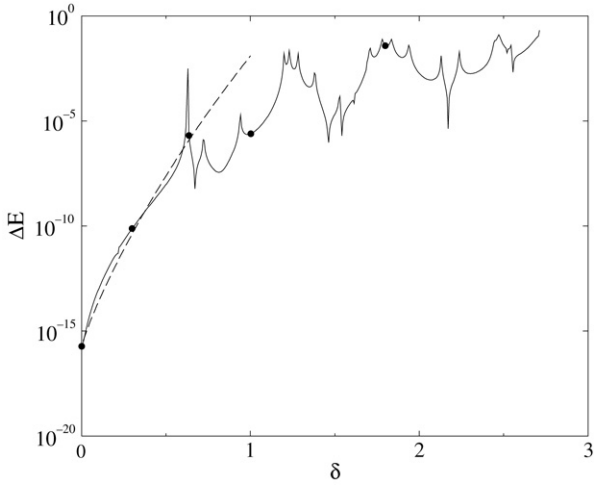


**Fig. 45.** Level splitting versus $\delta$ for a level pair as described in the text. Solid line — numerical result. Dashed line — semiclassical approximation. Filled circles — location of wave function analysis in Fig. 46. Figure from [120].

the splitting value approaches the mean level spacing (of order one in the figure). Only then one may say that the pair is destroyed since it can be hardly distinguished among the other trimer levels.

Another observation is presented in Fig. 46 [120]. We plot the intensity distribution of the logarithm of the squared symmetric wave function of our chosen pair for five different values of $\delta = 0, 0.3, 0.636, 1.0, 1.8$ (their locations are indicated by filled circles in Fig. 45). We use the eigenstates of $B$ as basis states. They can be represented as $|x, y, z>$ where $x, y, z$ are the particle numbers on sites 1, 2, 3, respectively. Due to the commutation of $B$ with $H$ two site occupation numbers are enough if the total particle number is fixed. Thus the final encoding of states (for a given value of $b$) can be chosen as $|x, z$. The abscissa in Fig. 46 is $x$ and the ordinate is $z$. Thus the intensity plots provide us with information about the order of particle flow in the course the tunneling process. For $\delta = 0$ (Fig. 46(a)) the only possibility for the 26 particles on site 1 is to directly tunnel to site 2. Site 3 is decoupled with its 14 particles not participating in the process. The squared wave function takes the form of a compact rim in the $(x, z)$ plane which is parallel to the $x$ axis. Nonzero values of the wave function are observed only on the rim. This direct tunneling has been described in chapter 9.2. When switching on some nonzero coupling to the third site, the particle number on the dimer (sites 1, 2) is no longer conserved. The third site serves as a particle reservoir which is able either to collect particles from or supply particles to the dimer. This coupling will allow for nonzero values of the wave function away from the rim. But most importantly, it will change the shape of the rim. We observe that the rim is bent down to smaller $z$ values with increasing $\delta$. That implies that the order of tunneling (when, e.g., going from large to small $x$ values) is as follows: first, some particles tunnel from site 1 to site 2 and simultaneously from site 3 to site 2 (Fig. 47(a)). Afterwards particles flow from site 1 to both sites 2 and 3 (Fig. 47(b)). With increasing $\delta$ the structure of the wave function intensity becomes more and more complex, possibly revealing information about the classical phase space flow structure. Thus we observe three intriguing features. First, the tunneling splitting increases by eight orders of magnitude when $\delta$ increases from zero to 0.5. This seems to be unexpected, since at those values perturbation theory in $\delta$ should be applicable (at least Fig. 44 indicates that this should be true for the levels themselves). The semiclassical explanation of this result was obtained in [120].

The second observation is that the tunneling begins with a flow of particles from the bath (site 3) directly to the empty site which is to be filled (with simultaneous flow from the filled dimer site to the empty one). At the end of the tunneling process the initially filled dimer site is giving particles back to the bath site. Again this is an unexpected result, since it implies that the particle number on the dimer is increasing during the tunneling, which seems to decrease the tunneling probability, according to the results for an isolated dimer. These first two results are closely connected (see [120] for a detailed explanation).

The third result concerns the resonant structure on top of the smooth variation in Fig. 45. The resonant enhancements and suppressions of tunneling are related to avoided crossings. Their presence implies that a fine tuning of the system parameters may strongly suppress or enhance tunneling which may be useful for spectroscopic devices. In Fig. 48 we show the four various possibilities of avoided crossings between a pair and a single level and between two pairs, and the schematic outcome for the tunneling splitting [120]. If the interaction to further more distant states in the spectrum is added, the tunneling splitting can become exactly zero [315] for some specific value of the control parameter. In such a rare situation the tunneling is suppressed for all times.

### *9.4. Quantum roto-breathers*

When discussing classical breather solutions we have been touching some aspects of roto-breathers, including their property of being not invariant under time reversal symmetry. In a recent study Dorignac et al. have performed [79] an

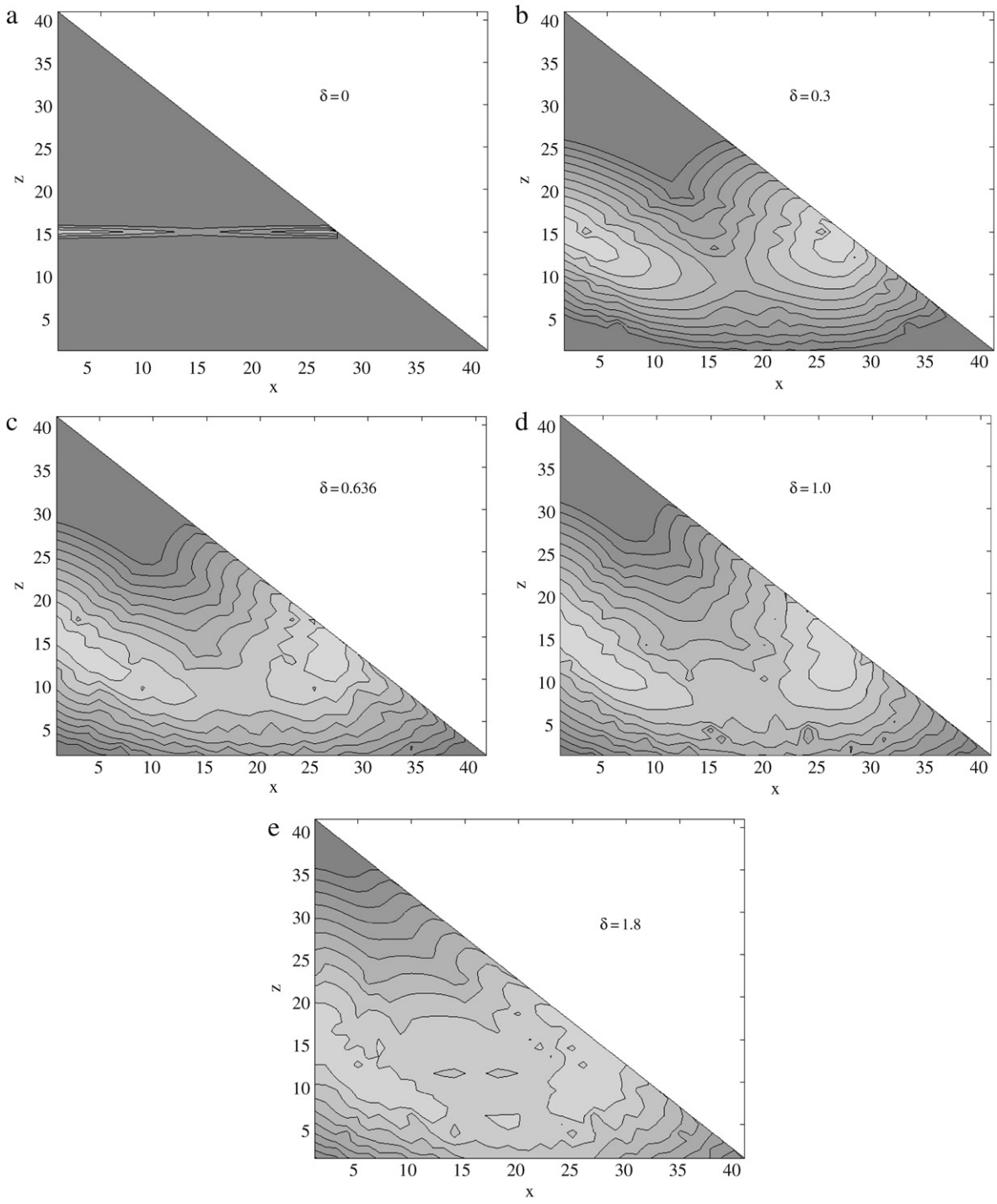


**Fig. 46.** Contour plot of the logarithm of the symmetric eigenstate of the chosen tunneling pair (cf. Fig. 44) for five different values of $\delta = 0, 0.3, 0.636, 1.0, 1.8$ (their location is indicated by filled circles in Fig. 45). (a): three equidistant grid lines are used; (b)–(e): ten grid lines are used. Minimum value of squared wave function is $10^{-30}$, maximum value is about 1. Figure from [120].

analysis of the corresponding quantum roto-breather properties in a dimer with the Hamiltonian

$$H = \sum_{i=1}^{2} \left\{ \frac{p_i^2}{2} + \alpha(1 - \cos x_i) \right\} + \varepsilon(1 - \cos(x_1 - x_2)). \tag{9.16}$$

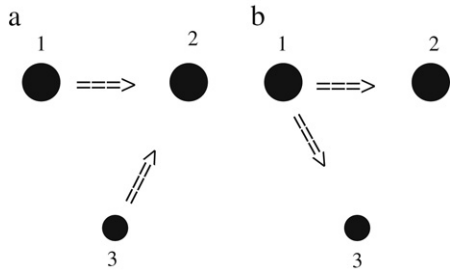


**Fig. 47.** Order of tunneling in the trimer. Filled large circles — sites 1 and 2, filled small circle — site 3. Arrows indicate direction of transfer of particles. Figure from [120].

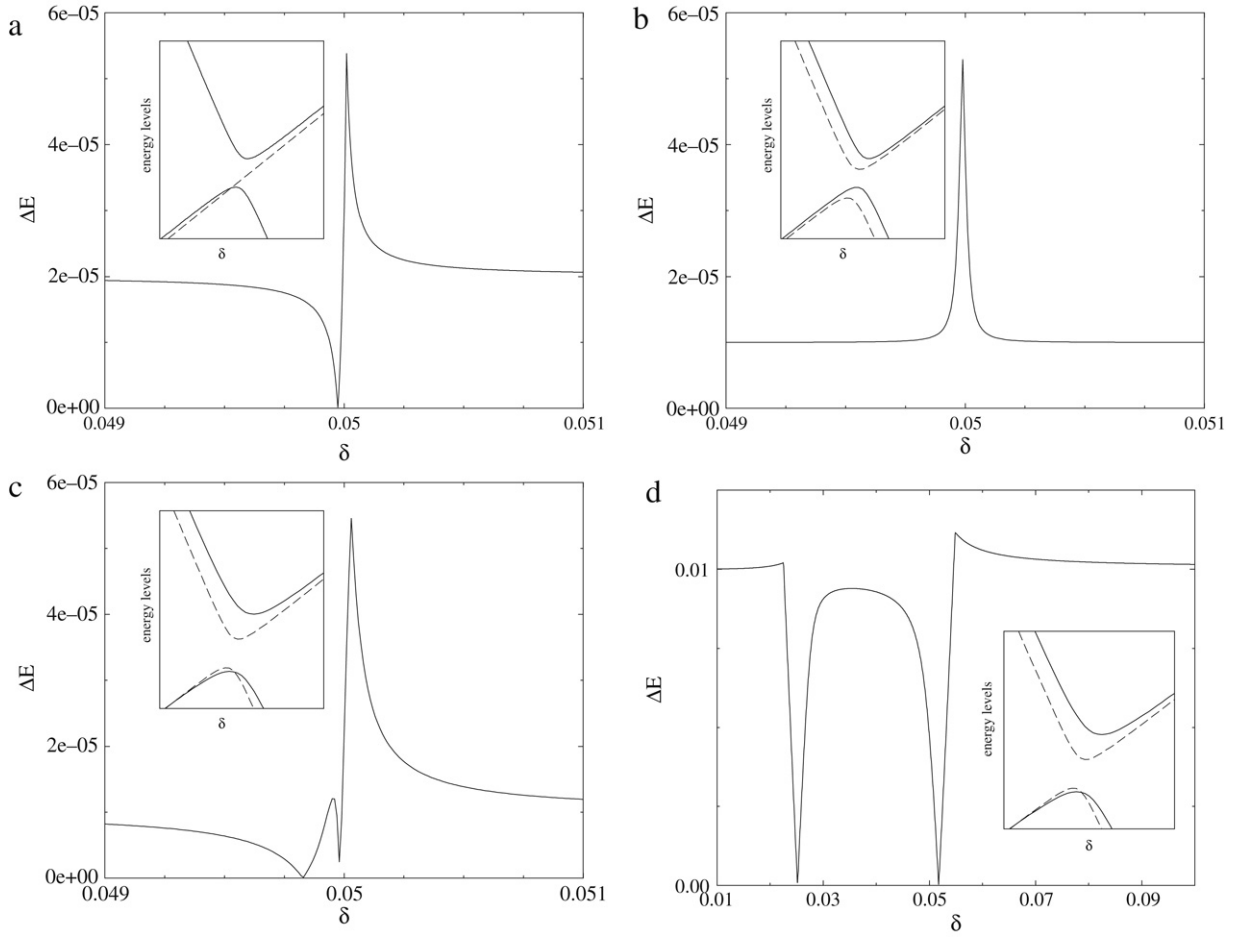


**Fig. 48.** Level splitting variation at avoided crossings. Inset: Variation of individual eigenvalues participating in the avoided crossing. Solid lines — symmetric eigenstates, dashed lines — antisymmetric eigenstates. Figure from [120].

The classical roto-breather solution consists of one pendulum rotating and the other oscillating with a given period $T_b$. Since the model has two symmetries – permutation of the indices and time-reversal symmetry – which may be both broken by classical trajectories, the irreducible representations of quantum eigenstates contain four symmetry sectors (with possible combinations of symmetric or antisymmetric states with respect to the two symmetry operations). Consequently, a quantum roto-breather state belongs to a quadruplet of weakly split states rather than to a pair as discussed above. The schematic representation of the appearance of such a quadruplet is shown in Fig. 49 [79]. The obtained quadruplet has an additional fine structure as compared to the tunneling pair of the above considered dimer and trimer. The four levels in the quadruplet define three characteristic tunneling processes. Two of them are energy or momentum transfer from one pendulum to the other one, while the third one corresponds to total momentum reversal (which restores time reversal symmetry). The dependence of the corresponding tunneling rates on the coupling $\varepsilon$ is shown for a specific quadruplet from [79] in Fig. 50. For

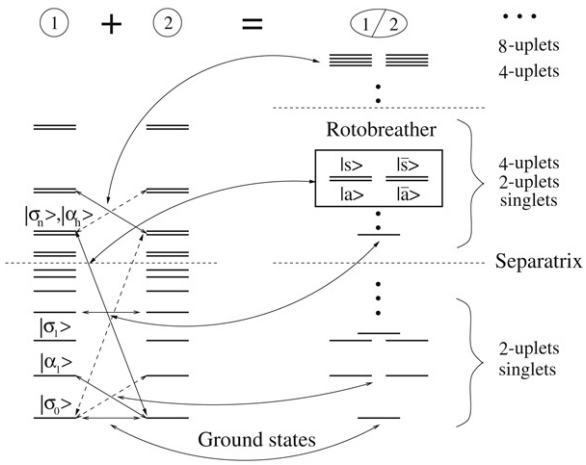


**Fig. 49.** Schematic representation of the sum of two pendula spectra. Straight solid arrows indicate the levels to be added and dashed arrows the symmetric (permutation) operation. The result is indicated in the global spectrum by a curved arrow. The construction of the quantum roto-breather state is explicitly represented. Figure from [79].

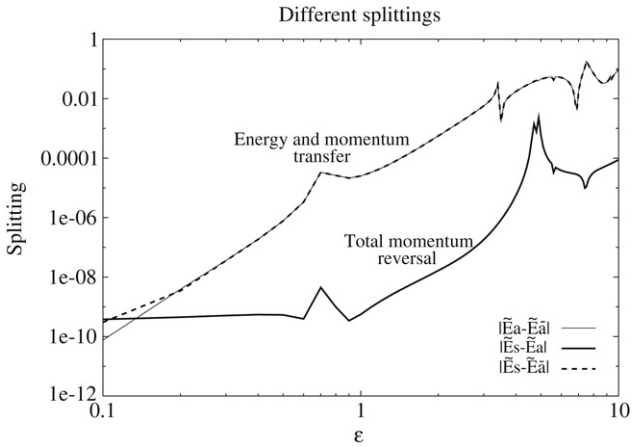


**Fig. 50.** Dependence of different splittings of a quadruplet on $\varepsilon$. Only three of them have been displayed, each being associated with a given tunneling process. Figure from [79].

very weak coupling $\varepsilon \ll 1$ the fastest tunneling process will be momentum reversal, since tunneling between the pendula is blocked. However as soon as the coupling is increased, the momentum reversal becomes the slowest process, with breather tunneling from one pendulum to the other one being orders of magnitude faster. Note that again resonant features on these splitting curves are observed, which are related to avoided crossings.

### *9.5. Large lattices with fluctuating numbers of quanta*

A number of publications are devoted to the properties of quantum breathers in chains and two-dimensional lattices of coupled anharmonic oscillators. For the respective one-dimensional case, the Hamiltonian is given by

$$H = \sum_n \left[ \frac{1}{2} p_n^2 + V(x_n) + W(x_n - x_{n-1}) \right]. \tag{9.17}$$

Here $V(x) = \frac{1}{2}x^2 + \frac{1}{4}v_4 x^4$ (or similar) and the nearest neighbour coupling $W(x) = \frac{1}{2}Cx^2$. The classical version of such models conserves only the energy, but not any equivalent of a norm. Therefore, no matter whether one uses creation and annihilation operators of the harmonic oscillator [321], or similar operators which diagonalize the single anharmonic oscillator problem [322], the resulting Hamiltonian matrix will not commute with the corresponding number operator. Calculations will typically be restricted to 4–6 quanta, and lattice sizes of the order of 30 for $d = 1$, $13 \times 13$ for $d = 2$ [321]. With these parameters one can calculate properties of quantum breather states, which correspond to typically two quanta which are bound (with unavoidable states with different number of quanta, contributing as well). For large enough $v_4$ a

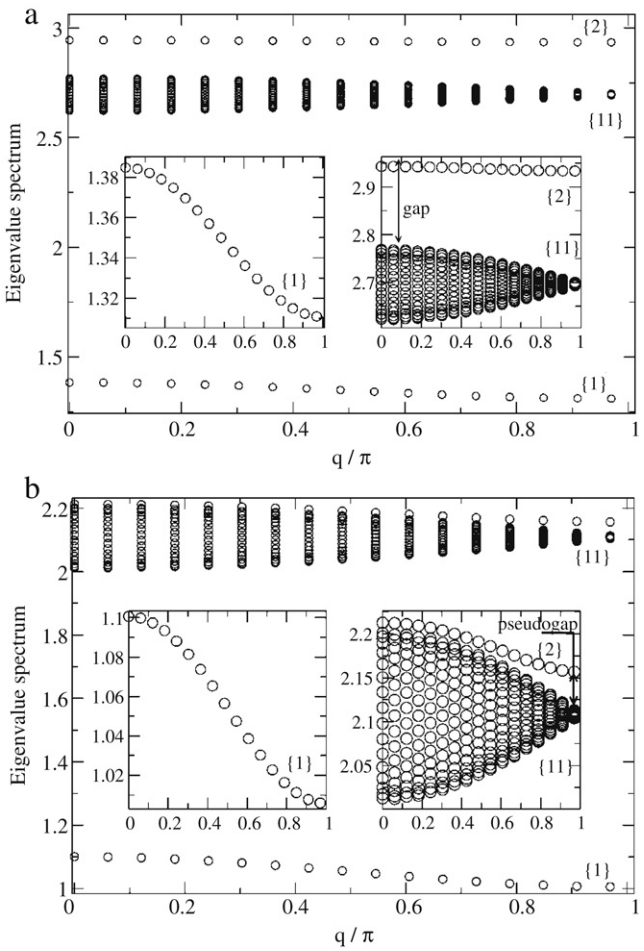


**Fig. 51.** Eigenspectrum of a chain with 33 sites for parameters (a) $C = 0.05$, $v_4 = 0.2$, and (b) $C = 0.05$, $v_4 = 0.02$. The inserts show magnifications of the fundamental branch (left) and overtone region (right). The quantum breather branch is marked by (2), and the two-phonon band by (11). Figure from [321].

complete gap opens between the two-quanta continuum and quantum breather states [398,321] (Figs. 51 and 52). When decreasing the anharmonic constant $v_4$, Proville found, that the gap closes for certain wave numbers, but persists for others, becoming a pseudogap [323,321] (Fig. 51).

Involved calculations of the dynamical structure factor (e.g. available by neutron scattering in crystals) have shown, that signatures of quantum breathers are imprinted in these integral characteristics of the underlying lattice dynamics [398,322], yet the working out of these differences may become a subtle task (see Fig. 53 for an example).

Finally, Fleurov et al. [140] estimated the influence of the tunnel splitting of a dimer, when embedded in an infinite chain. This situation is close to the tunneling of a very localized DB, so that the nonlinearity (interaction between bosons) can be taken into account only on the two sites, which participate in the tunneling, while the nonlinearity can be neglected on all other sites. Using path integral techniques, the computed tunneling splitting has been shown to become smaller as compared to the case of an isolated dimer. This is due to the fact, that a DB in an infinite chain has a core and a localized tail. That tail has to be carried through the tunneling process as well, and in analogy with a single particle tunneling in a double well, the tail increases the effective mass of such a particle. Consequently the exponential tail of a DB in an infinite chain tends to decrease its ability to perform quantum tunneling motion, yet it never leads to a full suppression of tunneling [140].

### *9.6. Evolution of quantum localized states*

Suppose that we initially excite only one site in the trimer from above. If this initial state has strong enough overlap with tunneling pair eigenstates, its evolution in time should show distinct properties as compared to the case when the overlap is vanishing, or when there are simply no tunneling pair states available. Several results have been reported. First, a quantum echo was observed in [117] by calculating the survival probability of the initial state as a function of time. That quantity measures the probability to find the system in the initial state at later times. If the initial state has strong overlap with

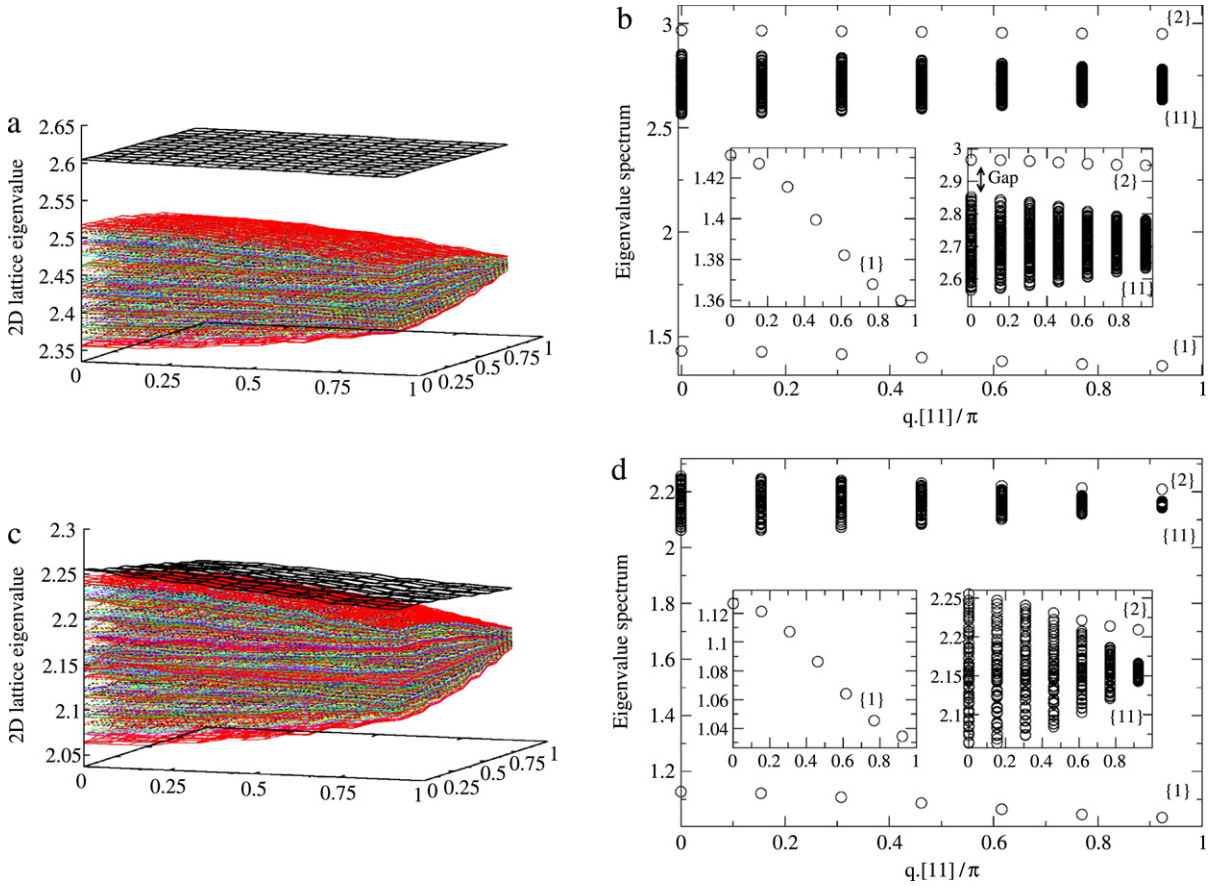


**Fig. 52.** Eigenspectrum of a lattice with $13 \times 13$ sites for parameters (top) $C = 0.025$, $v_4 = 0.1$, and (bottom) $C = 0.025$, $v_4 = 0.025$. Left plots — spectra over the whole Brillioin zone. Right plots — profiles of the spectra along the direction [11]. The insets show the magnifications of the phonon branch (left) and the quantum breather energy region (right). Figure from [321].

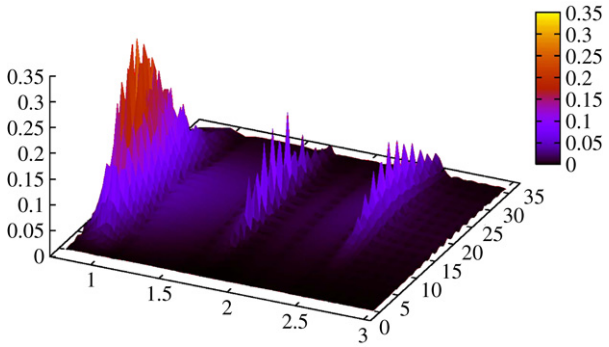

**Fig. 53.** A 3D plot of the inelastic structure factor $S(q, \omega)$ as a function of the dimensionless energy transfer $0 \leq \omega \leq 3$ and the scalar product of the transfer momentum **q** and the polarization **u**. Figure from [322].

many eigenstates, it is expected to quickly decohere into these different states. Yet, if a substantial overlap with quantum breathers takes place, the survival probability first rapidly decays to zero, but cycles after regular time intervals (Fig. 54, left plot). If one simply measures the dependence of the number of quanta, then a similar situation will show up with a very slow beating of the occupation numbers in time, if the overlap of the initial state and a tunneling pair is strong [315,192] (see Fig. 54, right plot).

Recent studies of Pinto et al. [317,316] deal with quantum breather excitations in two capacitively coupled Josephson junctions. Such systems are currently under experimental investigation, being candidates for quantum information processing, and show remarkably long coherence times up to 100 ns for few quanta excitations. The system does not

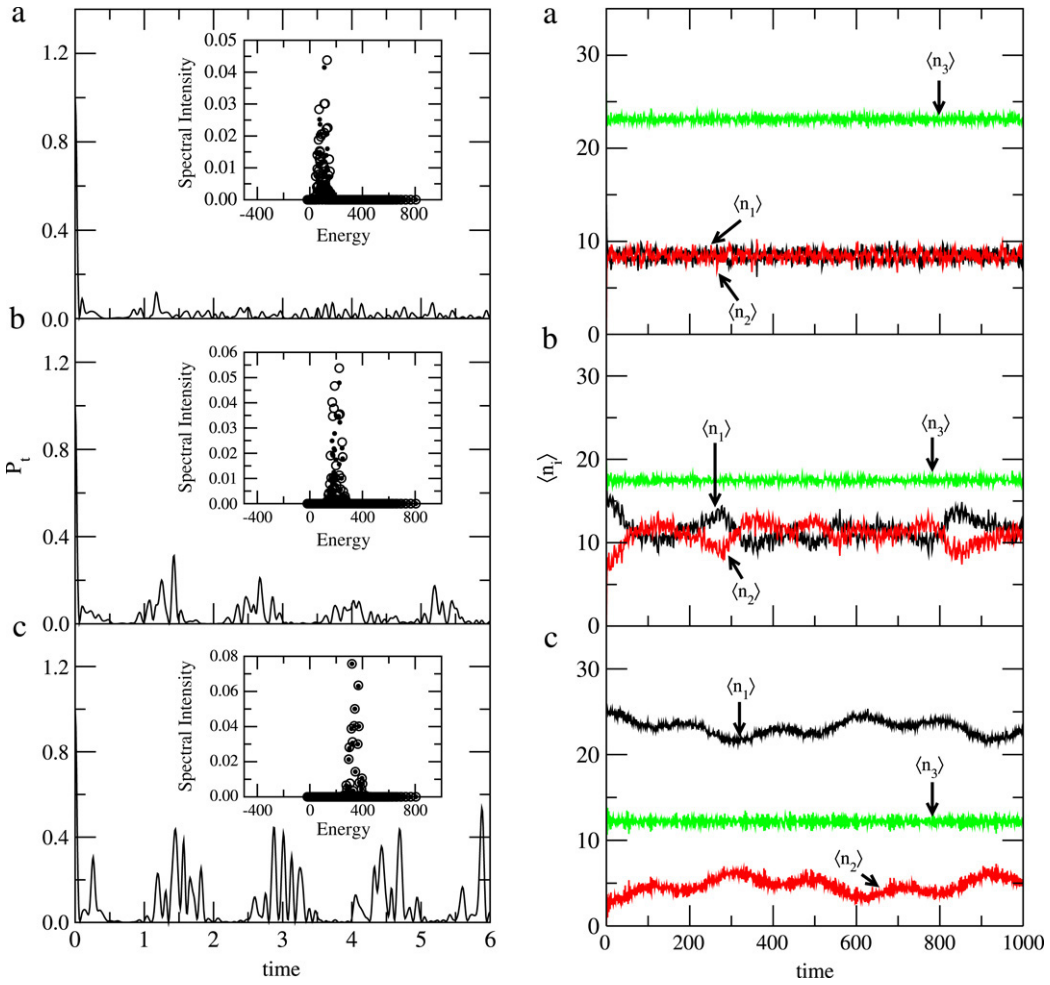


**Fig. 54.** Left plot: Survival probability of the initial state $|\Psi_0\rangle = |20+\nu, 0, 20-\nu\rangle$. $\nu =$ (a) −6, (b) 0, and (c) 6. Insets: spectral intensity of the initial state $|\Psi_0\rangle$. Filled circles — symmetric eigenstates; open circles — antisymmetric eigenstates. Right plot: Time evolution of expectation values of the number of bosons at each site of the trimer for different initial states $|\Psi_0\rangle = |20+\nu, 0, 20-\nu\rangle$. $\nu =$ (a) −6, (b) 0, and (c) 6. Figures from [315].

conserve the number of excited quanta, and can be best compared with the above Bose–Hubbard trimer. Quantum breather signatures are found simultaneously in the spectra (tunneling splittings), correlation functions, entanglement, and quanta number fluctuations.

Suppose we have a large lattice, and initially put many quanta on one site. Then any tunneling of this packet as a whole will occur on very long time scales. On much shorter time scales, we may describe the excitation as a classical discrete breather state plus a small perturbation. Treating that perturbation quantum mechanically, one could expect that the time-periodic DB acts as a constant source of quantum radiation for the quantized phonon field. It turns out to be impossible, for very much the same reasons as in the purely classical treatment (see [118]). This result implies, that there is almost no other source of decay for a localized initial state in a quantum lattice, but to slowly tunnel as a whole along the lattice, if nonlinearities allow for the formation of exact classical DB states [359,360]. Numerical calculations for such a case, but with few quanta, were performed by Proville [324], and, similar to the above trimer discussion, showed that if quantum breather states exist in the system, then localized excitations stay localized for times which are much longer than the typical phonon diffusion times in the absence of anharmonicity.

## 10. Applications

There is a fast growing amount of experimental and related theoretical work on applying the discrete breather concept to many different branches in physics, like superconducting materials, Bose–Einstein condensates, antiferromagnetic structures, crystals and molecules, micromechanical systems, and others. We will discuss some of these at length, while others will be reviewed more briefly.

### 10.1. Josephson junction networks

A Josephson junction is a sandwich consisting of two superconductors separated by a non-superconducting barrier. An electric current may flow freely within the superconductors, but the barrier prevents the current from flowing freely between them. However, the supercurrent may tunnel through the barrier, depending on the quantum phase of the superconductors. The amount of supercurrent that may tunnel through the barrier depends on the thickness of the barrier. The maximum value the supercurrent may attain is called the critical current of the Josephson junction, and is an important parameter of a junction.

Josephson junctions have two basic electrical properties. The first is an inductive reactance, which depends on the current. The second is that a constant voltage across a junction will produce an oscillating current through the barrier, and vice versa. Thus, Josephson junctions convert a dc voltage to an ac current.

There are two main types of Josephson junctions: overdamped and underdamped. In overdamped junctions, e.g. superconductor-normal metal-superconductor (SNS), the barrier is conducting. An overdamped junction will quickly reach a unique equilibrium state for any given set of conditions. The barrier of an underdamped junction is an insulator. In such superconductor-insulator-superconductor (SIS) junctions the effects of the junction's internal resistance R are minimal. In the following we will discuss the observation and the properties of discrete breathers in arrays of underdamped Josephson junctions. Most of the results concern junctions in their classical regime. Notably the development of qubits using junction technology opens the possibility of experimental studies of quantum discrete breathers. The typical length scale (size) of a junction here will be of the order of microns, while the characteristic frequencies are in the range from GHz to THz.

#### 10.1.1. Basic principles and modelling

The physical origin of the Josephson effect (see e.g. [357]) is based on the quantum nature of the superconducting state. Electrons form a condensate of Cooper pairs, which obey the Bose statistics. At low temperatures the ground state is described by one macroscopic wave function — the order parameter $\Psi = \sqrt{n}e^{i\Theta}$, where $n$ is the electronic density and $\Theta$ is the phase of the order parameter.

For a Josephson junction the two functions of the two weakly linked superconductors overlap and may generate a tunneling current. The first Josephson equation states, that the current $I$ flowing through the junction is given by

$$I = I_c \sin\phi, \quad \phi = \Theta_1 - \Theta_2. \tag{10.1}$$

Here $I_c$ is the critical current. The second equation of Josephson states, that a temporal change of $\phi$ will lead to a voltage drop $V$:

$$\dot{\phi} = \frac{2eV}{\hbar}. \tag{10.2}$$

The resistively shunted junction model takes the two basic electrical properties of a junction into account, and derives the following equation of state in dimensionless units:

$$\ddot{\phi} + \alpha\dot{\phi} + \sin\phi = \gamma. \tag{10.3}$$

Here the current $\gamma$ is measured in units of the critical current, and $\alpha$ is a dimensionless damping parameter. Eq. (10.3) corresponds to the mechanical analogue of a mathematical pendulum with (weak) damping and an external torque ($\gamma$).

If a small external torque is applied to the pendulum, it deflects to an angle and remains in the static equilibrium $\phi = \arcsin\gamma$. At the critical value $\gamma = 1 \phi = \pi/2$, and the static equilibrium can no longer be maintained. Further increase of $\gamma$ switches the pendulum to the rotating state and for large values of the torque Ohm's law $V = \dot{\phi} = \gamma/\alpha$ holds. However when decreasing the torque below the critical value $\gamma_c = 1$, the pendulum keeps rotating. It will switch back to the static state at a substantially lower value $\gamma_r \approx 4\alpha/\pi$. Thus the pendulum (and junction) supports two stable states – a static one with zero voltage drop, and a rotating one with a nonzero voltage drop – for the range $\gamma_r < \gamma < \gamma_c$ (see Fig. 55). It is this coexistence, which will be used for obtaining breather solutions.

The basic ladder geometry of a Josephson junction ladder (JJL) supporting discrete breathers is shown in Fig. 56, together with a corresponding schematic network topology. It was first proposed by Floria et al. [141], but with an ac bias instead of a dc one — which is technically complicated in the 100 GHz frequency range. Each cell of the ladder harbours one vertical junction and two (upper and lower) horizontal ones. Note that ladders are in general anisotropic, i.e. the critical currents for horizontal and vertical junctions may differ. Also each cell of the ladder will be now characterized by some inductance.

The equations of motion were derived first in [157,130], and later refined. Here we follow the notations from [280]:

$$\begin{aligned}
\ddot{\phi}_n^v + \alpha\dot{\phi}_n^v + \sin\phi_n^v &= \gamma + \frac{1}{\beta_L}(\triangle\phi_n^v + \nabla\phi_{n-1}^h - \nabla\tilde{\phi}_{n-1}^h)\\
\ddot{\phi}_n^h + \alpha\dot{\phi}_n^h + \sin\phi_n^h &= -\frac{1}{\eta\beta_L}(\nabla\phi_n^v + \phi_n^h - \tilde{\phi}_n^h)\\
\ddot{\tilde{\phi}}_n^h + \alpha\dot{\tilde{\phi}}_n^h + \sin\tilde{\phi}_n^h &= \frac{1}{\eta\beta_L}(\nabla\phi_n^v + \phi_n^h - \tilde{\phi}_n^h),
\end{aligned} \tag{10.4}$$

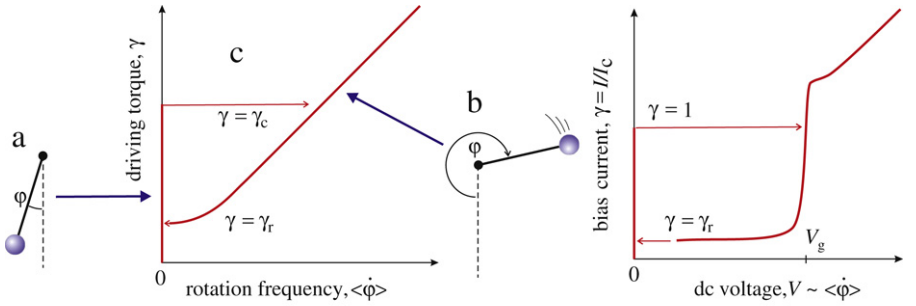


**Fig. 55.** Left plot: States of a driven and weakly damped pendulum. (a) static case; (b) rotating case; (c) dependence of the pendulum rotation frequency on the driving torque, which is similar to the current–voltage curve of an underdamped Josephson junction (cf. right plot). Right plot: Sketch of the typical experimentally measured current–voltage curve of an underdamped Josephson junction. Figure from [391].

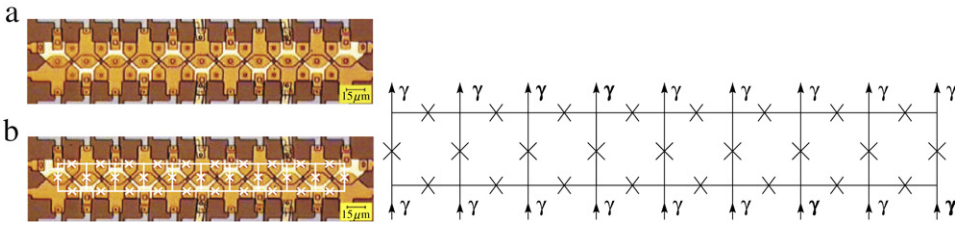


**Fig. 56.** Left plot: (a) A photograph of a ladder under a microscope. (b) The same picture which shows by crosses the actual positions of Josephson junctions. From [391]. Right plot: Josephson junction ladder topology. Crosses mark the individual junctions. Arrows indicate the direction of external current flow (dc bias $\gamma$). Figure from [280].

where $\Delta f_n \equiv f_{n-1} - 2f_n + f_{n+1}$ and $\nabla f_n \equiv f_{n+1} - f_n$. Note that $\beta_L$ is the normalized cell inductance, and $\eta$ is the ratio of the horizontal to the vertical junction critical currents. The static (superconducting) state, $\phi_n^{*v} = \arcsin\gamma$ and $\phi_n^{*h} = \tilde{\phi}_n^{*h} = 0$ is the ground state of the ladder. We are now interested in excitations.

Small deviations from the superconducting ground state will fluctuate and die out exponentially in time due to the damping $\alpha$. However, if that time scale is long enough, the frequencies of these underdamped oscillations will form a spectrum of linear plane-wave like states. Three degrees of freedom per unit cell make three branches of that spectrum. These have been calculated in [280]. The first is given by

$$\omega_0^2 = 1, \qquad \Delta_v = 0, \qquad \Delta_h = \tilde{\Delta}_h. \tag{10.5}$$

This branch is dispersionless and the waves corresponding to this branch are characterized by nonactive vertical junctions and in phase (symmetric) librations of the Josephson phases of upper and lower horizontal junctions.

The two other solutions are generalizations of those discussed in [130], namely

$$\begin{aligned} \omega_\pm^2 &= F \pm \sqrt{F^2 - G}, \\ F &= \frac{1}{2} + \frac{1}{\beta_L\eta} + \frac{1}{2}\sqrt{1-\gamma^2} + \frac{1}{\beta_L}(1-\cos q), \\ G &= \left(1 + \frac{2}{\beta_L\eta}\right)\sqrt{1-\gamma^2} + \frac{2}{\beta_L}(1-\cos q). \end{aligned} \tag{10.6}$$

The branch $\omega_+$ is characterized by $\Delta_h = -\tilde{\Delta}_h$ for all wave vectors $q$, i.e. the upper and lower horizontal phases are antisymmetric. The frequency range of the branch is above the degenerate branch $\omega_0$, i.e. $\omega_+(q) > \omega_0$ and it depends strongly on $\beta_L$. As the parameter $\beta_L$ increases, the width of $\omega_+(q)$ decreases and the branch approaches the dispersionless one, $\omega_0$. In the opposite case of small $\beta_L$, the frequencies $\omega_+(q)$ increase as $1/\sqrt{\beta_L}$. For zero wave number $q = 0$, the amplitudes of waves in this branch are characterized by $\Delta_v = 0$ and $\Delta_h = -\tilde{\Delta}_h$, which means that only horizontal junctions are excited. The branch $\omega_-$ becomes dispersionless for the particular case of $\gamma = 0$. The frequency range of this branch is located below $\omega_0$ i.e. $\omega_-(q) < \omega_0(q)$. For zero wave number $q = 0$ the horizontal junctions are not active ($\Delta_h = \tilde{\Delta}_h = 0$) and only vertical junctions are excited.

Due to the damping we can not obtain persistent breather states where the junction phases are only oscillating. However we may try to make a few junctions resistive (rotating), while the rest of the junctions is oscillating at most. It turns out, that such states make perfect sense, and can be obtained — both numerically and experimentally.

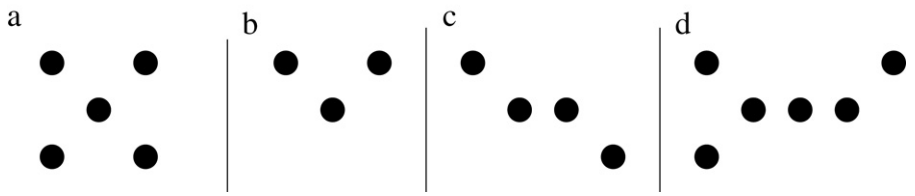


**Fig. 57.** Possible realizations of discrete breathers in a linear ladder. Black spots indicate the positions of resistive junctions. Ladders with periodic boundary conditions do not support (c) or (d) states. Figure from [280].

For a finite size ladder with open boundary conditions and $N$ cells, i.e. $N+1$ vertical junctions, the spectrum of linear waves is discrete and characterized by the following choice of allowed wave number values:

$$q_l = \frac{l\pi}{N+1}, \quad l = 0, 1, 2, \ldots, N. \tag{10.7}$$

These plasmon waves are the *cavity modes* of the JJL. Odd values of $l$ correspond to antisymmetric eigenvectors (with respect to reflections at the center of the ladder), whereas even values correspond to symmetric ones.

*10.1.2. Rotobreather solutions and their current–voltage dependencies*

The rotobreather states correspond to a few junctions being in the resistive state with all other junctions oscillating around the superconducting state. These oscillations are induced by the coupling to the resistive junctions. All rotations and oscillations are characterized by a fundamental frequency $\Omega_b$.

The first experiments [386,40] (see also [39,41]) have revealed different breather structures, as depicted in Fig. 57: (a) up–down symmetry, (b) left–right symmetry, (c) inversion symmetry, (d) no symmetry. Each group of breathers can also have an arbitrary number $n_r$ of vertical resistive junctions.

Experimentally, each discrete breather is characterized by its current–voltage dependence [40]. Such a time-averaged measurement does not resolve the details of the oscillatory dynamics of a state, which is almost impossible due to the absence of spectroscopical tools at frequencies of the order of 100 GHz. The average voltage drop on the $l$th vertical junction equals $V = (1/T_b)\int_0^{T_b} \dot{\phi}_l^v \mathrm{d}t$. For type (a, d) breathers $V = 2\Omega_b$ and for type (b, c) ones $V = \Omega_b$.

Further experiments demonstrated the generation of DBs from extended resonant states, perhaps via modulational instability [362].

*10.1.3. Resonances with cavity modes*

Using the approximation $\phi \sim t$ for resistive junctions, one can compute the dependence of the average voltage drop on the dc bias [280]:

$$V = \frac{k\gamma}{\alpha[k + (3 - \frac{1}{2}\delta)\eta]}, \tag{10.8}$$

where $k$ is the number of vertical rotating junctions and $\delta$ denotes the number of resistive horizontal junctions. Note that $\delta = 4$ for breathers with up–down symmetry, $\delta = 2$ for left–right or inversion symmetry, and $\delta = 3$ for no symmetry. Numerical calculations of the current–voltage characteristics (Fig. 58) showed very good qualitative agreement with experiments [361]. In addition numerical studies allow one to directly access the tricky details of the nonlinear dynamics of the obtained states. Note, that the variation of the parameters allows for breathers with frequencies located both above the entire plasmon spectrum, as well as in its gaps. The presence of dissipation leads to a temporal decay of plasmon waves, if excited homogeneously in the ladder. In addition it also leads to a spatial decay of plasmon waves, if a local resonant source is generating them. Thus a rotobreather in the JJL can be brought into resonance with plasmon waves. The tuning parameter is simply the dc bias, which is the main control parameter in the experiments. When the breather frequency is tuned into resonance, the breather starts to generate plasmons, which will localize in space. Their localization length, though finite, will grow with decreasing dissipation constant $\alpha$. In a finite ladder one expects to observe a resonant breather tail, which extends to the end of the ladder, and appears at discrete values of the bias, due to the discrete set of cavity mode frequencies. That was indeed numerically observed e.g. in the left picture in Fig. 58, where the cavity modes resonate with the second harmonics of the breather frequency. At the same time almost no indication for that resonance is observable in the current–voltage characteristics.

In the right picture in Fig. 58 the breather frequency itself resonates with the plasmon waves. Still the breather survives, due to the presence of dissipation. However the resonant breather–plasmon interaction is now strong, and leads to a strong change in the current–voltage characteristics. Almost vertical resonant steps are observed, which correspond to a locking of the breather frequency to a particular cavity mode frequency. These resonances allow one to use the tunable rotobreather as a spectroscopical tool to study the properties of cavity modes in a JJL.

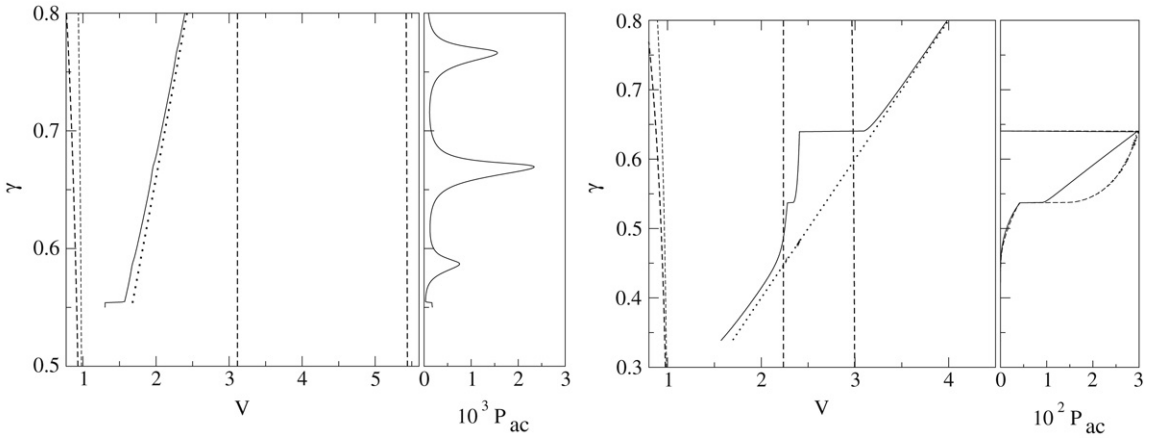


**Fig. 58.** Current–voltage dependence and the edge average power $P_{ac} = \frac{1}{2}\langle \dot{\phi}_N^{v^2} \rangle$ dependence for breathers of type (b) in a ladder with $N = 10$ vertical Josephson junctions. Solid lines — numerical results. Dotted lines — approximation (10.8). Vertical dashed lines — band edges of the plasmon wave spectrum. Left picture — $\alpha = 0.1$, $\beta_L = 0.2$, $\eta = 1.15$. Right picture — $\alpha = 0.1$, $\beta_L = 1.0$, $\eta = 0.5$. Figure adapted from Ref. [280].

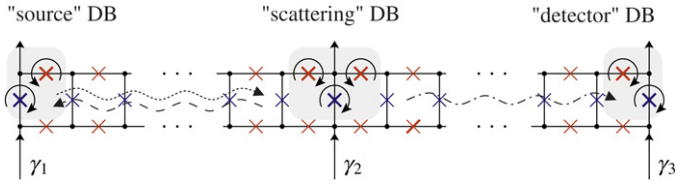


**Fig. 59.** Schematic experimental setup for measuring the plasmon scattering by a DB, showing source, scattering, and detector DB. The individual DBs are controlled using local bias currents. Figure adapted from Ref. [282].

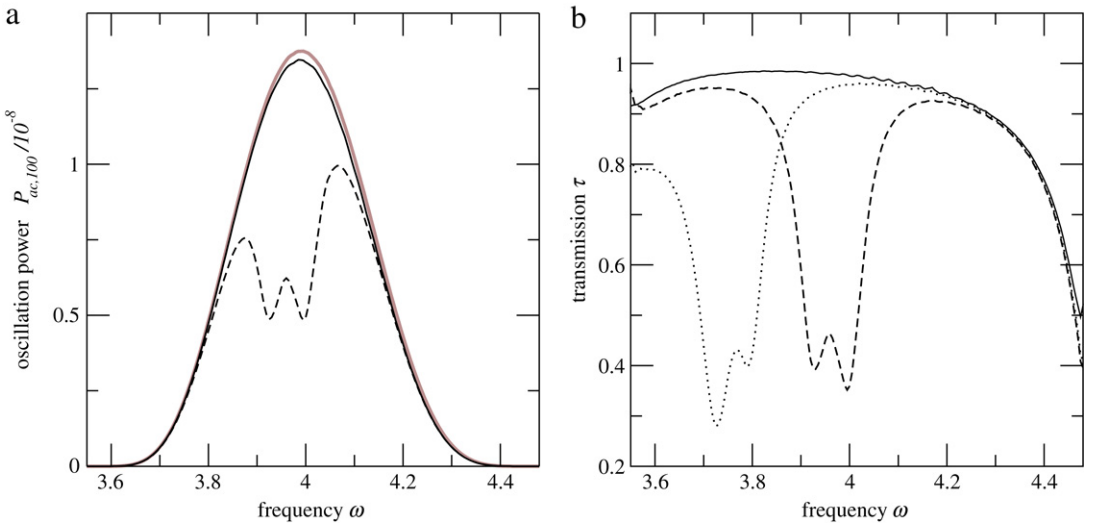


**Fig. 60.** Direct numerical simulation of the linear wave propagation in a JJL with $N = 100$ cells, $\alpha = 0.05$, $\beta_L = 0.5$, $\eta = 0.35$ with a boundary ac bias $\gamma_1 = \gamma_{ac}\cos(\omega t)$. (a) Oscillation power of vertical junction $n = 101$ versus excitation frequency $\omega$ for an empty system (dotted line), for an A DB at site $n = 50$ with frequency $\Omega_b = 2.777$ (solid line), and $\Omega_b = 3.284$ (dashed line). (b) Transmission coefficient $\tau$ for an A DB of frequency $\Omega_b = 2.777$ (solid line), $\Omega_b = 3.284$ (dashed line), and frequency $\Omega = 3.082$ (dotted line). Figure from Ref. [282].

The strong interaction of breathers with cavity modes in JJLs leads to the possibility of studying resonant scattering of cavity modes by rotobreathers [282] (see schematic setup in Fig. 59). Again the dissipation helps in stabilizing the breather during the scattering process. The transmission for plasmons is strongly dependent on their wavenumber. In addition strong resonances can be obtained in the scattering, ranging from resonant transmission to resonant reflection. By changing the DC bias, the rotobreather is changed, and thus the scattering potential as well. Consequently rotobreathers may serve as tunable frequency filters for plasmon waves in the 100 GHz frequency domain (see Fig. 60).

Another consequence of the presence of dissipation is the possibility of exciting genuine quasiperiodic breathers. This has been achieved both theoretically and experimentally by using the fact that when driving a breather into a resonance, not

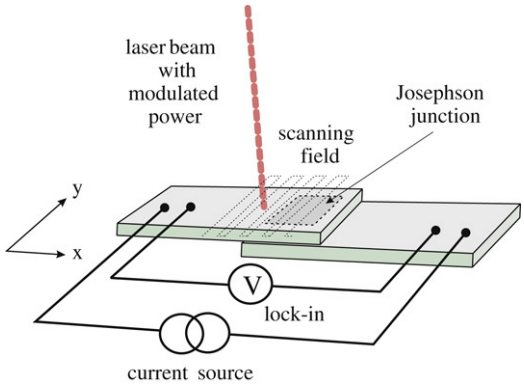


**Fig. 61.** The principle of low temperature scanning microscopy. Figure from Ref. [391].

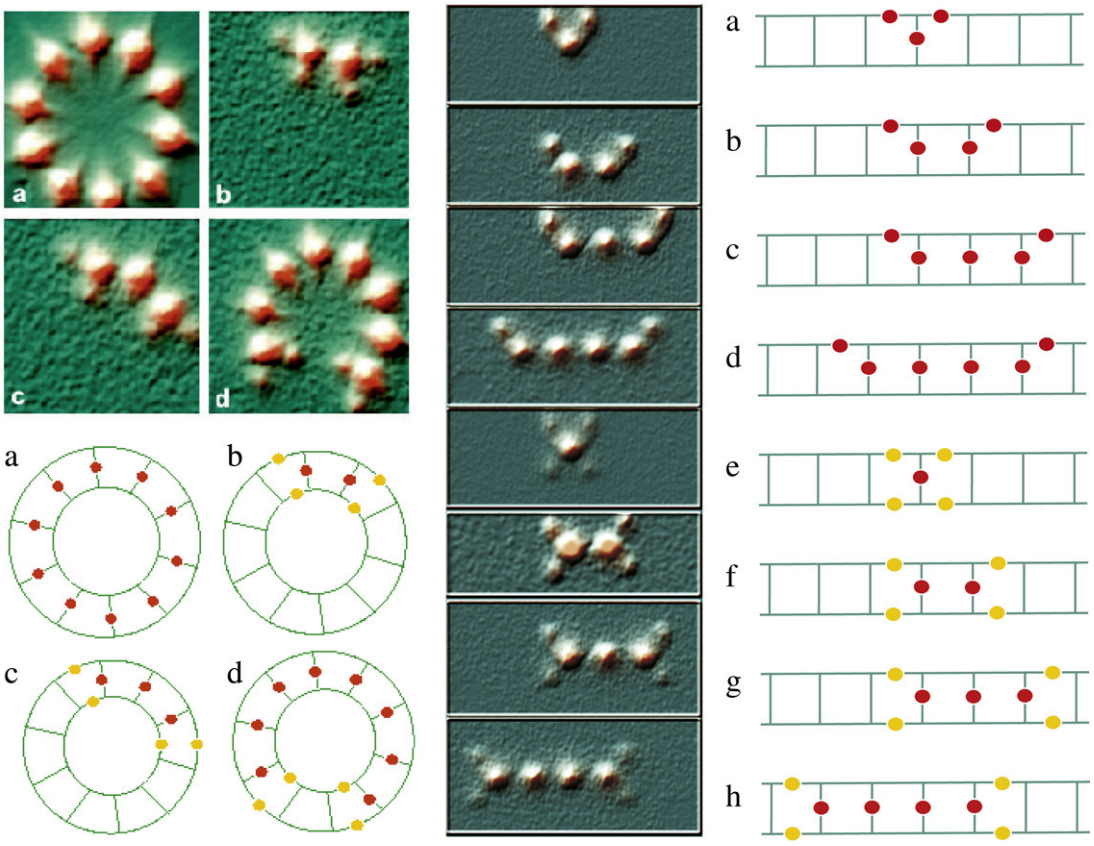


**Fig. 62.** Experimental and schematic images of rotobreathers driven by a DC current. Left plot: Annular Josephson ladder, (a) a highly excited, spatially homogeneous resistive state and (b–d) localized states corresponding to several distinct rotobreathers. Right plot: Linear Josephson ladder, (a)–(d) asymmetric rotobreathers, (e)–(h) symmetric rotobreathers. Figures from Ref. [391].

all resistive junctions have to lock to to the cavity mode [109]. In such a case the breather becomes an object, where different resistive junctions rotate at different incommensurate frequencies. Due to the interaction the final state is quasiperiodic in time.

*10.1.4. Laser scanning microscopy*

The technique of laser scanning microscopy allowed the visualization of experimentally obtained breather states [40]. For that the ladder is prepared in a given state, and the voltage drop across the ladder is monitored. Then the probe is scanned by a laser beam with moderate intensity and a diameter of a few micrometers (see Fig. 61). The laser beam is locally heating the probe. If it hits a resistive junction, the local temperature change will induce a change of the junction characteristics, and finally a change in the measured voltage drop. Otherwise the voltage drop will show no response. In Fig. 62 the outcome

of such experiments and the corresponding schematics are shown for the case of annular ladders [41]. Both delocalized resistive states and rotobreather states are clearly visible. In the schematics, Josephson junctions (each about 3 μm wide) lie at the midpoints of each green line segment that signifies superconducting leads connecting the junctions. A pure green ladder in the schematic and a pure green background in the data would signal a superconducting state of all junctions at low DC current — the linear regime. But a larger DC current switches some of the junctions into a resistive state that supports a voltage across the junctions; in the schematic, red and yellow dots resistive junctions having different voltages. The resistive junctions belong to discrete breather excitations localized at various sites of the ladder.

#### *10.1.5. More*

Further studies focussed on the theory [30,108] and experiments [314] with single plaquettes of Josephson junctions, where discrete breathers can be excited, and controlled with the help of external magnetic fields. Recent studies deal with quantum breather excitations in two capacitively coupled Josephson junctions [317,316]. Such systems are currently under experimental investigation, being candidates for quantum information processing, and show remarkably long coherence times up to 100 ns for few quanta excitations. The interested reader could also consult the publications by Ustinov [391, 392], Fistul [107] and Mazo and Orlando [270,269], where a more detailed description of the theoretical and experimental investigations of breathers in Josephson networks can be found.

### *10.2. Coupled nonlinear optical waveguides*

Coupled optical waveguides form periodical structures in one and two dimensions [64,136,216]. Each individual waveguide is a narrow channel (typical widths are of the order of several $\mu m$) surrounded by a medium with slightly *lower* index of refraction. The latter plays the role of an optical insulator due to the total internal reflection of light at an interface between two optically transparent media [291]. Under certain approximations, light propagation in the waveguide can be described with an amplitude $E(z)$ of the linear waveguide mode, slowly varying with propagation distance. Its transverse profile $\mathcal{F}(x, y)$ is fixed by the waveguide geometry [216]. The resulting equation for $E(z)$ is similar to a nonlinear oscillator problem with time being replaced by the propagation distance $z$. The nonlinearity is due to the dependence of the effective refractive index of the medium on light intensity (Kerr effect). Placing two waveguides close to each other, light from one of the waveguides can couple to the neighboring one [178], similar to a quantum particle tunneling in a double well potential. This happens due to the overlap of evanescent tails of waveguide modes in neighbouring waveguides. Extending the system to many coupled waveguides, one can design one- and two-dimensional structures. Their dynamics is similar to that of the corresponding nonlinear lattices discussed here.

#### *10.2.1. Basic principles and modeling*

The standard theoretical approach for studying light propagation in waveguide arrays is based on the concept of coupled waveguide modes, see Fig. 63(b), which generalizes the nonlinear optical coupler introduced by Jensen [178]. It is similar to the tight-binding approximation used in solid state theory. Typical propagation distances in waveguide arrays are rather short, so that usually the effects of light dispersion in each individual waveguide are neglected.[7] Under this assumption, the total field distribution in a one-dimensional waveguide array, see Fig. 63, can be approximated as the superposition of linear waveguide modes of each individual waveguide

$$E(x, z) = \sum_n E_n(z)\psi_n(x)\exp(-\mathrm{i}\lambda_0 z), \tag{10.9}$$

where $\psi_n(x) \equiv \psi_0(x - nd)$, $\psi_0(x)$ is the linear waveguide mode with corresponding propagation constant $\lambda_0$:

$$\frac{\mathrm{d}^2\psi_0}{\mathrm{d}x^2} + [k_0^2 f_0^2(x) - \lambda_0^2]\psi_0 = 0, \tag{10.10}$$

$k_0$ is the wavenumber of the optical field in vacuum, $f_0(x)$ is the refractive index of a single waveguide, and $d$ is the transverse period of the structure. Each individual waveguide is assumed to support a single mode. The more complicated situation of multimode waveguides would involve additional indexing in expression (10.9).

Overlapping between modes of adjacent waveguides, together with a nonlinear response of the medium, causes a variation of amplitudes $E_n(z)$ with propagation distance $z$. The corresponding evolution equations are eventually reduced to the DNLS model [2,216]

$$\mathrm{i}\frac{\mathrm{d}E_n}{\mathrm{d}z} + C(E_{n-1} + E_{n+1}) + \gamma|E_n|^2 E_n = 0. \tag{10.11}$$

[7] Note that glass and semiconductor based waveguide arrays usually require picosecond and sub-picosecond pulsed lasers in order to achieve high enough intensities for nonlinear response. This can introduce spatio-temporal effects [60].

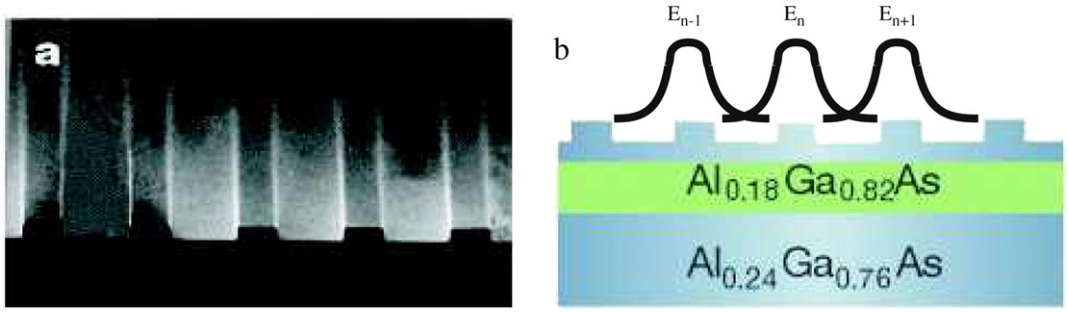


**Fig. 63.** A one-dimensional AlGaAs waveguide array. It is composed of three layers of AlGaAs material: the substrate and cladding with a lower refractive index and the guiding layer with the higher refractive index. Periodical etching of the cladding forms coupled waveguides, inducing modulation of the effective refractive index inside the core layer. (a) A snapshot of the waveguide array. (b) Schematic structure of the waveguide array with illustration of modal overlap. Figures from [64].

Here the simplest case of the so-called Kerr nonlinearity is considered. $C$ is the coupling coefficient between adjacent waveguide modes and $\gamma$ is the nonlinear parameter [63,2,216]. In the simplest approximation only couplings between nearest neighbours are taken into account, and nonlinear coupling terms are neglected. For waveguide arrays created by optical induction in photorefractive materials [136] the nonlinear term in Eq. (10.11) is modified to account for saturation and takes the form $\gamma E_n/(1+|E_n|^2)$ [374]. Generalization to higher dimensional problems is straightforward (see Eq. (4.6)). The actual evolution coordinate in the above model is the propagation distance $z$, which plays the role of an effective time. For that reason we will refer to wave propagation constants along the $z$-axis as spatial frequencies, in analogy with other discrete models introduced earlier.

An obvious advantage of the above approximation is the simplicity of the resulting DNLS-like models, which is convenient for further theoretical treatment. Certainly, this approximation has limitations: it is applicable only when overlapping between adjacent waveguide modes is relatively weak.

A more rigorous approach is based on the consideration of the continuous NLS equation

$$\mathrm{i}\frac{\partial E}{\partial z} + \Delta_{xy}E + \mathcal{F}(x,y;|E|^2)E = 0, \tag{10.12}$$

where $\Delta_{xy}$ is the Laplacian in transverse dimensions, and $\mathcal{F}(x,y;|E|^2)$ accounts for both nonlinear and periodic modulations of the effective refractive index. As the result of transverse periodicity, the eigenstates of the corresponding linear problem have Floquet–Bloch states $\phi_{\vec{k},\alpha}(\vec{r})\mathrm{e}^{-\mathrm{i}\vec{k}\vec{r}}\mathrm{e}^{-\mathrm{i}\beta_\alpha z}$. Here $\phi(\vec{r})$ is a periodic function in the transverse plane $(x,y)$, $\vec{k}$ is the transverse component of the wavevector, and $\beta_\alpha$ is the longitudinal component of the wavevector. In full analogy to a quantum mechanical particle in a periodic potential, the spectrum of $\beta_\alpha$ (corresponding to the particle energy) has one or several forbidden bandgaps with $\alpha$ denoting different bands. Typical bandgap structures of 1D and 2D setups are shown in Figs. 65 and 66, respectively.

When considering local initial excitations, it is more convenient to work with spatially localized Wannier functions, instead of extended Floquet–Bloch functions:

$$w_{n,\alpha}(\vec{r};\vec{R}) = \sqrt{(D/2\pi)^l}\int \mathrm{d}\vec{k}\phi_{\vec{k},\alpha}(\vec{r})\mathrm{e}^{-\mathrm{i}\vec{k}(\vec{r}_n-\vec{R})}. \tag{10.13}$$

Here $n$ is a one- or two-dimensional index, each Wannier function $w_{n,\alpha}$ is centered around its position $\vec{r}_n$, the set of vectors $\vec{r}_n$ spans a periodic lattice (either one- or two-dimensional), $l=1,2$ is the number of transverse dimensions, and $\vec{R}$ is an arbitrary parameter which can be tuned in order to obtain maximum localization of Wannier functions [268,52]. Expanding solutions of Eq. (10.12) in Wannier functions

$$E(\vec{r},z) = \sum_{n,\alpha} c_{n,\alpha}(z)w_{n,\alpha}(\vec{r}), \tag{10.14}$$

one eventually obtains a set of coupled equations for $c_{n,\alpha}$. In the simplest case of Kerr nonlinearity $\mathcal{F}(x,y;|E|^2) = V(x,y)+\gamma|E|^2$ these equations read [9]

$$-\mathrm{i}\frac{\mathrm{d}c_{n,\alpha}}{\mathrm{d}z} = \sum_m c_{m,\alpha}\hat{\beta}_{n-m,\alpha} + \gamma\sum_{\alpha_1,\alpha_2,\alpha_3}\sum_{n_1,n_2,n_3} c^*_{n_1,\alpha_1}c_{n_2,\alpha_2}c_{n_3,\alpha_3}W^{nn_1n_2n_3}_{\alpha\alpha_1\alpha_2\alpha_3}, \tag{10.15}$$

where $\hat{\beta}_{n,\alpha}$ are the spatial Fourier transform coefficients of the corresponding linear bands $\beta_{n,\alpha}$ and

$$W^{nn_1n_2n_3}_{\alpha\alpha_1\alpha_2\alpha_3} = \int w_{n,\alpha}w_{n_1,\alpha_1}w_{n_2,\alpha_2}w_{n_3,\alpha_3}\mathrm{d}\vec{r} \tag{10.16}$$

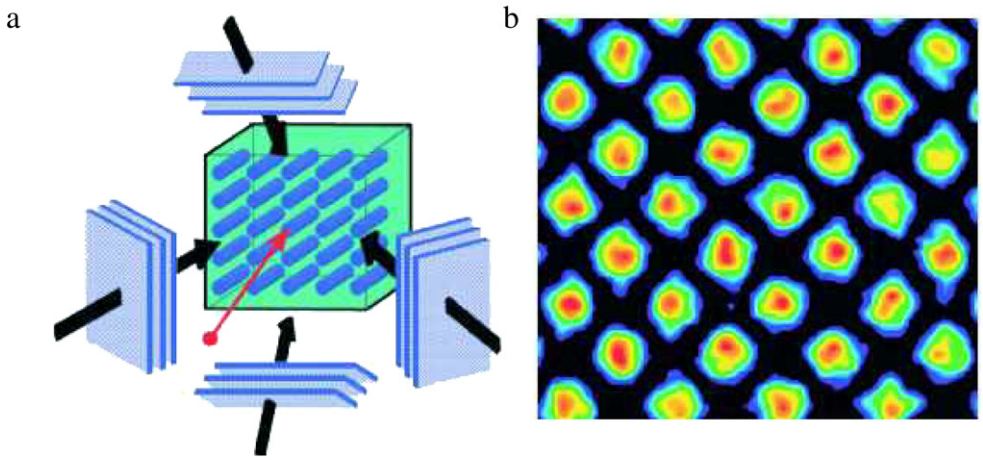


**Fig. 64.** (a) Diagram of an experimental setup to observe two-dimensional discrete localized structures with use of a photorefractive crystal: two interfering pairs of ordinarily polarized plane waves induce the photonic array, while the extraordinarily polarized probe beam is focused into a single waveguide to form a discrete soliton. (b) Typical observation of a waveguide array at the exit face of the crystal. Each waveguide is approximately 7 μm in diameter, with an 11 μm spacing between nearest neighbours. Figures from [138].

are overlap matrix elements. Eq. (10.15) can be viewed as a generalized DNLS model for a multi-component (vector) field $c$ with long-range interactions. Restricting to a single band $\alpha = \alpha_0$, considering rapidly decaying Fourier coefficients $\hat{\beta}_{n,\alpha_0}$ and neglecting nonlinear couplings between neighboring Wannier functions, Eq. (10.15) is eventually reduced to the DNLS equation (10.11). Other reductions can be performed, e.g. in order to consider excitations with propagation constants inside a finite gap, when only the two corresponding neighboring bands are taken into account, while the other ones are neglected. Note however, that complications arise for $d = 2, 3$ due to additional symmetry points in the dispersion relation of the linear problem [278].

### *10.2.2. Experiments*

There are two main approaches to experimentally realize coupled waveguide arrays: either by etching fixed waveguides in nonlinear materials, such as semiconductors [275], or by induction of periodic structures in compliant media, such as optical induction in photorefractive crystals [136] and periodic voltage biasing in liquid crystals [146]. Figs. 63 and 64 illustrate typical one- and two-dimensional waveguide arrays produced by the two methods, respectively. Etched waveguide arrays are the most stable configurations, but the techniques are so far limited only to one transverse dimension, and the resulting arrays have fixed geometry. In contrast, optically induced lattices are more sensitive to external conditions, but they allow one to produce different, easily reconfigurable, two-dimensional lattices. An additional advantage of using optically induced lattices is that photorefractive crystals support both focusing ($\gamma > 0$) and defocusing ($\gamma < 0$) nonlinearities, which is controlled by the applied voltage [136].

Various types of discrete breathers are observed in experiments by launching a laser beam at the input facet and monitoring the resulting field distributions at the output facet of the array. The most straightforward method is to excite a single waveguide at the input facet. At low powers one observes linear diffraction, so that many waveguides become excited at the output facet. Increasing the power, the light distribution at the output facet becomes more and more localized, so that eventually most of light stays in the initially excited waveguide, which is the result of localization due to discreteness and nonlinearity, see Fig. 67. In such experiments one excites discrete breathers with propagation constants $\beta$ lying above the first transmission band, i.e. inside the semi-infinite bandgap, cf. Figs. 65 and 66, which are supported by the focusing Kerr nonlinearity. Other types of DBs have propagation constants inside bandgaps for either type of the nonlinearity. Their excitation requires more accurate control of the input beam phase distribution across the array and the range of propagation constants $\beta$ of the input beam, i.e. of a spatial Fourier composition of the beam. The former is done by superimposing two beams coming at an angle to the input facet [138], see Fig. 67(d), or by imprinting specially designed phase masks [59], while the latter is achieved by exciting the array from a side [253,254], rather than from the input facet. By imprinting phase topology on the input beam, different types of discrete vortices have been successfully observed in two-dimensional optically induced square lattices as well [289,137,29].

One of the advantages of using optical waveguide arrays, is the visual control of the obtained localized states. A snapshot, taken by a high-resolution camera at the output facet of the array, illustrates the light intensity distribution among the coupled waveguides. Information about relative phases in different waveguides and the spatial Fourier decomposition of the output light distribution is obtained by using standard optical techniques. Finally, optical setups allow one to observe the actual propagation dynamics by monitoring the light intensity evolution along the propagation distance. This is done e.g. by

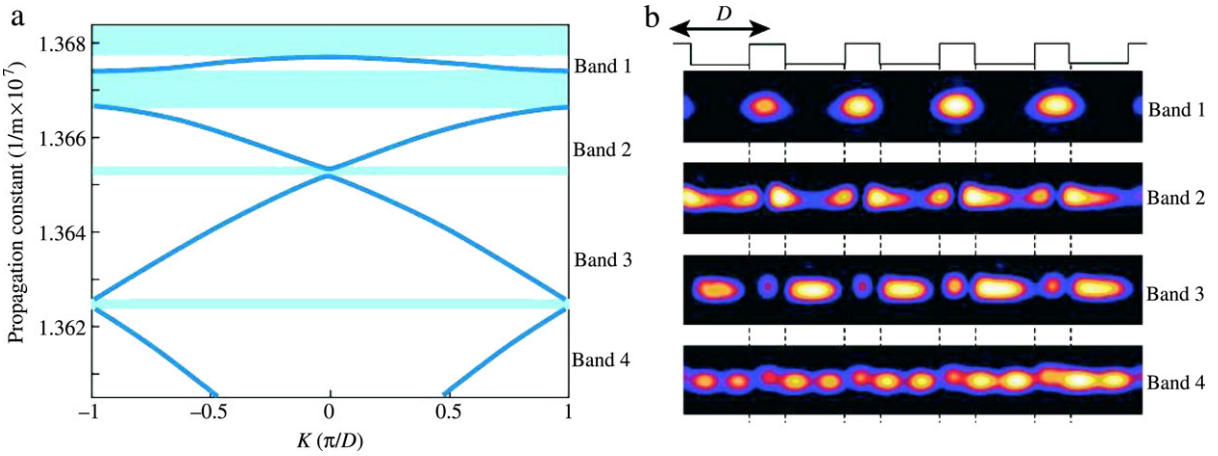


**Fig. 65.** (a) Bandgap structure of a typical waveguide array, folded into the first Brillouin zone. The Floquet–Bloch propagation constant as a function of the transverse wavevector $k$ is plotted with solid lines. Shaded areas indicate forbidden gaps. (b) Experimentally obtained images of different Floquet–Bloch modes $\phi_{k,\alpha}(x)$ from the first four bands, measured in a AlGaAs waveguide array using a 1.55 μm pump laser. Figures from [253].

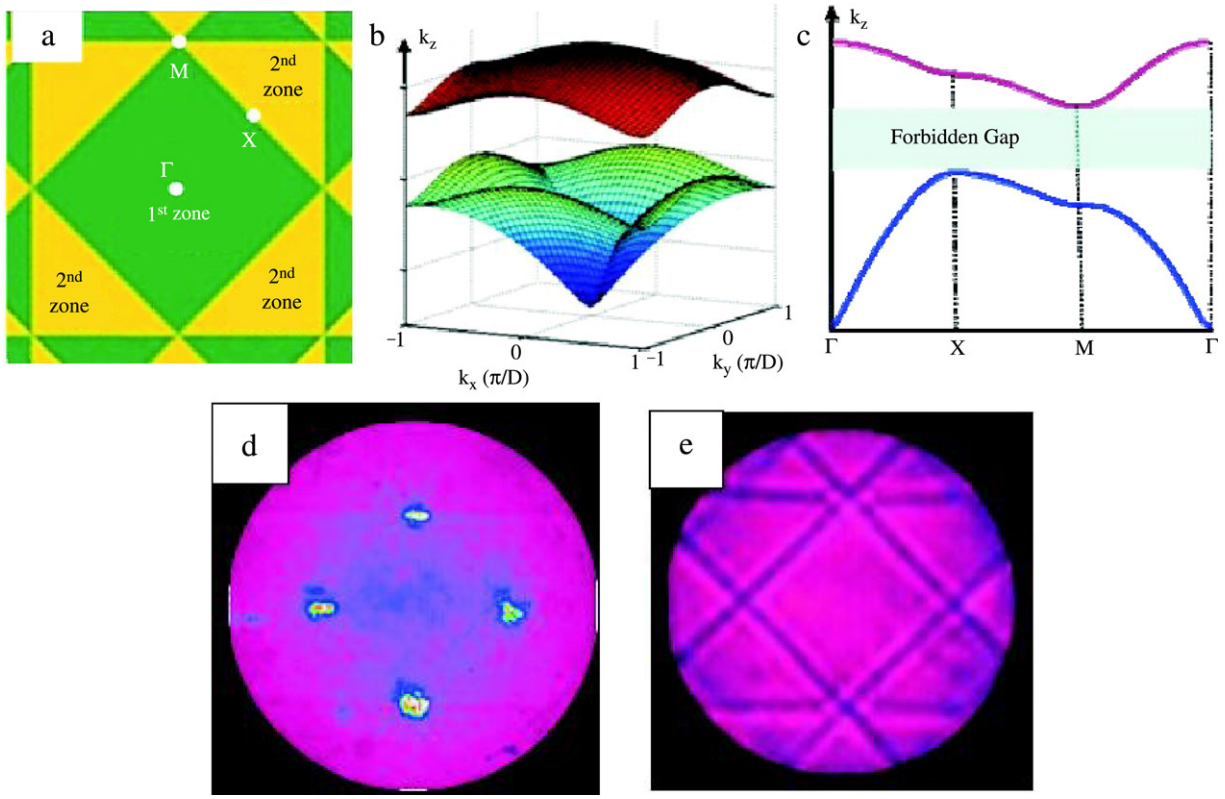


**Fig. 66.** (a) First and second Brillouin zones of a 2D square lattice, high symmetry points $\Gamma$, $X$ and $M$ are marked with white dots. (b) The first two transmission bands of a 2D square lattice. (c) Dispersion curves between the symmetry points of the first two bands. (d) Fourier spectrum of the input probe beam (broad circle) and lattice-forming beams (four sharp peaks) in the Brillouin zone spectroscopy experiment performed on a 2D optically induced square lattice, the corresponding setup is shown in Fig. 64. (e) Experimental picture illustrating the Fourier spectrum of the probe beam at the output facet of the crystal. Figures from [28].

scanning the evanescent light from the top of the waveguide array [244]. As a result, different intriguing aspects of the DB dynamics have been tested [284,306,307,91], and modulational instability has been observed [272]. Interactions between highly localized discrete solitons and propagating broad wavepackets have been recently studied in AlGaAs waveguide

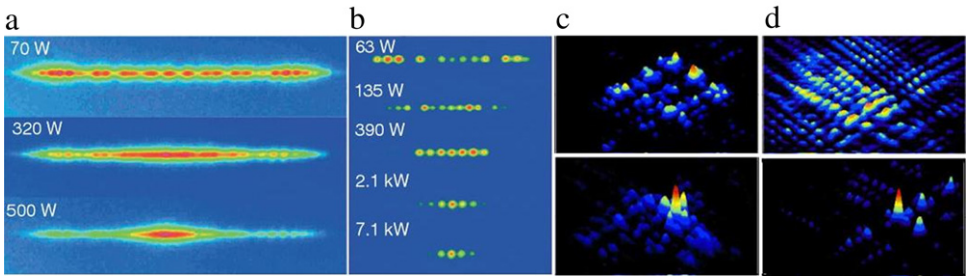


**Fig. 67.** Experimental observation of discrete diffraction in the linear regime (small input power) and localization in nonlinear regime (high input power). (a) Experimental images of a Kerr-type AlGaAs one-dimensional waveguide array with waveguide spacing $D = 8\ \mu$m operated at the wavelength $\lambda = 1.53\ \mu$m. Figures from [92]. (b) The same for periodically poled lithium niobate array with $D = 15\ \mu$m operated at the wavelength $\lambda = 1.56\ \mu$m. Figures from [64]. (c) and (d) The same for a two-dimensional optically induced waveguide array, shown in Fig. 64, with the input beam at normal incidence and at the angle 0.55° to the lattice plane (at the edge of the first Brillouin zone), respectively. The signs of the applied voltage to the photorefractive crystal in (c) and (d) are different, corresponding to the focusing and defocusing nonlinearities, respectively. Figures from [138].

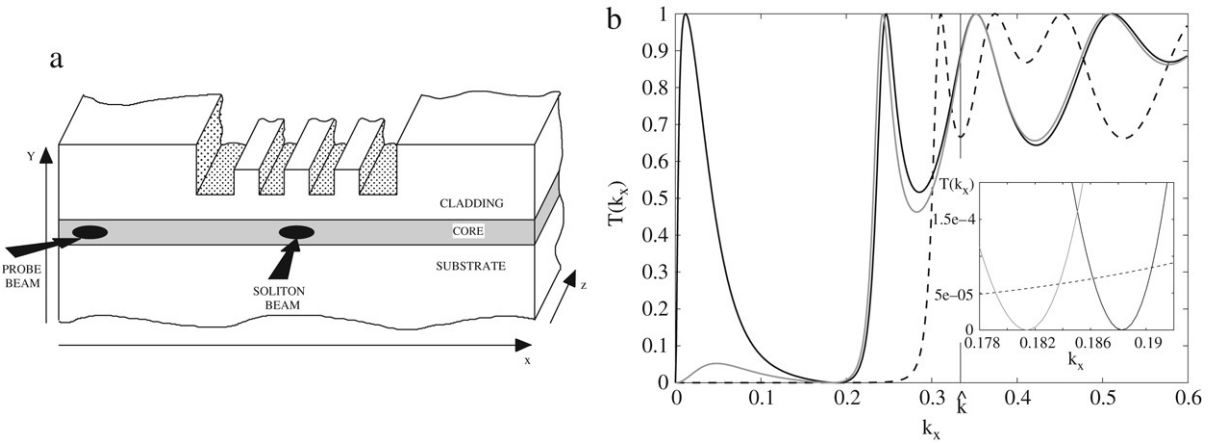


**Fig. 68.** (a) Schematic structure of the wave scattering setup. The soliton beam is sent along the $z$-axis, while the probe beam propagates in the $xz$-plane at some angle to the soliton. (b) Transmission coefficient $T(k_x)$ for the system without a soliton (dashed line), and with solitons having slightly different intensities (solid black and gray lines). Figures from Ref. [119].

arrays [273,271]. Also, experimental setups for the direct observation of resonant wave scattering by DBs and associated spectral hole burning effects have been developed on the basis of optical waveguides [119,156], see next chapter.

### *10.2.3. Resonant light scattering*

Resonant scattering of plane waves by discrete breathers is one of the demanding tasks for experimental investigation. Not only has the scattering setup to be carefully designed, but one also needs to have proper means for detecting the reflected and transmitted portions of waves. Coupled optical waveguides seem to be one of the best candidates to perform such experiments. The coupled modes model (10.11) calls for the use of the results of wave scattering by a DNLS breather discussed in Section 5.4. However, in the DNLS model the Fano resonance is observed on the background of a very low transmission ($\sim 10^{-8}$), see Fig. 26, which makes it practically impossible to observe in an experiment. One of the possibilities for enhancing the background transmission is to modify the properties of plane waves far away from the breather center [119]. The corresponding setup is shown in Fig. 68(a). It consists of a section with a periodically modulated index of refraction, surrounded by planar waveguide sections. In order to place a Fano resonance within the transmission band one needs to make the effective refractive index $n_0$ in the surrounding planar waveguide sections higher than the average index inside the modulated section [119]. The breather (discrete soliton) is excited in the modulated section by injection of a highly intense beam in one of the embedded waveguides. Since it is well localized in the transverse direction $x$, it is enough to have only a few coupled waveguides inside the modulated section. To complete the scattering setup, an additional probe beam is sent at an angle to the breather. As mentioned above, the actual dynamical variable in Eqs. (10.11) and (10.12) is the light propagation direction $z$. Therefore, scanning the transverse wave vector $k_x$ of the incident wave is equivalent to scanning the inclination angle of the probe beam. The resulting transmission curves are shown in Fig. 68(b). Because of the refractive index contrast at the interface between homogeneous and modulated sections, incoming waves are

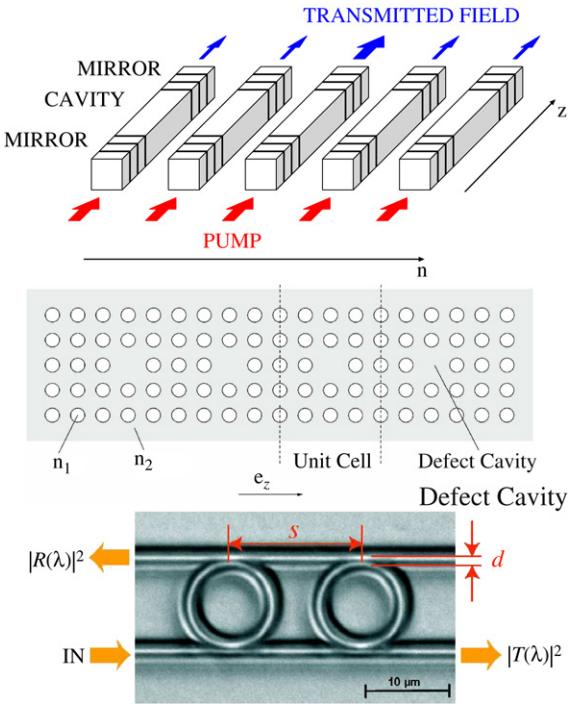


**Fig. 69.** Different setups of coupled optical resonators. Top: coupled semiconductor resonators with applied mirrors at the input and output facets of waveguides. Figure from [305]. Middle: periodically arranged defect cavities in a photonic crystal, figure from [407]. Bottom: coupled microring resonators. Figure from [404].

strongly reflected at small angles $k_x < \hat{k}$. The resonances in reflection appear precisely in this window, when the breather is present. For low intensities of the breather, resonant reflection is surrounded by two resonant transmission peaks (see solid black curve in Fig. 68(b)). Thus the Fano resonance should be detectable experimentally. First attempts to study these fine effects were reported by Linzon et al. [245], where nonlinear trapping and resonant transmission were observed when scattering light by light in local photonic structures.

Another possibility to improve the transmission contrast is to detune the frequencies of the breather and the probe beam. This would involve certain modifications in the corresponding model equations, more details can be found in Ref. [156].

And finally, a promising way to improve the contrast is to use spatially inhomogeneous nonlinear response, see chapter 10.3.

### *10.2.4. Coupled resonators*

A closely related and intensively developing subfield of nonlinear optics deals with coupled optical resonators. A straightforward generalization of the above waveguide array setups is given by a set of coupled resonators [305], where mirrors are applied to the input and output facets of the array, see Fig. 69(a). Other possible setups include periodically arranged defect cavities in photonic crystals and coupled microring resonators, see Fig. 69(b) and (c), respectively.

The corresponding theoretical models include dissipation, which is a principal ingredient of any resonator system. One of the simplest models is the driven and damped DNLS system [305], in which dissipative terms are taken to be linear in the field amplitude:

$$\left(\mathrm{i}\frac{\partial}{\partial\tau} + \Delta + \mathrm{i} + \gamma|E_n|^2\right)E_n + C(E_{n+1} + E_{n-1} - 2E_n) = A_n^{in}. \tag{10.17}$$

Here $\tau$ is the effective evolution coordinate, $E_n$ is the field amplitude in the $n$th resonator, $C$ is the coupling between adjacent resonators, $\Delta$ is the detuning from linear resonance, $\gamma$ is the nonlinear Kerr coefficient, and the damping term is rescaled to unity. The amplitudes $A_n^{in}$ of the input field (pump) can be inhomogeneous across the array.

In the case of a homogeneous pump $A_n^{in} = \text{const}$. Eq. (10.17) support different types of bright and dark stationary DBs, see Fig. 70. Due to dissipation, these objects no longer form families of solutions, but correspond to attractors in phase space. All the parameters of such DBs, including their amplitude and phase, are fully determined by the model parameters and the

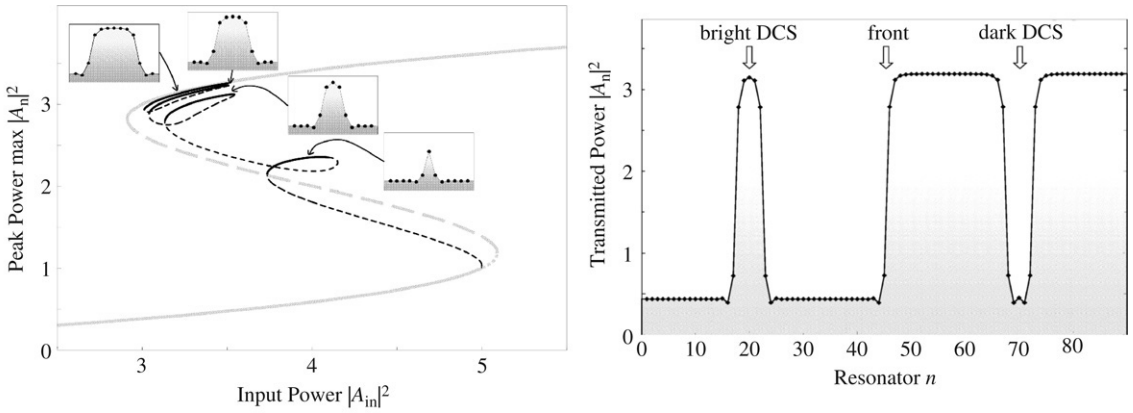


**Fig. 70.** Left panel: bifurcation diagram for the bistable homogeneous ground state of Eq. (10.17), gray lines, and different types of bright stationary DBs (black lines). Solid curves indicate stable solutions, dashed curves — unstable. Parameter values are: $\gamma = 1$, $\Delta = -3$, $C = 0.25$. Right panel: co-existence of different types of stationary DBs. Parameter values are: $\gamma = -1$, $\Delta = 3$, $C = 0.25$, $|A_n^{in}|^2 = 3.3$. Figures from [305].

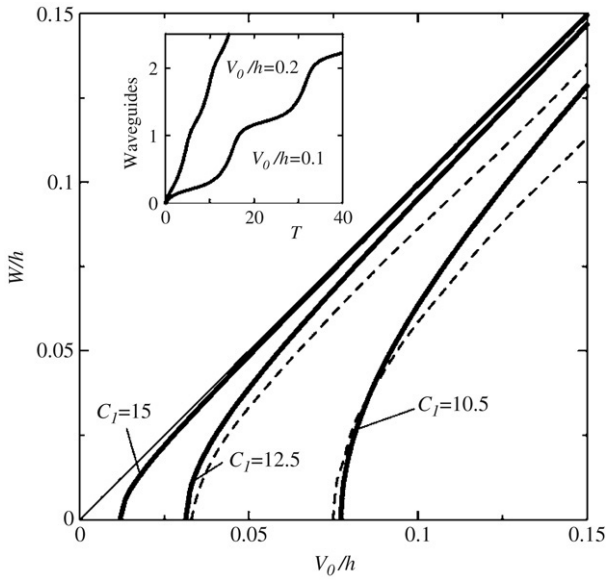


**Fig. 71.** Average velocity of a DB ($W/h$) *vs.* normalized tilt ($V_0/h$) for various coupling constants. The inset illustrates the position of the center of moving DBs for various tilts. Figure from [86].

pump (its amplitude and phase). Dissipation can suppress resonances with extended states of the system, which otherwise do not allow quasiperiodic and moving DBs to exist.

A tilted pump $A_n^{in} = a\exp(\mathrm{i}\phi_{in}n)$, which corresponds e.g. to an inclination of the incidence field in the setup in Fig. 69(a), induces a transverse force acting on a DB. This, in turn, can cause the DB to move across the array, see Fig. 71. The discreteness of the system hinders and, in some cases, prevents such motion [86]. Generally, there exists a critical value of the tilt $\phi_{in}^{(cr)}$, below which a given type of DB cannot move, see Fig. 71. This is in contrast to continuous systems, where the resulting velocity of a cavity soliton is linearly proportional to the tilt [100].

The nonlinear dependence of the DB velocity on the tilt $V(\phi_{in})$ in a vicinity of the critical point $\phi_{in}^{(cr)}$, allows for a ratchet motion of the DB. For that one needs a periodically changing tilt with zero average [154], see Fig. 72. The necessary condition for the observation of such a DB ratchet effect is the violation of certain symmetries of the system, which can be realized e.g. by applying a bi-harmonic variation of the tilt, or by a superposition of two pumps with varying tilts at different frequencies [154]. For adiabatically changing tilt(s) the average velocity of the resulting net motion of a DB can be estimated as $\bar{V} = \frac{1}{T}\int_0^{\mathrm{T}} V[\phi_{in}(\tau)]\mathrm{d}\tau$, where $T$ is the period of the tilt. The ratchet effect vanishes in the continuous limit, where the function $V(\phi_{in})$ becomes linear.

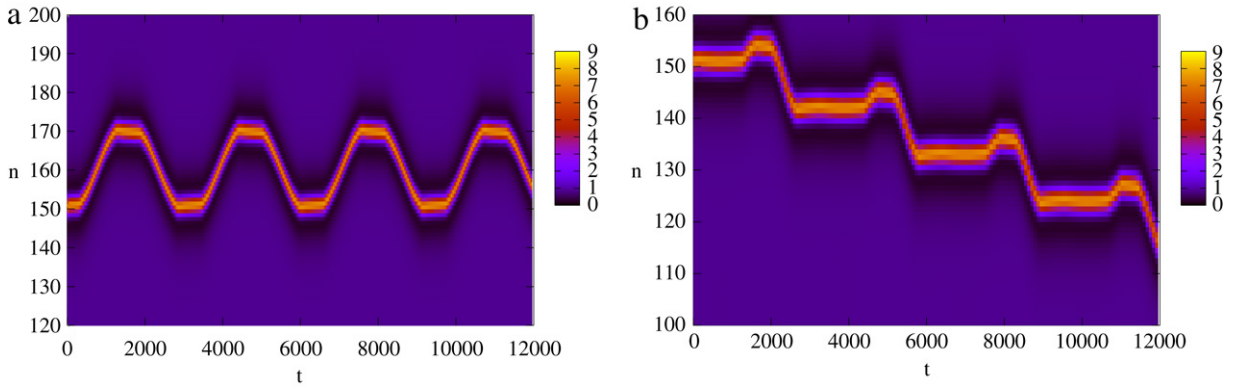


**Fig. 72.** Density plots of $|E_n|^2$ for DB motion under a periodically changing tilt of the input field. (a) Periodic motion of a DB under the influence of single-harmonic periodically changing tilt. (b) Ratchet motion of a DB under the influence of superimposed pumps with varying tilts at different frequencies. Figures from [154].

### *10.3. Ultracold atoms in optical lattices*

In the 1970s it was suggested that the Doppler effect due to thermal motion of atoms could be exploited to make them absorb laser light at different rate. The net momentum kick could be used to cool a gas of atoms. When implemented in the 1980s, that principle immediately led to cold gases at a few hundreds of micro-Kelvins. The spatial interference patterns created by the laser beams generates a three-dimensional periodic potential for the atoms.

Further use of magnetic dipole forces allowed the use of evaporative cooling and overcame fundamental limitations due to photon scattering. Temperatures as low as a few nano-Kelvins were reached, and large enough densities of the gas satisfied the conditions of Bose–Einstein condensation (BEC).

#### *10.3.1. Light-matter interaction*

The interaction between the atoms and the light field is based on the principle of the ac Stark effect. The oscillating electric field of the light induces an electric dipole moment in the atom. That dipole interacts with the electric field and as a result an energy shift $\Delta E$ of an atomic energy level takes place which is given by

$$\Delta E = -\frac{1}{2}\alpha(\omega)\langle E^2(t)\rangle \tag{10.18}$$

where $\alpha$ is the dynamic polarizability at frequency $\omega = \omega_{\rm res} + \delta$, $\omega_{\rm res}$ is the resonance frequency, and $\delta$ is the detuning of the light field from that resonance. For red-detuned light fields the dipole response will be in phase with the field, and the resulting optical potential will have minima where the light field amplitude is largest. Thus for a standing wave (generated by several interfering light beams with wavelength $\lambda$) a spatially periodic potential $V(x)$ will be generated for the atoms:

$$V(x) = V_0 \cos^2(2\pi x/\lambda). \tag{10.19}$$

Note that such potentials can be easily generated in one, two and three spatial dimensions, with various symmetry properties. An atom in such a potential is absorbing and reemitting photons through virtual transitions. That process is dissipative by nature and leads to a scattering rate of photons by atoms of the order $1/\delta^2$. However the potential well depth scales like $1/\delta$, which means that for large detuning the scattering is negligible, and the atom cloud moves in the optical potential almost like a conservative system (for more details see Morsch et al. [286]).

#### *10.3.2. Basic principles and modelling*

The general way of describing N interacting atoms (bosons) in a periodic potential is to consider the corresponding Schrödinger equation of the many-body wave function $i\hbar\partial\hat{\Psi}/\partial t = \hat{H}\hat{\Psi}$. The interaction results from binary collisions, which are characterized by the $s$-wave scattering length $a_s$. The Hamiltonian reads

$$\hat{H} = \int {\rm d}x\hat{\Psi}^\dagger(x)\left[-\frac{\hbar^2}{2m}(\partial/\partial x)^2 + V(x)\right]\hat{\Psi}(x) + a_s\hbar\omega_t\int {\rm d}x\hat{\Psi}^\dagger(x)\hat{\Psi}^\dagger(x)\hat{\Psi}(x)\hat{\Psi}(x). \tag{10.20}$$

Here it is assumed, that atoms are confined in a cylindrically symmetric trap with a transverse trapping frequency $\omega_t$. For low enough temperatures and not too strong interactions, the remaining energy scales are smaller than the energy splitting of the transverse vibrational states $\hbar\omega_t$. Then only the lowest transverse (ground)state will be occupied. The trapping along the $x$-direction is neglected, assuming that its characteristic length scale is orders of magnitude larger than the laser light wavelength $\lambda$.

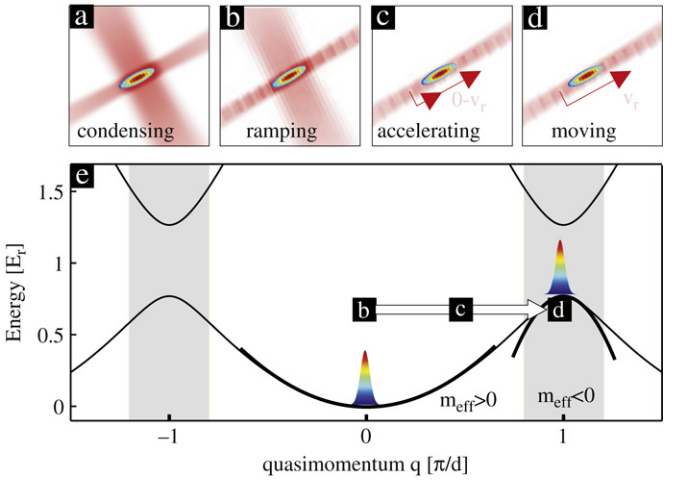


**Fig. 73.** (a) Top view of the crossed dipole trap geometry. (b) Ramping the periodic potential. (c), (d) Preparation of the band edge state. (e) Dispersion relation for the two lowest bands of the periodic potential. Figure from [87].

At the experimentally reachable nano-Kelvin temperature range the de-Broglie wavelength of individual atoms becomes larger than the average distance between pairs of them. In that case, the atoms condense into a macroscopical quantum state — the Bose–Einstein condensate (BEC). Within a mean field approach one replaces operators by expectation values and arrives at the Gross–Pitaevskii equation for the mean field $\psi(x, t)$:

$$i\hbar\frac{\partial}{\partial t}\psi = \left(-\frac{\hbar^2}{2m}\frac{\partial^2}{\partial x^2} + V(x)\right)\psi + 2a_s\hbar\omega_t|\psi|^2\psi. \tag{10.21}$$

This equation is the nonlinear Schrödinger equation in the presence of an external space-periodic potential $V(x)$. When neglecting the nonlinear term, it is reduced to a linear Schrödinger equation in a periodic potential. The spectrum will be a band structure of eigenvalues, with infinitely many bands. For low enough temperatures only a finite number of bands will have to be considered. Restriction to a finite number of bands reduces the problem to a lattice. In the extreme limit of just one (lowest) band, adding nonlinearity back will yield the discrete nonlinear Schrödinger equation.

### *10.3.3. Gap solitons with repulsive interaction and nonlinear self-trapping*

Using about 1000 $^{87}$Rb atoms, Eiermann et al. [87] prepared a BEC state with Bloch momentum $q = 0$ in the ground state of the lowest band (see Fig. 73). After that a ramping, accelerating and moving of the periodic potential allows the Bloch momentum to be adiabatically changed towards the band gap value $q = 2\pi/\lambda$. The atoms are repulsively interacting with each other. In a spatially homogeneous case, there would be no reason for the atoms to stay close, as they could lower their energy by increasing their distance (and thus lowering the density). However the lowest band has a finite width, and thus each atom can only take a finite amount of kinetic energy, which is given by the width of that band. If that energy is lower than the interaction energy of an atom with the rest of the atomic cloud, energy conservation forbids the escape of that atom. It will thus stay inside the cloud. Since this is true for each atom, finally a localized state persists, which is coined a gap soliton (or discrete soliton, or discrete breather). The experimental observation is shown in Fig. 74. A theoretical study of that case, as well as of self-trapping in higher dimensional optical lattices, was recently performed by Xue et al. [405].

In a subsequent experiment by Anker et al. [13] the dynamics in the lowest band was studied. The initially localized state would spread (as a usual wave packet) in the linear case. Experimentally this is realized by reducing the number of atoms (and thus the density). In the presence of interactions the corresponding nonlinear state will radiate a part of the atoms, while a substantial part will stay trapped in a localized state which is close to an exact discrete breather solution. This effect was observed by increasing the number of atoms in the BEC [13].

### *10.3.4. Self-trapping in the dimer*

In a further experimental study the $^{87}$Rb BEC was loaded onto a lattice containing just two sites, i.e. a double well potential [8]. Different asymmetries in the populations of the wells for the initial state were prepared by distorting the potential, giving the BEC time to relax, and finally by nonadiabatically ramping the potential back to its symmetric shape (Fig. 75).

The observed features are captured by the simple dimer model from chapters 1.1 and 9.2. If the initial state is weakly asymmetric, oscillations between both wells are observed, which are obtained from linearizing the dimer equations around

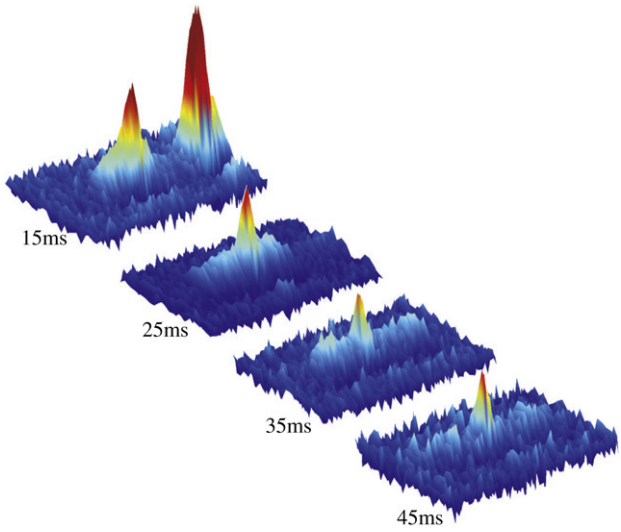


**Fig. 74.** Observation of a gap soliton. The atomic density is shown for different propagation times. Excessive atoms are radiated and disperse (right peak at 15 ms). The remaining peak corresponds to an immobile gap soliton. Figure from [87].

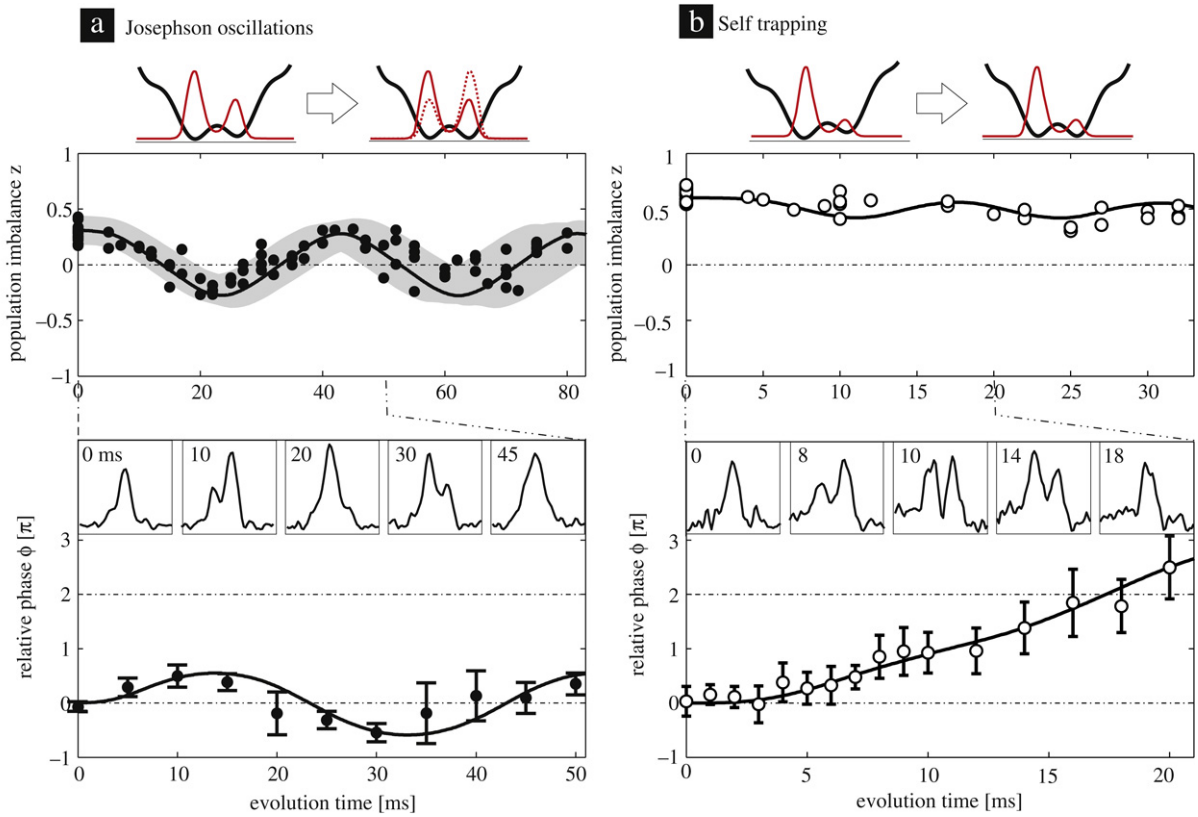


**Fig. 75.** Population imbalance and relative phase of the BEC in the two wells of the double well potential. (a) Initial state is weakly asymmetric, and fast oscillations of the BEC are observed (note that the oscillation period is an order of magnitude higher than the estimated one for noninteracting atoms; this is due to the frequency renormalization by nonlinearity, which is proportional to the number of interacting atoms). (b) Initial state is strongly asymmetric, and self trapping (localization) is observed in the initially populated well. Figure from [8].

a time-periodic state $\Psi_1 = \Psi_2$. The experimental realization shows a strong renormalization of the resulting oscillation frequency due to the nonlinearity, which is tuned in the experiment by the number of participating atoms (see Fig. 76). If the initial state is strongly asymmetric, e.g. $\Psi_2 = 0$, then the time evolution will keep the state close to a symmetry broken periodic orbit (1.6).

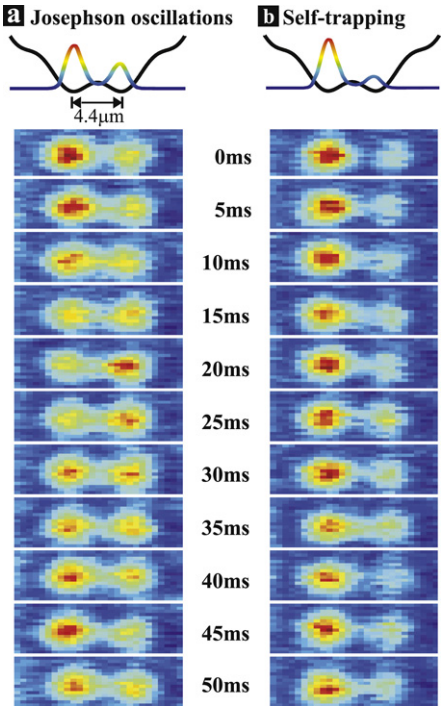


**Fig. 76.** Observation of the tunneling dynamics of two weakly linked Bose–Einstein condensates in a symmetric double well potential. (a) Fast oscillations due to weak asymmetry of the initial state. (b) No oscillations due to strong asymmetry of the initial state. Figure from [8].

Recently the ac and dc Josephson effects were explored for a two mode BEC [240]. The quantum analogue of self trapping (for two interacting atoms) was observed in Ref. [144].

*10.3.5. Fano blockade by a BEC*

We continue with a recent proposal to utilize a discrete breather state with a BEC for observing Fano resonances in the scattering of ultracold atoms. To describe the dynamics of the BEC, it is assumed that only the lowest band has to be taken into account [393]. Without further manipulations, that would correspond to considering the scattering problem by a DNLS breather discussed in Section 5.4. Note however that the Fano resonance is obtained there on a background of a very small transmission (of the order of $10^{-8}$). The idea then is to manipulate the BEC in the optical lattice, such that the interaction between the atoms (i.e. the nonlinearity in the Gross–Pitaevskii equation) takes place in a spatially confined region. This is in principle possible by e.g. applying spatially varying magnetic fields, which sensitively tune the $s$-wave scattering length [393] (see Fig. 77). The corresponding modified DNLS equation is given by

$$\mathrm{i}\frac{\partial \Psi_n}{\partial t} = -(\Psi_{n+1} + \Psi_{n-1}) - \gamma |\Psi_{n_c}|^2 \Psi_{n_c} \delta_{n,n_c}. \tag{10.22}$$

The localized BEC state is given by $\Psi_n(t) = b_n(t) = b_{n_c} x^{|n-n_c|} \exp(-\mathrm{i}E_b t)$, where $b_{n_c}$ is the condensate amplitude, $|x| < 1$, and $E_b$ is the respective energy:

$$E_b = -\sqrt{4+g^2} \quad \text{and} \quad x = -(E_b + g)/2. \tag{10.23}$$

The parameter $g \equiv \gamma b_{n_c}^2$ ($g > 0$).

The scattering analysis goes along the lines of the DNLS case from Section 5.4, with a slight change in the outcome for the transmission:

$$T(k) = \frac{4\sin^2 k}{4\sin^2 k + \left(2g + \frac{g^2}{\sqrt{(E_k - 2E_b)^2 - 4} - 2g}\right)^2}, \tag{10.24}$$

where $E_k = -2\cos k$. Resonances occur when the denominator diverges or when $\sqrt{(E_k - 2E_b)^2 - 4} - 2g = 0$. The condition for the resonance is

$$E_k = E_L \Rightarrow k_L \equiv \arccos(-E_L/2). \tag{10.25}$$

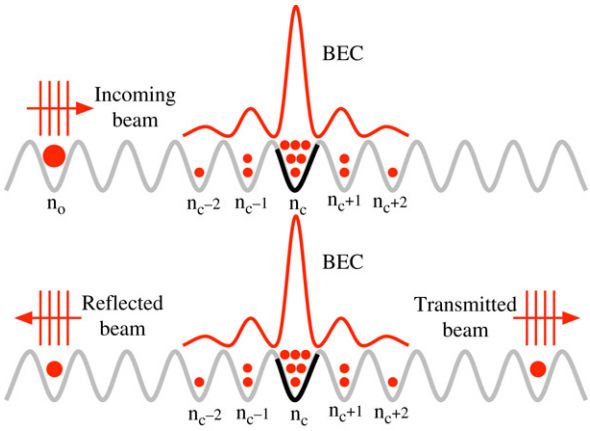


**Fig. 77.** Scattering scheme in the optical lattice. The atoms interact only around $n = n_c$, where the BEC is centered. Figure from [393].

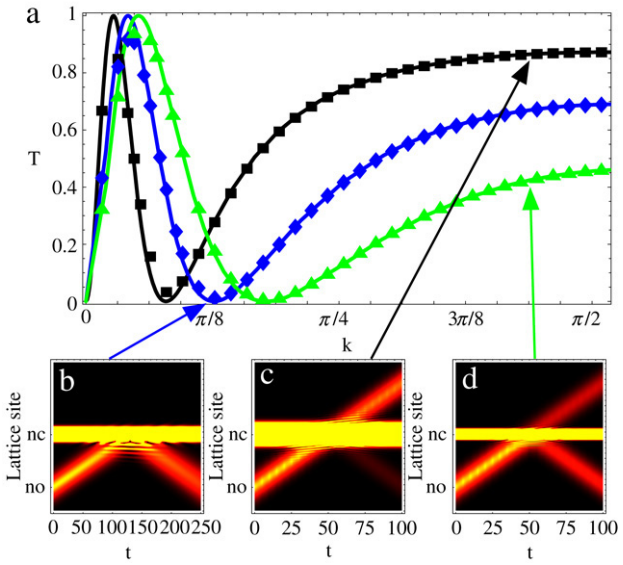


**Fig. 78.** $T$ versus $k$ for the three values of $g$. Lines: Eq. (10.24), points: real time numerical simulations of Eq. (10.22) for $g_1 = 0.36$ (boxes), $g_2 = 0.6$ (diamonds), and $g_3 = 0.9$ (triangles). (b)–(d) Evolution of $|\Psi_n(t)|^2$ in space and time: (b) $g_2$, $k = 0.39$, (c) $g_1$, $k = 1.37$, (d) $g_3$, $k = 1.37$. Figure from [393].

The Fano resonance of zero transmission is now taking place on a background of transmission of the order of 0.5–1 (Fig. 78). The comparison with the scattering of wavepackets shows excellent agreement. Finally, more realistic calculations demonstrate that the effect is robust with respect to an increase of the size of the spatial region in which the atoms interact [393].

### *10.3.6. Repulsively bound atom pairs*

Winkler et al. [401] performed experiments with a three-dimensional optical lattice with initially each site being either not occupied, or being occupied by two Rb atoms bound in a pair due to attractive interaction. A magnetic field sweep across the Feshbach resonance changes the sign of interaction, turning attraction into repulsion. The dynamics of ultracold atoms loaded into the lowest band of the optical potential is described by the quantum DNLS model, which is equivalent to the Bose–Hubbard model (9.1). Lifetime measurements have shown, that repulsive pairs of Rb atoms have larger lifetimes than pairs of weakly or almost non interacting atoms (Fig. 79). The two-particle bound states discussed in chapter 9.1 — the simplest versions of a quantum discrete breather — are the obvious explanation of the experimental findings. Indeed, neglecting Landau–Zener transitions to higher lying bands in the optical potential, the Bose–Hubbard model is justified. The sign of the interaction does not play any role, since it only changes quantum discrete breathers from being low-lying to being excited states, not affecting their localization properties. The most simple argument of why two quanta (or atoms) placed initially close to each other, do not separate despite repelling each other, is based on the fact, that if they were to do so, the (large) interaction energy would be converted into kinetic energy, which is restricted to be less than two times

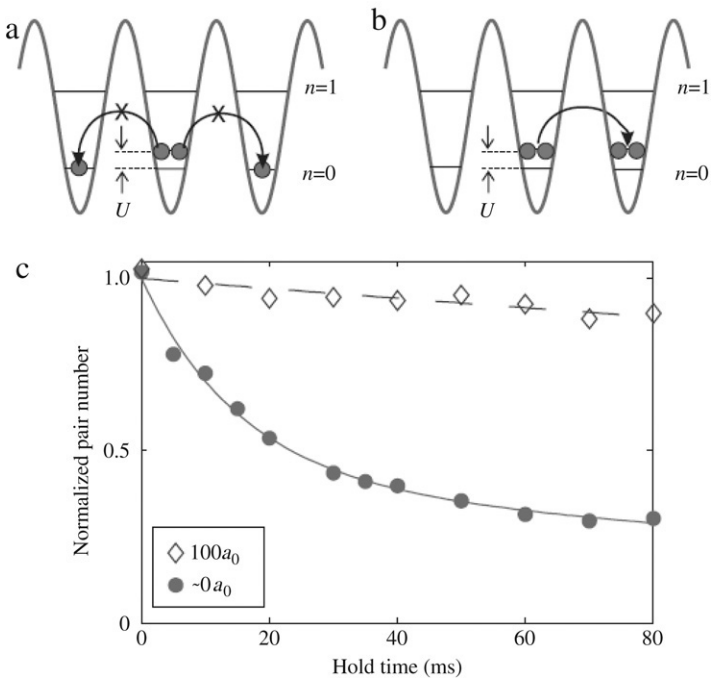


**Fig. 79.** (a) Repulsive interaction between two atoms sharing a lattice site gives rise to an interaction energy $U$. Breaking up of the pair is suppressed owing to the lattice band structure and energy conservation. This is the simplest version of a quantum discrete breather. (b) The discrete breather can tunnel along the lattice. (c) Long lifetimes of strongly repulsive atoms. The plot shows the remaining fraction of pairs for strong interaction (open diamonds) and for almost vanishing interaction (filled circles). Figures from [401].

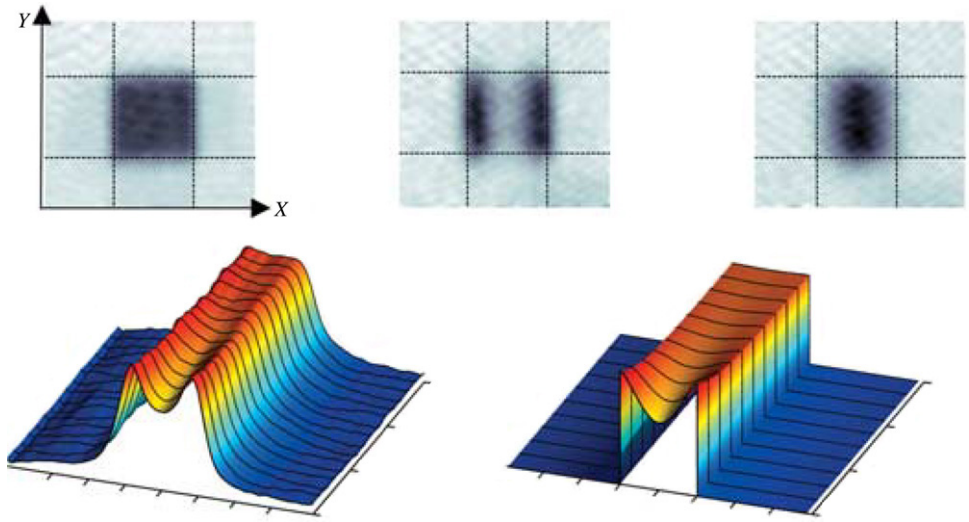


**Fig. 80.** (Upper row) Absorption images of the atomic distribution after release from the 3D lattice and a subsequent 15 ms time of flight. The horizontal and vertical black lines enclose the first Brillouin zone. (upper left) Lattice sites are occupied by single atoms; (upper middle) Repulsively bound atom pairs; (upper right) Attractively bound atom pairs; (bottom row) Quasi-momentum distribution for pairs in one direction as a function of the lattice depth after integrating out the other direction. (bottom left) Experiment; (bottom right) Numerical calculations. Figure from [401].

the width of the single particle band. In other words, repulsively bound atom pairs are a straightforward consequence of quantum discrete breather states with two quanta.

Another sophisticated experimental investigation aimed at measuring the quasi-momentum distribution of atom pairs in various regimes by mapping it onto a spatial distribution, which was finally measured using standard absorption imaging (Fig. 80). Therefore predictions of such states, which were made more than 30 years ago by Ovchinnikov [298], were beautifully confirmed experimentally with ultracold repulsive atoms.

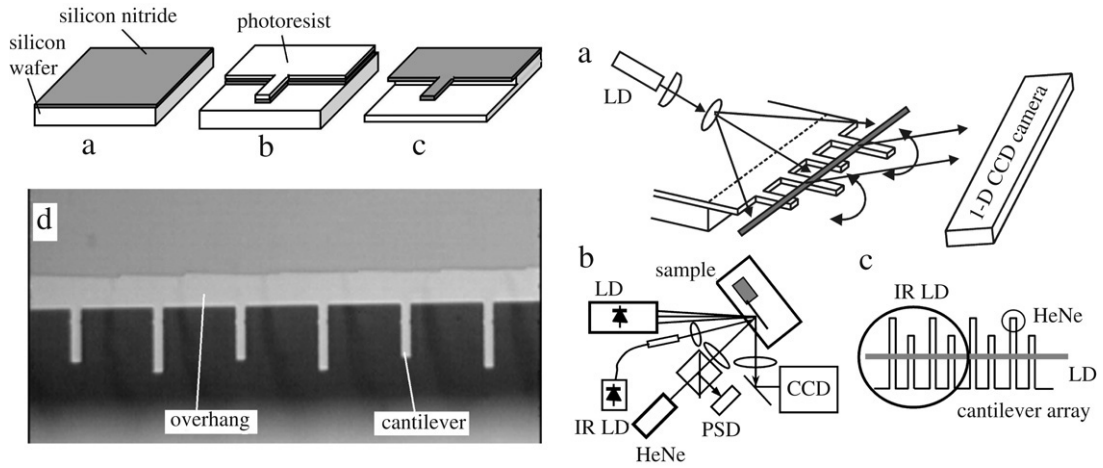


**Fig. 81.** Left plot: Fabrication of a micromechanical array. (a) Silicon nitride deposition; (b) photolithography and plasma etching; (c) KOH wet etching; (d) Microscope image of the top view. Right plot: Experimental setup. (a) a low power laser beam probes the motion of cantilevers, the reflected image is detected by a CCD camera; (b) complete optical arrangement. An infrared laser diode heats locally few elements to produce movable impurities; (c) schematic representation of three kinds of laser images. Figures from [348].

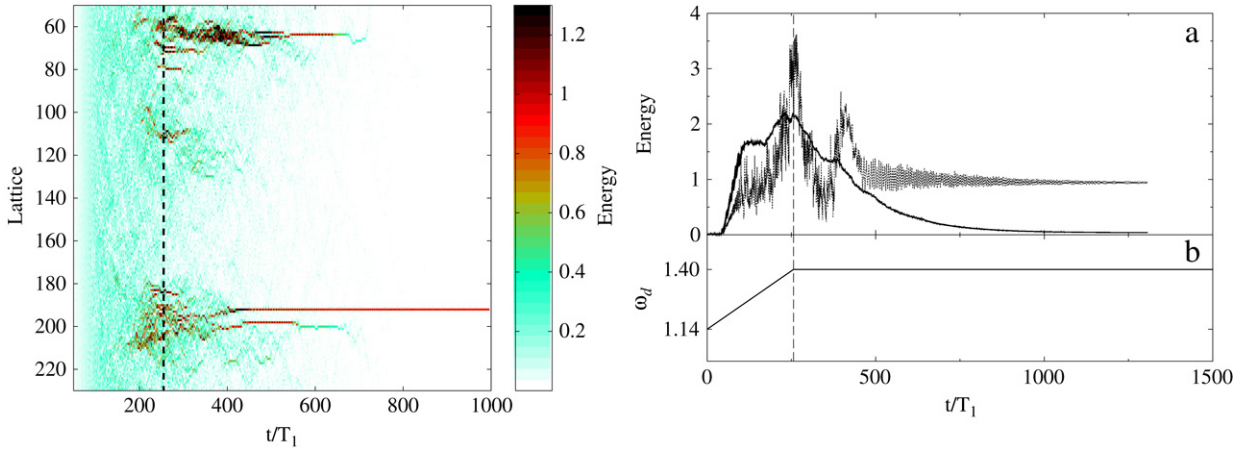


**Fig. 82.** Left plot: Energy density as a function of time. The driving frequency is initially ramped from $\omega_d = 1.14$ to $\omega_d = 1.4$, and then it remains fixed (marked by the vertical dashed line). Energy pumping is observed during the ramping. At the end of the ramping process, breathers are created, and one of them locks to the driving and survives. Right plot: (a) Average energy per oscillator as a function of time (solid line, scaled by a factor of 10 for better observation) and the energy of the locked oscillator (strongly fluctuating dotted line). (b) The frequency ramping scheme. After the vertical dashed line the driving frequency remains constant. Figures from [256].

### *10.4. Driven micromechanical cantilever arrays*

Experiments on silicon-nitride cantilever arrays have been successful in providing data on the existence of discrete breathers [350], as well as on a number of their properties [347,349,353], and are of interest for the design of coupled nano-electro-mechanical system (NEMS) structures, used for the generation of microinstruments for high-precision measurements. These silicon micromachines usually involve a dense array of identical meso-scale units on a chip.

#### *10.4.1. Sample preparation*

The cantilever arrays are produced using standard optical lithography techniques (see left plot in Fig. 81, where (d) shows a top view of the resulting structure). The width of the overhang provides a coupling mechanism between the individual cantilevers, which are excited into oscillating states. Their thickness is about 300 nm, while their length and distance to each other is of the order of 50 $\mu$m.

The length of the cantilevers can be alternating — short, long, short etc, which is seen in the left plot (d) in Fig. 81. In addition a gold film can be deposited on the cantilevers. Applying a bias voltage between the gold and the conductive silicon substrate will strongly modify the nonlinear vibrational properties of the cantilevers. For zero voltage the frequency of the cantilever oscillation increases with its amplitude (hard anharmonicity). For nonzero voltage this dependence can be

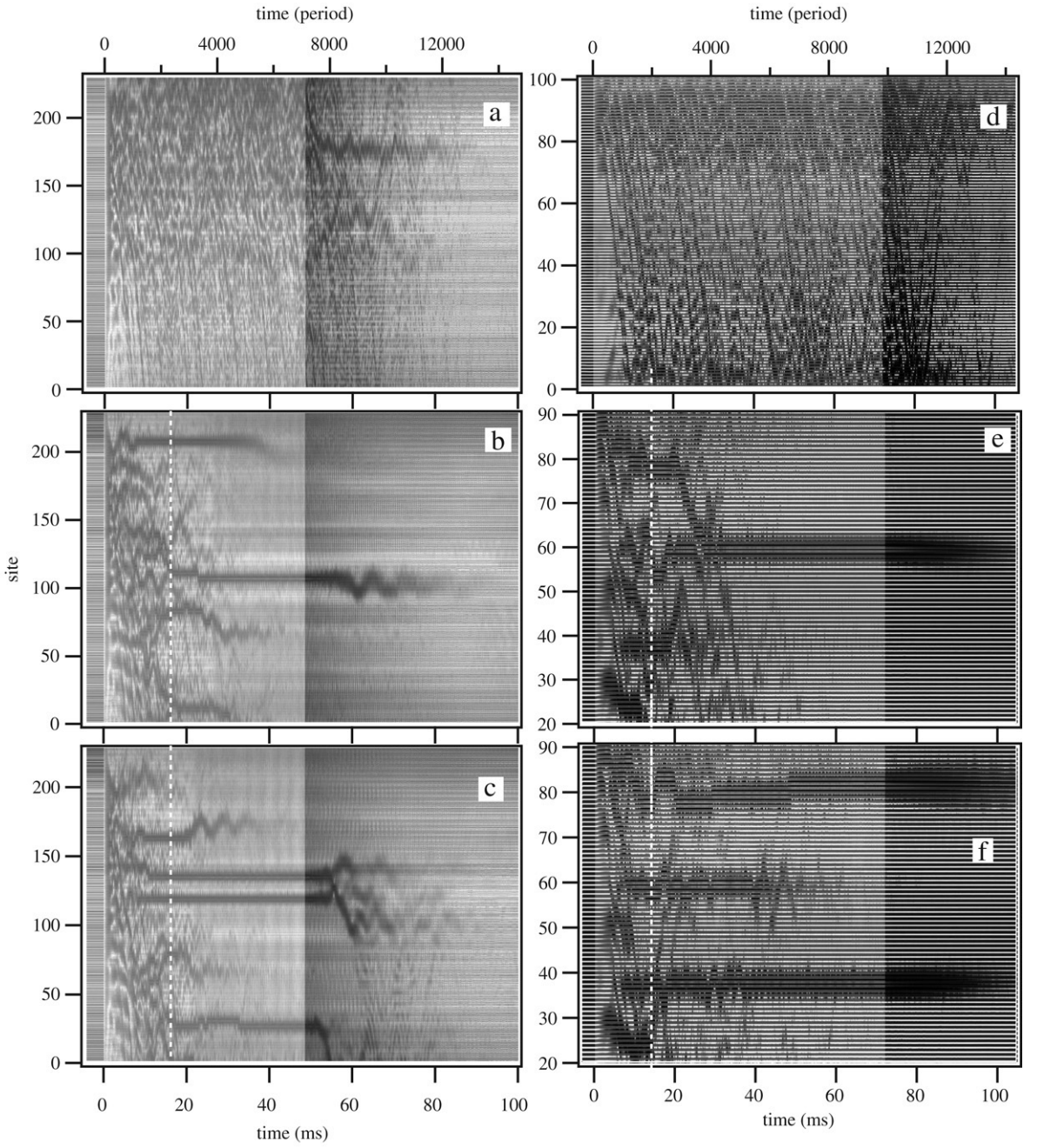


**Fig. 83.** Cantilever excitations vs time showing the production, interaction and decay of discrete breathers (ILM). (a)–(c): 248 elements, (d)–(f): 152 elements. Only a fraction of the array is shown. The dark regions identify localized excitations. Some of them become trapped during the cw phase. Figure from [348].

changed such that the frequency decreases with increasing amplitude (soft anharmonicity) [348]. The oscillation frequency for small amplitudes is of the order of 100 kHz.

### *10.4.2. Basic principles and modelling*

Experiments are performed by mounting the sample in a vacuum chamber to a piezoelectric transducer. A HeNe beam is focused on the cantilever, reflected from it, and directed to a position sensitive detector CCD camera to measure the linear vibrational response. The speed of the camera, about 18 kHz, is insufficient to monitor the actual oscillation of the cantilevers (with frequencies of the order of 100 kHz); however, it can measure the vibrational envelope. If a cantilever is performing

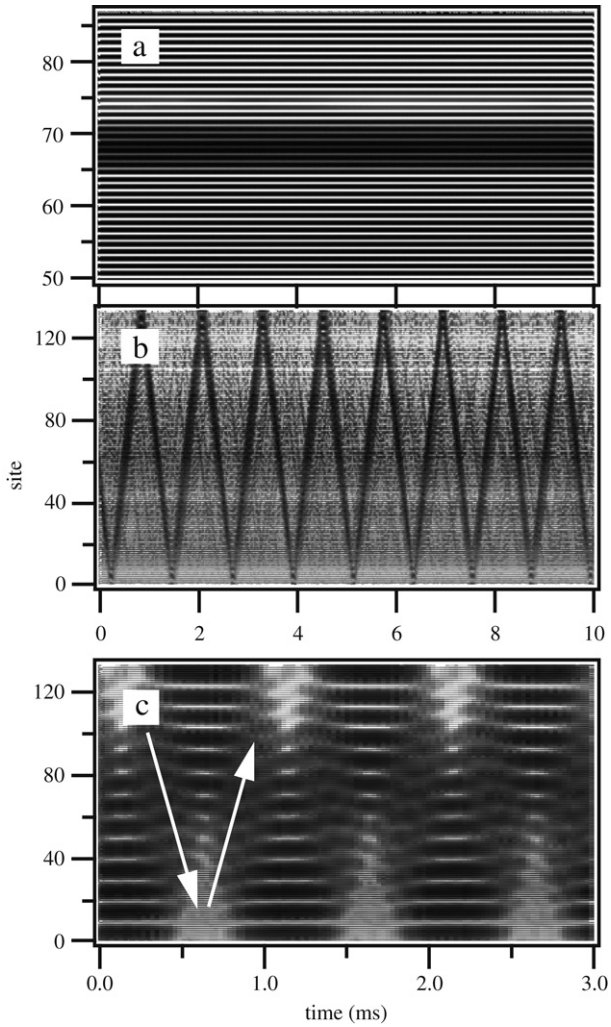


**Fig. 84.** Several kinds of breathers (ILM) produced experimentally with the driver at different frequencies. (a) A stationary bright ILM is recorded as a thick black horizontal band, (b) a bright traveling ILM as a dark zigzag pattern, (c) a dark traveling ILM zigzag pattern is identified by the arrows. In the region where the dark ILM travels, the large amplitude standing wave pattern vanishes. Driving frequencies: (a) 138 kHz, (b) 110 kHz, (c) 81 kHz. Figure from [353].

small amplitude oscillations, more light is detected, than when it is performing large amplitude oscillations. Images show corresponding light regions (weakly excited cantilevers) and dark regions (strongly excited cantilevers).

The theoretical modelling for the oscillation of a single cantilever follows the Euler-Bernoulli beam theory and one arrives at an anharmonic oscillator equation [348]. The overhang mediates an interaction between cantilevers via damped acoustic waves. The simplest model of the driven cantilever array accounts for nearest neighbour interaction only, and reads in dimensionless variables [256]

$$\ddot{x}_l + \gamma \dot{x}_l + a_2 x_l + a_4 x_l^3 - C(x_{l+1} + x_{l-1} - 2x_l) = A(t). \tag{10.26}$$

The oscillator displacements $x_l$ describe the deflection angle of the $l$th cantilever from its equilibrium position. The hard-type anharmonicity tends to increase the oscillation frequencies with growing amplitudes. This model neglects the influence of longer than nearest neighbour interaction range, which is not crucial for the understanding of the main qualitative DB properties. The dimensionless parameters are related to the ones of the experiment in Ref. [348]. Using them and setting $a_2 = a_4 = 1$, the friction and coupling parameters become $\gamma = 1.534 \times 10^{-4}$ and $C = 0.07953$. The spatially uniform ac driving $A(t) = A_0 \cos(\omega_d t)$ in (10.26) is generated by a corresponding piezoelectric crystal vibration in the original experiments. The analysis of the nonlinear response manifold of Eq. (10.26) yields that stable discrete breather states are not directly connected to the stable branch of extended low-amplitude oscillations [256]. To excite them one has to rely on fluctuations. That can be done by ramping the driving frequency across the upper band edge of linear oscillations, where modulational instability is expected [348]. The results are shown in Fig. 82.

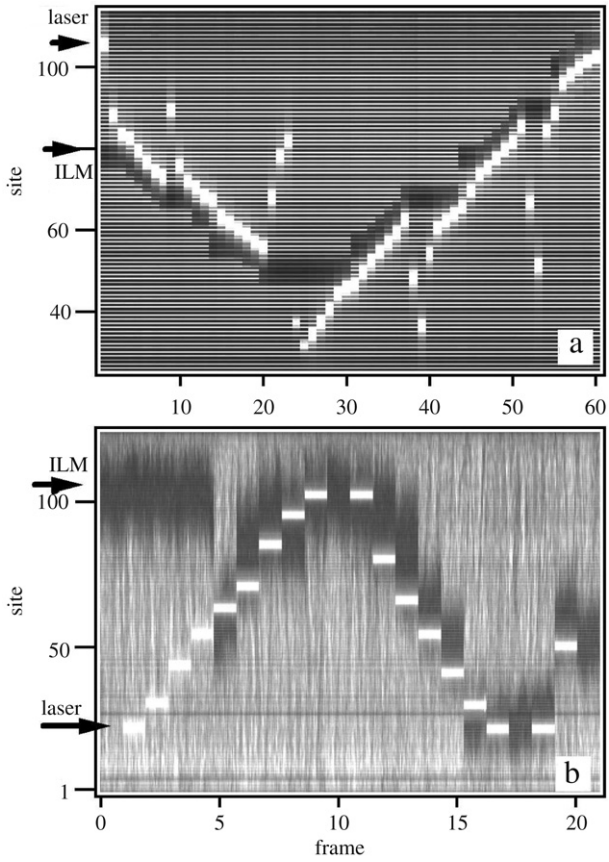


**Fig. 85.** Laser manipulation of a discrete breather (ILM) in cantilever arrays with different signs of anharmonicities. The dark region in each picture corresponds to a highly excited breather (ILM). (a) Repulsive interaction with hard anharmonicity. As the laser spot approaches, the breather (ILM) is repelled and hops away. When the laser spot is far away, the breather (ILM) remains fixed. (b) Attractive interaction with soft anharmonicity. The breather (ILM) is attracted and captured by the laser spot. As the laser spot moves, so does the captured breather (ILM). When the laser is turned off, the breather (ILM) remains fixed. Figure from [349].

### *10.4.3. Detecting stationary and moving discrete breathers*

Experimental observations of localized excitations in cantilever arrays are shown in Fig. 83. The plot shows the cantilever amplitudes versus time for two different arrays. The initial cantilever positions are identified by the horizontal lines to the left of the $t = 0$ time marker. The darker region of the pictures beyond 49 ms for (a)–(c) and 72 ms for (d)–(f) indicates that the cw driver is turned off. Fig. 83(a) shows the cantilever excitation with a high-power PZT driver frequency being fixed at the top of the small amplitude frequency spectrum (136 kHz). No particular pattern is evident. A breather-like excitation (ILM) forms after the CW driver is switched off around the cantilever 170, but it decays again quite fast. In Fig. 83(b), (c) the driver is chirped from slightly lower (99.86%) to slightly higher (101.6%) frequencies over a time interval of 16 ms. Formation of discrete breathers (ILM) is evident. These two different experimental runs show that breathers (ILM) form at different sites, which excludes potential randomness in the array as a primary cause. As expected these localized excitations (ILM) die out, once the driver is switched off. A similar picture is also observed for a different array with fewer cantilevers, see Fig. 83(d)–(f).

In another experiment [353], the driver frequency is still chirped up, but all its values may be located inside the spectrum of small amplitude waves. In that case one observes a transition from the generation of stationary locked breathers (ILM) as seen in Fig. 84(a), to a breather-like excitation which is traveling and reflects at the ends of the array (Fig. 84(b)), down to the case of a so-called dark ILM, or simply a localized depletion of an overall excited array, which also travels and reflects (Fig. 84(c)).

### *10.4.4. Optical manipulation by laser guiding*

By adding an electrode to one of the cantilevers in an array, the anharmonicity can be changed locally, and breathers (ILM) are attracted by the impurity. This concept has been extended by generating an optically-induced real-time impurity. It has been realized using a fiber-coupled IR diode laser (50–100 mW) which generates a 200 micron hot spot and heats a few cantilevers in the array. The heating decreases the Young's modulus and hence the spring constant. Both repulsive

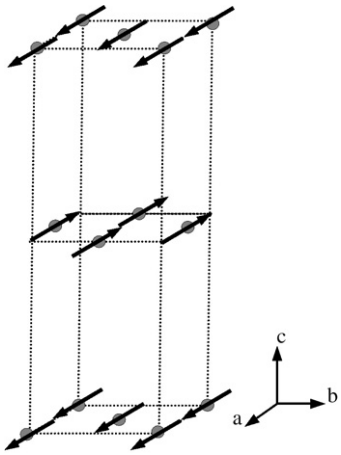


**Fig. 86.** Lattice and spin structure of $(C_2H_5NH_3)_2CuCl_4$. Circles denote $Cu^{2+}$ ions and arrows indicate spin configuration in the antiferromagnetic state. Only $Cu^{2+}$ ions are shown in this layered, face centered, orthorhombic compound. The easy, second easy, and hard spin axes are labeled the *a*, *b* and *c* crystal directions, respectively. Figure from [352].

and attractive interactions between the laser spot impurity and a discrete breather (ILM) have been reported [349], and are shown in Fig. 85. The arrows on the left identify the breather (ILM) and laser starting points.

### *10.5. Antiferromagnetic layered structures*

Spin waves in magnetic media have already been used to analyze nonlinear phenomena and soliton dynamics in condensed matter for several decades [225]. Both interactions between spins and spin anisotropy are intrinsically nonlinear, giving rise to different types of nonlinearities in the corresponding macroscopic phenomenological models. Dissipation of spin waves is usually rather weak, as compared e.g. to vibrational modes in crystals. Thus magnetically ordered crystals are good candidates for experimental studies of various types of nonlinear waves. The underlying lattice structure can lead to novel localized spin excitations, as discussed in Section 8.

#### *10.5.1. Layered antiferromagnets*

Below the Néel temperature of a layered antiferromagnetic crystal ($\sim$10 K for a $(C_2H_5NH_3)_2CuCl_4$ crystal) the spin 1/2 ions are oriented along the easy-axis in alternating sheets, as illustrated in Fig. 86. The intralayer ferromagnetic coupling between the spins is much stronger than the interlayer antiferromagnetic coupling (the antiferromagnetic to ferromagnetic exchange fields ratio is $\sim 10^{-3}$ for the $(C_2H_5NH_3)_2CuCl_4$ crystal at 1.4 K [352]), so that the system is effectively one-dimensional. The anharmonicity associated with the antiferromagnetic coupling is soft, so that an effective external on-site potential is needed to create a gap below the small amplitude spin waves spectrum for localized excitations to exist. This potential is provided by the anisotropic ferromagnetic exchange interaction between spins within a layer [237].

Because of the weak antiferromagnetic coupling between the layers, the total spin in each layer can be represented by a classical macroscopic spin $S_n$, for which the one-dimensional spin lattice model, Eqs. (8.1)–(8.3), applies. Different types of discrete breathers in this model have been discussed in Section 8.

#### *10.5.2. Detection of discrete breathers (ILMs)*

Due to the atomic scale of the spin lattice it is experimentally difficult to excite a localized excitation at a given location inside the crystal. Instead, one can drive the crystal with a continuous microwave. Extended spin waves are excited, which then break up into localized excitations as a result of modulational instability. Lai and Sievers have performed the modulational stability analysis of extended waves in easy-axis antiferromagnetic chains and determined that the uniform excitation ($q = 0$ mode) is unstable [235]. This has lead to the proposal of experimental investigation of discrete breathers in antiferromagnetic crystals [234,236]. By using molecular dynamics simulations with realistic parameters computed for two different crystals and with the account of dissipation, Lai et al. [234], and Schwartz et al. [363] have investigated the long time evolution of the unstable continuous wave with added noise and observed spontaneous formation of localized structures accompanied by an asymmetric spectral broadening, with the formation of spectral peaks inside the gap.

The optimal conditions for experimental observation of discrete breathers (ILMs) have been reported for the $(C_2H_5NH_3)_2CuCl_4$ crystal [234]. Rod-shaped samples (directed along the *c*-axis in Fig. 86) with typical dimensions $3 \times 3 \times 0.5$ mm$^3$ have been used in experiments. The lowest antiferromagnetic resonance (AFMR) frequency for these samples is located around 1.5 GHz [234], which allows the use of a laboratory microwave cw field as the driving source. Some tuning of the AFMR frequency is possible by applying a dc magnetic field along the easy or second-easy axis [95]. The overall experimental setup is schematically shown in the left panel of Fig. 87. The first oscillator produces a spectrally narrow

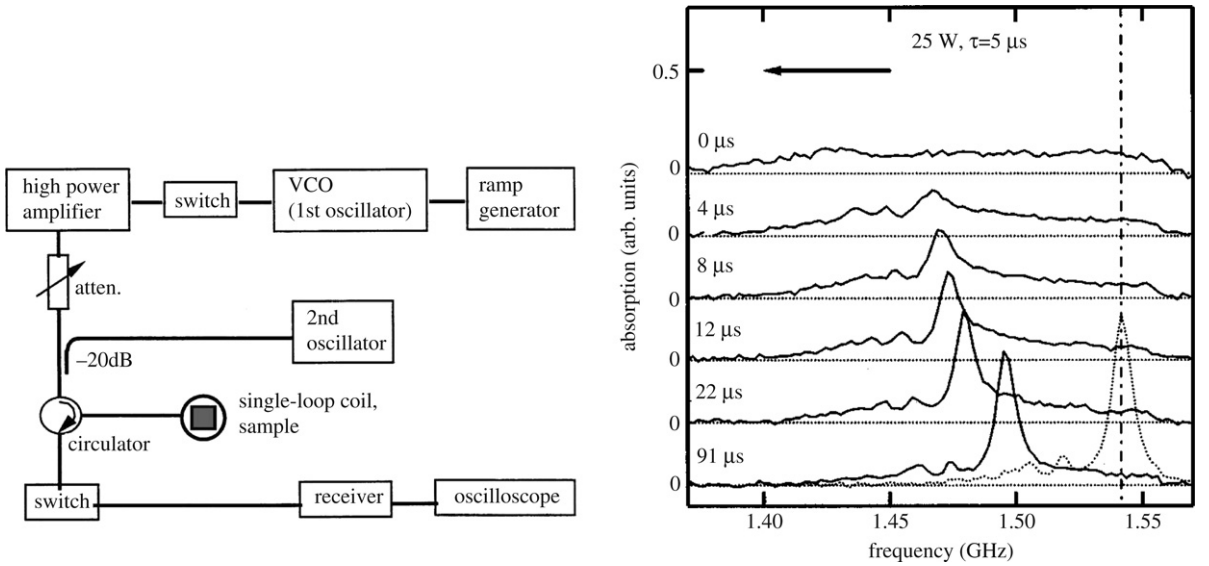


**Fig. 87.** *Left panel*: Schematic experimental setup for the measurement. An intense chirped microwave pump pulse is produced by a high power amplifier driven by a voltage-controlled oscillator. A low power cw microwave probe from a tunable second oscillator is coupled to the single-loop coil through a circulator. The reflected probe signal is detected by a spectrum analyzer, used as a receiver tuned to the second oscillator, and recorded by an oscilloscope. The switch before the spectrum analyzer eliminates the pump. All switches, the ramp generator, and the oscilloscope are synchronized by a pulse generator (not shown). *Right panel*: Time development of the absorption spectrum after the excitation pulse. The time sequence after the end of the 5 ms pulse is identified in the figure. The dotted spectrum is a low power trace before the pulse. The pulse chirping from 1.45 to 1.40 GHz is indicated by the arrow. Peak pulse power: 25 W; width: 5 ms. Figures from [95].

driving field, amplified to a maximum power of 40 W before being applied to the crystal. The second oscillator generates a weak continuous wave tunable signal (within a wide spectral range below the excitation frequency), used for pump-probe measurements. After removing the reflected pump pulse by a switch, the reflected probe signal is detected by a receiver and recorded by an oscilloscope. Spectra are obtained by recording the reflected power as a function of time at fixed frequency and then incrementing the frequency of the probe oscillator.

While the initial experiments reported in Ref. [234] did not provide sufficient information about formation of discrete breathers (ILMs) due to long driving pulse lengths used (400 μs) and limited time resolution (20 μs), significant improvements were reported in the subsequent set of experiments with shorter driving pulses [95]. Typical spectra measured at different time instants after the initial excitation with the intense 5 μs chirped pulse are shown in the right panel of Fig. 87. The linear spectrum (recorded as a low power trace) is shown with the dotted line, and the vertical dash-dotted line indicates the lowest AFMR frequency. Shortly after the application of the pump pulse the sharp AFMR peak (shifted from its linear position due to the soft anharmonicity) is replaced with a very broad and flat spectrum due to the emergence of discrete breathers (ILMs) with different energies (and thus different frequencies). Formation of similar broad asymmetric spectra due to a statistical distribution of different discrete breathers (ILMs) emerging via modulational instability of the continuous wave has been observed in molecular dynamics simulations [234], confirming experimental measurements. In the subsequent time measurements a gradual reappearance and buildup of the uniform mode ($q = 0$) is observed due to the gradual decay of discrete breathers (ILMs). According to the spectral data, discrete breathers (ILMs) stay excited for up to ∼12 μs [95]. After about 20 μs the spectrum contains only a nonlinear uniform mode which then relaxes to its small amplitude (linear) frequency with the decay time $T_1 \sim 3$ ms [234,95].

More recent studies [346,96] optimized the sample geometry for excitation of discrete breathers (ILMs) via modulational instability of the uniform AFMR mode. It was reported, that the sample shape significantly influences the resulting dynamics and can lead to the appearance of an amplitude threshold for the modulational instability [96].

### *10.5.3. Counting discrete emission steps from discrete breathers (ILMs)*

A new surprising feature of discrete breathers (ILMs) has been reported from a series of experiments in which discrete breathers (ILMs) have been locked to the additional continuous wave source [351,352]. The initial excitation of discrete breathers (ILMs) is realized by driving the modulationally unstable uniform spin mode to a large amplitude by a microwave pulse (frequency $f_1$), as discussed above. As the result of modulational instability, DBs (ILMs) with different frequencies emerge. A few of these DBs (ILMs) are then locked by the continuous wave source (frequency $f_2$). The number of locked DBs (ILMs) strongly depends on the parameters of the $f_2$ locking field and is expected to be too small for these DBs (ILMs) to be visible in absorption spectra. Instead, a nonlinear energy magnetometer has been developed [351], which relies on the nonlinear frequency mixing process between a weak probe (frequency $f_3$) and the signal. Because of the third-order nonlinearity of the antiferromagnet [10], which is similar to $\chi^{(3)}$ nonlinearity in optics [216], the mixing of a strong signal at

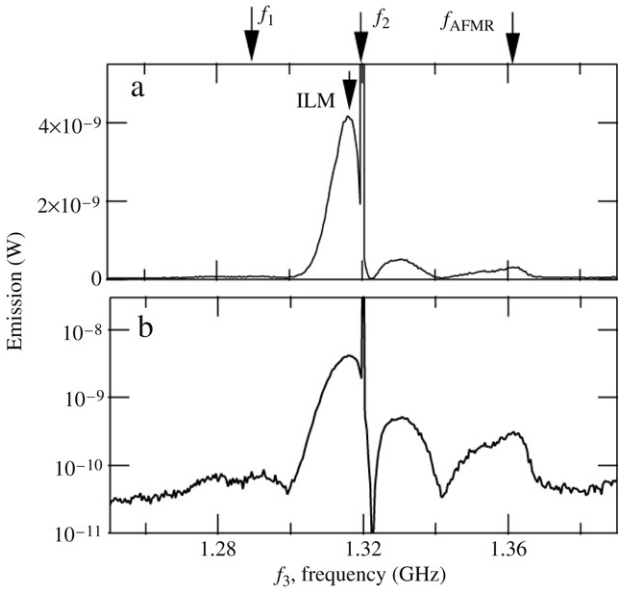


**Fig. 88.** (a) Mixing data taken 2 ms after the 3 μs-long, 52 W pulse at $f_1 = 1.29$ GHz. Here $f_2 = 1.32$ GHz at a c.w. power of 240 mW. The weak (approx 1 mW) probe oscillator of variable frequency $f_3$ is scanned. The sample is immersed in 1.2 K liquid helium. (b) Logarithmic plot of the same mixing data to bring out the weaker spectral features. The peak at 1.362 GHz comes from the resonant four wave mixing signal with the AFMR, and is also observed without the $f_1$ pulse. Figure from [351].

frequency $f_2$ with a weak probe $f_3$ should produce a signal at frequency $f_{\rm det} = 2f_2 - f_3$. Fig. 88 illustrates the power spectrum recorded at a particular time instant by scanning the probe signal $f_3$ and fixing the narrow band detector at frequency $f_{\rm det}$. One can see three spectral peaks. The strongest and the second strongest peaks on either side of the driver frequency $f_2$ are associated with the locked DBs (ILMs) [352], while the third strongest peak is due to emission from the uniform mode, also observed without the $f_1$ pulse.

The time dependence of the mixing signal for different parameters of the $f_2$ field is illustrated in Fig. 89, where the position of the strongest peak is traced with time. The overall exponential decay is apparently due to dissipation. The important new features are the step-like decays emerging at different time instants and forming rather similar structures for different parameters of the locking field $f_2$. A single step could be explained due to the unlocking of an individual DB (ILM). Indeed, the power emitted by DBs (ILMs) via frequency mixing with the probe, $P_{DB}^{(3)}$, is a function of the integer number of locked DBs (ILMs) $n_{DB}$ [352]:

$$\sqrt{P_{DB}^{(3)}} = n_{DB} f_{\rm det}\, \chi(f_{\rm det}) P_2 \sqrt{P_3}, \tag{10.27}$$

where $\chi(f_{\rm det})$ is an effective nonlinear susceptibility, $P_2$ and $P_3$ are the powers of the driver field $f_2$ and probe field $f_3$, respectively. The uniformity of these steps and the apparent weak dependence of the step height on time remains puzzling. The observed multi-step decay is argued to be connected to an interaction between the locked DBs (ILMs) [352], which should lead to a dispersion of the locked DBs (ILMs) energies and frequencies. Yet, a complete theoretical explanation of the effect is lacking.

### *10.5.4. Controlled switching of discrete breathers (ILMs)*

While in the above experiments two separate fields $f_1$ and $f_2$ have been used to produce DBs (ILMs) and then lock them, recently a simplified scheme has been proposed for the generation and controlled switching of DBs (ILMs) which does not require the pump pulse $f_1$ [403]. The idea is to tune the frequency $f_2$ of the driving field sufficiently close to that of the uniform mode. Then individual locked DBs (ILMs) can be produced and detected both via AFMR absorption and the nonlinear emission technique described above. Fig. 90 illustrates the formation of a locked DB (ILM). Here the driving field at frequency $f_2 = 1.330$ GHz is switched on at $t = 0$. For small powers of the driving field, such as in Fig. 90(a), one can observe the narrow AFMR absorption peak, which is pulled to lower frequencies due to the soft anharmonicity. Increasing the driving field power, one can observe a rapid downshift of the AFMR peak together with a significant spectral broadening, see Fig. 90(b) and (c) after 9 ms. This spectral broadening is accompanied by a step increase in the nonlinear emission, as shown in Fig. 90(c), which indicates the formation of a locked DB (ILM). Notably, the step size in emission is quite similar to the emission steps reported in earlier experiments, see Fig. 89.

The relatively long times needed to produce DBs (ILMs) by this technique allow one to observe the controllable switching of DBs (ILMs) by changing the sample temperature or modulating the driving field power [403]. Since the AFMR frequency

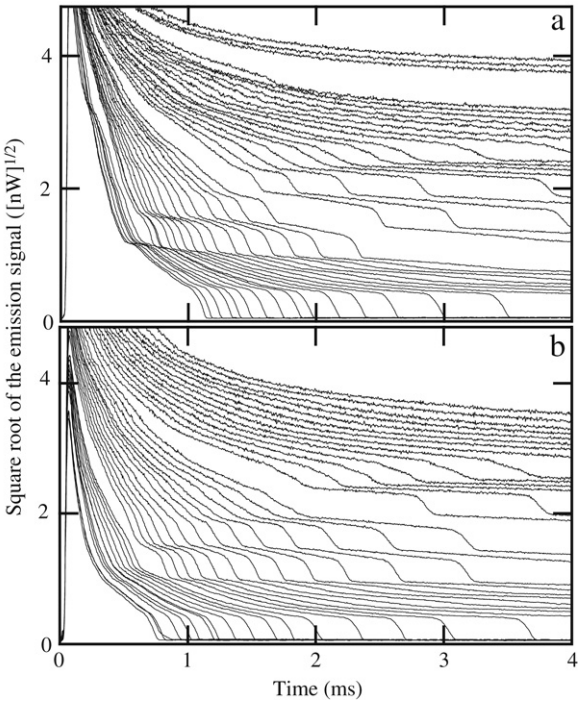


**Fig. 89.** (a) Square root of the time-dependent emission output as a function of the c.w. $f_2$ power level. The 2.3% increments between the curves vary the $f_2$ power from 34.7 to 87.1 mW. Superimposed on the smooth time-dependent signal are steps in many of the traces. When a DB (ILM) disappears, a step is recorded. (b) Square root of the time-dependent emission output as a function of the $f_2$ frequency. The frequency is scanned from 1.33 to 1.34 GHz at a power level of 55 mW so that $0.01/(f_{AFMR} - f_2)$ approximately 33%. Figure from [351].

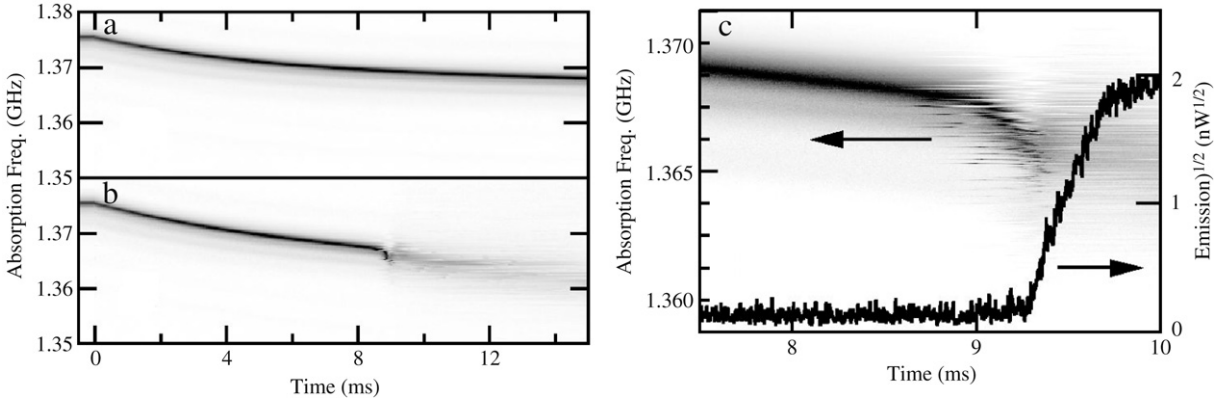


**Fig. 90.** AFMR absorption vs time in the presence of a low frequency driver. $f_2 = 1.330$ GHz. Darker density represents stronger absorption. (a) Driver power = 1.1 W and (b) Driver power = 1.4 W. At about 9 ms a transition occurs to a broadened resonance. (c) Enhanced view of the broadening transition at 9 ms in (b). The four-wave mixing (emission)$^{1/2}$ is superimposed. The nonlinear emission step occurs in tandem with the broadening of the AFMR. Figure from [403].

depends on the temperature, a gentle manipulation of the frequency detuning $\Delta f$ of the driving field $f_2$ from the resonance can be achieved. Fig. 91 illustrates changes in emission due to variation of the sample temperature by a few mK per second. Apparent hysteresis loops in emission are observed due to capture and loss of a DB (ILM). A qualitative explanation of these loops can be done by analogy with a driven nonlinear oscillator near its fundamental frequency. The corresponding amplitude response as a function of the driving frequency detuning from the resonance is schematically shown in Fig. 91(b), and is similar to the response function for the case of the driven dissipative DNLS model in Fig. 70(a).

### *10.5.5. Observation of two-magnon bound states*

While the above discussed experiments deal with mesoscopic spin excitations, well described within classical spin lattice models, see Section 8, recently Zvyagin and co-workers have experimentally detected two-magnon bound states in

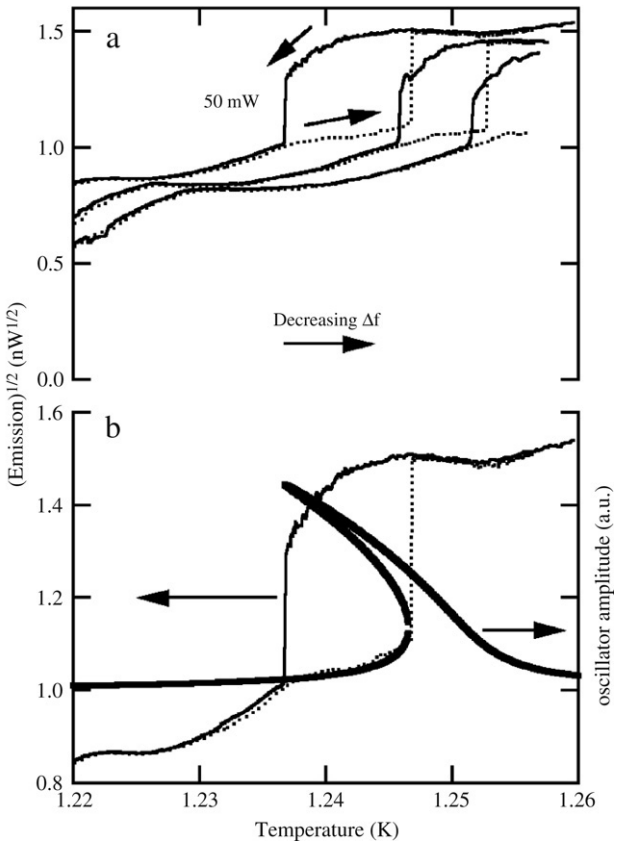


**Fig. 91.** Step hysteresis in (emission)$^{1/2}$ vs temperature. (The abscissa also identifies the linear temperature dependence of the AFMR frequency in the presence of the $f_2$ driver.) (a) $f_2 = 1.350$ GHz with three powers: 50 mW, 47.4 mW, and 45.7 mW. Dotted lines: increasing temperatures; solid lines: decreasing temperatures. The hysteresis due to capture and loss of a single ILM is evident. (b) Comparison of the 50 mW data with a model. Thick line: hysteresis characteristic of the amplitude response for a driven nonlinear oscillator. Figure from [403].

strongly anisotropic antiferromagnetic crystals [295,411]. Similar to two-particle bound states in the Bose–Hubbard chain, see Section 9.1, bound magnon states can be considered as the quantum counterparts of magnetic discrete breathers. The experiments in Refs. [295,411] have been performed with strongly anisotropic easy-plane antiferromagnetics. By applying a sufficiently strong external magnetic field along the hard axis, the spins are flipped into the direction of the field, forming a ferromagnetic ground state. A one-magnon excited state is obtained by decreasing the azimuthal spin value by one unit at a given site, while two-magnon states are constructed either by decreasing azimuthal spin values by one unit at two different sites, or by two units at a given site. The latter corresponds to the two-magnon bound state. Using electron spin resonance measurements, and comparing resulting transmission spectra with theoretically obtained frequency-field dependencies for different one- and two-magnon states, transitions from the ground state and from single-magnon excited states to two-magnon bound states have been detected.

### *10.6. Localized atomic vibrations in molecules and solids*

#### *10.6.1. Molecules*

Intramolecular vibrational energy redistribution (IVR) has been a central issue in the field of chemical physics for many decades. In particular, pathways and rates are of importance there, since understanding them allows one to describe e.g. the dynamics of various chemical reactions, and dissociation processes [188]. Spectroscopical studies, where single vibrational quanta are excited, allow the measurement of the frequencies of the normal vibrational modes, i.e. to characterize the dynamics of a molecule for small amplitude vibrations. These normal modes consist of coherent combinations of vibrational excitations of several bonds (or rotational groups) in a molecule. However, in order e.g. to dissociate a molecule, a multi quanta excitation is needed, and nonlinearities will certainly become important. It was realized then, that strong vibrational excitations of molecules are much better described by so-called *local modes*, i.e. basically one or few bond vibrational excitations. That transition from normal to local modes presented a puzzle for a long time. A practically complete modern theoretical account on these issues can be found in a recent monograph by Ovchinnikov, Erikhman and Pronin [299] (see also [105]). On its most abstract level, the transition from normal to local modes is identical with the bifurcation in the

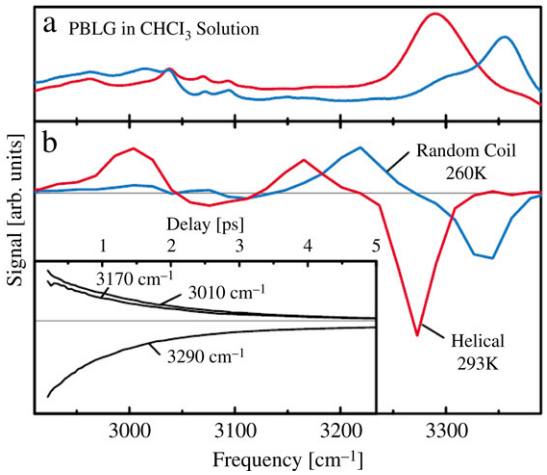


**Fig. 92.** (a) Absorption spectra of PBLG in chloroform at 293 K (red line, helical conformation) and at 260 K (blue line, random coil). (b) Pump-probe spectra 600 fs after excitation under the same conditions. Inset: Decay of negative and both positive bands at 293 K. Figure from [85].

dimer model discussed in chapters 1.1 and 9.2. Thus, local modes are essentially discrete breathers or slight perturbations of them. Note, that the connection between local modes, breathers and periodic orbits has been recently studied by Farantos in the context of large biological molecules [99]. Discrete breathers (ILMs) have been theoretically predicted to exist in ionic crystals [211], ways of optical excitation of DBs (ILMs) have been proposed [335–337], and their possible presence in hydrocarbon structures has been discussed [222].

Exciting local modes in molecules with discrete symmetries leads to small tunneling splittings of excitation levels [299], and goes back to the work of Child and Lawton [61], see also a recent comprehensive review by Keshavamurthy [201] and references therein. On its most abstract level, this effect is identical with the tunneling splitting in the permutationally symmetric dimer model discussed in chapter 9.2.

An early example of experimental evidence of discrete breather excitations in molecules comes from spectroscopical studies of visible red absorption spectra of benzene, naphtalene, and anthracene by Swofford et al. [376]. The C–H stretching vibrations have been excited to the sixth quantum level, and red shifts of the lines show, that instead of a delocalized excitation of six bonds to the first level (yielding six quanta), the excitation resides on just one of the six available bonds. While it can tunnel (as a quantum discrete breather) to the other bonds, this tunneling time is a new large time scale in the problem, strongly affecting e.g. dissociation rates.

A recent study of femtosecond infrared pump-probe spectroscopy of the N–H mode of a stable $\alpha$-helix (poly-$\gamma$-benzyl-L-glutamate (PBLG)) revealed two excited-state absorption bands, which disappear upon unfolding of the helix [85]. PBLG forms extremely stable, long $\alpha$-helices in both helicogenic solvents and films grown from these solvents. The monomeric unit of PBLG is a non-natural amino-acid with a long side chain that stabilizes the helix. PBLG has served as the standard model helix since the very early days of structural investigations of proteins. Fig. 92(a) (red line) shows the absorption spectrum of the helix at 293 K, which is dominated by the strong N–H stretching band at 3290 $cm^{-1}$. Fig. 92(b) (red line) shows the pump-probe response 600 fs after excitation with an ultrashort broadband pulse. One negative (3280 $cm^{-1}$) and two positive bands (3160 and 3005 $cm^{-1}$) are observed. If the N-H stretching modes were isolated, a negative band associated with bleach and stimulated emission, and a positive band associated with excited-state absorption, would be expected. This is indeed observed here for the unfolded molecule. In contrast, the observation of *two* positive bands for the intact helix rather than just one, is exceptional. Edler et al. [85] argue, that these features can not be explained due to intensity dependencies, or Fermi resonances. A consistent explanation is reached by assuming that two vibron states are excited, and these vibrons may form two different types of bound states, self trapped either on the same site, or on neighbouring ones (see Fig. 93). The latter states originate from the acoustic phonons of the helix, which correlate adjacent sites (see also [159]).

### *10.6.2. Crystal surfaces*

Depositing atoms or molecules on crystal surfaces can be controlled experimentally, and as a result a planar regular two-dimensional lattice structure of the deposited material can be obtained. Guyot-Sionnest [158] used Hydrogen to be deposited on Si(111) surfaces. The Si–H bonds can be excited using pump-probe techniques with infrared dye lasers. There is substantial interaction between the Si–H bonds on the Si(111) surface. The pump excites one phonon (quantum), while the tunable probe frequency finds a substantial red shift of the two-phonon excitation, and allows one to conclude that two-phonon bound states are observed.

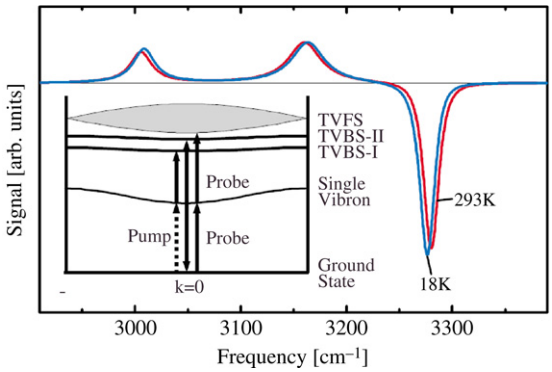


**Fig. 93.** Simulated pump-probe spectrum for 293 K (red line) and 18 K (blue line). Inset: schematic of the energy levels. Figure from [85].

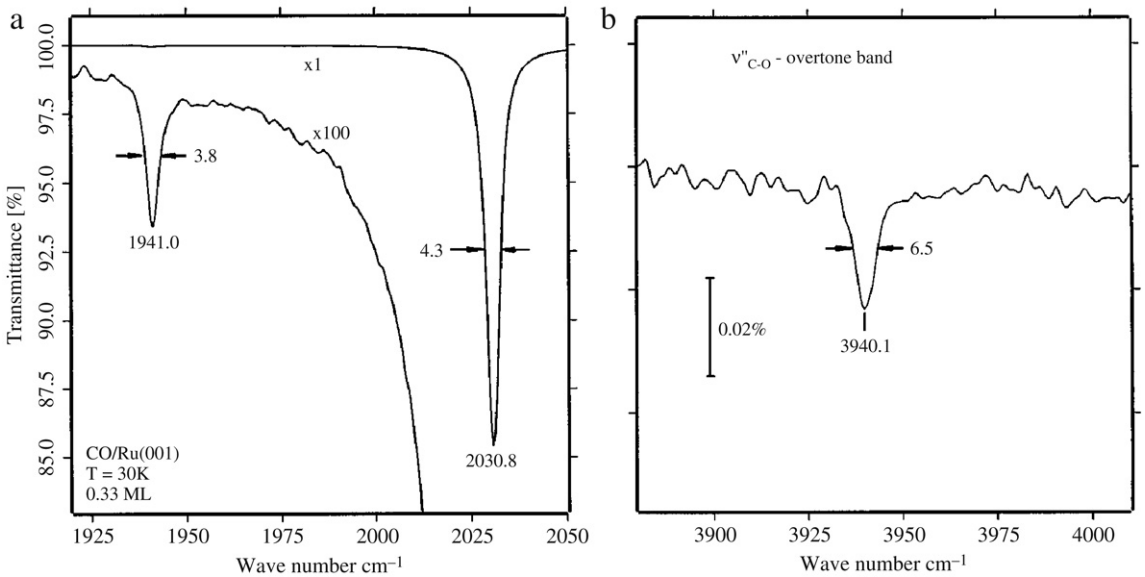


**Fig. 94.** (a) Infrared absorption spectra of the C–O stretching mode at 30 K. The corresponding mode of naturally abundant $^{13}C^{16}O$ is displayed in an enlarged vertical scale; (b) the overtone band observed at less than twice the frequency of the fundamental mode. Figure from [171].

Another set of experiments was performed by Jakob [171–173]. Carbon monoxide (CO) was deposited on a Ru(001) single crystal surface. The C–O stretching modes constitute a two-dimensional array of weakly interacting anharmonic oscillators with 4.7 Å intermolecular distance. Intermolecular coupling is provided by means of the electric field of the oscillating dipoles. Experimental spectra at 30 K are shown in Fig. 94. The one phonon mode frequency is at 2031 $cm^{-1}$. This has to be compared to the naturally abundant $^{13}C^{16}O$ frequency at 1941 $cm^{-1}$. The corresponding blue shift for the adsorbate is thus due to additional stiffness provided by the Ru surface coupling. Excitation of two uncorrelated phonons would yield a two phonon continuum at about 4062 $cm^{-1}$. The narrow line observed at 3940 $cm^{-1}$ can be thus attributed to a two-phonon bound state, or a discrete breather excitation.

The temperature dependence of the line positions also clearly shows, that the two-phonon bound state line softens much slower than the line of the one-phonon delocalized state (Fig. 95). This is, among other facts, a strong indication that the observed red shift of the overtone line is due to the formation of a localized two-phonon bound state, or a (quantum) discrete breather.

### *10.6.3. In the bulk of solids*

Vibrational spectra in the overtone or combination region of molecular crystals have been studied intensively in the 1970s and 1980s. A pioneering theoretical proposal was due to Agranovich, who predicted the existence of two-exciton bound states in various molecular crystal materials [4]. Experimental studies of infrared absorption spectra for $CO_2$ crystals were

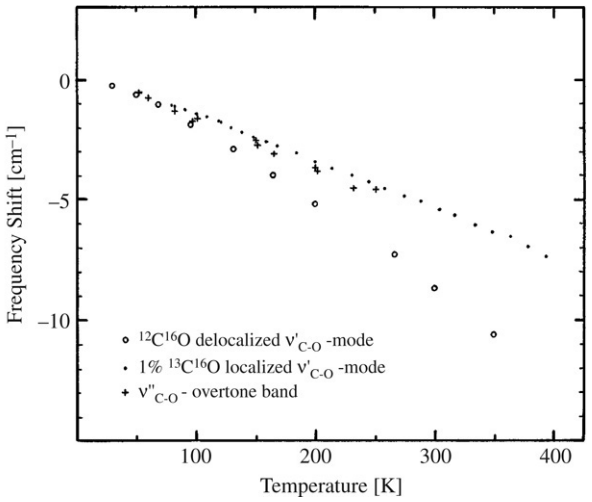


**Fig. 95.** Frequency shifts of the vibrational bands with temperature: crosses — overtone band, dots — fundamental of naturally abundant $^{13}C^{16}O$, open circles — delocalized fundamental of $^{12}C^{16}O$. Figure from [171].

conducted by Dows et al. [81] and gave evidence of two-phonon bound states. Dressler et al. studied the slow vibrational relaxation of $N_2$, which also indicates the presence of many-phonon bound states [82]. In a remarkable theoretical paper, Bogani calculated the spectrum of two phonon excitations in molecular crystals [44], to some extent one of the first accurate calculations of quantum discrete breathers. More recently Bini et al. reconsidered the theory of three-phonon bound states in crystal $CO_2$ [42]. While there certainly are many other results worth mentioning, we recommend reading related chapters in [5,299].

The pioneering studies of Swanson et al. [375] have shown that up to seven phonons can bind and form a localized state. The system of choice was a PtCl based crystal — a halide-bridged mixed-valence transition metal complex, which is a model low-dimensional electronic material where the ground states can be systematically tuned (with chemistry, doping, pressure, and temperature). It is a very strong charge-density wave (CDW) example. The material is a well-formed crystal with a homogeneous lattice consisting of quasi-1D chains (see Fig. 96). The CDW ground state consists of alternating $Pt^{+2}$ and $Pt^{+4}$ sites with a corresponding distortion of the chloride ions towards the $Pt^{+4}$ site. Resonance Raman spectra were used to probe both ground and photoexcited states. They probe the fundamental Cl–Pt–Cl stretch and the progression of many overtones. At low temperatures, the fundamental exhibits a fine structure with up to six discrete, well-resolved modes. The analysis of the evolution of the spectral structure in the overtones was performed for isotopically pure samples, in order to avoid exciting localized states due to isotopic disorder. The fundamental and overtone spectra for the pure $Pt^{35}Cl$ sample are shown in Fig. 97. The data are presented in a stack plot in which each successive trace is offset along the horizontal axis by increasing multiples of the fundamental frequency 312 cm$^{-1}$. Such plots clearly expose the relation of features in the overtone spectrum to multiples of the fundamental peak. The lowest energy dominant feature in each trace (marked by vertical lines) demonstrates a strongly increasing anharmonic redshift. Further, at higher overtones, each of these dominant peaks recurs, offset by the fundamental frequency, in the next trace above. A simple interpretation is that the lowest-energy dominant peaks in the overtone spectra correspond to all quanta of vibrational energy localized in approximately one $PtCl_2$ unit, while the higher energy peaks correspond to having all quanta but one in a localized $PtCl_2$ unit combined with one quanta in the more extended fundamental. The schematic process of the energy transfer is shown in Fig. 98 and has been analyzed theoretically in [217]. An incoming photon at frequency $\nu$ is exciting an electron from a $Pt^{+2}$ to a $Pt^{+4}$ site. The Cl ion between them starts oscillating. Finally the electron relaxes back to its original position, and releases a photon with frequency $\nu'$. The energy difference remains in a localized vibration. The effect of isotope disorder was treated by Kalosakas et al. [193]. The experimentally observed redshifts were also theoretically described by Fehske et al. [101] using Peierls-Hubbard models, and by Wellein et al. using the Holstein model [400].

Inelastic X-ray and neutron scattering was used by Manley et al. [258,259,257] to probe phonon dispersion in $\alpha$-uranium single crystals. Variation of temperature showed softening, and the abrupt appearance of a new dynamical mode, without a typically observed phase transition. The authors argue that this mode is a discrete breather, and forms due to strong electron–phonon interaction.

Russell and Eilbeck reported evidence for moving breathers in the layered crystal muscovite at 300 K [341]. Breathers were created by bombardment of the crystal surface with heavy ions. Ejection of atoms at the opposite (shielded) crystal surface was attributed to breathers, which were able to carry the vibrational energy without dispersing over more than $10^7$ unit cells of the crystal.

Finally Abrasonis et al. [3] reported on anomalous bulk diffusion of interstitial Nitrogen in steel microcrystals. N ions were deposited in a micron-thick layer, and are trapped by local structures, with a characteristic binding energy. Ar ion

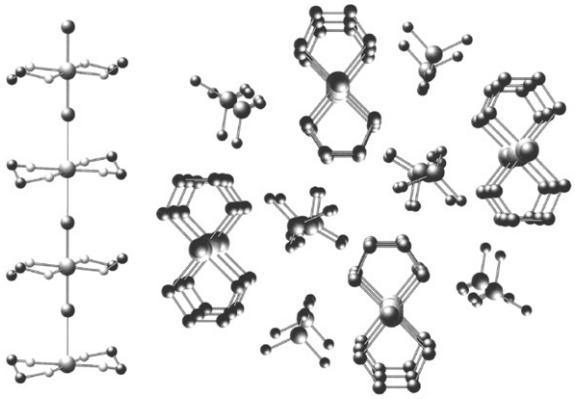

**Fig. 96.** Structure of the PtCl crystal. One PtCl chain is shown on the left. Each Pt atom is coordinated by two ethylenediamine units in a near square planar geometry, while Cl ions connect Pt sites along the chain. The packing arrangement of the 1D chains and their $ClO_4^-$ counterions is shown on the right. Figure from [375].

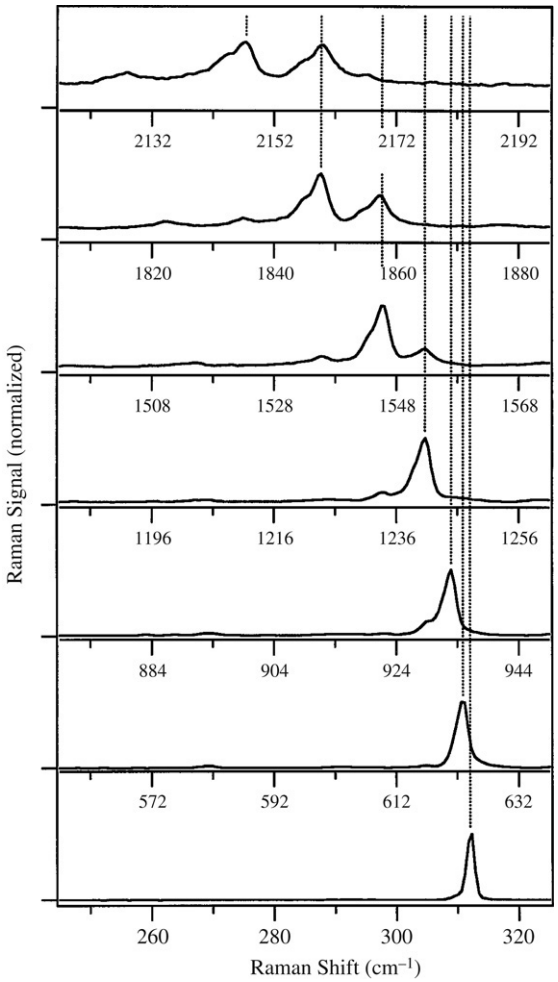


**Fig. 97.** Fundamental and overtone spectra of isotopically pure $Pt^{35}Cl$. Moving upward in each panel, each $x$ axis is offset by the appropriate integral multiple of the 312 $cm^{-1}$ fundamental frequency. All spectra have been scaled vertically to equal peak intensities. Figure from [375].

bombardment increases the N mobility at depths far beyond the ion penetration depth. The authors see evidence for coherent transfer of vibrational energy deep into the bulk of the material.

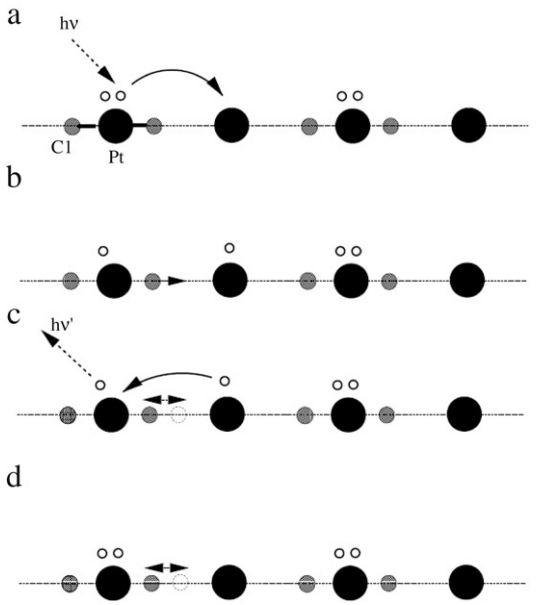


**Fig. 98.** A simple picture of a resonant Raman scattering event in the localized atomic limit. Large filled circles mark Pt ions, small grey circles mark Cl ions. Open circles mark the positions of electrons. Figure from [217].

## *10.7. Macroscopic devices, scales, and predictions*

### *10.7.1. Macroscopic devices*

Discrete breathers have been obtained in electrical lattices [266,373]. They essentially represent an electrical transmission line, where each element of the chain contains a capacitor, and an inductance, with unavoidable loss via a finite resistance. Such an element is a damped oscillator, which can be easily designed to be nonlinear. Driving the system at few hundreds of kHz, discrete breathers can be stabilized and observed. A recent twist was taken by Sato et al. [354]. Locked discrete breathers (ILM) were manipulated by adding static lattice impurities, which are capable of seeding, destroying, attracting or repelling them.

Discrete breathers have been also obtained in chains of pendula which interact via magnetic dipole–dipole interaction [342]. These devices are actually simple table experiments, extremely useful for demonstration in classes. Each pendulum is about 10 cm long, the distance is of the order of a few cm. The typically realizable periods of a discrete breather vibration are of the order of one second, and achievable lifetimes are of the order of 30 s (in the absence of pumping). Similar studies are reported in [238].

### *10.7.2. Time and length scales*

The experimental studies listed in the above sections, demonstrate a surprisingly wide variety of time and length scales. Josephson networks operate on $\mu$m length scales and $10^{-11}$ s time scales, with some flexibility towards even shorter $l$ and $\tau$. Lifetimes of rotobreather states are of the order of minutes (due to external dc bias stabilization). Nonlinear optical waveguides operate on $\mu$m length scales (note that there is no time scale involved here, since time is replaced by the propagation distance of light, with a characteristic scale of the order of the wavelength of the light). Bose–Einstein condensates in optical lattices operate again on $\mu$m length scales, while the time scale is of the order of ms. Lifetimes of discrete breathers are in the range of 10–100 ms. Micromechanical cantilever arrays operate at 50 $\mu$m length scales, and $10^{-5}$ s time scales, with lifetimes up to 100 ms. Discrete breather excitations in molecules and solids are characterized by few Å length scales, and $10^{-13}$ s time scales. Since laboratory setups easily mimic such excitations on macroscopic length scales (5 cm) and time scales of the order of seconds, we may state, that discrete breathers can be excited on virtually any time and length scale, depending on the system design.

### *10.7.3. More theoretical predictions*

As a consequence, there are many theoretical speculations on the possible observation of discrete breathers in various other systems. Without claiming completeness, we want to mention a few of them. Peyrard and Bishop formulated a lattice model which describes the denaturation of DNA [310]. The model was refined by Dauxois et al. [76]. Base pair openings are related to large amplitude localized excitations (perhaps discrete breathers) [309,311,384,383]. The model is used to predict various dynamical properties of base pair openings and their relation to DNA transcription processes [195,194,

15]. Peyrard and Sire speculate about the persistence of breathers in biomolecules [312], and Savin and Manevitch — in polyethylene chains [356]. Juanico and coworkers argue in favor of the appearance of DBs in nonlinear network models of proteins [189]. The role of discrete breathers in a targeted energy transfer in complex systems was discussed [24,224,223]. Mingaleev et al. [277] studied the conformational dynamics of biopolymers, and identify localized excitations at bending sites, which strongly affect the further dynamics of the biopolymer. Kourakis and Shukla [231] study the dynamics of dusty plasma crystals (see also Koukouloyannis et al. [229]). Vertical dust grain oscillations are predicted to form discrete breather modes. Localized electromagnetic waves in magnetic metamaterials were proposed [239,94]. Finally, Savin and Kivshar compute discrete breather states in the lattice vibration of carbon nanotubes [355], which have been further studied by Kinoshita et al. [209]. Yamayose et al. study intrinsic localized modes in a graphene sheet [406]. While the future has to show, whether any of these predictions will be correct or not, we may safely say that there is good chance that some of them will succeed.

## 11. Conclusions

### 11.1. Summary

Nonlinear classical Hamiltonian lattices exhibit generic solutions in the form of discrete breathers. These solutions are time-periodic and (typically exponentially) localized in space. The lattices exhibit discrete translational symmetry. Discrete breathers are not confined to certain lattice dimensions. We introduced the concept of these localized excitations and reviewed their basic properties including dynamical and structural stability. We then focused on advances in the theory of discrete breathers in three directions — scattering of waves by these excitations, persistence of discrete breathers in long transient processes and thermal equilibrium, and their quantization. The second part of this review was devoted to a detailed discussion of recent experimental observations and studies of discrete breathers, including theoretical modelling of these experimental situations on the basis of the general theory of discrete breathers. In particular we focused on their detection in Josephson junction networks, arrays of coupled nonlinear optical waveguides, Bose–Einstein condensates loaded on optical lattices, antiferromagnetic layered structures, PtCl based single crystals and driven micromechanical cantilever arrays.

On the theoretical side, the issues of quantum discrete breathers, and the impact of discrete breathers on statistical properties, remain as fields which still await a much more thorough and detailed investigation. On the experimental side, we expect many more fields of application of the discrete breather concept, and also many more detailed studies of discrete breather properties and their impact on other properties of the systems under investigation.

### 11.2. q-breathers, localization in normal mode space, and the Fermi–Pasta–Ulam problem

The concept of discrete breathers – time-periodic and spatially localized orbits – had a surprising twist recently. It turns out, that the idea can be extended to localization in normal mode space. Indeed, think about any of the lattices discussed in this work, assume the lattice to be finite, and remove nonlinearity completely. Then the dynamics of the system can be completely solved by going into normal mode space. Each normal mode is a harmonic oscillator. The dynamics of this linear problem is characterized by a set of noninteracting normal mode oscillators. Adding nonlinearity will induce a network of nonlinear interactions between the normal mode oscillators. It has been shown recently with the help of a theorem of Lyapunov, that the periodic orbits of the linear system, which correspond to exactly one normal mode being excited, are continued into the nonlinear regime. The periodic orbits of the nonlinear system are exponentially localized in normal mode space, and are thus called $q$-breathers [122,123,287,196,304]. If one normal mode is excited in such a system, the trajectory will stay close to a $q$-breather periodic orbit for long times, in close similarity to the observations of localization in real space being related to nearby located discrete breathers, see Section 3.1. Then we observe localization in normal mode space. But that is exactly what was observed by Fermi, Pasta and Ulam (FPU) in their seminal work on the equipartition of a nonlinear atomic chain [102], and what has been considered as one of the big problems in statistical physics since [145,56]. Since $q$-breathers are periodic orbits, they are well-defined low-dimensional invariant manifolds in phase space, and can be rigorously characterized with respect to e.g. their degree of localization, linear stability, etc. That work has been accomplished [123]. Furthermore it was shown, that the localization properties of $q$-breathers depend only on intensive quantities (energy density and frequency), and they have been shown to persist in arbitrarily large lattices [196]. These properties of $q$-breathers are directly related to many properties of the trajectory initially studied by FPU, including recurrence [123], and resonant excitation of tail modes [304]. Certainly this is just the beginning of a systematic study of the relation between periodic orbits and equipartition routes in nonlinear extended systems. Among others there is the interesting question, whether and how these periodic orbits are linked to the continuation of standing waves from the anticontinuous limit [285].

Another intriguing question is the relation between time-periodic and spatially localized solutions in nonlinear disordered lattices [7,366,219,14,221,220,197] and the diffusion of an initially localized excitation [367,283]. This is currently an active field of research, and we can expect to receive fresh news in the very near future.

### 11.3. Some closing words

The aim of this review was to give the reader an introduction into the fascinating field of *localizing energy by nonlinearity and discreteness*, to discuss details of recent achievements, and to review for the first time recent experimental studies. Most certainly we have not adequately mentioned several results, and for this we sincerely apologize. At this place we want to thank many colleagues for sharing their views and discussing related problems with us. Especially important were discussions with G. Abrasonis, B. Altshuler, S. Aubry, A. Benabdallah, A.R. Bishop, T. Bountis, D.K. Campbell, T. Dauxois, S. Denisov, J. Dorignac, M. Fistul, V. Fleurov, M. Floria, P. Hänggi, M.V. Ivanchenko, M. Johansson, G. Kalosakas, O.I. Kanakov, Yu. Kivshar, K. Kladko, G. Kopidakis, A. Lichtenberg, R.S. MacKay, P. Maniadis, S. Mingaleev, K. Mishagin, A. Miroshnichenko, A. A. Ovchinnikov, J. Page, T. Penati, M. Peyrard, R. Pinto, A. Ponno, R. Schilling, L. Schulman, A.J. Sievers, M. Spicci, V. Shalfeev, G. Tsironis, A. Ustinov, R. Vicencio, C.R. Willis, Y. Zolotaryuk, and many others.

## References


[1] M.J. Ablowitz, J.F. Ladik, Nonlinear differential-difference equations and Fourier analysis, J. Math. Phys. 17 (1976) 1011–1018.
[2] M.J. Ablowitz, Z.H. Musslimani, Discrete spatial solitons in a diffraction-managed nonlinear waveguide array: A unified approach, Physica D 184 (2003) 276–303.
[3] G. Abrasonis, W. Moeller, X.X. Ma, Anomalous ion accelerated bulk diffusion of interstitial nitrogen, Phys. Rev. Lett. 96 (2006) 065901.
[4] V.M. Agranovich, Theory of biexitons in molecular crystals for infrared region, Sov. Phys.-Solid St. 12 (1970) 430.
[5] V.M. Agranovich, R.M. Hochstrasser, Spectroscopy and Excitation Dynamics of Condensed Molecular Crystals, North-Holland, Amsterdam, 1983.
[6] T. Ahn, R.S. MacKay, J.A. Sepulchre, Dynamics of relative phases: Generalised multibreathers, Nonlinear Dynamics 25 (2001) 157–182.
[7] C. Albanese, J. Frohlich, Perturbation theory for periodic orbits in a class of infinite dimensional Hamiltonian systems, Comm. Math. Phys. 138 (1991) 193–205.
[8] M. Albiez, R. Gati, J. Fölling, S. Hunsmann, M. Cristiani, M.K. Oberthaler, Direct observation of tunneling and nonlinear self-trapping in a single bosonic Josephson junction, Phys. Rev. Lett. 95 (2005) 010402.
[9] G.L. Alfimov, P.G. Kevrekidis, V.V. Konotop, M. Salerno, Wannier functions analysis of the nonlinear Schrödinger equation with a periodic potential, Phys. Rev. E 66 (2002) 046608.
[10] N.S. Almeida, D.L. Mills, Nonlinear infrared response of antiferromagnets, Phys. Rev. B 36 (1987) 2015–2023.
[11] B.P. Anderson, M.A. Kasevich, Macroscopic quantum interference from atomic tunnel arrays, Science 282 (1998) 1686–1689.
[12] P.W. Anderson, Localized magnetic states in metals, Phys. Rev. 124 (1961) 41–53.
[13] Th. Anker, M. Albiez, R. Gati, S. Hunsmann, B. Eiermann, A. Trombettoni, M.K. Oberthaler, Nonlinear self-trapping of matter waves in periodic potentials, Phys. Rev. Lett. 94 (2005) 020403.
[14] J.F.R. Archilla, R.S. MacKay, J.L. Marin, Discrete breathers and Anderson modes: Two faces of the same phenomenon? Physica D 134 (1999) 406–418.
[15] S. Ares, G. Kalosakas, Distribution of bubble lengths in DNA, Nano Lett. 7 (2007) 307–311.
[16] V.I. Arnold, Mathematical Methods of Classical Mechanics, 2nd ed., Springer-Verlag, New York, 1989.
[17] V.I. Arnold, A. Avez, Ergodic Problems of Classical Mechanics, W.A. Benjamin Inc., New York, 1968.
[18] S. Aubry, Breathers in nonlinear lattices: Existence, linear stability and quantization, Physica D 103 (1997) 201–250.
[19] S. Aubry, Discrete breathers in anharmonic models with acoustic phonons, Ann. Inst. H. Poincare 68 (1998) 381–420.
[20] S. Aubry, Discrete breathers: Localization and transfer of energy in discrete Hamiltonian nonlinear systems, Physica D 216 (2006) 1–30.
[21] S. Aubry, T. Cretegny, Mobility and reactivity of discrete breathers, Physica D 119 (1998) 34–36.
[22] S. Aubry, S. Flach, K. Kladko, E. Olbrich, Manifestation of classical bifurcation in the spectrum of the integrable quantum dimer, Phys. Rev. Lett. 76 (1996) 1607.
[23] S. Aubry, G. Kopidakis, V. Kadelburg, Variational proof for hard discrete breathers in some classes of Hamiltonian dynamical systems, Discrete Contin. Dynam. Syst. B 1 (2001) 271–298.
[24] S. Aubry, G. Kopidakis, A.M. Morgante, G.P. Tsironis, Analytic conditions for targeted energy transfer between nonlinear oscillators or discrete breathers, Physica B 296 (2001) 222–236.
[25] C. Baesens, R.S. MacKay, Exponential localization of linear response in networks with exponentially decaying coupling, Nonlinearity 10 (1997) 931–940.
[26] D. Bambusi, Exponential stability of breathers in Hamiltonian networks of weakly coupled oscillators, Nonlinearity 9 (1996) 433–457.
[27] D. Bambusi, Some stability properties of breathers in Hamiltonian networks of oscillators, Physica D 119 (1998) 47–55.
[28] G. Bartal, O. Cohen, H. Buljan, J.W. Fleischer, O. Manela, M. Segev, Brillouin zone spectroscopy of nonlinear photonic lattices, Phys. Rev. Lett. 94 (2005) 163902.
[29] G. Bartal, O. Manela, O. Cohen, J.W. Fleischer, M. Segev, Observation of second-band vortex solitons in 2d photonic lattices, Phys. Rev. Lett. 95 (2005) 053904-4.
[30] A. Benabdallah, M.V. Fistul, S. Flach, Breathers in a single plaquette of Josephson junctions: Existence, stability and resonances, Physica D 159 (2001) 202–214.
[31] J.M. Bergamin, T. Bountis, Discrete breathers and homoclinic dynamics, Prog. Theor. Phys. Suppl. 150 (2003) 330–333.
[32] J.M. Bergamin, T. Bountis, C. Jung, A method for locating symmetric homoclinic orbits using symbolic dynamics, J. Phys. A 33 (2000) 8059–8070.
[33] J.M. Bergamin, T. Bountis, M.N. Vrahatis, Homoclinic orbits of invertible maps, Nonlinearity 15 (2002) 1603–1619.
[34] A. Berger, R.S. MacKay, V.M. Rothos, A criterion for non-persistence of travelling breathers for perturbations of the Ablowitz-Ladik lattice, Discrete Contin. Dynam. Syst. B 4 (2004) 911–920.
[35] L. Bernstein, J.C. Eilbeck, A.C. Scott, The quantum theory of local modes in a coupled system of nonlinear oscillators, Nonlinearity 3 (1990) 293–323.
[36] L.J. Bernstein, Quantizing a self-trapping equation, Physica D 68 (1993) 174–179.
[37] S.R. Bickham, S.A. Kisilev, A.J. Sievers, Stationary and moving intrinsic localized modes in one-dimensional monoatomic lattices with cubic and quartic anharmonicity, Phys. Rev. B 47 (1993) 14206–14211.
[38] A. Bikaki, N.K. Voulgarakis, S. Aubry, G.P. Tsironis, Energy relaxation in discrete nonlinear lattices, Phys. Rev. E 59 (1999) 1234–1237.
[39] P. Binder, D. Abraimov, A.V. Ustinov, Diversity of discrete breathers observed in a Josephson ladder, Phys. Rev. E 62 (2000) 2858–2862.
[40] P. Binder, D. Abraimov, A.V. Ustinov, S. Flach, Y. Zolotaryuk, Observation of breathers in Josephson ladders, Phys. Rev. Lett. 84 (2000) 745–748.
[41] P. Binder, A.V. Ustinov, Exploration of a rich variety of breather modes in Josephson ladders, Phys. Rev. E 66 (2002) 016603.
[42] R. Bini, P.R. Salvi, V. Schettino, H.J. Jodl, The spectroscopy and relaxation dynamics of three-phonon bound states in crystal $CO_2$, J. Chem. Phys. 98 (1993) 164–177.
[43] A.R. Bishop, G. Kalosakas, K.O. Rasmussen, P.G. Kevrekidis, Localization in physical systems described by discrete nonlinear Schrödinger-type equations, Chaos 13 (2003) 588–595.
[44] F. Bogani, Two-phonon resonances and bound-states in molecular crystals, J. Phys. C.: Solid State Phys. 11 (1978) 1283–1295.
[45] S.V. Bolotin, R.S. MacKay, Isochronous potentials, in: L. Vazquez, R.S. MacKay, M.P. Zorzano (Eds.), Localization and Energy Transfer in Nonlinear Systems, World Scientific, Singapore, 2003, pp. 217–224.

[46] D. Bonart, J.B. Page, Intrinsic localized modes and chaos in damped driven rotator lattices, Phys. Rev. E 60 (1999) R1134–R1137.
[47] D. Bonart, T. Rossler, J.B. Page, Intrinsic localized modes in complex lattice dynamical systems, Physica D 113 (1998) 123–128.
[48] T. Bountis, H.W. Capel, M. Kollmann, J.C. Ross, J.M. Bergamin, J.P. van der Weele, Multibreathers and homoclinic orbits in 1-dimensional nonlinear lattices, Phys. Lett. A 268 (2000) 50–60.
[49] T.J. Bridges, A geometric formulation of the conservation of wave action and its implications for signature and the classification of instabilities, Proc. R. Soc. Lond. A 453 (1997) 1365–1395.
[50] C. Brunhuber, F.G. Mertens, Y. Gaididei, Persistent breathers in long-ranged discrete nonlinear Schrödinger models, Phys. Rev. E 73 (2006) 056610.
[51] V.M. Burlakov, S.A. Kiselev, V.I. Rupasov, Localized excitations of uniform anharmonic lattices, JETP Lett. 51 (1990) 544–547.
[52] K. Busch, S.F. Mingaleev, A. Garcia-Martin, M. Schillinger, D. Hermann, The Wannier function approach to photonic crystal circuits, J. Phys.: Condens. Matter 15 (2003) R1233–R1256.
[53] I.A. Butt, J.A.D. Wattis, Discrete breathers in a two-dimensional Fermi–Pasta–Ulam lattice, J. Phys. A – Math. General 39 (2006) 4955–4984.
[54] D.K. Campbell, Nonlinear physics: Fresh breather, Nature 432 (2004) 455–456.
[55] D.K. Campbell, M. Peyrard, in: D.K. Campbell (Ed.), CHAOS — Soviet American Perspectives on Nonlinear Science, American Institute of Physics, New York, 1990.
[56] D.K. Campbell, P. Rosenau, G.M. Zaslavsky, The Fermi–Pasta–Ulam problem — the first fifty years (focus issue), Chaos 15 (2005).
[57] D.K. Campbell, S. Flach, Y.S. Kivshar, Localizing energy through nonlinearity and discreteness, Phys. Today 57 (1) (2004) 43–49.
[58] D. Chen, S. Aubry, G.P. Tsironis, Breather mobility in discrete $\phi^4$ lattices, Phys. Rev. Lett. 77 (1996) 4776–4779.
[59] F Chen, M. Stepić, C. Rüter, D. Runde, D. Kip, V. Shandarov, O. Manela, M. Segev, Discrete diffraction and spatial gap solitons in photovoltaic $LiNbO_3$ waveguide arrays, Opt. Expr. 13 (2005) 4314–4324.
[60] D. Cheskis, S. Bar-Ad, R. Morandotti, J.S. Aitchison, H.S. Eisenberg, Y. Silberberg, D. Ross, Strong spatiotemporal localization in a silica nonlinear waveguide array, Phys. Rev. Lett. 91 (2003) 223901.
[61] M.S. Child, R.T. Lawton, Local mode degeneracies in the vibrational spectrum of $H_2O$, Chem. Phys. Lett. 87 (1982) 217–220.
[62] P.L. Christiansen, Yu.B. Gaididei, M. Johansson, K.Ø. Rasmussen, Breatherlike excitations in discrete lattices with noise and nonlinear damping, Phys. Rev. B 55 (1997) 5759–5766.
[63] D.N. Christodoulides, R.I. Joseph, Discrete self-focusing in nonlinear arrays of coupled wave-guides, Opt. Lett. 13 (1988) 794–796.
[64] D.N. Christodoulides, F. Lederer, Y. Silberberg, Discretizing light behaviour in linear and nonlinear waveguide lattices, Nature 424 (2003) 817–823.
[65] O.A. Chubykalo, Magnetic gap solitons in a one-dimensional Heisenberg antiferromagnetic chain, Phys. Lett. A 189 (1994) 403–408.
[66] K.W. Chung, X. Yuan, Existence and stability of quasiperiodic breathers in networks of Ginzburg–Landau oscillators, Physica D 227 (2007) 43–50.
[67] C. Claude, Yu.S. Kivshar, O. Kluth, K.H. Spatschek, Moving localized modes in nonlinear lattices, Phys. Rev. B 47 (1993) 14228–14232.
[68] T. Cretegny, S. Aubry, Spatially inhomogeneous time-periodic propagating waves in anharmonic systems, Phys. Rev. B 55 (1997) R11929–R11932.
[69] T. Cretegny, S. Aubry, S. Flach, 1d phonon scattering by discrete breathers, Physica D 119 (1998) 73–87.
[70] T. Cretegny, T. Dauxois, S. Ruffo, A. Torcini, Localization and equipartition of energy in the $\beta$-FPU chain: Chaotic breathers, Physica D 121 (1998) 109–126.
[71] T. Cretegny, S. Aubry, Spatially inhomogeneous time-periodic propagating waves in anharmonic systems, Phys. Rev. B 55 (1997) R11929.
[72] T. Cretegny, S. Aubry, Patterns of energy flux in periodic solutions of Klein-Gordon lattices, Physica D 113 (1998) 162–165.
[73] I. Daumont, T. Dauxois, M. Peyrard, Modulational instability: First step towards energy localization in nonlinear lattices, Nonlinearity 10 (1997) 617–630.
[74] T. Dauxois, A. Litvak-Hinenzon, R.S. MacKay, A. Spanoudaki (Eds.), Energy Localization and Transfer, World Scientific, Singapore, 2004.
[75] T. Dauxois, M. Peyrard, Physics of Solitons, Cambridge University Press, Cambridge, 2006.
[76] T. Dauxois, M. Peyrard, A.R. Bishop, Entropy-driven DNA denaturation, Phys. Rev. E 47 (1993) R44–R47.
[77] B. Dey, M. Eleftheriou, S. Flach, G.P. Tsironis, Shape profile of compact-like discrete breathers in nonlinear dispersive lattice systems, Phys. Rev. E 65 (2001) 017601.
[78] J. Dorignac, J.C. Eilbeck, M. Salerno, A.C. Scott, Quantum signatures of breather–breather interactions, Phys. Rev. Lett. 93 (2004) 025504.
[79] J. Dorignac, S. Flach, Tunneling of quantum rotobreathers, Phys. Rev. B 65 (2002) 214305.
[80] J. Dorignac, S. Flach, Isochronism and tangent bifurcation of band edge modes in Hamiltonian lattices, Physica D 204 (2005) 83–109.
[81] D.A. Dows, V. Schettino, Two-phonon infrared absorption spectra in crystalline carbon dioxide, J. Chem. Phys. 58 (1973) 5009–5016.
[82] K. Dressler, O. Oehler, D.A. Smith, Measurement of slow vibrational relaxation and fast vibrational energy transfer in solid $N_2$, Phys. Rev. Lett. 34 (1975) 1364–1367.
[83] W. Dreyer, M. Herrmann, A. Mielke, Micromacro transition in the atomic chain via Whitham's modulation equation, Nonlinearity 19 (2006) 471–500.
[84] E.N. Economou, Green's Functions in Quantum Physics, Springer-Verlag, Berlin, 1990.
[85] J. Edler, R. Pfister, V. Pouthier, C. Falvo, P. Hamm, Direct observation of self-trapped vibrational states in $\alpha$-helices, Phys. Rev. Lett. 93 (2004) 106405.
[86] O. Egorov, U. Peschel, F. Lederer, Mobility of discrete cavity solitons, Phys. Rev. E 72 (2005) 066603-7.
[87] B. Eiermann, T. Anker, M. Albiez, M. Taglieber, P. Treutlein, K.P. Marzlin, M.K. Oberthaler, Bright Bose-Einstein gap solitons of atoms with repulsive interactions, Phys. Rev. Lett. 92 (2004) 230401.
[88] J.C. Eilbeck, Some exact results for quantum lattice problems, in: L. Vazquez, R.S. MacKay, M.P. Zorzano (Eds.), Localization and Energy Transfer in Nonlinear Systems, World Scientific, Singapore, 2003, pp. 177–186.
[89] J.C. Eilbeck, M. Johansson, The discrete nonlinear Schrödinger equation — 20 years on, in: L. Vazquez, R.S. MacKay, M.P. Zorzano (Eds.), Localization and Energy Transfer in Nonlinear Systems, World Scientific, Singapore, 2003, pp. 44–67.
[90] J.C. Eilbeck, F. Palmero, Trapping in quantum chains, Phys. Lett. A 331 (2004) 201–208.
[91] H.S. Eisenberg, R. Morandotti, Y. Silberberg, J.M. Arnold, G. Pennelli, J.S. Aitchison, Optical discrete solitons in waveguide arrays. i. Soliton formation, J. Opt. Soc. Am. B 19 (2002) 2938–2944.
[92] H.S. Eisenberg, Y. Silberberg, R. Morandotti, A.R. Boyd, J.S. Aitchison, Discrete spatial optical solitons in waveguide arrays, Phys. Rev. Lett. 81 (1998) 3383–3386.
[93] M. Eleftheriou, S. Flach, Discrete breathers in thermal equilibrium: Distributions and energy gaps, Physica D 202 (2005) 142–154.
[94] M. Eleftheriou, N. Lazarides, G.P. Tsironis, Magnetoinductive breathers in metamaterials, Phys. Rev. E 77 (2008) 036608.
[95] L.Q. English, M. Sato, A.J. Sievers, Nanoscale intrinsic localized modes in an antiferromagnetic lattice, J. Appl. Phys. 89 (2001) 6707–6709.
[96] L.Q. English, M. Sato, A.J. Sievers, Modulational instability of nonlinear spin waves in easy-axis antiferromagnetic chains. ii. Influence of sample shape on intrinsic localized modes and dynamic spin defects, Phys. Rev. B 67 (2003) 024403.
[97] C. Falvo, V. Pouthier, Vibron-polaron in alpha-helices. ii. Two-vibron bound states, J. Chem. Phys. 123 (2005) 184710.
[98] U. Fano, Effects of configuration interaction on intensities and phase shifts, Phys. Rev. 124 (1961) 1866–1878.
[99] S.C. Farantos, Periodic orbits in biological molecules: Phase space structures and selectivity in alanine dipeptide, J. Chem. Phys. 126 (2007) 175101.
[100] S. Fedorov, D. Michaelis, U. Peschel, C. Etrich, D.V. Skryabin, N. Rosanov, F. Lederer, Effects of spatial inhomogeneities on the dynamics of cavity solitons in quadratically nonlinear media, Phys. Rev. E 64 (2001) 036610.
[101] H. Fehske, G. Wellein, H. Buettner, A.R. Bishop, M.I. Salkola, Local mode behaviour in quasi-1d cdw systems, Physica B 281 (2000) 673–674.
[102] E. Fermi, J. Pasta, S. Ulam, Studies of nonlinear problems (Los Alamos, Report Nr. LA-1940, 1955), in: D.C. Mattis (Ed.), Many-Body Problems, World Scientific, Singapore, 1993.
[103] A. Ferrando, Discrete-symmetry vortices as angular Bloch modes, Phys. Rev. E 72 (2005) 036612.
[104] A. Ferrando, M. Zacares, M.-A. Garcia-March, Vorticity cutoff in nonlinear photonic crystals, Phys. Rev. Lett. 95 (2005) 043901-4.
[105] F. Fillaux, Vibrational spectroscopy and quantum localization, in: T. Dauxois, A. Litvak-Hinenzon, R. MacKay, A. Spanoudaki (Eds.), Energy Localization and Transfer, World Scientific, Singapore, 2004, pp. 73–148.

[106] F. Fischer, Self-localized single-anharmonic vibrational modes in two-dimensional lattices, Ann. Phys. 2 (1993) 296–307.
[107] M.V. Fistul, Resonant breather states in Josephson coupled systems, Chaos 13 (2003) 725–732.
[108] M.V. Fistul, S. Flach, A. Benabdallah, Magnetic-field-induced control of breather dynamics in a single plaquette of Josephson junctions, Phys. Rev. E 65 (2002) 046616.
[109] M.V. Fistul, A.E. Miroshnichenko, S. Flach, M. Schuster, A.V. Ustinov, Incommensurate dynamics of resonant breathers in Josephson junction ladders, Phys. Rev. B 65 (2002) 174524.
[110] S. Flach, Conditions on the existence of localized excitations in nonlinear discrete systems, Phys. Rev. E 50 (1994) 3134–3142.
[111] S. Flach, Existence of localized excitations in nonlinear Hamiltonian lattices, Phys. Rev. E 51 (1995) 1503–1507.
[112] S. Flach, Obtaining breathers in nonlinear Hamiltonian lattices, Phys. Rev. E 51 (1995) 3579–3587.
[113] S. Flach, Tangent bifurcation of band edge plane waves, dynamical symmetry breaking and vibrational localization, Physica D 91 (1996) 223–243.
[114] S. Flach, Breathers on lattices with long range interactions, Phys. Rev. E 58 (1998) R4116–R4119.
[115] S. Flach, Computational studies of discrete breathers, in: T. Dauxois, A. Litvak-Hinenzon, R. MacKay, A. Spanoudaki (Eds.), Energy Localization and Transfer, World Scientific, Singapore, 2004, pp. 1–71.
[116] S. Flach, J. Dorignac, A.E. Miroshnichenko, V. Fleurov, Discrete breathers, close to the anticontinuum limit: Existence and wave scattering, Int. J. Mod. Phys. B 17 (2003) 3996–4002.
[117] S. Flach, V. Fleurov, Tunneling in the nonintegrable trimer — A step towards quantum breathers, J. Phys.: Cond. Mat. 9 (1997) 7039–7061.
[118] S. Flach, V. Fleurov, A. Gorbach, Classical and quantum radiation of perturbed discrete breathers, Phys. Rev. B 71 (2005) 064302.
[119] S. Flach, V. Fleurov, A.V. Gorbach, A.E. Miroshnichenko, Resonant light scattering by optical solitons, Phys. Rev. Lett. 95 (2005) 023901.
[120] S. Flach, V. Fleurov, A.A. Ovchinnikov, Tunelling of localized excitations: Giant enhancement due to fluctuations, Phys. Rev. 63 (2001) 094304.
[121] S. Flach, A. Gorbach, Discrete breathers in Fermi–Pasta–Ulam lattices, Chaos 15 (2005) 015112.
[122] S. Flach, M.V. Ivanchenko, O.I. Kanakov, q-breathers and the Fermi–Pasta–Ulam problem, Phys. Rev. Lett 95 (2005) 064102.
[123] S. Flach, M.V. Ivanchenko, O.I. Kanakov, q-breathers in Fermi–Pasta–Ulam chains: Existence, localization and stability, Phys. Rev. E 73 (2006) 036618.
[124] S. Flach, K. Kladko, Moving discrete breathers? Physica D 127 (1999) 61–72.
[125] S. Flach, K. Kladko, R.S. MacKay, Energy thresholds of discrete breathers in one-, two- and three-dimensional lattices, Phys. Rev. Lett. 78 (1997) 1207–1210.
[126] S. Flach, K. Kladko, S. Takeno, Acoustic breathers in two-dimensional lattices, Phys. Rev. Lett. 79 (1997) 4838–4841.
[127] S. Flach, K. Kladko, C.R. Willis, Localized excitations in two-dimensional lattices, Phys. Rev. E 50 (1994) 2293–2303.
[128] S. Flach, A.E. Miroshnichenko, M.V. Fistul, Wave scattering by discrete breathers, Chaos 13 (2003) 596–609.
[129] S. Flach, A.E. Miroshnichenko, V. Fleurov, M.V. Fistul, Fano resonances with discrete breathers, Phys. Rev. Lett. 90 (2003) 084101.
[130] S. Flach, M. Spicci, Rotobreather dynamics in underdamped Josephson junction ladders, J. Phys.: Cond. Mat. 11 (1999) 321–334.
[131] S. Flach, C.R. Willis, Localized excitations in a discrete Klein-Gordon system, Phys. Lett. A 181 (1993) 232–238.
[132] S. Flach, C.R. Willis, in: M. Peyrard (Ed.), Nonlinear Excitations in Biomolecules, in: Editions de Physique, Springer-Verlag, 1995.
[133] S. Flach, C.R. Willis, Discrete breathers, Phys. Rep. 295 (1998) 182–264.
[134] S. Flach, C.R. Willis, E. Olbrich, Integrability and localized excitations in nonlinear discrete systems., Phys. Rev. E 49 (1994) 836–850.
[135] S. Flach, Y. Zolotaryuk, K. Kladko, Moving lattice kinks and pulses: An inverse method, Phys. Rev. E 59 (1999) 6105–6115.
[136] J.W. Fleischer, G. Bartal, O. Cohen, T. Schwartz, O. Manela, B. Freedman, M. Segev, H. Buljan, N.K. Efremidis, Spatial photonics in nonlinear waveguide arrays, Opt. Express 13 (2005) 1780–1796.
[137] J.W. Fleischer, G. Bartal, O. Cohen, O. Manela, M. Segev, J. Hudock, D.N. Christodoulides, Observation of vortex-ring "discrete" solitons in 2d photonic lattices, Phys. Rev. Lett. 92 (2004) 123904-4.
[138] J.W. Fleischer, M. Segev, N.K. Efremidis, D.N. Christodoulides, Observation of two-dimensional discrete solitons in optically induced nonlinear photonic lattices, Nature 422 (2003) 147–150.
[139] V. Fleurov, Discrete quantum breathers: What do we know about them? Chaos 13 (2003) 676–682.
[140] V. Fleurov, R. Schilling, S. Flach, Tunneling of a quantum breather in a one-dimensional chain, Phys. Rev. E 58 (1998) 339–346.
[141] L.M. Floria, J.L. Marin, S. Aubry, P.J. Martinez, F. Falo, J.J. Mazo, Josephson-junction ladder: A benchmark for nonlinear concepts, Physica D 113 (1998) 387–396.
[142] L.M. Floria, J.L. Marín, P.J. Martinez, F. Falo, S. Aubry, Intrinsic localization in the dynamics of a Josephson-junction ladder, Europhys. Lett. 36 (1996) 539–544.
[143] N. Flytzanis, S. Pnevmatikos, M. Remoissenet, Kink, breather and assymmetric envelope or dark solitons in nonlinear chains: I. Monoatomic chain, J. Phys. C: Solid State Phys. 18 (1985) 4603–4629.
[144] S. Foelling, S. Trotzky, P. Cheinet, M. Feld, R. Saers, A. Widera, T. Mueller, I. Bloch, Direct observation of second-order atom tunneling, Nature 448 (2007) 1029.
[145] J. Ford, The Fermi–Pasta–Ulam problem: Paradox turns discovery, Phys. Rep. 213 (1992) 271–310.
[146] A. Fratalocchi, G. Assanto, K.A. Brzdakiewicz, M.A. Karpierz, Discrete propagation and spatial solitons in nematic liquid crystals, Opt. Lett. 29 (2004) 1530–1532.
[147] Yu.B. Gaididei, S.F. Mingaleev, P.L. Christiansen, K.Ø Rasmussen, Effects on nonlocal dispersive interactions on self-trapping excitations, Phys. Rev. E 55 (1997) 6141–6150.
[148] B. Gershgorin, Y.V. Lvov, D. Cai, Renormalized waves and discrete breathers in beta-Fermi–Pasta–Ulam chains, Phys. Rev. Lett. 95 (2005) 264302.
[149] J. Giannoulis, A. Mielke, Dispersive evolution of pulses in oscillator chains with general interaction potentials, Discrete Contin. Dynam. Syst. B 6 (2006) 493–523.
[150] J. Gomez-Gardenes, F. Falo, L.M. Floria, Mobile localization in nonlinear Schrödinger lattices, Phys. Lett. A 332 (2004) 213–219.
[151] J. Gomez-Gardenes, L.M. Floria, M. Peyrard, A.R. Bishop, Nonintegrable Schrodinger discrete breathers, Chaos 14 (2004) 1130–1147.
[152] A.V. Gorbach, M. Johansson, Discrete gap breathers in a diatomic Klein-Gordon chain: Stability and mobility, Phys. Rev. E 67 (2003) 066608.
[153] A.V. Gorbach, M. Johansson, Gap and out-gap breathers in a binary modulated discrete nonlinear Schrödinger model, Eur. Phys. J. D 29 (2004) 77–93.
[154] A.V. Gorbach, S. Denisov, S. Flach, Optical ratchets with discrete cavity solitons, Opt. Lett. 31 (2006) 1702–1704.
[155] A.V. Gorbach, S. Flach, Compact-like discrete breathers in systems with nonlinear and nonlocal dispersive terms, Phys. Rev. E 72 (2005) 056607.
[156] A.V. Gorbach, V. Fleurov, S. Flach, A.M. Miroshnichenko, Resonant light–light interaction in slab waveguides: Angular filters and spectral hole burning, in: A.M. Sergeev (Ed.), Topical Problems of Nonlinear Wave Physics, in: Proc. SPIE, vol. 5975, 2006, pp. 297–306.
[157] G. Grimaldi, G. Filatrella, S. Pace, U. Gambardella, Flux distribution and critical currents in a one-dimensional row of a Josephson junction square lattice, Phys. Lett. A 223 (1996) 463–469.
[158] P. Guyot-Sionnest, Two-phonon bound state for the hydrogen vibration on the H/Si(111) surface, Phys. Rev. Lett. 67 (1991) 2323–2326.
[159] P. Hamm, J. Edler, Nonlinear vibrational spectroscopy: A method to study vibrational self-trapping, in: T. Dauxois, A. Litvak-Hinenzon, R. MacKay, A. Spanoudaki (Eds.), Energy Localization and Transfer, World Scientific, Singapore, 2004, pp. 301–324.
[160] D.W. Heerman, Computer Simulation Methods, Springer, Berlin, 1990.
[161] D. Hennig, Periodic, quasiperiodic, and chaotic localized solutions of a driven, damped nonlinear lattice, Phys. Rev. E 59 (1999) 1637–1645.
[162] D. Hennig, S. Fugmann, L. Schimansky-Geier, P. Haenggi, Self-organized escape of oscillator chains in nonlinear potentials, Phys. Rev. E 76 (2007) 041110.
[163] D. Hennig, H. Gabriel, Designing localized multipulse solutions of the discrete nonlinear Schrödinger equations with an external potential, Phys. Rev. E 57 (1998) 2371–2376.
[164] D. Hennig, K.Ø. Rasmussen, H. Gabriel, A. Bülow, Solitonlike solutions of the generalized discrete nonlinear Schrödinger equation, Phys. Rev. E54 (1996) 5788–5801.

[165] D. Hennig, L. Schimansky-Geier, P. Hänggi, Self-organized, noise-free escape of a coupled nonlinear oscillator chain, Europhys. Lett. 78 (2007) 20002.
[166] G. Huang, Z. Shi, Z. Xu, Asymmetric intrinsic localized modes in a homogeneous lattice with cubic and quartic anharmonicity, Phys. Rev. B47 (1993) 14561–14564.
[167] G. Huang, Z. Xu, W. Xu, Magnetic gap solitons as the intrinsic self-localized magnons in Heisenberg antiferromagnetic chain, J. Phys. Soc. Japan 62 (1993) 3231–3238.
[168] G. Iooss, G. James, Localized waves in nonlinear oscillator chains, Chaos 15 (2005) 015113.
[169] M.V. Ivanchenko, O, I. Kanakov, V.D. Shalfeev, S. Flach, Discrete breathers in transient processes and thermal equilibrium, Physica D 198 (2004) 120–135.
[170] A.G. Izergin, V.E. Koperin, A lattice model corresponding to the non-linear Schrodinger-equation, Dokl. Akad. Nauk SSSR 259 (1981) 76–79.
[171] P. Jakob, Dynamics of the C-O stretch overtone vibration of Co/Ru(001), Phys. Rev. Lett. 77 (1996) 4229–4232.
[172] P. Jakob, Localization and relaxation effects of weakly interacting anharmonic oscillators studied by infrared absorption spectroscopy, Physica D 119 (1998) 109.
[173] P. Jakob, Lateral interactions in (no+o) coadsorbate layers on Ru(001): Fundamental and overtone modes, Surf. Sci. 428 (1999) 309–317.
[174] G. James, Existence of breathers on FPU lattices, C. R. Acad. Sci. Paris 332 (2001) 581–586.
[175] G. James, Centre manifold reduction for quasilinear discrete systems, J. Nonlinear Sci. 13 (2003) 27–63.
[176] G. James, M. Kastner, Bifurcations of discrete breathers in a diatomic Fermi–Pasta–Ulam chain, Nonlinearity 20 (2007) 631–657.
[177] G. James, P. Noble, Breathers on diatomic Fermi–Pasta–Ulam lattices, Physica D 196 (2004) 124–171.
[178] S.M. Jensen, The non-linear coherent coupler, IEEE J. Quant. Electronics 18 (1982) 1580–1583.
[179] M. Johansson, Decay of discrete nonlinear Schrödinger breathers through inelastic multiphonon scattering, Phys. Rev. E 63 (2001) 037601.
[180] M. Johansson, Oscillatory instabilities in Hamiltonian nonlinear lattices: Examples and consequences, in: Proceedings of the International Conference "NONLINEAR DYNAMICS", National Technical University "Kharkov Polytechnical Institute", Ukraine, 2004, pp. 82–86.
[181] M. Johansson, Discrete nonlinear Schrödinger approximation of a mixed Klein-Gordon/Fermi–Pasta–Ulam chain: Modulational instability and a statistical condition for creation of thermodynamic breathers, Physica D 216 (2006) 62.
[182] M. Johansson, S. Aubry, Existence and stability of quasiperiodic breathers in the discrete nonlinear Schrödinger equation, Nonlinearity 10 (1997) 1151–1178.
[183] M. Johansson, S. Aubry, Growth and decay of discrete nonlinear Schrödinger breathers interacting with internal modes or standing-wave phonons, Phys. Rev. E 61 (2000) 5864–5879.
[184] M. Johansson, A.V. Gorbach, Quasiperiodic localized oscillating solutions in the discrete nonlinear Schrödinger equation with alternating on-site potential, Phys. Rev. E 70 (2004) 057604.
[185] M. Johansson, A.M. Morgante, S. Aubry, G. Kopidakis, Standing wave instabilities, breather formation and thermalization in a Hamiltonian anharmonic lattice, Eur. Phys. J. B 29 (2002) 279–283.
[186] M. Johansson, K.Ø. Rasmussen, Statistical mechanics of general discrete nonlinear Schrödinger models: Localization transition and its relevance for Klein-Gordon lattices, Phys. Rev. E 70 (2004) 066610.
[187] M. Johansson, S. Aubry, Y.B. Gaididei, P.L. Christiansen, K.O. Rasmussen, Dynamics of breathers in discrete nonlinear Schrödinger models, Physica D 119 (1998) 115–124.
[188] M. Joyeux, S.Y. Grebenshchikov, J. Bredenbeck, R. Schinke, S.C. Farantos, Intramolecular dynamics along isomerization and dissociation pathways, Adv. Chem. Phys. 130 (2005) 267–303.
[189] B. Juanico, Y.-H. Sanejouand, F. Piazza, P. De Los Rios, Discrete breathers in nonlinear network models of proteins, Phys. Rev. Lett. 99 (2007) 238104.
[190] G. Kalosakas, Multi-peaked localized states of DNLS in one and two dimensions, Physica D 216 (2006) 44–61.
[191] G. Kalosakas, A.R. Bishop, Small-tunneling amplitude boson-Hubbard dimer: Stationary states, Phys. Rev. A 65 (2002) 043616.
[192] G. Kalosakas, A.R. Bishop, V.M. Kenkre, Multiple-timescale quantum dynamics of many interacting bosons in a dimer, J. Phys. B 36 (2003) 3233–3238.
[193] G. Kalosakas, A.R. Bishop, A.P. Shreve, Nonlinear disorder model for Raman profiles in naturally abundant PtCl, Phys. Rev. B 66 (2002) 094303.
[194] G. Kalosakas, K.O. Rasmussen, A.R. Bishop, Non-exponential decay of base-pair opening fluctuations in DNA, Chem. Phys. Lett. 432 (2006) 291–295.
[195] G. Kalosakas, K.O. Rasmussen, A.R. Bishop, C.H. Choi, A. Usheva, Sequence-specific thermal fluctuations identify start sites for DNA transcription, Europhys. Lett. 68 (2004) 127–133.
[196] O.I. Kanakov, S. Flach, M.V. Ivanchenko, K.G. Mishagin, Scaling properties of $q$-breathers in nonlinear acoustic lattices, Phys. Lett. A 365 (2007) 416–420.
[197] N.I. Karachalios, A remark on the existence of breather solutions for the discrete nonlinear Schrödinger equation in infinite lattices: The case of site-dependent anharmonic parameters, Proc. Edinburgh Math. Soc. 49 (2006) 115–129.
[198] Y.V. Kartashov, A. Ferrando, A.A. Egorov, L. Torner, Soliton topology versus discrete symmetry in optical lattices, Phys. Rev. Lett. 95 (2005) 123902-4.
[199] M. Kastner, Dimension dependent energy thresholds for discrete breathers, Nonlinearity 17 (2004) 1923–1939.
[200] M. Kastner, Energy thresholds for discrete breathers, Phys. Rev. Lett. 92 (2004) 104301.
[201] S. Keshavamurthy, Dynamical tunneling in molecules: Quantum routes to energy flow, Int. Rev. Phys. Chem. 26 (2007) 521–584.
[202] P.G. Kevrekidis, B.A. Malomed, Z. Chen, D.J. Frantzeskakis, Stable higher-order vortices and quasivortices in the discrete nonlinear Schrödinger equation, Phys. Rev. E 70 (2004) 056612-9.
[203] P.G. Kevrekidis, K.O. Rasmussen, A.R. Bishop, Two-dimensional discrete breathers: Construction, stability, and bifurcations, Phys. Rev. E 61 (2000) 2006–2009.
[204] J.M. Khalack, Y. Zolotaryuk, P.L. Christiansen, Discrete breathers in classical ferromagnetic lattices with easy-plane anisotropy, Chaos 13 (2003) 683–692.
[205] A. Khare, K.Ø. Rasmussen, M.R. Samuelsen, A. Saxena, Exact solutions of the saturable discrete nonlinear Schrödinger equation, J. Phys. A 38 (2005) 807–814.
[206] S. Kim, C. Baesens, R.S. MacKay, Phonon scattering by localized equilibria of nonlinear nearest-neighbor chains, Phys. Rev. E 56 (1997) R4955–R4958.
[207] S.W. Kim, S. Kim, The structure of eigenmodes and phonon scattering by discrete breathers in the discrete nonlinear Schrödinger chain, Physica D 141 (2000) 91–103.
[208] S.W. Kim, S. Kim, Fano resonances in translationally invariant nonlinear chains, Phys. Rev. B 63 (2001) 212301.
[209] Y. Kinoshita, Y. Yamayose, Y. Doi, A. Nakatani, T. Kitamura, Selective excitations of intrinsic localized modes of atomic scales in carbon nanotubes, Phys. Rev. B 77 (2008) 024307.
[210] S.A. Kiselev, S.R. Bickham, A.J. Sievers, Anharmonic gap modes in a perfect one-dimensional diatomic lattice for standard two-body nearest-neighbor potentials, Phys. Rev. B 48 (1993) 13508–13511.
[211] S.A. Kiselev, A.J. Sievers, G.V. Chester, Eigenvectors of strongly anharmonic intrinsic gap modes in three-dimensional ionic crystals, Physica D 123 (1998) 393–402.
[212] Y.S. Kivshar, M. Peyrard, Modulational instabilities in discrete lattices, Phys. Rev. A 46 (1992) 3198–3205.
[213] Y.S. Kivshar, Creation of nonlinear localized modes in discrete lattices, Phys. Rev. E 48 (1993) 4132–4135.
[214] Yu.S. Kivshar, Intrinsic localized modes as solitons with compact support, Phys. Rev. E 48 (1993) R43–R45.
[215] Yu.S. Kivshar, Localized modes in a chain with nonlinear on-site potential, Phys. Lett. A 173 (1993) 172–178.
[216] Yu.S. Kivshar, G.P. Agrawal, Optical Solitons: From Fibers to Photonic Crystals, Elsevier Science, 2003.
[217] K. Kladko, J. Malek, A.R. Bishop, Intrinsic localized modes in the charge-transfer solid PtCl, J. Phys.: Condens. Matter 11 (1999) L415–L422.
[218] M. Kollmann, T. Bountis, A Mel'nikov approach to soliton-like solutions of systems of discretized nonlinear Schrödinger equations, Physica D 113 (1998) 397–406.
[219] G. Kopidakis, S. Aubry, Intraband discrete breathers in disordered nonlinear systems. i. Delocalization, Physica D 130 (1999) 155–186.

[220] G. Kopidakis, S. Aubry, Discrete breathers and delocalization in nonlinear disordered systems, Phys. Rev. Lett. 84 (2000) 3236–3239.
[221] G. Kopidakis, S. Aubry, Intraband discrete breathers in disordered nonlinear systems. ii. Localization, Physica D 139 (2000) 247–275.
[222] G. Kopidakis, S. Aubry, Discrete breathers in realistic models: Hydrocarbon structures, Physica B 296 (2001) 237–250.
[223] G. Kopidakis, S. Aubry, Localization and targeted transfer of atomic-scale nonlinear excitations: Perspectives for applications, in: T. Dauxois, A. Litvak-Hinenzon, R. MacKay, A. Spanoudaki (Eds.), Energy Localization and Transfer, World Scientific, Singapore, 2004, pp. 355–404.
[224] G. Kopidakis, S. Aubry, G.P. Tsironis, Targeted energy transfer through discrete breathers in nonlinear systems, Phys. Rev. Lett. 87 (2001) 165501.
[225] A.M. Kosevich, B.A. Ivanov, A.S. Kovalev, Magnetic solitons, Phys. Rep. 194 (1990) 117–238.
[226] A.M. Kosevich, A.S. Kovalev, Selflocalization of vibrations in a one-dimensional anharmonic chain, JETP 67 (1974) 1793.
[227] Yu.A. Kosevich, G. Corso, Temporal Fourier spectra of stationary and slowly moving breathers in Fermi–Pasta–Ulam anharmonic lattices, Physica D 170 (2002) 1–12.
[228] Yu.A. Kosevich, S. Lepri, Modulational instability and energy localization in anharmonic lattices at finite energy density, Phys. Rev. B 61 (2000) 299–307.
[229] V. Koukouloyannis, I. Kourakis, Existence of multisite intrinsic localized modes in one-dimensional Debye crystals, Phys. Rev. E 76 (2007) 016402.
[230] V. Koukouloyannis, R.S. MacKay, Existence and stability of 3-site breathers in a triangular lattice, J. Phys. A – Math. General 38 (2005) 1021–1030.
[231] I. Kourakis, P.K. Shukla, Discrete breather modes associated with vertical dust grain oscillations in dusty plasma crystals, Phys. Plasma 12 (2005) 014502.
[232] R. Lai, S.A. Kiselev, A.J. Sievers, Intrinsic localized spin-wave modes in antiferromagnetic chains with single-ion easy-axis anisotropy, Phys. Rev. B 54 (1996) R12665–R12668.
[233] R. Lai, A.J. Sievers, Intrinsic localized spin wave modes in easy-axis antiferromagnetic chains, J. Appl. Phys. 81 (1997) 3972–3974.
[234] R. Lai, A.J. Sievers, $(c_2h_5nh_3)_2cucl_4$: A physical system for the experimental investigation of intrinsic localized modes, Phys. Rev. Lett. 81 (1998) 1937–1940.
[235] R. Lai, A.J. Sievers, Modulational instability of nonlinear spin waves in easy-axis antiferromagnetic chains, Phys. Rev. B 57 (1998) 3433–3443.
[236] R. Lai, A.J. Sievers, Studies of the modulational instability of antiferromagnetic spin waves in 1d, Physica D 123 (1998) 308–314.
[237] R. Lai, A.J. Sievers, Nonlinear nanoscale localization of magnetic excitations in atomic lattices, Phys. Rep. 314 (1999) 147–236.
[238] C. Laroche, T. Dauxois, M. Peyrard, Discreteness effects on soliton dynamics: A simple experiment, Amer. J. Phys. 68 (2000) 552–555.
[239] N. Lazarides, M. Eleftheriou, G.P. Tsironis, Discrete breathers in nonlinear magnetic metamaterials, Phys. Rev. Lett. 97 (2006) 157406.
[240] S. Levy, E. Lahoud, I. Shomroni, J. Steinhauer, The a.c. and d.c. Josephson effects in a Bose–Einstein condensate, Nature 449 (2007) 579.
[241] A.J. Lichtenberg, V.V. Mirnov, C. Day, Dynamics of oscillator chains from high frequency initial conditions: Comparison of phi(4) and FPU-beta models, Chaos 15 (2005) 015109.
[242] E.M. Lifšic, L.P. Pitaevskij, Theory of the Condensed State, in: Statistical Physics, vol. 2, Pergamon Press, Oxford, 1996.
[243] S.-C. Lim, J. Osman, D.R. Tilley, Calculation of nonlinear magnetic susceptibility tensors for a uniaxial antiferromagnet, J. Phys. D: Appl. Phys. 33 (2000) 2899–2910.
[244] Y. Linzon, I. Ilsar, D. Cheskis, R. Morandotti, J.S. Aitchison, S. Bar-Ad, Near-field imaging of nonlinear pulse propagation in planar silica waveguides, Phys. Rev. E 72 (2005) 066607-5.
[245] Y. Linzon, R. Morandotti, M. Volatier, V. Aimez, R. Ares, S. Bar-Ad, Nonlinear scattering and trapping by local photonic potentials, Phys. Rev. Lett. 99 (2007) 133901.
[246] R. Livi, M. Spicci, R.S. MacKay, Breathers on a diatomic FPU chain, Nonlinearity 10 (1997) 1421–1434.
[247] R.S. MacKay, Discrete breathers: Classical and quantum, Physica A 288 (2000) 174–198.
[248] R.S. MacKay, Slow manifolds, in: T. Dauxois, A. Litvak-Hinenzon, R. MacKay, A. Spanoudaki (Eds.), Energy Localization and Transfer, World Scientific, Singapore, 2004, pp. 149–192.
[249] R.S. MacKay, S. Aubry, Proof of existence of breathers for time-reversible or Hamiltonian networks of weakly coupled oscillators, Nonlinearity 7 (1994) 1623–1643.
[250] R.S. MacKay, J.A. Sepulchre, Stability of discrete breathers, Physica D 119 (1998) 148–162.
[251] R.S. MacKay, J.A. Sepulchre, Effective Hamiltonian for travelling discrete breathers, J. Phys. A – Math. General 35 (2002) 3985–4002.
[252] B.A. Malomed, P.G. Kevrekidis, Discrete vortex solitons, Phys. Rev. E 64 (2001) 026601.
[253] D. Mandelik, H.S. Eisenberg, Y. Silberberg, R. Morandotti, J.S. Aitchison, Band-gap structure of waveguide arrays and excitation of floquet-Bloch solitons, Phys. Rev. Lett. 90 (2003) 053902.
[254] D. Mandelik, R. Morandotti, J.S. Aitchison, Y. Silberberg, Gap solitons in waveguide arrays, Phys. Rev. Lett. 92 (2004) 093904-4.
[255] P. Maniadis, T. Bountis, Quasiperiodic and chaotic discrete breathers in a parametrically driven system without linear dispersion, Phys. Rev. E 73 (2006) 046211.
[256] P. Maniadis, S. Flach, Mechanism of discrete breather excitation in driven micro-mechanical cantilever arrays, Europhys. Lett. 74 (2006) 452–458.
[257] M.E. Manley, J.W. Lynn, Y. Chen, G.H. Lander, Intrinsically localized mode in $\alpha$-u as a precursor to a solid-state phase transition, Phys. Rev. B 77 (2008) 052301.
[258] M.E. Manley, M. Yethiraj, H. Sinn, H.M. Volz, A. Alatas, J.C. Lashley, W.L. Hults, G.H. Lander, J.L. Smith, Formation of a new dynamical mode in alpha-uranium observed by inelastic x-ray and neutron scattering, Phys. Rev. Lett. 96 (2006) 125501.
[259] M.E. Manley, M. Yethiraj, H. Sinn, H.M. Volz, A. Alatas, J.C. Lashley, W.L. Hults, G.H. Lander, D.J. Thoma, J.L. Smith, Intrinsically localized vibrations and the mechanical properties of $\alpha$-uranium, J. Alloys Comp. 444–445 (2007) 129–132.
[260] A.A. Maradudin, E.W. Montroll, G.H. Weiss, Theory of Lattice Dynamics in the Harmonic Approximation, Academic Press, New York, 1963.
[261] J.L. Marín, S. Aubry, Breathers in nonlinear lattices: Numerical calculation from the anticontinuous limit, Nonlinearity 9 (1996) 1501–1528.
[262] J.L. Marín, S. Aubry, Fininte size effects on instabilities of discrete breathers, Physica D 119 (1998) 163–174.
[263] J.L. Marín, S. Aubry, L.M. Floria, Intrinsic localized modes: Discrete breathers. Existence and linear stability, Physica D 113 (1998) 283–292.
[264] J.L. Marin, J.C. Eilbeck, F.M. Russell, Localized moving breathers in a 2d hexagonal lattice, Phys. Lett. A 248 (1998) 225–229.
[265] J.L. Marín, F. Falo, P.J. Martínez, L.M. Floría, Discrete breathers in dissipative lattices, Phys. Rev. E 63 (2001) 066603.
[266] P. Marquie, J.M. Bilbaut, M. Remoissenet, Observation of nonlinear localized modes in an electrical lattice, Phys. Rev. E 51 (1995) 6127–6133.
[267] P.J. Martinez, M. Meister, L.M. Floria, F. Falo, Dissipative discrete breathers: Periodic, quasiperiodic, chaotic, and mobile, Chaos 13 (2003) 610–623.
[268] Nicola Marzari, David Vanderbilt, Maximally localized generalized Wannier functions for composite energy bands, Phys. Rev. B 56 (1997) 12847–12865.
[269] J.J. Mazo, Localized excitations in Josephson arrays. Part i: Theory and modelling, in: T. Dauxois, A. Litvak-Hinenzon, R. MacKay, A. Spanoudaki (Eds.), Energy Localization and Transfer, World Scientific, Singapore, 2004, pp. 193–246.
[270] J.J. Mazo, T.P. Orlando, Discrete breathers in Josephson arrays, Chaos 13 (2003) 733–743.
[271] J. Meier, G.I. Stegeman, D.N. Christodoulides, R. Morandotti, G. Salamo, H. Yang, M. Sorel, Y. Silberberg, J.S. Aitchison, Incoherent blocker soliton interactions in kerr waveguide arrays, Opt. Lett. 30 (2005) 3174–3176.
[272] J. Meier, G.I. Stegeman, D.N. Christodoulides, Y. Silberberg, R. Morandotti, H. Yang, G. Salamo, M. Sorel, J.S. Aitchison, Experimental observation of discrete modulational instability, Phys. Rev. Lett. 92 (2004) 163902.
[273] J. Meier, G.I. Stegeman, D.N. Christodoulides, Y. Silberberg, R. Morandotti, H. Yang, G. Salamo, M. Sorel, J.S. Aitchison, Beam interactions with a blocker soliton in one-dimensional arrays, Opt. Lett. 30 (2005) 1027–1029.
[274] T.R.O. Melvin, A.R. Champneys, P.G. Kevrekidis, J. Cuevas, Radiationless traveling waves in saturable nonlinear Schrödinger lattices, Phys. Rev. Lett. 97 (2006) 124101-4.
[275] P. Millar, J.S. Aitchison, J.U. Kang, G.I. Stegeman, A. Villeneuve, G.T. Kennedy, W. Sibbett, Nonlinear waveguide arrays in AlGaAs, J. Opt. Soc. Am. B 14 (1997) 3224–3231.

[276] P.D. Miller, A.C. Scott, J. Carr, J.C. Eilbeck, Binding energies for discrete nonlinear Schrdinger equations, Phys. Scr. 44 (1991) 509–516.
[277] S.F. Mingaleev, Y.B. Gaididei, P.L. Christiansen, Y.S. Kivshar, Nonlinearity-induced conformational instability and dynamics of biopolymers, Europhys. Lett. 59 (2002) 403–409.
[278] S.F. Mingaleev, A.E. Miroshnichenko, Yu.S. Kivshar, K. Busch, All-optical switching, bistability, and slow-light transmission in photonic crystal waveguide-resonator structures, Phys. Rev. E 74 (2006) 046603.
[279] V.V. Mirnov, A.J. Lichtenberg, H. Guclu, Chaotic breather formation, coalescence, and evolution to energy equipartition in an oscillatory chain, Physica D 157 (2001) 251–282.
[280] A.E. Miroshnichenko, S. Flach, M.V. Fistul, Y. Zolotaryuk, J.B. Page, Breathers in Josephson junction ladders: Resonances and electromagnetic waves spectroscopy, Phys. Rev. E 64 (2001) 066601.
[281] A.E. Miroshnichenko, S.F. Mingaleev, S. Flach, Yu.S. Kivshar, Nonlinear Fano resonance and bistable wave transmission, Phys. Rev. E 71 (2005) 036626.
[282] A.E. Miroshnichenko, M. Schuster, S. Flach, M.V. Fistul, A.V. Ustinov, Resonant plasmon scattering by discrete breathers in Josephson junction ladders, Phys. Rev. B 71 (2005) 174306.
[283] M.I. Molina, Transport of localized and extended excitations in a nonlinear Anderson model, Phys. Rev. B 58 (1998) 12547–12550.
[284] R. Morandotti, U. Peschel, J.S. Aitchison, H.S. Eisenberg, Y. Silberberg, Dynamics of discrete solitons in optical waveguide arrays, Phys. Rev. Lett. 83 (1999) 2726–2729.
[285] A.M. Morgante, M. Johansson, G. Kopidakis, S. Aubry, Standing wave instabilities in a chain of nonlinear coupled oscillators, Physica D 162 (2002) 53–94.
[286] O. Morsch, M. Oberthaler, Dynamics of Bose–Einstein condensates in optical lattices, Rev. Modern. Phys. 78 (2006) 179–215.
[287] M.V. Ivanchenko, O.I. Kanakov, K.G. Mishagin, S. Flach, q-breathers in finite two- and three-dimensional nonlinear acoustic lattices, Phys. Rev. Lett. 97 (2006) 025505.
[288] A.H. Nayfeh, Introduction to Perturbation Techniques, John Wiley and Sons, New York, 1993.
[289] Dragomir N. Neshev, Tristram J. Alexander, Elena A. Ostrovskaya, Yuri S. Kivshar, Hector Martin, Igor Makasyuk, Zhigang Chen, Observation of discrete vortex solitons in optically induced photonic lattices, Phys. Rev. Lett. 92 (2004) 123903-4.
[290] S. Neususs, R. Schilling, Multiparticle breathers for a chain with double-quadratic on-site potential, Phys. Rev. E 60 (1999) 6128–6136.
[291] A.C. Newell, J.V. Moloney, Nonlinear Optics, Addison-Wesley, 1992.
[292] J.P. Nguenang, M. Peyrard, A.J. Kenfack, T.C. Kofane, On modulational instability of nonlinear waves in 1d ferromagnetic spin chains, J. Phys. – Condensed Matter 17 (2005) 3083–3112.
[293] P. Noble, Existence of breathers in classical ferromagnetic lattices, Nonlinearity 17 (2004) 803–816.
[294] J. Ohishi, M. Kubota, K. Kawasaki, S. Takeno, Stationary self-localized magnons in Heisenberg antiferromagnets, Phys. Rev. B 55 (1997) 8812–8820.
[295] M. Orendáč, S. Zvyagin, A. Orendáčová, M. Sieling, B. Lüthi, A. Feher, M.W. Meisel, Single-ion bound states in s=1 Heisenberg antiferromagnetic chains with planar anisotropy and subcritical exchange coupling, Phys. Rev. B 60 (1999) 4170–4175.
[296] M. Öster, M. Johansson, A. Eriksson, Enhanced mobility of strongly localized modes in waveguide arrays by inversion of stability, Phys. Rev. E 67 (2003) 056606.
[297] M. Öster, M. Johansson, Stable stationary and quasiperiodic discrete vortex breathers with topological charge $s = 2$, Phys. Rev. E 73 (6) (2006) 066608-6.
[298] A.A. Ovchinnikov, Localized long-lived vibrational states in molecular crystals, Zh. Eksp. Teor. Fiz. / Soviet Phys. JETP 57/30:263/ (1969–1970) 147.
[299] A.A. Ovchinnikov, N.S. Erikhman, K.A. Pronin, Vibrational-Rotational Excitations in Nonlinear Molecular Systems, Kluwer Academic/Plenum Publishers, 2001.
[300] A.A. Ovchinnikov, S. Flach, Discrete breathers in systems with homogeneous potentials: Analytic solutions, Phys. Rev. Lett. 83 (1999) 248–251.
[301] J.B. Page, Asymptotic solutions for localized vibrational modes in strongly anharmonic periodic systems, Phys. Rev. B 41 (1990) 7835–7838.
[302] A. Pankov, Travelling Waves and Periodic Oscillations in Fermi–Pasta–Ulam Lattices, Imperial College Press, London, 2005.
[303] D.E. Pelinovsky, P.G. Kevrekidis, D.J. Frantzeskakis, Persistence and stability of discrete vortices in nonlinear Schrödinger lattices, Physica D 212 (2005) 20–53.
[304] T. Penati, S. Flach, Tail resonances of FPU q-breathers and their impact on the pathway to equipartition, Chaos 17 (2007) 023102.
[305] U. Peschel, O. Egorov, F. Lederer, Discrete cavity solitons, Opt. Lett. 29 (2004) 1909–1911.
[306] U. Peschel, F. Lederer, R. Morandotti, J.S. Aitchison, H. Eisenberg, Y. Silberberg, Steering and locking of discrete solitons in optical waveguide arrays, Act. Phys. Pol. A 99 (2001) 57–65.
[307] U. Peschel, R. Morandotti, J.M. Arnold, J.S. Aitchison, H.S. Eisenberg, Y. Silberberg, T. Pertsch, F. Lederer, Optical discrete solitons in waveguide arrays. 2. Dynamic properties, J. Opt. Soc. Am. B 19 (2002) 2637–2644.
[308] M. Peyrard, The pathway to energy localization in nonlinear lattices, Physica D 119 (1998) 184–199.
[309] M. Peyrard, Using DNA to probe nonlinear localized excitations? Europhys. Lett. 44 (1998) 271–277.
[310] M. Peyrard, A.R. Bishop, Statistical mechanics of a nonlinear model for DNA denaturation, Phys. Rev. Lett. 62 (1989) 2755–2758.
[311] M. Peyrard, J. Farago, Nonlinear localization in thermalized lattices: Application to DNA, Physica A 288 (2000) 199–217.
[312] M. Peyrard, Y. Sire, Breathers in biomolecules? in: T. Dauxois, A. Litvak-Hinenzon, R. MacKay, A. Spanoudaki (Eds.), Energy Localization and Transfer, World Scientific, Singapore, 2004, pp. 325–340.
[313] F. Piazza, S. Lepri, R. Livi, Cooling nonlinear lattices toward energy localization, Chaos 13 (2003) 637–645.
[314] F. Pignatelli, A.V. Ustinov, Observation of breatherlike states in a single Josephson cell, Phys. Rev. E 67 (2003) 036607.
[315] R.A. Pinto, S. Flach, Quantum dynamics of localized excitations in a symmetric trimer molecule, Phys. Rev. A 73 (2006) 022717.
[316] R.A. Pinto, S. Flach, Quantum breathers in capacitively coupled Josephson junctions: Correlations, number conservation, and entanglement, Phys. Rev. B 77 (2008) 024308.
[317] R.A. Pinto, S. Flach, Quantum localized modes in capacitively coupled Josephson junctions, Europhys. Lett. 79 (2007) 66002.
[318] A. Ponno, J. Ruggiero, E. Drigo, J. De Luca, Energy localization in the phi(4) oscillator chain, Phys. Rev. E 73 (2006) 056609.
[319] V. Pouthier, Two-vibron bound states in alpha-helix proteins: The interplay between the intramolecular anharmonicity and the strong vibron-phonon coupling, Phys. Rev. E 68 (2003) 021909.
[320] V. Pouthier, Two-vibron bound states lifetime in a one-dimensional molecular lattice coupled to acoustic phonons, J. Chem. Phys. 118 (2003) 3736–3747.
[321] L. Proville, Biphonons in the Klein-Gordon lattice, Phys. Rev. B 71 (2005) 104306.
[322] L. Proville, Dynamical structure factor of a nonlinear Klein-Gordon lattice, Phys. Rev. B 72 (2005) 184301.
[323] L. Proville, Two-phonon pseudogap in the Klein-Gordon lattice, Europhys. Lett. 69 (2005) 763.
[324] L. Proville, Quantum breathers in a nonlinear Klein Gordon lattice, Physica D 216 (2006) 191–199.
[325] Wen-Xin Qin, Xufeng Xiao, Homoclinic orbits and localized solutions in nonlinear Schrödinger lattices, Nonlinearity 20 (2007) 2305–2317.
[326] S. Rakhmanova, D.L. Mills, Nonlinear spin excitations in finite Heisenberg chains, Phys. Rev. B 54 (1996) 9225–9231.
[327] K.Ø. Rasmussen, S. Aubry, A.R. Bishop, G.P. Tsironis, Discrete nonlinear Schrödinger breathers in a phonon bath, Eur. Phys. J. B 15 (2000) 169–175.
[328] K.Ø. Rasmussen, A.R. Bishop, N. Grønbech-Jensen, Creation and annihilation of intrinsic localized excitations, Phys. Rev. E 58 (1998) R40–R43.
[329] K.Ø. Rasmussen, T. Cretegny, P.G. Kevrekidis, N. Grønbech-Jensen, Statistical mechanics of a discrete nonlinear system, Phys. Rev. Lett. 84 (2000) 3740–3743.
[330] R. Reigada, A. Sarmiento, K. Lindenberg, Breathers and thermal relaxation in Fermi–Pasta–Ulam arrays, Chaos 13 (2003) 646–656.
[331] P. Rosenau, Nonlinear dispersion and compact structures, Phys. Rev. Lett. 73 (1994) 1737–1741.
[332] P. Rosenau, J.M. Hyman, Compactons — solitons with finite wavelength, Phys. Rev. Lett. 70 (1993) 564–567.
[333] P. Rosenau, S. Schochet, Almost compact breathers in anharmonic lattices near the continuum limit, Phys. Rev. Lett. 94 (2005) 045503.

[334] P. Rosenau, S. Schochet, Compact and almost compact breathers: A bridge between an anharmonic lattice and its continuum limit, Chaos 15 (2005) 015111.
[335] T. Rossler, J.B. Page, Driven intrinsic localized modes and their stability in anharmonic lattices with realistic potentials, Physica B 220 (1996) 387–389.
[336] T. Rossler, J.B. Page, Creation of intrinsic localized modes via optical control of anharmonic lattices, Phys. Rev. Lett. 78 (1997) 1287–1290.
[337] T. Rossler, J.B. Page, Optical creation of vibrational intrinsic localized modes in anharmonic lattices with realistic interatomic potentials, Phys. Rev. B 62 (2000) 11460–11472.
[338] B. Rumpf, Simple statistical explanation for the localization of energy in nonlinear lattices with two conserved quantities, Phys. Rev. E 69 (2004) 016618.
[339] B. Rumpf, Transition behavior of the discrete nonlinear Schrödinger equation, Phys. Rev. E 77 (2008) 036606.
[340] B. Rumpf, A.C. Newell, Localization and coherence in nonintegrable systems, Physica D 184 (2003) 162–191.
[341] F.M. Russell, J.C. Eilbeck, Evidence for moving breathers in a layered crystal insulator at 300K, Europhys. Lett. 78 (2007) 10004.
[342] F.M. Russell, Y. Zolotaryuk, J.C. Eilbeck, T. Dauxois, Moving breathers in a chain of magnetic pendulums, Phys. Rev. B 55 (1997) 6304–6308.
[343] B. Sanchez-Rey, G. James, J. Cuevas, J.F.R. Archilla, Bright and dark breathers in Fermi–Pasta–Ulam lattices, Phys. Rev. B 70 (2004) 014301.
[344] K.W. Sandusky, J.B. Page, Interrelation between the stability of extended normal modes and the existence of intrinsic localized modes in nonlinear lattices with realistic potentials, Phys. Rev. B 50 (1994) 866–887.
[345] K.W. Sandusky, J.B. Page, K.E. Schmidt, Stability and motion of intrinsic localized modes in nonlinear periodic lattices, Phys. Rev. B46 (1992) 6161.
[346] M. Sato, L.Q. English, B.E. Hubbard, A.J. Sievers, Influence of sample shape on the production of intrinsic localized modes in an antiferromagnetic lattice, J. Appl. Phys. 91 (2002) 8676–8678.
[347] M. Sato, B.E. Hubbard, L.Q. English, A.J. Sievers, B. Ilic, D.A. Czaplewski, H.G. Craighead, Study of intrinsic localized vibrational modes in micromechanical oscillator arrays, Chaos 13 (2003) 702–715.
[348] M. Sato, B.E. Hubbard, A.J. Sievers, Nonlinear energy localization and its manipulation in micromechanical oscillator arrays, Rev. Modern Phys. 78 (2006) 137–157.
[349] M. Sato, B.E. Hubbard, A.J. Sievers, B. Ilic, H.G. Craighead, Optical manipulation of intrinsic localized vibrational energy in cantilever arrays, Europhys. Lett. 66 (2004) 318–323.
[350] M. Sato, B.E. Hubbard, A.J. Sievers, B. Ilic, D.A. Czaplewski, H.G. Craighead, Observation of locked intrinsic localized vibrational modes in micromechanical oscillator arrays, Phys. Rev. Lett. 90 (2003) 044102.
[351] M. Sato, A.J. Sievers, Direct observation of the discrete character of intrinsic localized modes in an antiferromagnet, Nature 432 (2004) 486–488.
[352] M. Sato, A.J. Sievers, Counting discrete emission steps from intrinsic localized modes in a quasi-one-dimensional antiferromagnetic lattice, Phys. Rev. B 71 (2005) 214306–2143014.
[353] M. Sato, A.J. Sievers, Driven localized excitations in the acoustic spectrum of small nonlinear macroscopic and microscopic lattices, Phys. Rev. Lett. 98 (2007) 214101.
[354] M. Sato, S. Yasui, M. Kimura, T. Hikihara, A.J. Sievers, Management of localized energy in discrete nonlinear transmission lines, EPL 80 (2007) 30002.
[355] A.V. Savin, Y.S. Kivshar, Discrete nonlinear breathing models in carbon nanotubes. arXiv:0705.4482v1 [nlinl.ps], 2007.
[356] A.V. Savin, L.I. Manevitch, Discrete breathers in a plyethylene chain, Phys. Rev. B 67 (2003) 144302.
[357] V.V. Schmidt, The Physics of Superconductors, Springer, Berlin, 1997.
[358] S.A. Schöefield, R.E. Wyatt, P.G. Wolynes, Computational study of many-dimensional quantum vibrational energy redistribution. i. Statistics of the survival probability, J. Chem. Phys. 105 (1996) 940–952.
[359] L.S. Schulman, D. Tolkunov, E. Mihokova, Stability of quantum breathers, Phys. Rev. Lett. 96 (2006) 065501.
[360] L.S. Schulman, D. Tolkunov, E. Mihokova, Structure and time-dependence of quantum breathers, Chem. Phys. 322 (2006) 55–74.
[361] M. Schuster, P. Binder, A.V. Ustinov, Observation of breather resonances in Josephson ladders, Phys. Rev. E 65 (2002) 016606.
[362] M. Schuster, F. Pignatelli, A.V. Ustinov, Spontaneous creation of discrete breathers in Josephson arrays, Phys. Rev. B 69 (2004) 094507.
[363] U.T. Schwarz, L.Q. English, A.J. Sievers, Experimental generation and observation of intrinsic localized spin wave modes in an antiferromagnet, Phys. Rev. Lett. 83 (1999) 223–226.
[364] A.C. Scott, J.C. Eilbeck, H. Gilhoj, Quantum lattice solitons, Physica D 78 (1994) 194–213.
[365] J.A. Sepulchre, R.S. MacKay, Localized oscillations in conservative or dissipative networks of weakly coupled autonomous oscillators, Nonlinearity 10 (1997) 679–713.
[366] J.A. Sepulchre, R.S. MacKay, Discrete breathers in disordered media, Physica D 113 (1998) 342–345.
[367] D.L. Shepelyansky, Delocalization of quantum chaos by weak nonlinearity, Phys. Rev. Lett. 70 (1993) 1787–1790.
[368] A.J. Sievers, J.B. Page, Unusual anharmonic local mode systems, in: G.K. Horton, A.A. Maradudin (Eds.), Dynamical Properties of Solids VII Phonon Physics The Cutting Edge, Elsevier, Amsterdam, 1995, p. 137.
[369] A.J. Sievers, S. Takeno, Intrinsic localized modes in anharmonic crystals, Phys. Rev. Lett. 61 (1988) 970–973.
[370] Y. Sire, G. James, Numerical computation of travelling breathers in Klein-Gordon chains, Physica D 204 (2005) 15–40.
[371] D.V. Skryabin, Energy of internal modes of nonlinear waves and complex frequencies due to symmetry breaking, Phys. Rev. E 64 (2001) 055601(R).
[372] J.M. Speight, P.M. Sutcliffe, Discrete breathers in anisotropic ferromagnetic spin chains, J. Phys. A: Math. General 34 (2001) 10839–10858.
[373] R. Stearrett, L.Q. English, Experimental generation of intrinsic localized modes in a discrete electrical transmission line, J. Phys. D 40 (2007) 5394–5398.
[374] M. Stepic, D. Kip, L. Hadzievski, A. Maluckov, One-dimensional bright discrete solitons in media with saturable nonlinearity, Phys. Rev. E 69 (2004) 066618.
[375] B.I. Swanson, J.A. Brozik, S.P. Love, G.F. Strouse, A.P. Shreve, A.R. Bishop, W.-Z. Wang, M.I. Salkola, Observation of intrinsically localised modes in a discrete low-dimensional material, Phys. Rev. Lett. 82 (1999) 3288–3291.
[376] R.L. Swofford, M.E. Long, A.C. Albrecht, C-h vibrational states of benzen, naphtalene, and anthracene in the visible region by thermal lensing spectroscopy and the local mode model, J. Chem. Phys. 65 (1976) 179.
[377] S. Takeno, K. Kawasaki, Intrinsic self-localized magnons in one-dimensional antiferromagnets, Phys. Rev. B 45 (1992) 5083–5086.
[378] S. Takeno, K. Kisoda, A.J. Sievers, Intrinsic localized vibrational modes in anharmonic crystals, Prog. Theor. Phys. Suppl. 94 (1988) 242–269.
[379] S. Takeno, M. Peyrard, Nonlinear rotating modes: Green's function solution, Phys. Rev. E 55 (1997) 1922–1928.
[380] S. Takeno, A.J. Sievers, Anharmonic resonant modes in perfect crystals, Solid State Commun. 67 (1988) 1023–1026.
[381] S. Takeno, K. Kawasaki, Stationary self-localized magnons in Heisenberg antiferromagnets, J. Phys. Soc. Japan 60 (1991) 1881–1884.
[382] S. Takeno, K. Kawasaki, SU(2) coherent state path integral formulation of nonlinear collective modes of magnons in Heisenberg antiferromagnets self-localized magnons and vortices, J. Phys. Soc. Jpn. 61 (1992) 4547–4558.
[383] N. Theodorakopoulos, Statistical physics of localized vibrations, in: T. Dauxois, A. Litvak-Hinenzon, R. MacKay, A. Spanoudaki (Eds.), Energy Localization and Transfer, World Scientific, Singapore, 2004, pp. 341–354.
[384] N. Theodorakopoulos, M. Peyrard, R.S. MacKay, Nonlinear structures and thermodynamic instabilities in a one-dimensional lattice system, Phys. Rev. Lett. 93 (2004) 258101.
[385] M. Toda, Theory of Nonlinear Lattices, Springer Verlag, Berlin, 1989.
[386] E. Trías, J.J. Mazo, T.P. Orlando, Discrete breathers in nonlinear lattices: Experimental detection in a Josephson array, Phys. Rev. Lett. 84 (2000) 741–744.
[387] G.P. Tsironis, If "discrete breathers" is the answer, what is the question? Chaos 13 (2003) 657–666.
[388] G.P. Tsironis, S. Aubry, Slow relaxation phenomena induced by breathers in nonlinear lattices, Phys. Rev. Lett. 77 (1996) 5225–5228.
[389] A. Tsurui, Wave modulations in anharmonic lattices, Prog. Theor. Phys. 48 (1972) 1196.

[390] K. Ullmann, A.J. Lichtenberg, G. Corso, Energy equipartition starting from high-frequency modes in the Fermi–Pasta–Ulam beta oscillator chain, Phys. Rev. E 61 (2000) 2471–2477.
[391] A.V. Ustinov, Imaging of discrete breathers, Chaos 13 (2003) 716–724.
[392] A.V. Ustinov, Localized excitations in Josephson arrays. Part i: Experiments, in: T. Dauxois, A. Litvak-Hinenzon, R. MacKay, A. Spanoudaki (Eds.), Energy Localization and Transfer, World Scientific, Singapore, 2004, pp. 247–272.
[393] R.A. Vicencio, J. Brand, S. Flach, Fano blockade by a Bose–Einstein condensate in an optical lattice, Phys. Rev. Lett. 98 (2007) 184102.
[394] R.A. Vicencio, M. Johansson, Discrete soliton mobility in two-dimensional waveguide arrays with saturable nonlinearity, Phys. Rev. E 73 (2006) 046602.
[395] R.A. Vicencio, A.V. Gorbach, S. Flach, Fano resonance in two-dimensional optical waveguide arrays with a bi-modal defect, Phys. Lett. A 354 (2006) 210–213.
[396] R.F. Wallis, D.L. Mills, A.D. Boardman, Intrinsic localized spin modes in ferromagnetic chains with on-site anisotropy, Phys. Rev. B 52 (1995) R3828–R3831.
[397] W.Z. Wang, A.R. Bishop, J.T. Gammel, R.N. Silver, Quantum breathers in electron–phonon systems, Phys. Rev. Lett. 80 (1998) 3284–3287.
[398] W.Z. Wang, J. Tinka Gammel, A.R. Bishop, M.I. Salkola, Quantum breathers in a nonlinear lattice, Phys. Rev. Lett. 76 (1996) 3598–3601.
[399] M.I. Weinstein, Excitation thershold for nonlinear localized modes on lattices, Nonlinearity 12 (1999) 673–691.
[400] G. Wellein, H. Fehske, Self-trapping problem of electrons or excitons in one dimension, Phys. Rev. B 58 (1998) 6208–6218.
[401] K. Winkler, G. Thalhammer, F. Lang, R. Grimm, J. Hecker Denschlag, A.J. Daley, A. Kantian, H.P. Buechler, P. Zoller, Repulsively bound atom pairs in an optical lattice, Nature 441 (2006) 853–856.
[402] G.B. Witham, Linear and Nonlinear Waves, Wiley, New York, 1974.
[403] J.P. Wrubel, M. Sato, A.J. Sievers, Controlled switching of intrinsic localized modes in a one-dimensional antiferromagnet, Phys. Rev. Lett. 95 (2005) 264101–264104.
[404] Q. Xu, S. Sandhu, M.L. Povinelli, J. Shakya, S. Fan, M. Lipson, Experimental realization of an on-chip all-optical analogue to electromagnetically induced transparency, Phys. Rev. Lett. 96 (2006) 123901–123904.
[405] J.-K. Xue, A.-X. Zhang, J. Liu, Self-trapping of Bose–Einstein condensates in optical lattices: The effect of lattice dimension, Phys. Rev. A 77 (2008) 013602.
[406] Y. Yamayose, Y. Kinoshita, Y. Doi, A. Nakatani, T. Kitamura, Excitation of intrinsic localized modes in a graphene sheet, EPL 80 (2007) 40008.
[407] A. Yariv, Y. Xu, R.K. Lee, A. Scherer, Coupled-resonator optical waveguide: A proposal and analysis, Opt. Lett. 24 (1999) 711–713.
[408] K. Yoshimura, Y. Doi, Moving discrete breathers in a nonlinear lattice: Resonance and stability, Wave Motion 45 (2007) 83–99.
[409] X. Yuan, Construction of quasiperiodic breathers via KAM technique, Commun. Math. Phys. 261 (2002) 61–100.
[410] Y. Zolotaryuk, S. Flach, V. Fleurov, Discrete breathers in classical spin lattices, Phys. Rev. B 63 (2001) 214422.
[411] S.A. Zvyagin, J. Wosnitza, C.D. Batista, M. Tsukamoto, N. Kawashima, J. Krzystek, V.S. Zapf, M. Jaime Jr., N.F. Oliveira, A. Paduan-Filho, Magnetic excitations in the spin-1 anisotropic Heisenberg antiferromagnetic chain system, Phys. Rev. Lett. 98 (2007) 047205.
[412] A. Zygmund, Trigonometric Series, Cambridge University Press, 1968.